LWI

Leichtweiß-Institute for Hydraulic Engineering and Water Resources
Dept. of Hydromechanics and Coastal Engineering

Technische
Universität
Braunschweig

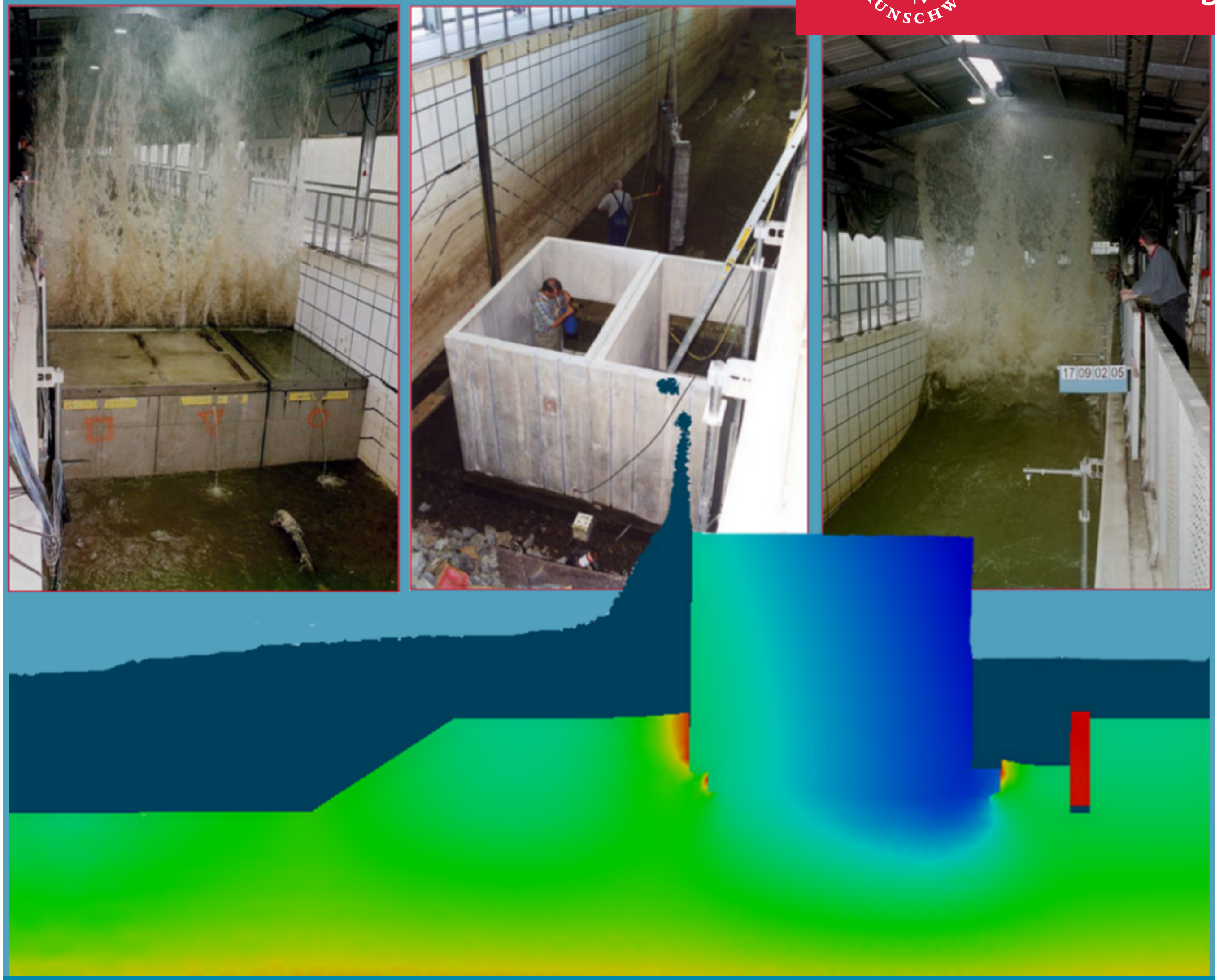

Modelling and Analysis of Wave-Structure-Foundation Interaction for Monolithic Breakwaters

Hisham Elsafti

Braunschweig, 2015

Modelling and Analysis of Wave-Structure-Foundation Interaction for Monolithic Breakwaters

Von der
Fakultät Architektur, Bauingenieurwesen und Umweltwissenschaften
der Technischen Universität Carolo-Wilhelmina
zu Braunschweig

zur Erlangung des Grades eines
Doktoringenieurs (Dr.-Ing.)
genehmigte

Dissertation

von
Hisham Elsafti, M.Sc.
geboren am 04. Dezember 1980
aus Alexandria, Ägypten

Eingereicht am: 08. Mai 2015
Disputation am: 30. Juli 2015

Berichterstatter: Prof. Dr.-Ing. Hocine Oumeraci
Prof. Dr. Peter Troch

2015

To my family and in loving memory of my father

Acknowledgment

My PhD has been a long and hard endeavour, not short of frustrations. I would not have made this journey without the help and support of several individuals, for whom I am forever obliged.

My sincere gratitude is to my adviser Professor Hocine Oumeraci for accepting me as his student and giving me the chance to do my doctoral studies in Germany and letting me be part of a coastal engineering worldwide leading research team. Regardless of his persistent commitments, he always takes the initiative to reach out to his students. I am indebted to him for his patience and help throughout the time of my PhD. I enjoyed our long meetings and how they sometimes deviate off topic and turn into discussions on science and its history. I have always admired his enthusiasm and passion for science and engineering. It is an honour to work with him.

I am grateful to Matthias Kudella for introducing me to the large-scale GWK caisson breakwater experiments and providing assistance with their results. His previous work on the topic has been invaluable to me and to this thesis. Discussions with Matthias have always been enlightening and educational.

I greatly appreciate the effort of Professor Peter Troch in reviewing the manuscript and providing me with valuable comments. I would like to thank Professor Andreas Kortenhaus and Stefan Schimmels for their constant help and support during my doctoral studies. I would like to extend my thanks to Rainer Kvapil for providing technical support and helping with the numerical servers.

I owe my heartfelt gratitude to Gabriele Fournier, Markus Brühl and their families for their kind and warm reception of my family and me. I am also privileged to have worked with many wonderful colleges at the Leichtweiss Institute in Braunschweig and the Coastal Research Center (FZK) in Hanover and hope our friendship will last.

Financial support for my doctoral studies from the Egyptian Ministry of Higher Education and Scientific Research (MHESR) and the German Academic Exchange Service (DAAD) through the German-Egyptian Long-Term Scholarship (GERLS) is gratefully acknowledged.

Last but definitely not least I am forever indebted to my family for their love, support and sacrifices, especially my dear wife who has always provided me with great moral support and had to sacrifice the most during the period of my PhD. I dedicate this work to my family and to the memory of my father. May God receive my parents with great mercy for striving to raise me from young.

Hisham Elsafti
Braunschweig, 2015

Abstract

New breakwaters are needed to meet the growing international maritime trade. Caisson breakwaters are generally preferred to other types of structures in terms of construction time, quality control, maintenance, multi-purpose use and environmental aspects. Nevertheless, they are more vulnerable to foundation failures, especially to stepwise failures. Due to the highly complex processes involved in wave-structure-foundation interaction, no reliable model yet exists for this failure mechanism, which may occur under relatively moderate wave conditions. Therefore, a semi-coupled CFD-CSD model and a simplified model are developed in OpenFOAM to describe wave-structure-foundation interaction for monolithic breakwaters, and particularly stepwise failures.

The CFD model is an extension of the incompressible multiphase Eulerian solver of OpenFOAM by introducing different seepage laws for non-deformable porous media. Moreover, a term is added in the continuity equation to account for fluid compressibility without noticeable increase in computational time. The extended CFD model is successfully applied to reproduce measured breaking wave impact loads including the effect of entrapped air.

A new CSD model is developed to solve the fully coupled, fully dynamic Biot equations. A new approach to solve these equations is implemented taking advantage of the segregated approach and using the PISO algorithm to resolve pore fluid velocity-pressure coupling. Soil-structure interaction is introduced via a frictional contact model that can simulate sliding, separation and reattachment of the structure and the underlying soil. A multi-surface plasticity model is implemented to reproduce the most relevant aspects of the response of the soil beneath a monolithic breakwater (e.g. cyclic mobility). The CSD model is validated against benchmark cases, analytical solutions and laboratory experiments. The model succeeded to reproduce measured wave-induced residual pore pressure buildup and soil densification followed by pore pressure dissipation.

A one-way coupling of both CFD and CSD models is implemented, which transforms the CFD model output into input for the CSD model. The semi-coupled model system is applied successfully to reproduce selected results of a caisson breakwater subject to breaking wave impact loads tested in the Large Wave Flume (GWK). Moreover, the model system is applied to expand the range of conditions tested in GWK for the response of the soil foundation, with a particular focus on the role of transient and residual pore pressure on residual deformations of soil and subsequent residual displacements of the structure.

Based on the results of the analysis of the numerical and experimental data, a new concept, called *load eccentricity concept*, is proposed to classify the response of the foundation in *four load eccentricity regimes*. This concept is based on the relative eccentricity e/B, i.e. the ratio of eccentricity e of the vertical force resultant from the mid-point of the foundation-structure interface related to width B of this interface. In fact, the relative eccentricity carries all significant information related to the wave loads (horizontal and uplift forces) and to the properties of the structure (mass and geometry).

In the light of the results obtained from the analysis of both numerical and experimental data using this new concept, recommendations are drawn for the design of monolithic breakwaters, and a new simplified nonlinear 3-DOF mass-spring-dashpot model is developed for preliminary analysis. Elastoplastic vertical springs are introduced by updating the stiffness at each time step and separating loading from unloading states for each spring. Model parameters are calibrated using the results from the CFD-CSD model for different types of sand identified by their relative density and different load eccentricities. The simplified model can simulate stepwise failure (sliding, settlement and tilt) as well as the overall failure (overturning).

The limitations of the model are discussed and recommendations for further development and research are provided.

Zusammenfassung

Aufgrund des stark wachsenden internationalen Seehandels wird auch der Bedarf an neuen Wellenbrechern entsprechend zunehmen. Caisson Wellenbrecher werden in der Regel anderen herkömmlichen Bauweisen, insbesondere aufgrund Bauzeit, Qualitätskontrolle, Unterhaltung, Mehrzwecknutzung und Umweltaspekten bevorzugt. Jedoch sind sie für das Versagen des Baugrundes, insbesondere gegen schrittweises Versagen, empfindlicher. Aufgrund der hohen Komplexität der Wellen-Bauwerk-Boden Interaktion liegt noch kein verlässliches Modell zur Beschreibung dieses Versagensmechanismus vor, der bei moderatem Seegang eintreten kann. Um diese Interaktion und diesen Versagensmechanismus für monolithische Wellenbrecher beschreiben zu können, werden ein semi-gekoppeltes CFD-CSD Modellsystem und ein vereinfachtes Modell in OpenFOAM entwickelt.

Das CFD-Modell stellt eine durch mehrere Sickerströmungsgesetze erweiterte Version (in nicht verformbaren porösen Medien) des inkompressiblen mehrphasigen Euler Strömingslösers von OpenFOAM dar. Für die Fluidkompressibilität wird ein Term in die Kontinuitätsgleichung eingeführt, ohne die Rechenzeit merklich zu erhöhen. Das erweiterte CFD-Modell wird erfolgreich eingesetzt, um gemessene Druckschlagbelastungen durch brechende Wellen mit Lufteinschlüssen zu reproduzieren.

Ein neues CSD-Modell wird für die Lösung der voll gekoppelten, voll dynamischen Biot-Gleichungen entwickelt. Für die Lösung dieser Gleichungen wird ein neuer Ansatz implementiert. Dabei werden die Vorteile des getrennten Ansatzes und des PISO-Algorithmus genutzt, um die Kopplung von Geschwindigkeit und Druck des Porenfluids zu lösen. Die Bauwerk-Boden Interaktion wird über ein Reibungs-Kontaktmodell eingeführt. Dadurch können das Gleiten, die Trennung und die Wiederzusammenführung der Struktur und des darunter liegenden Bodens simuliert werden.

Für die Plastizität des Bodens wird ein Mehrflächenmodell implementiert, um die relevantesten Prozesse des Bodenverhaltens unter einem monolithischen Wellenbrecher (z.B. zyklische Mobilität) zu reproduzieren. Das CSD-Modell wird durch Benchmarking-Fälle, analytische Lösungen und Laborversuche validiert. Mit dem Modell ist es gelungen, Messungen über die Entwicklung des welleninduzierten Porenwasserdruckaufbaus, der Bodenverdichtung und der anschließenden Dissipation des Porenwasserdruckes relativ gut zu reproduzieren.

Es wird eine Einweg-Kopplung der beiden CFD- und CSD-Modelle implementiert. Dabei werden die Outputs des CFD-Modells als Inputs für das CSD-Modell aufbereitet. Das validierte semi-gekoppelte Modellsystem wird erfolgreich verwendet, um ausgewählte Experimente im Großen Wellenkanal (GWK) zur Druckschlagbelastung eines Caisson-Wellenbrechers zu reproduzieren. Darüber hinaus wird das Modellsystem eingesetzt, um die Bandbreite der im GWK getesteten Bedingungen hinsichtlich des dynamischen Baugrunderhaltens zu erweitern. Dabei wird insbesondere auf die transienten und die verbleibenden Porenwasserdrücke/Bodenverformungen sowie auf die anschließenden Verschiebungen des Bauwerkes fokussiert.

Auf der Grundlage der Analyse der numerischen und experimentellen Daten wird ein neues Konzept, genannt *„Lastexzentrizitätskonzept“*, eingeführt, das die Klassifizierung des Gründungsverhaltens in vier *Lastexzentrizität-Regime* ermöglicht. Dieses Konzept basiert auf der relativen Exzentrizität e/B, d.h. dem Verhältnis der Exzentrizität e der resultierenden Vertikalkraft im Mittelpunkt der Schnittstelle Bauwerk-Gründung zur Breite B dieser Schnittstelle. Der Parameter e/B fasst alle relevanten Informationen der Wellenbelastung (Horizontal- und Auftriebskräfte) und der Bauwerkseigenschaften (Masse und Geometrie) zusammen.

Aus den Ergebnissen der Analyse der numerischen und gemessenen Daten unter Anwendung dieses neuen Konzepts werden Empfehlungen für die Bemessung monolithisches Wellenbrechers ausgesprochen. Darüber hinaus wird ein vereinfachtes nichtlineares 3-DOF Masse-Feder-Dämpfer Modell für Analysen in der Vorentwurfsphase entwickelt. Dabei werden die elasto-plastischen Vertikalfedern durch Aktualisierung der Steifigkeit bei jedem Zeitschritt und durch Trennung der Belastungs- und Entlastungszustande eingefügt. Die Modellparameter werden anhand der CFD-CSD Modellergebnisse für unterschiedliche Sandböden, die durch deren relative Dichte und Lastexzentrizität identifiziert werden, kalibriert. Das vereinfachte Modell kann das schrittweise Versagen (Gleiten, Setzung und Kippen) sowie das Gesamtversagen (Umkippen) simulieren. Eine Diskussion der Grenzen des Modells sowie Empfehlungen für die weitere Entwicklung und Forschung werden aufgeführt.

Contents

List of Tables

List of Figures

Nomenclature

α	Solid skeleton compressibility [m^2/kN]
α_{bed}	Angle of seabed slope
β	Fluid compressibility [m^2/kN]
$\boldsymbol{\sigma}$	Stress tensor [kN/m^2]
$\boldsymbol{\tau}$	Shear stress tensor [kN/m^2]
$\boldsymbol{\varepsilon}$	Strain tensor
χ	Factor for the damping coefficient to account for effect of elastoplastic springs
Δh	Horizontal displacement of caisson at midpoint of deck
Δv	Vertical displacement of caisson at midpoint of deck
Δ	The mean filter size for LES models [m]
ϵ	The energy dissipation rate caused by fluid viscous effects
Γ	Numerical domain boundary
γ	Phase fraction
$\mathbf{C}$	The damping matrix
$\mathbf{f}$	The external force vector
$\mathbf{I}$	The identity tensor
$\mathbf{K}$	The stiffness matrix
$\mathbf{M}$	The mass matrix
$\mathbf{R}$	Tensor of additional stress induced by unresolved fluid turbulence fluctuations [kN/m^2]
$\mathbf{S}$	Sink term (vector) for modelling porous media resistance to flow in momentum balance equation [kN]
$\mathbf{u}_\mathbf{w}^\mathbf{r}$	Total pore fluid displacement relative to solid skeleton
$\mathbf{u}_\mathbf{w}$	Total pore fluid displacement
$\mathbf{U}$	Fluid mixture (intrinsic) velocity vector [m/s]
$\mathbf{u}$	The displacement vector [m]
μ	Dynmic viscosity [N.s/m^2]
μ	Friction coefficient
μ_t	Dynmic eddy viscosity [N.s/m^2]

∇	The del (Nabla) operator
ν	Kinematic viscosity [m$^2/s$]
ν_t	Kinematic eddy viscosity [m$^2/s$]
ω	Specific dissipation rate
$\overline{\mathbf{U}}$	Fluid mixture ensemble average (Darcy's) velocity vector [m/s]
ϕ	Angle of internal friction
ϕ_{cv}	Angle of internal friction at critical state
ρ_f	Air-water fluid mixture mass density [kg/m^3]
ρ_s	The mass density of the solid phase (particles) [kg/m^3]
σ'_{v0}	The initial effective vertical stress [kN/m^2]
σ_{VM}	Von Mises stress [kN/m^2]
τ	Shear stress [kN/m^2]
θ	Caisson angle of rotation (tilt)
ζ	Loading flag; 1 is loading and 0 is unloading
B	Caisson base breadth (defined at interface with foundation) [m]
c_A	The added mass coefficient
c_i	Damping coefficient of the i^{th} dashpot [kN.s/m]
C_M	The virtual mass coefficient
c_v	Coefficient of consolidation [m$^2/s$]
$d\Phi$	Densification increment
D_r	Relative density
d_s	Breaking water depth at the wall [m]
d_w	Still water depth at the wall [m]
D_{15}	The sieve size at which 15% particles pass [m]
D_{50}	The equivalent mean diameter of the porous media particles [m]
D_{EQ}	The equivalent diameter of porous media particles [m]
$d_{vb,r}$	Residual component of the caisson shoreside vertical motion [m]
$d_{vb,t}$	Transient component of the caisson shoreside vertical motion [m]
E	Modulus of elasticity [kN/m^2]
e	Load eccentricity [m]
e	Voids ratio

F_H	Horizontal force on caisson [kN/m]
F_U	Uplift force on caisson [kN/m]
F_V	Vertical force on caisson [kN/m]
G	Shear modulus [kN/m^2]
H	Water wave height [m]
h_s	Still water depth measured from seabed level [m]
I	The hydraulic gradient
I_z	Moment of inertia at pivot of caisson [m^4]
I_D	Soil density index
K	Average bulk modulus of the solid skeleton
k	Hydraulic conductivity [m/s]
k	Turbulence kinetic energy [m$^2/s^2$]
K_i	Stiffness of the i^{th} spring [kN/m]
K_s	Bulk modulus of the solid grains material
L	Water wave length [m]
L_D	Length of drainage path [m]
M	Rotational moment [kN.m/m]
m_x, m_y	Caisson mass in x, y directions [kg]
M_{50}	The average mass of a rock grading [kg]
m_{geo}	Geodynamic added mass [kg]
m_{hyd}	Hydrodynamic added mass [kg]
M_t	Time history of total moment around caisson heel [kN.m/m]
n	Porosity
N_L	Number of loading cycles to liquefaction
p	Fluid (pore) pressure [kN/m^2]
P_i	Load on the i^{th} spring [kN]
p_r	Residual pore pressure [kN/m^2]
p_t	Pore pressure time history [kN/m^2]
P_{ult}	Ultimate spring load [kN]
q_c	Cone resistance for cone penetration test [kN/m^2]
q_{ult}	Ultimate soil bearing capacity [kN/m^2]

Re_p	Pore Reynolds number
S	Degree of Saturation
S_s	The magnitude of the strain rate tensor
T	Water wave period [s]
T_{Drain}	Drainage period [s]
T_{Load}	Cyclic load period [s]
v_H	Horizontal velocity of breaker [m/s]
v_V	Vertical upward velocity of the water surface directly at the wall [m/s]
W	The deviatoric strain energy [kg.m$^2/s^2$]
ALE	Arbitrary Lagrangian Eulerian
BEM	Boundary Element Method
CEM	Coastal Engineering Manual
CFD	Computational Fluid Dynamics
CG	Center of gravity
COBRAS	COrnell BReaking waves And Structures
CPT	The cone penetration test
CSD	Computational Structural Dynamics
CSSR	Cyclic shear stress ratio
DEM	Distinct Elements Method
DES	Detached Eddy Simulation
DIN	Deutsches Institut für Normung, German Institute for Standardization
DNS	Direct Numerical Simulation
DOF	Degrees Of Freedom
EFG	Element-Free Galerkin Method
FD	Fully Dynamic
FDM	Finite Difference Method
FEA	Finite Element Analysis
FEM	Finite Element Method
FVM	Finite Volume Method
FZK	Forschungszentrum Küste, Coastal Research Center
GWK	Großer Wellenkanal, The Large Wave Flume

LES	Large Eddy Simulation
LHS	Left hand side
LIMAS	Liquefaction around Marine Structures, a project of the EU
MLPG	Meshless Local Petrov-Galerkin Method
MPM	Material Point Method
NEES	Network for Earthquake Engineering Simulation
NN	Neural Networks
NSE	Navier Stokes Equations
OCR	Over Consolidation Ratio
ODE	Ordinary Differential Equation(s)
OpenFOAM®	The Open Field Operation And Manipulation framework, OpenFOAM® is a registered trademark of OpenCFD Ltd.
OpenSees	Open System for Earthquake Engineering Simulation
OWC	Oscillating Water Column
PD	Partially Dynamic
PE	Polyethylene
PISO	Pressure Implicit with Splitting of Operators algorithm
PT	Phase transformation line
QS	Quasi Static
RANS	Reynolds-Averaged Navier Stokes
SANS	Spatially-Averaged Navier Stokes
SGS	Sub-grid scale
SPH	Smoothed Particle Hydrodynamics
SPM	Shore Protection Manual
SSI	Soil-Structure Interaction
SST	Shear Stress Transport model
SWE	Shallow Water Equation
VARANS	Volume-Averaged Reynolds-Averaged Navier Stokes
VOF	Volume Of Fluid

1 Introduction

1.1 Motivation and Problem Statement

Monolithic vertical breakwaters are in many cases more advantageous than rubble mound structures in terms of cost, multi-purpose use, construction time, maintenance and quality control. However, vertical breakwaters are also more vulnerable to foundations failure. Available numerical models could not reproduce properly the processes observed by Kudella et al. (2006) and the subsequent residual soil displacement and failures. In addition, numerous severe and catastrophic failures were experienced by vertical breakwaters.

A review and analysis of failures of 17 vertical breakwaters by Oumeraci (1994) concluded that the large permanent deformations of the subsoil observed to date underneath vertical breakwaters are an accumulation of small irreversible strains at repetitive peak stresses rather than a pore pressure buildup after each load cycle; likely not due to soil liquefaction.

Within the EU funded MAST III project PROVERBS (Probabilistic Design Tools for Vertical Breakwaters), special attention was paid to the effects of the duration and frequency of wave loading and to the dynamic response of vertical breakwaters and their foundations (Oumeraci et al., 2001). In PROVERBS, the aforementioned conclusion of Oumeraci (1994) was confirmed by centrifuge tests and theoretical results showed that residual pore pressures may significantly contribute to foundation failure under special conditions. These conditions were simulated, later within the EU-LIMAS project, in the large scale tests described in Kudella et al. (2006).

Total or partial liquefaction may lead to complete failures of the foundation of marine structures as reported by Zen et al. (1986) in the case of a caisson breakwater. The occurrence of significant residual pore water pressure in the subsoil represents the most important process governing the liquefaction potential of soil foundations. Therefore, the main focus of the EU-LIMAS project was set on the observation and analysis of the development of instantaneous and residual pore pressure in the sandy seabed beneath a caisson breakwater (Oumeraci and Kudella, 2004).

The study by Oumeraci and Kudella (2004) showed that even under unfavourable drainage and soil conditions of the seabed beneath a caisson breakwater as well as under very severe wave load conditions, only 25% of the critical residual pore pressure ratio for complete liquefaction could be achieved. It was found that both high transient and residual pore pressure generations are essentially due to caisson motions, and that the frequency and magnitude of these motions should be large enough to generate residual pore pressure. Moreover, it was found that such large and high frequency caisson motions can only be induced by severe breaking wave impacts (Kudella et al., 2006).

In Fig. 1.1, the transient component of the caisson vertical motion, at the shoreward edge, $d_{vb,t}(t)$ and pore pressure $p(t)$ start to increase after 128 load cycles resulting in the inflexion point (I) of the response curves of the residual components $d_{vb,r}(t)$ and $p_r(t)$; i.e. after point (I) the generation of residual pore pressure becomes more dominant and both $d_{vb,t}$ and p_t increase at a higher rate up to a "saturation point" (S) where the generation and dissipation of the residual pore pressure are in balance. After point (S) where the relative excess pore pressure was determined to be about 0.25 (no liquefaction) the residual pore pressure decreases while the residual soil deformation (settlement) still increases.

A quantitative analysis of the relative contribution of the generation and dissipation process has been conducted in Oumeraci and Kudella (2004), showing that the gradient of pore pressure generation starts to decrease after point (S) due to the increasing compaction of the subsoil, while the dissipation gradient remains constant, thus leading to a decrease of the $p_r(t)$ curve after the “saturation point” (S).

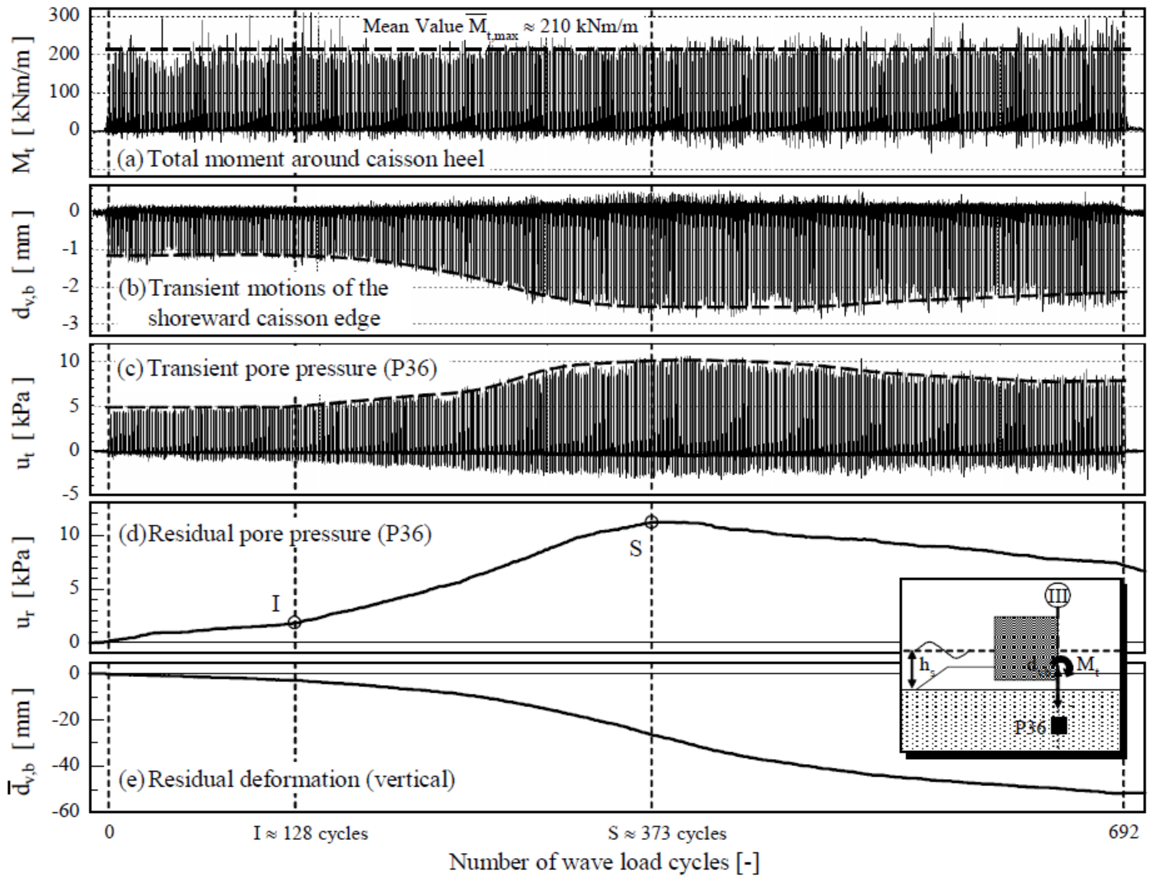

Figure 1.1: Wave load, pore pressure response and soil deformation for one test results from the large-scale caisson breakwater experiments (Oumeraci and Kudella, 2004)

The stepwise residual deformations of the caisson closely follow the stepwise increase of residual pore pressure until generation and dissipation are in balance (saturation point (S) in Fig. 1.1). After point S the dissipation process dominates over the pore pressure generation process leading to a decrease in residual pore pressure. Finally, the study by Oumeraci and Kudella (2004) concluded that further analysis of the results, combined with numerical modelling should focus on the closer examination of the balance between pore pressure generation and dissipation in order to come up with some design guidance based on allowable soil deformations.

A numerical study by Kudella and Oumeraci (2008a) investigated the experimental findings. However, the applied numerical model did not succeed to properly reproduce the GWK experiments by Oumeraci and Kudella (2004), especially for impact loads and the induced structural response.

Further research is therefore required to reproduce properly the results from the large-scale experiments numerically. A re-analysis of experimental results will also be carried out alongside in order to possibly examine the observed processes from another perspective that can be verified numerically. A closer examination of step-wise failure mechanism of monolithic breakwaters should represent the key task for further research.

1.2 Organisation of The Thesis

This report is organized in seven chapters, including this introductory chapter.

In chapter 2, the current knowledge and modelling tools for the physical processes involved in the wave-structure-foundation interaction are analysed, the knowledge gaps and modelling weaknesses are identified, and implications for this PhD study are drawn. Based on these implications, the objectives and methodology for this study are specified more precisely.

In chapter 3, the hydrodynamic model is described. The model is based on the multiphase volume-of-fluid (VOF) Eulerian solver of OpenFOAM and on the wave generation and absorption via relaxation zones. The model validation using dam break flow through a porous barrier and large scale experimental data for wave forces on a caisson breakwater is also included.

In chapter 4, a hydro-geotechnical solver (*geotechFoam*) is developed and validated using benchmark elastic, poro-elastic and contact problems as well as data from centrifuge soil liquefaction tests and from laboratory tests with a rocking plate in a sand box. The numerical solver is based on the fully-coupled fully-dynamic Biot's equations, on a multi-surface plasticity model with capabilities to properly describe the cyclic mobility and partial liquefaction of sand material and on a frictional contact model for describing soil-structure interaction.

In chapter 5, the validated hydrodynamic model and hydro-geotechnical model are used as a (one-way) coupled CFD-CSD model for a parameter study for the analysis of the transient and residual pore pressures in the sand bed beneath a caisson breakwater, including their effect on the residual displacement of the breakwater. Recommendations for the design of caisson breakwaters and implications on the capabilities and limitations of the weakly coupled model are finally drawn from the analysis of the results.

In chapter 6, a simpler model, called *caissonFoam* solver, which essentially consists of a 3-DOF mass-spring-dashpot model of monolithic breakwaters subject to wave loading, is developed and applied to reproduce the dynamic response of the caisson breakwater and its foundation (including residual settlement and tilt) as obtained from the large scale tests in GWK. A discussion of the capabilities and limitations of the *caissonFoam* model is also provided.

In chapter 7, a summary of the key results, concluding remarks and suggestions for a further development of the weakly coupled CFD-CSD model and the simpler *caissonFoam* model are provided.

2 Current Knowledge and Models

In this chapter, the current knowledge and modelling tools for the physical processes involved in wave-structure-foundation interaction are reviewed and analysed, the knowledge gaps and modelling weaknesses are identified, and implications are drawn for this PhD study. First, the hydrodynamic processes such as wave reflection and wave breaking (in front of a vertical barrier) and the hydro-geotechnical processes related to the seabed response to water wave loading such as pore pressure generation and dissipation, soil liquefaction and cyclic mobility are addressed. Second, the most relevant soil constitutive models for the studied problem are outlined. Third, an overview is provided on the physical, analytical, numerical and simplified models to describe wave-structure-foundation interaction for monolithic breakwaters. In the concluding section, the objectives and methodology for this study are precisely derived from the results of previous sections.

2.1 Hydrodynamic Processes and Models

2.1.1 Hydrodynamic Processes

a. Waves in front of the structure

As water waves approach the structure, the most significant processes affecting wave transformation are wave shoaling, breaking and reflection. These processes determine the type and characteristics of waves that hit the structure. Horizontal and vertical (uplift) loads acting on the structure greatly differ according to the type of incident waves. Hence, a proper understanding and modelling of these processes is required.

High reflection can also strongly affect the character of breaking (location and breaker type), and hence the amount and distribution of entrapped air, known to be essentially determined by the breaker shape. This suggests that the latter primarily determines not only the magnitude but also the distribution and the duration of the impact pressures. Therefore, the need for the identification and classification of breaker types in presence of vertical structures, wave reflection, is obvious (Oumeraci et al., 1993).

Breakers, in front of a vertical breakwater, are classified mainly into four distinct breaker types, with natural continuous variation of breaker shape among these four types. These types were identified empirically (Oumeraci et al., 1993) using a physical model. The classification of breakers (Fig. 2.1) was found to depend on wave steepness, the ratio of the breaking water depth and the still-water depth directly at the wall (d_s/d_w), and the ratio of the horizontal velocity of the breaker and the vertical upward velocity of the water surface directly at the wall (v_H/v_V).

Hull and Müller (2002) investigated the breaker heights, shapes and pressures on a vertical wall in the laboratory tests and they observed breaker types similar to those described by Oumeraci et al. (1993).

Implication 1 (Waves in front of the structure) *1. Reflection of waves affects both wave field and characteristics of the waves in front of the structure.*

2. For the wave loads on a structure, it is important to distinguish between breaking and non-breaking waves as well as between the different breaker types in front of a structure.

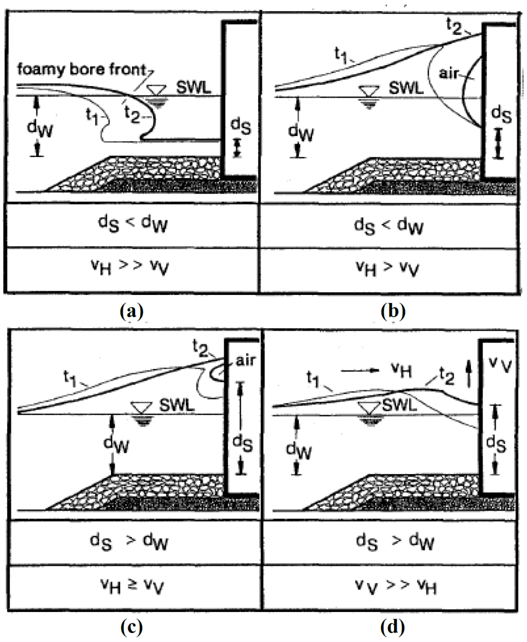

Figure 2.1: Classification of breaker types in front of a vertical obstacle: (a) turbulent bore; (b) well-developed plunging; (c) plunging; (d) upward deflected (Oumeraci et al., 1993)

b. Horizontal wave loads on vertical structures

The highly dynamic and stochastic nature of wave loads on vertical structures makes a reliable prediction very difficult. Wave breaking magnifies the dynamic effect of wave loads, as the loading frequency approaches natural frequencies of the structure whereas non-breaking and totally broken waves can mostly be simplified as equivalent static loads for design purposes without a significant risk of structural resonance. Therefore, a classification of wave loads in impact and non-impact loads (or pulsating loads) such as that proposed in Fig. 2.2 or in the parameter map of the PROVERBS project (Oumeraci et al., 2001) is important.

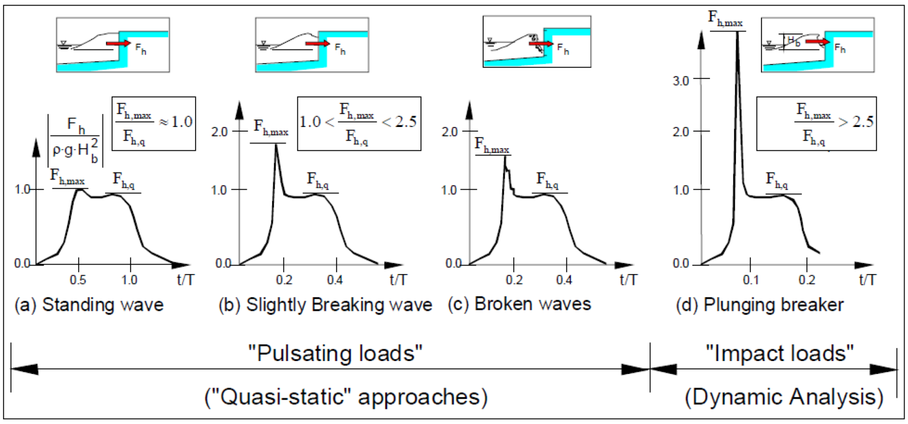

Figure 2.2: Distinction between "impact" and "pulsating" loads (Oumeraci et al., 2001)

Horizontal loads from non-breaking or pulsating waves can be calculated using Sainflou's prediction method (Sainflou et al., 1928). Wave tank experiments by Bagnold (1939) led to an explanation of the water waves breaking phenomenon. Bagnold found that impact pressures occur at the instant that the vertical front face of a breaking wave hits the wall and only when a plunging wave entraps a cushion of air against the wall. Due to their very short duration, impact loads might be less relevant for the safety against sliding or overturning than for the safety against stepwise failure as described by Oumeraci (1994). On the other hand, lower dynamic forces which last longer are more important in terms of overall failure modes.

Goda's method was developed based on a theoretical approach and modified according to experimental data to provide a better representation of experimental observations (Goda, 1974). Further research in Japan extended the original method by Goda to account for the effect of a berm, sloping top, wave breaking and incident wave angle. Goda (2010) contains a comprehensive description of the Japanese experience regarding the topic. Goda's method is recommended by Oumeraci et al. (2001) for the prediction of pulsating wave loads.

Through the PROVERBS project, a prediction method for the calculation of impact pressure of breaking waves that can be used for purposes of preliminary design (initial calculations of impact forces) of vertical breakwaters (Allsop et al., 1996; Allsop and Vicinanza, 1996) was developed. The method is recommended in Oumeraci et al. (2001) for preliminary design purposes when the waves are identified as slightly breaking waves or impact loads according to the PROVERBS parameter map. It is also adopted by the British Standards (BS6349-1, 2000).

In the PROVERBS project Oumeraci et al. (2001), an approach is proposed based on the statistical distribution of forces and theoretical considerations derived from the solitary wave theory (Oumeraci and Kortenhaus, 1997) for the prediction of the impact force of breaking waves. In this approach, a formula for estimating the maximum horizontal impact force on the structure is provided. Moreover, the actual and more complicated force history is also simplified to equivalent triangular force time history having the same peak value and the same force impulses (momentum of water mass involved in the impact and momentum of the total mass in the breaking wave), but different rise time and total impact duration. Based on the analysis of almost 1000 breakers of different types hitting a vertical wall, a simplified distribution of impact pressure just at the time when the maximum impact force occurs was developed (Oumeraci and Kortenhaus, 1997).

Due to lack of studies on broken wave forces, an approximate method is presented by CEM (2006) based on simplifying assumptions to estimate design loads on uniform slopes, but not valid for composite slopes.

Implication 2 (Horizontal wave loads on the structure) *1. Breaking waves exert highly dynamic impact on the structure that cannot be simplified to an equivalent static load for the analysis of stepwise failures in the soil foundation.*

2. A breaking wave impact on a structure has its highest value when the breaker face is almost parallel to the structural face (perfect breaking).

3. Entrapped air cushion between the wave and the structure as well as entrained air significantly affects the wave impact (dynamics) on the wall.

c. Wave-induced uplift forces beneath gravity structures

The wave-induced pore pressure in soil foundation (excess to hydrostatic pressure) represents an additional hydraulic uplift pressure on gravity structures, which tends to destabilize them. A linear uplift pressure distribution (triangular shape) beneath monolithic breakwaters is suggested by Goda's method (Goda, 1974).

Liu (1985) developed an exact solution for wave-induced seepage flow in a porous seabed under a gravity structure. The uplift pressure was found to be nonlinear. The model, however, neglects both compressibility of soil skeleton and pore fluid, which led to quite reasonable agreement with laboratory results. Liu (1985) also suggests that for special cases (e.g. for a compressibility of the fluid much smaller than that of the soil skeleton and for short waves) the behaviour of both pore fluid and solid skeleton (of soil) can be uncoupled; i.e. the pore pressures are not affected by the soil deformations.

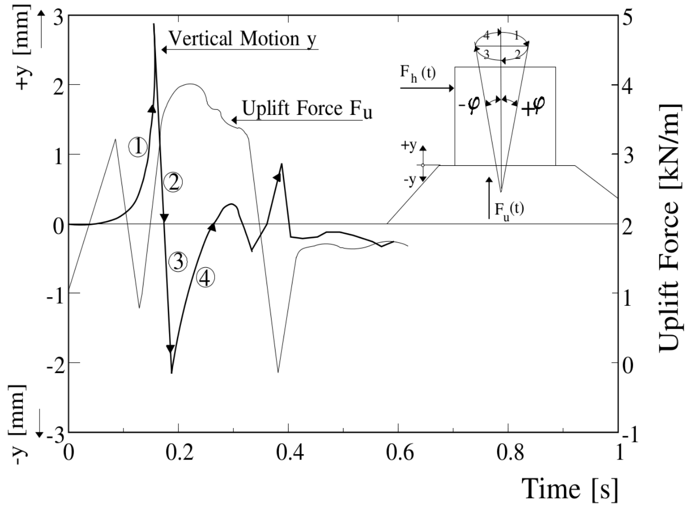

Figure 2.3: Effect of caisson rocking motion on uplift force (Oumeraci et al., 2001)

Mase et al. (1994) developed a poro-elastic FEM model for the dynamic response of a composite breakwater subject to linear waves by using Biot's quasi-static equations. They found that the uplift pressure distribution under a caisson base may change from linear towards nonlinear for a rubble foundation with low permeability. However, the wave field and the porous media were not linked in their model and the transmitted wave to the onshore side was neglected.

Nonlinear uplift pressure distributions were also found experimentally when the inner top corner of the rubble foundations consists of relatively fine material and the rest of relatively coarse material. Such distribution was also found underneath the Porto Torres. A deviation from the conventional triangular distribution of the uplift pressure may be due to the bi-dimensional character of the flow underneath the caisson resulting in flow concentrations around the corners and lower horizontal gradients at lower levels Oumeraci et al. (2001).

Kortenhaus et al. (1994), within the PROVERBS project, analysed laboratory data from large-scale tests on wave-induced uplift loading of caisson breakwaters. They observed water surface fluctuations on the onshore side of the caisson and a dynamic pressure on the onshore surface of the rubble base. They also observed that the uplift pressure underneath a caisson breakwater takes a trapezoidal shape rather than a triangular one. Mostafa et al. (1999) confirmed the trapezoidal uplift shape found by Kortenhaus et al. (1994) via a numerical coupled boundary element (for water waves and pore fluid) finite element (for porous media), BEM-FEM, model that was verified using physical experiments.

Laboratory experiments on a caisson breakwater with protecting concrete blocks (Sakakiyama and Liu, 2001) show that maximum uplift pressures generated under the caisson are quite similar for both non-breaking and breaking waves having the same wave height.

Results from different hydraulic model tests did not show any phase lag between the horizontal wave force and the uplift force (e.g. Shimosako et al. (1994) and Klammer et al. (1994)). This, however, may not be the case of a full-size caisson founded at a much greater water depth (Ling et al., 1999). The latter investigated the possible effects of this phase difference by introducing a phase angle into the considered simple harmonic uplift force. In this model, the wave force was also considered as simple harmonic. They conclude that considering an in-phase relationship between water waves and uplift pressure yields a more conservative design; however, more research into the phase lag between wave impact and uplift forces would be needed.

While the horizontal wave load is not significantly affected by the motions of the caisson breakwater, this is not the case for wave-induced uplift force. The interaction between wave, structure and foundation is significant for the uplift loads as they are strongly affected by the rocking motion of the structure. Experimental results, Fig. 2.3, show that caisson rocking due to breaking wave impact can reduce or increase the uplift force by a magnitude up to 30%, which forms a solid base for the argument of the importance of wave-structure-foundation interaction (Oumeraci et al., 2001).

Implication 3 (Wave-induced uplift loads) *1. The wave-induced uplift pressure is not zero at the caisson's shoreward edge, i.e. the pressure distribution is rather trapezoidal than triangular.*

2. The wave-induced uplift pressure is nonlinear with a phase-lag with the horizontal wave pressure that can be neglected for a more conservative design.

3. The wave-induced uplift pressure might be significantly affected by the rocking motions of the gravity structure.

2.1.2 Hydrodynamic Models

Generally, numerical methods can be classified according to how approximation is achieved (approximation to the equation vs. approximation to the solution). They can also be classified into mesh-based and meshless methods. In Coastal Engineering, a distinction is also made between depth averaged (e.g. SWE) and depth resolved models (e.g. NSE). Flow in porous media can be introduced to depth-averaged models via a damping term (e.g. Kobayashi and Wurjanto (1990)). Nevertheless, depth-averaged models (such as SWE or Boussinesq) are not optimum for modelling local phenomena relevant to the current research and therefore a depth resolved model is used.

Solving the Laplace equation based on potential flow theory is not adequate for the problem at hand because of the assumption of irrotational flow. For this reason, such models are (typically) unable to simulate fully the process of wave breaking as well as wave interaction with small bodies, during which the flow becomes rotational. This eliminates the use of BEM models for this study.

Models that solve the NSE are the best choice for modelling breaking waves, as they provide the most accurate representation of fluid flow modelling. A great advantage of these models is that they allow for the introduction of air to the model. The greatest disadvantage of the NSE models is their computational expense. A disadvantage that can be partially mitigated by modelling turbulence (RANS, LES or DES). Meshless methods (e.g SPH) are promising in providing a Lagrangian approach to fluid simulations but they are generally still not as mature as mesh/grid based models.

Mesh/grid based models (e.g. FVM, FDM, etc.) are usually used in an Eulerian (or ALE) framework to model fluid flows. Each numerical method has its strengths and limitations, depending on the specific purpose. Nevertheless, the FVM and the FEM are more flexibile than the FDM in terms of geometrical complexities.

In mesh-based models, air and water can be simulated as two overlapping continua or simply as a single fluid mixture. The VOF method is the most frequently used approach to track the air-water interface in an Eulerian framework.

In studying water wave and porous-structure interactions, it is still not practical to resolve the intrinsic flow field inside the pores, whose geometry is usually random. Therefore, it is more manageable if the flow equations are averaged over a control volume that is larger than the characteristic pore size and is much smaller than the scale of the spatial variation of the physical variables in the flow domain.

In their approach, Van Gent (1993) and Liu et al. (1999) averaged the NSE over space to have a new set of equations that have similar characteristics to the NSEs but the additional friction in porous media is also included, Spatially-Averaged Navier Stokes (SANS). Liu et al. (1999) assumed that turbulence inside the porous media is negligible. The turbulence boundary layer adjacent to the porous wall was modified by including the effects of the percolation velocity along the porous boundary. Hsu et al. (2002) developed a volume-average Reynolds-averaged Navier-Stokes (VARANS) along with the k-ϵ turbulence closure model. In this model, a set of governing equations were derived to describe flow and turbulence inside a protective armour layer. This consideration is especially important in case of high porosity; nevertheless, for flow inside relatively small porosity materials, turbulence can be negligible. The concept of volume averaging is not a property of RANS. It can also be introduced to models with different turbulence modelling approaches.

Implication 4 (Hydrodynamic models) *1. The mesh-based NSE models represent the most appropriate alternative for this study in terms of their accuracy, modelling capability of multiphase flow and higher adaptivity to complex geometries (compared to grid-based methods).*

2. Turbulence modelling is necessary to enhance computational speed without reducing accuracy.

3. Volume averaging is required to model the flow attenuation caused by non-deformable porous media.

2.2 Hydro-Geotechnical Processes

2.2.1 Seabed response to water waves and failure modes

When water waves attack a vertical breakwater; the underlying seabed is affected in two ways: Directly from water waves and indirectly by the breakwater motion induced by water wave loads. Both may result in failures of the foundation, which can affect the seabed locally or cause an overall failure of the structure. The overall failure of monolithic breakwaters may be divided in three major categories: sliding failure, overturning failure and excessive settlement (including differential settlement, i.e. rotation without overturning). However, the dynamic and stochastic nature of the involved hydraulic, structural, geotechnical and morphological processes and their complex interaction result in more complex failure modes that cannot be described by current static and deterministic design approaches, and must therefore be analysed by dynamic and probabilistic approaches (De Groot et al., 1996; Oumeraci et al., 2001). The modes of failure for caisson structures were extensively investigated under the PROVERBS (Probabilistic Design Tools for Vertical Breakwaters) project based on Oumeraci (1994) review of 22 cases of vertical breakwater failure. Modes of failure of caisson breakwaters are discussed in Oumeraci (2004), and Oumeraci et al. (2001). Failure modes associated with liquefaction (partial/complete) are described in more details in De Groot et al. (2006b).

Oumeraci (1994) classifies the reasons for vertical breakwater failures to be due to the structure itself, hydraulic conditions (e.g. wave load) or foundation and morphological conditions (i.e. geotechnical failures and scour). He stresses that postulating monolithic vertical breakwaters to be energy reflective structures, is a fallacy. Some of the most common modes of failure for caisson breakwaters are illustrated in Fig. 2.4.

According to Oumeraci (1994), several vertical breakwater failures resulted from a seaward tilt. Such a failure was also observed in centrifuge tests (Rowe et al., 1976; Rowe, 1981; Van der Poel and De Groot, 1998; Zhang et al., 2009a). Oumeraci (1994) also reports that most of the failed breakwaters had a low crest (and consequently heavily overtopped) and too high toe berm (however not composite breakwaters). These two observations may seem less relevant due to the configurations of centrifuge tests, e.g. Zhang et al. (2009a) (no rubble base and equivalent mechanical loading to simulate wave loading). The reason for the seaward tilt failure has been attributed to several mechanisms, including seabed scour or soil liquefaction underneath the breakwater heel (seaward side) and seawards directed impacts caused by excessive wave overtopping, which result in caisson's tilt seaward as shown in Fig. 2.5. This mode of failure is of special significance to structures of relatively low mass (Walkden et al., 2001). Nevertheless, a satisfactory explanation is still lacking.

In addition to the scour of the seabed and to the erosion of the toe berm, foundation failures may include: soil liquefaction flow failure (not likely in realistic conditions of wave attack but possible in seismic action), stepwise failure or stepwise liquefaction failure (De Groot et al., 2006b), the latter being accompanied by significant residual pore pressure unlike the first, and finally wobble failure; which is due to large (instantaneous) cyclic strain. This means that in addition to sudden failures caused by an extreme single wave, cumulative gradual/stepwise failures caused by repetitive moderate wave loads must also be considered. Moreover, Oumeraci (1994) suggests that the extreme impact load might also be caused by a rare combination of a succession of certain wave heights and periods rather than being caused by the highest wave in the wave train.

De Groot et al. (2006b) rules out the densification (contraction) of the subsoil and loads exceeding the strength of the subsoil. They suggests that the stepwise (liquefaction) failure beneath caisson breakwaters is mainly due to cyclic mobility. Fig. 2.6 shows how impact wave loads, though of short durations, can jeopardize the stability of the caisson via small cumulative residual displacements. This type of failure is yet not implemented in the current design codes. Nevertheless, general guidelines for design purposes are provided by De Groot et al. (2006b).

The analysis of the failure modes of monolithic breakwaters has revealed the significance of the consideration of dynamic, rather than quasi-static, approaches for stability analysis and of the poromechanical behaviour of the sub-soil. Although the latter is not implemented in the current design guidelines, it is deemed necessary because the successive buildup and dissipation of pore pressures strongly affect the mechanical behaviour of soils. On the other hand, the porosity of geomaterials is affected by their mechanical deformations. The consideration of local liquefaction potential in subsoil and the use of proper geotechnical models capable of modelling the multiphase nature of soils (solid, water and air) and relevant soil phenomena are crucial issues. Special attention to the hydraulic stability of rubble foundation and seabed against scour due to breaking waves is also required. The failures associated with these geotechnical aspects remain generally hidden until the collapse of the structure occurs. Therefore, research on failures due to incremental weakening of the seabed is urgently needed.

Implication 5 (Failure Modes of Vertical Breakwaters) *1. Failure modes of vertical breakwaters might be either global (e.g. sliding) or local (e.g. scour at toe).*

2. In addition to sudden failures of the structure (e.g. sliding and overturning) induced by extreme wave events, step-wise failures induced by moderate wave action should equally be incorporated in future stability analysis.

3. It has been observed that step-wise failure of vertical breakwaters in the field and in the laboratory is sometimes associated with the seaward tilting of the structure.

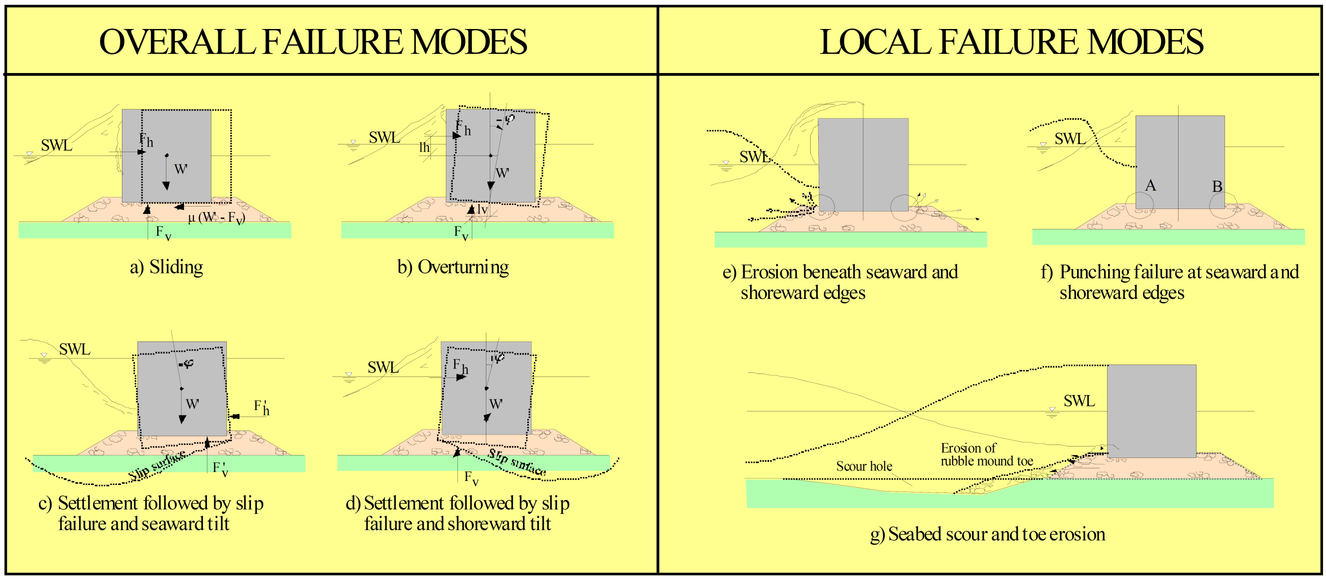

Figure 2.4: Significant modes of failure for a monolithic marine structure (Oumeraci, 1994)

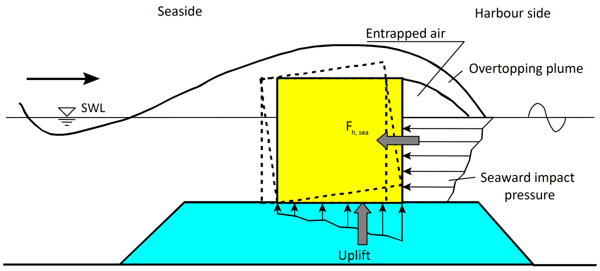

Figure 2.5: Failure due to excessive overtopping via seaward tilt (Oumeraci, 2004)

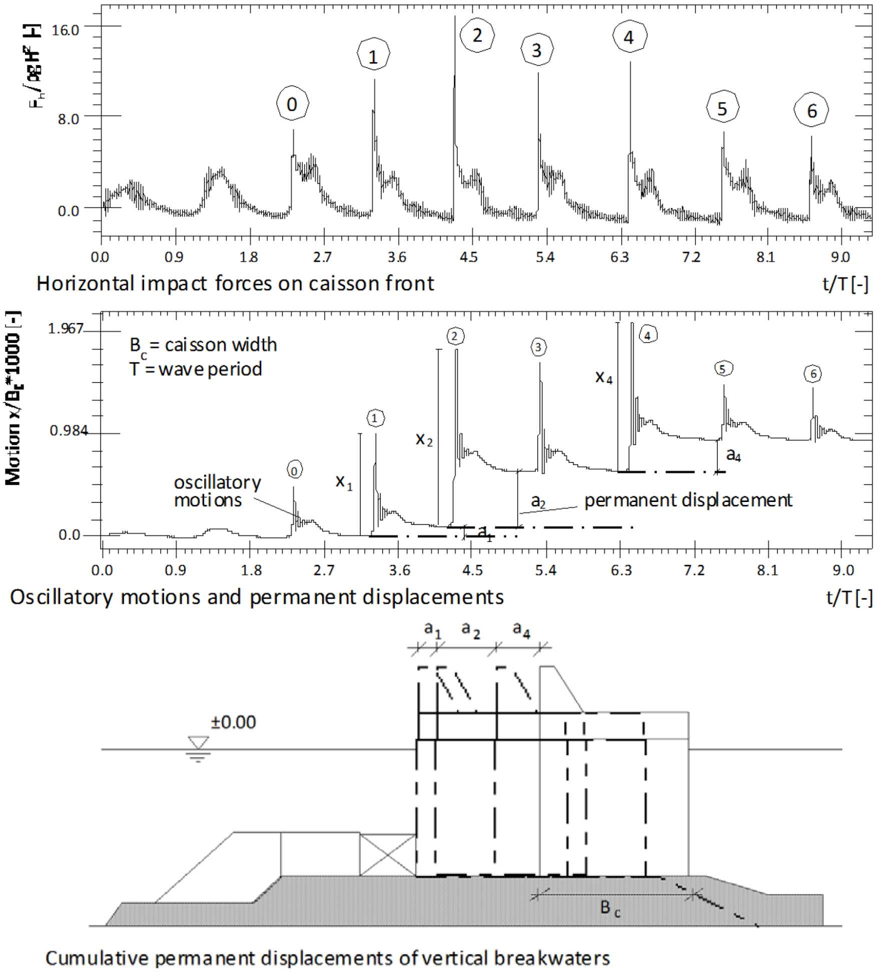

2.2.2 Pore pressure generation and dissipation

Modelling soil behaviour either as fully drained or fully undrained provides crude simplifications to avoid complications associated with the complex analysis of generation and dissipation of pore pressure. However, understanding the mechanisms of generation and dissipation of pore pressure and consequently also the mechanisms of pore pressure buildup is crucial for the analysis of the response of soils underneath marine structures to wave loads. Formulation of pore pressure generation and dissipation is significant for the implementation in empirical geotechnical models that consider effect of pore pressure on the foundation stability.

Pore pressure in a seabed underneath a monolithic marine structure is affected by wave action through two main mechanisms (as mentioned in Sec. 2.2.1): Pore pressure is affected directly by fluid percolation (wave-induced pore pressure) or indirectly by caisson motion (caisson-induced pore pressure). In their model, Oumeraci and Kudella (2004) considered the situation of a sandy seabed covered by a thin impermeable layer (to provide favourable conditions for liquefaction) that is situated underneath the rubble. Therefore, it is safe as well as convenient to consider that wave action and corresponding caisson response equivalently act as external loads (pressure and stress) at the seabed surface. The mechanism by which loads are transferred from the caisson structure to the seabed can be divided into two main components: (i) Changes in the total normal stresses induced by the caisson vertical and rocking motions in the rubble foundation (both normal effective 'grains contact' stress and pore/uplift pressure) and (ii) changes in shear stresses induced by the caisson horizontal motions (Kudella et al., 2006). Moreover, it is also convenient to decompose the pore pressure in the seabed into two components: A transient component accompanied by an attenuation of the amplitude and phase lag in the pore pressure changes (Madsen, 1978; Yamamoto et al., 1978) and a residual component due to contraction of soil under cyclic loads.

Kudella et al. (2006) found that the caisson-induced pore pressure beneath the structure, is much more significant than the wave-induced pore pressure. Further, only caisson-induced pore pressure due to regular breaking wave impact is capable of generating residual pore pressure, whereas wave-induced pore pressure as well as caisson-induced pore pressure due to pulsating waves can generate only transient pore pressure with no (residual) pressure buildup. Therefore, the generation of residual pore pressure depends not only on the soil drainage characteristics but also on the wave load conditions (Kudella and Oumeraci, 2006). Moreover, a very close correlation between both residual pore pressure and residual soil deformation was found.

The pore pressure distribution in a sandy seabed with incompressible pore water is quasi-stationary: At each moment it is completely determined by the pressure distribution along the soil, as shown in Fig. 2.7. In this figure, a sinusoidal wave with wavelength, L, over a horizontal bed and homogeneous soil is considered. The absolute value of the excess pore pressure decreases exponentially with depth, z, according to $exp(z/z_1)$, where $z_1 = L/2$ (Yamamoto et al., 1978; Verruijt, 1982). Under the wave crest, a vertical pressure gradient develops over the depth, z_1; therefore, water flows vertically into the seabed. This flow increases the effective stress in the seabed under the crest. On the other hand, under the wave trough an inverse vertical pressure gradient over the same depth, z_1, and the same amount of water flows out of the seabed pores. This in turn reduces the effective stress in the seabed soil under the wave trough. Halfway between wave crest and wave trough, the pore pressure gradient is horizontal. At this point the effective stresses are not affected. At the moment of maximum horizontal pressure gradient, i, along the seabed, the situation is completely different (Fig. 2.7). A maximum of the shear stress in a horizontal plane, τ_{zx}, is according to linear wave theory: $\tau_{xz} = \rho_w gzi = \Delta u(0).z/z_1$.

As the wave propagates, pore pressures and effective stresses are cyclically altered. This stress fluctuation cannot be simulated either in direct or triaxial shear tests (De Groot et al., 2006a).

There are good reasons to believe that gas content in seabed soil is often larger than 0.3% (Sandven et al.,

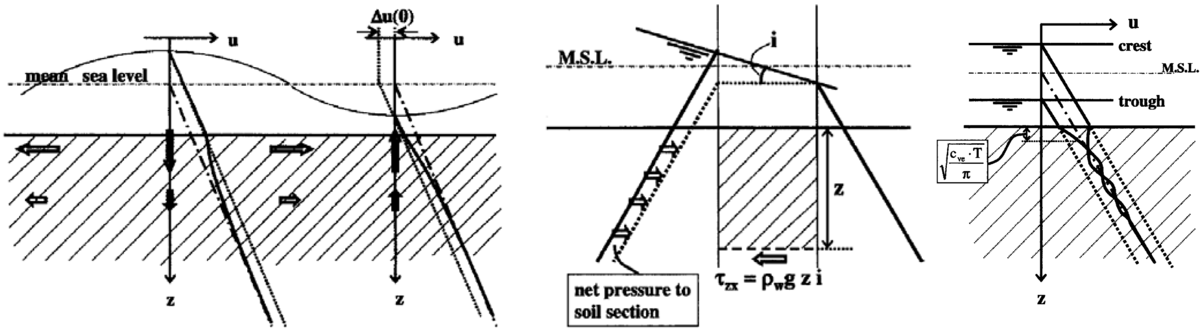

(a) (b) (c)

Figure 2.7: (a) Instantaneous pore pressures and pore flow under waves with incompressible pore fluid; (b) approximation of instantaneous pore pressures under wave halfway crest and trough with incompressible pore fluid and (c) instantaneous pore pressures under waves in seabed with compressible pore fluid (De Groot et al., 2006a)

2007), and even estimated up to 3% (Torum, 2007). With gas content larger than 0.3%, the pore fluid can no longer be considered incompressible. The compressibility of the pore fluid (water-gas mixture) is in the same order as that of the soil skeleton. The pore fluid compressibility consequently reduces the effects of soil contraction/dilation on pore pressure, mean effective stress and shear strength.

Pore fluid compressibility allows for water storage in the pores when the soil element is under a wave crest while the stored water volume seeps out of the seabed when the soil element is under the wave trough. Therefore, the pore pressure change is dampened and the effect of waves on it is less than that for the incompressible pore fluid case. Unlike the case of incompressible pore fluid, the pore pressure change is not in phase with the water waves. Moreover, the affected depth of the seabed soil is less in the case of compressible pore fluid and the amplitude of pore pressure fluctuation reduces faster with depth if the pore water compressibility, β, is much larger than the elastic skeleton compressibility, α (Fig. 2.7).

When a structure is present, the pore pressure in the seabed underneath the structure is not affected by water pressure fluctuations, unless a layer of high permeability is situated between the structure and seabed. Nevertheless, the effect is not significant compared to that of the structure motions induced by wave loads, especially on the harbour side.

Pore pressure fluctuations in the seabed beneath a caisson structure may not be affected by the structure due to high compressibility of pore fluid in comparison to compressibility of the soil skeleton (De Groot et al., 2006a), which in turn may make the solid skeleton carry all stress changes. This was observed in the large-scale caisson experiments in Richwien and Perau (2000), in which no pore pressure fluctuation is recorded after a depth of 30 cm. Nevertheless, large-scale experiments carried out in the same flume (Oumeraci and Kudella, 2004; Kudella et al., 2006), *with careful degassing of soil* and covering the soil with an impermeable sheet to provide more convenient conditions for liquefaction development, show that even a small vertical motion of the caisson affects the pore pressure underneath. This effect vanishes with increasing depth.

The wave-induced caisson motions dominate the change in transient pore pressure underneath. For locations away from the caisson, the direct wave effect on transient pore pressure is restored and the caisson effect vanishes. This conclusion is similar for both pulsating and impact loads. Nevertheless, for wave impact loads, amplitudes of pore pressure fluctuations are much larger and pore pressure in locations underneath the seaward side of the caisson is also influenced by direct wave action (wave-induced pore pressure). It is also noted that caisson-induced pore pressure underneath the seaward face is less affected by caisson motion than shoreward face for all wave types (Kudella et al., 2006).

For the seabed underneath a caisson, Kudella et al. (2006) found that the pore pressure induced by caisson

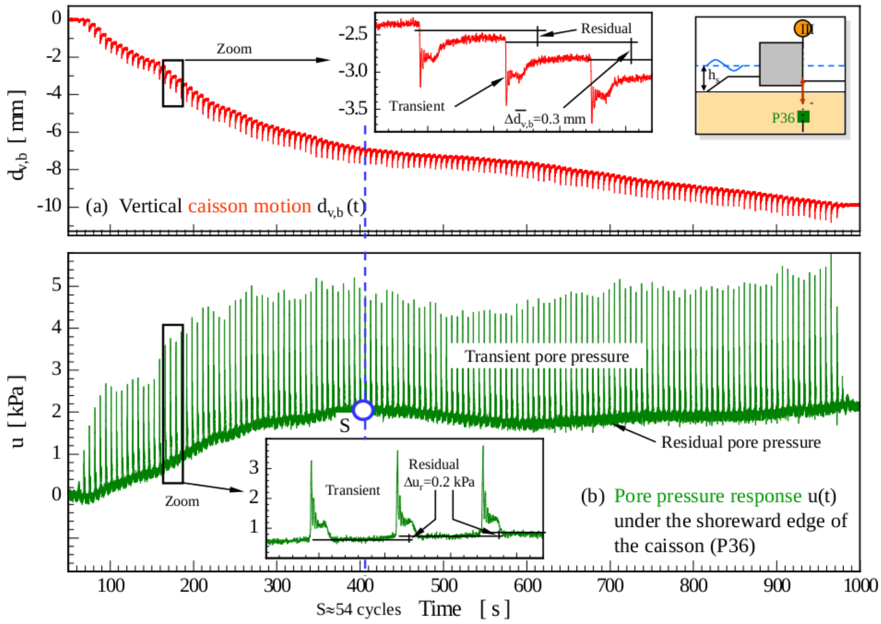

Figure 2.8: Pore pressure and caisson vertical motion (stepwise failure) in seabed underneath shoreside edge of a caisson breakwater subject to breaking wave impact (Kudella et al., 2006)

motions is one order of magnitude higher than that developed directly by wave action. Therefore, it can be assumed that the residual pressure underneath the structure develops only due to caisson motions. It was also found that only the frequency and amplitude of caisson motion due to wave impact loads are capable of developing residual pore pressure. Fig. 2.8 illustrates the development of both transient and residual pore pressure underneath the caisson due to caisson motions. This figure highlights the close correlation between residual pore pressure and residual soil deformation. Three stages for residual pore pressure generation and dissipation underneath the caisson were found. The residual pore pressure values are quite equal for different locations enclosed by the impermeable sheets beneath the breakwater during breaking wave action. These three stages are: (1) the generation dominates the dissipation; (2) quasi-equilibrium between generation and dissipation; and (3) residual pore pressure exclusively dissipates (Fig. 2.9). The third stage starts just at the end of the tests (end of wave action) and is characterized by an exponential decrease of residual pore pressure with time (Kudella and Oumeraci, 2004a).

The assessment of residual pore pressure increase in the subsoil is of great importance for the stability of monolithic marine structures. Increase in residual pore pressure makes such structures more vulnerable to various geotechnical failure modes ranging from excessive displacement to even total failure of foundation. In fact, the increase in residual pore pressure decreases soil strength (partial liquefaction) and may ultimately lead to complete liquefaction (in very special cases not likely to occur in nature) or more likely to cyclic mobility. According to Kudella and Oumeraci (2004a), significant factors increasing the probability of residual pore pressure generation are:

- *Pore fluid stiffness*: A reduction of the pore fluid compressibility in comparison with that of the solid skeleton increases the potential of residual pore pressure generation.

- *Soil relative density*: Residual pore pressure is likely to be generated in loose to medium dense soils.

- *Ratio of drainage to loading periods*: For buildup of appreciable residual pore pressure, there must exist quiet a large difference between drainage period (T_{Drain}) and the cyclic load period (T_{Load}). The drainage period can be estimated as: $T_{Drain} = A\frac{L_D^2}{c_v}$ In which (A) is a dimensionless factor, can be considered as unity (De Groot et al., 2006a), (L_D) the length of the drainage path and c_v is the coefficient of consolidation.

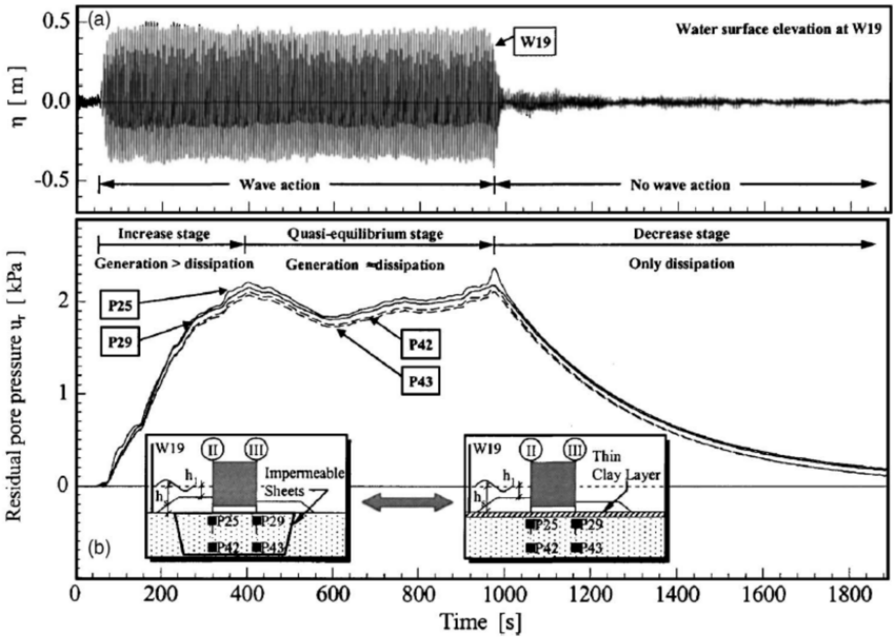

Figure 2.9: The three stages of residual pore pressure generation and dissipation underneath a caisson breakwater (Kudella et al., 2006)

- *Ratio of cyclic shear stress to vertical effective stress*: The increase of this ratio increases the residual pore pressure generation and consequently increase vulnerability to liquefaction in less number of loading cycles.

Implication 6 (Pore Pressure) *1. Wave-induced pore pressure in seabed can be decomposed into a transient component and a residual component. Transient pore pressure is mainly associated with elastic soil behaviour, whereas residual pore pressure is mostly associated with plastic soil behaviour. Therefore, modelling plastic soil behaviour is essential for modelling residual pore pressure.*

2. Pore pressure development is highly affected by pore fluid compressibility. Actually, pore fluid is compressible; therefore, only a small depth upper layer in the seabed is affected by transient pore pressure changes, unless special conditions are present which allow the maintenance of low air content in pore fluid.

3. Development of residual pore pressure is more favourable for: lower pore fluid compressibility, low to medium soil relative density, higher ratio of drainage to loading period and higher ratio of cyclic shear stress to vertical effective stress.

4. Only the frequency and amplitude of caisson motions induced by successive breaking wave loads are capable of generating residual pore pressure.

2.2.3 Soil liquefaction and cyclic mobility

Two types of soil liquefaction may be induced in the seabed by water waves: Instantaneous and residual liquefaction. Nonetheless, instantaneous liquefaction cannot occur in the seabed underneath a caisson breakwater, even in unfavourable drainage conditions. This is due to the large effective stresses induced by the own weight of the caisson breakwater (cf. Kudella et al. (2006)).

Residual liquefaction is associated with residual pore pressure, which changes gradually against load cycles. The residual pore pressure is mainly associated with soil skeleton plastic volumetric strain (contraction or dilation). Residual excess pore pressures are expected to eventually disappear after cyclic loading stops (due to drainage) or after soil relative density has reached a value such that the rate of pore pressure dissipation exceeds the rate of pore pressure generation (even if cyclic loading of the same amplitude is still applied). Loose to medium dense sands are most vulnerable to residual liquefaction during seismic action.

Around marine structures, wave loading can cause partial rather than complete liquefaction. This means that the excess pore pressure buildup does not reach a critical value for the soil foundation to liquefy. Excess pore pressure frequently causes a significant decrease in shear resistance of part of the soil body, which may result in a large deformation or even shear failure of the foundation (De Groot et al., 2006a), especially via the stepwise failure mechanism (Fig. 2.8).

Caisson motions caused by wave loads induce asymmetric (impact loads) or very asymmetric (quasi-static or pulsating loads) cyclic loads on the soil underneath, due to large mean load caused by own weight of the structure. In case of asymmetric (or very asymmetric) loading, no complete liquefaction is reached if the average relative shear stress is sufficiently large and the relative shear stress amplitude is sufficiently small. An "equilibrium" with constant average pore pressure is reached after a sufficient number of cycles. This "equilibrium" concerns only the residual pore pressure, which may not change. Such "equilibrium" generally takes place in undrained cyclic shear tests because of unfavourable drainage conditions that prohibits pore fluid to squeeze out of the soil sample. However, in natural seabed soil with normal drainage conditions, the residual pore pressure will buildup until an equilibrium point (saturation point "*S*" in (Kudella et al., 2006)). Afterwards, dissipation of pore pressure exceeds pore pressure generation as soil reaches its maximum densification potential corresponding to the applied cyclic load amplitude. Additionally, the sign of residual pore pressure is defined by the position of the current stress state in relation to the phase transformation line (or surface for 3D stress states). Generally, the phase transformation line divides stress states that cause contraction ($+ve$ residual pore pressure) or dilation ($-ve$ residual pore pressure) of soil.

Meanwhile, as the soil is cyclically loaded, the cycles are associated with continuous shear strain termed "cyclic mobility" (Castro, 1975), as illustrated in the upper parts of Fig. 2.10 (a) and (b). The equilibrium point in the stress path is laying at the intersection of the average shear stress and the phase transformation line (Vaid and Chern, 1983) as illustrated in Fig. 2.10 (a) and the upper curve in Fig. 2.10 (c). If the starting point lies between the phase transformation line and the failure line, i.e., if the average shear stress is high enough and the sand is not too loose, the mean pore pressure becomes negative and the effective stress increases, as illustrated in Fig. 2.10 (b) and the lower curve in Fig. 2.10 (c). The phase-transformation line is the line that seperates dilative and contractive behaviour (pore pressure decrease/increase) of the soil as it is sheared.

Sumer et al. (2008) performed simplified experiments with a rocking plate over a soil box to study the effect of the rocking amplitude and frequency on seabed response. Unlike underneath caisson structures, complete liquefaction occurred during some of the experiments. This is due to the absence of the massive weight of the structure, which causes higher confinement pressures and hence higher soil strength. The test conditions also neglect the rocking asymmetry of the structure. The tests, however, provided a good insight into the development and decay of residual pore pressure in relation to soil densification.

Implication 7 (Liquefaction) 1. *Instantaneous liquefaction due to direct wave action is not expected to occur beneath marine monolithic structures.*

2. *Cyclic loads exerted by the structure rocking motions are very asymmetric. Therefore, partial residual liquefaction is the relevant process for foundations underneath caisson breakwaters, in which pore pressure generation and dissipation are in equilibrium after a sufficient number of load cycles and soil shear strength is reduced by the accumulated pore pressure. After soil densifies as a result of several consecutive load cycles, residual pore pressure will reduce even with further loading cycles of the same load amplitude. The most relevant process for the study*

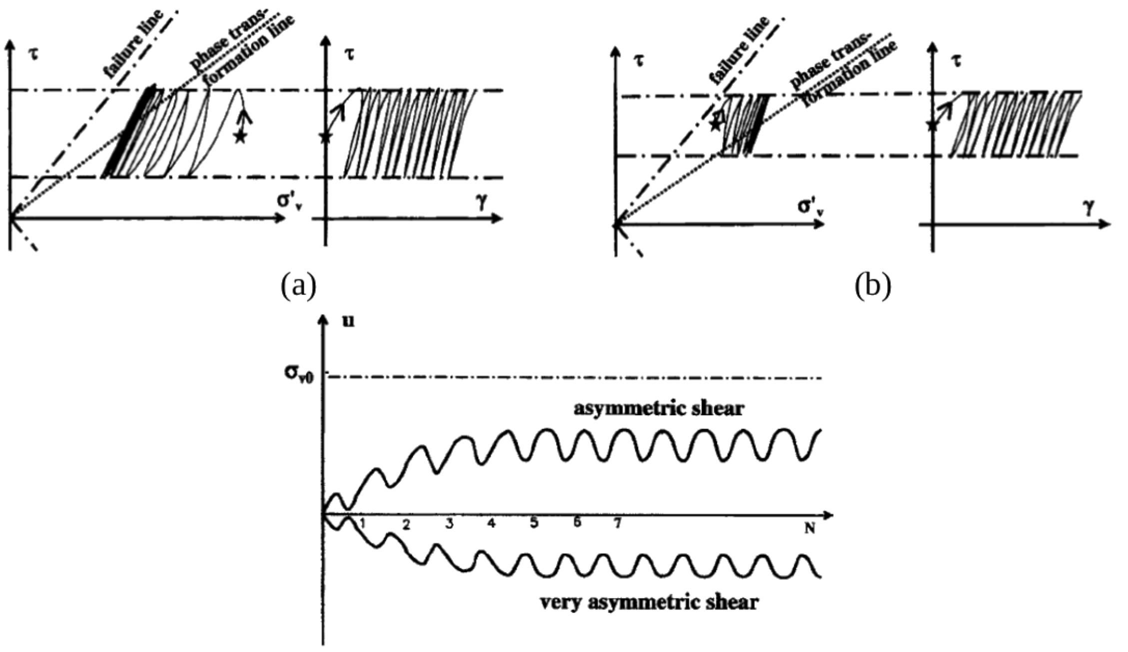

(a) (b)

(c)

Figure 2.10: Stresses and strains in dense sand with undrained cyclic shear (a) asymmetric loading: partial liquefaction and cyclic mobility; (b) very asymmetric loading: negative excess pore pressure and cyclic mobility; (c) corresponding pore pressure development. In this figure, u is the pore pressure and N is the number of load cycles (De Groot et al., 2006a)

problem is cyclic mobility.

3. *Liquefaction is affected by the relative density and the cyclic shear stress amplitude ratio.*

2.3 Modelling Seabed as a Porous Medium

Several studies focused on the applicability of different formulations of the governing equations for modelling seabed response (as a porous medium) to water waves (Ülker and Rahman, 2009; Ülker et al., 2009, 2010, 2012), in a similar approach as Zienkiewicz et al. (1980). The complete formulation was referred to as fully dynamic (FD), the u-p formulation as partially dynamic (PD) and the Biot's original formulation as quasi-static (QS). The equation sets were solved analytically, with no structure present, to form generalized analytical models for seabed response to water waves under plane strain conditions. The models were not validated against experimental results.

Jeng and Cha (2003) proposed a simple relation (between the two dimensionless parameters Π_1 and Π_2, defined in Zienkiewicz et al. (1980)) for the boundary between (QS) and (FD) solutions, assuming that for most cases in the wave-induced seabed response both the (PD) and (FD) solutions yield almost identical results. This simple relation was examined against the system proposed by Ülker and Rahman (2009); Ülker et al. (2009). It was found to be valid only for a specific range of Π_1 that depends on the problem characteristic. Nevertheless, the classification of Ülker et al. (2009) is more general. According to these studies, it was found that inclusion of inertial terms of soil skeleton and water displacement relative to the skeleton (complete formulation FD) have significant influence on seabed response in some cases and hence cannot be totally neglected. Apart from small wave periods, the quasi-static approach is sufficient for soils with small permeability (clays). From observing results of the latter study, it is apparent that the $u - p$ formulation yield results much closer to the quasi-static solution than to the complete formulation. For highly permeable soils, such as gravel, the complete formulation is a must. Nevertheless, for sandy seabed, considering the complete formulation or the $u - p$ formulation depends on many factors, among them; soil permeability, wave period, water depth and degree of saturation of soil.

Another important study by Ülker et al. (2009), which is extremely relevant to the problem under consideration, examined numerically via the FEM the effect of different formulations on the dynamic response of the rubble foundation and seabed under a caisson subject to breaking wave impact. The breaking wave impact was estimated using the PROVERBS method (Oumeraci et al., 2001). The study compared the FD, PD and QS formulations. Nevertheless, soil and rubble are considered as elastic media. The pore fluid was considered to be only water with a modified compressibility to account for gas content.

In their study, it was concluded that there exists a difference in the results from the different formulations. This difference is significant for pore pressures. Therefore, it is recommended to consider the FD formulation for a caisson subject to breaking wave impact. They also found that under the effect of wave impact load, a vertical breakwater experiences a rocking motion causing significant vertical displacements, high shear stresses and large pore pressures inside the rubble and in the underlying seabed. Furthermore, the saturation of the seabed generally affects the dynamic response (from all three formulations) both in the seabed and in the rubble foundation. Especially, the pore pressure response is affected more significantly. As the saturation increases, larger pore pressures are obtained in the seabed and the differences between the pore pressure responses obtained from three formulations increase.

The same model was also used to study the caisson-rubble-seabed system dynamic response to standing waves (Ülker et al., 2010). The three possible formulations are considered with respect to the inclusion of inertial terms associated with the motion of fluid and solids. The response is presented in terms of stress and pore pressure distributions at three locations (vertical sections) underneath the breakwater. The instability of seabed and rubble mound due to instantaneous liquefaction is also studied. The study of plastic deformations and buildup of pore water pressure was not possible due to the consideration of only an elastic constitutive relation for soil. An impermeable layer is considered to cover the seabed and pressure from harmonic waves is considered analytically (linear wave theory). Like the former study, the latter study found the inertial terms to be of great significance. Therefore, the use of a fully dynamic formulation is further emphasized. It was also found that the $u - p$ formulation (neglecting fluid acceleration) is significantly closer to the quasi-static solution than to a fully dynamic one. It was found that the model is in qualitative agreement with results from the large-scale model tests by Kudella et al. (2006).

The previous studies make it clear that there is a need for a complete dynamic formulation of the governing equations and it becomes more significant for cases of soils with higher permeability under higher frequency loading. Although the elastoplastic soil behaviour has not yet been tested under different formulations, the results from the aforementioned studies are apparently applicable to the current study. Simplifications of the model could be tested with a proper validation procedure. The validation of the simplifications should also account for model's specific conditions as well as for frequencies of the applied loads to the study problem, e.g. frequencies of caisson motion.

Implication 8 (Modelling Soil as Porous Media) *1. To account for pore pressure in geotechnical modelling one can consider the soil as undrained (not accurate but conservative) and apply empirical models that relate pore pressure to soil stresses or consider models that treat soil as a porous medium (theoretically sound and most accurate).*

2. Macro-mechanical theoretical models of porous media consider a porous medium to be a superposition of two or more overlapping continua; they all lead to a similar set of equations. In modelling soil, it is more convenient to adopt Biot's formulation (Biot, 1965) and to consider the soil as a superposition of a solid continuum and a single fluid continuum. The single fluid phase is water. The effect of air in the pores can be introduced via a reduced fluid bulk modulus.

3. The approximation of soil modelling as a porous medium may include the following simplifications: Neglecting only pore fluid accelerations or neglecting both accelerations of pore fluid and solid skeleton. Nevertheless, it was shown that a fully dynamic approach is essential for the analysis of a seabed underneath a caisson breakwater (due to the relatively high rocking frequency of the structure, which might be up to two orders of magnitude larger than the frequency of the incident waves).

2.4 Soil Constitutive Models

A soil constitutive model is needed to idealize the stress-strain relationship for the soil continuum. Here, the introduction of the effective stress principle is very important to directly use the soil constitutive models developed for fully drained conditions, which have been extensively addressed in the soil mechanics literature. Modelling soil behaviour is a complex task. The literature is rich with various soil constitutive models. However, no soil constitutive model remains a controversial issue and no single model can capture all aspects of soil behaviour and none has gained enough acceptance to be considered as a "standard" model.

To simulate residual pore pressure and residual deformations caused by cyclic loading, the soil constitutive model should be able to capture plasticity induced by small stress changes rather than by large continuous stresses (monotonic loading). Therefore, classical plasticity models (e.g. the Cam-Clay model) are not well suited for cyclic loading because under such conditions, almost all stress states occur inside the yield surface, and hence the classical elastoplastic models provides no advantage over purely elastic models.

Soil constitutive models can be classified in three main groups (Fig. 2.11):

- *Elastic models*: Linear (isotropic or non-isotropic with assumption of cross anisotropy) or non-linear (hyper- or hypo-elasticity)
- *Models based on soft computing*: Neural networks, generic programming and fuzzy logic. The model is trained for large data set and works like a "black-box"
- *Plasticity models*: Elasto-plastic models with a yield surface separating elastic and plastic response, and plasticity models without an explicitly defined yield surface.

Fig. 2.11 provides an overview of soil constitutive models, with highlight on relevant models for the study problem (in green) and the used components for the soil constitutive model selected for the PhD study (in yellow). In the following subsections, only the soil constitutive models that can simulate residual deformations of the soil are briefly discussed, including the implications for the PhD study. A more detailed discussion of these and further soil constitutive models is provided in El Safti and Oumeraci (2011).

2.4.1 Models based on soft computing

To avoid the complexity associated with mathematical modelling of materials, material models can be directly based on soft computing techniques such as neural networks (NN), genetic programming and fuzzy logic, which can be applied as alternative tools for the simulation of constitutive relations. Among these techniques only NN have been widely used. NN-based constitutive modelling started in the early 1990s by Ghaboussi and co-workers (Ghaboussi et al., 1990, 1991). Since then research in this field has expanded.

The NN material modelling approach is developed through learning from examples, which are obtained from experimental test data. During the training, the NN adapts to the new environment and self-organizes to eventually learn the underlying constitutive material behaviour present in the material data. The flexibility of NN models to adapt to new environments, which allows the NN model to be further trained by new data and information available from new studies , offers a fundamental advantage (Sidarta, 2000). The major limitation of these models are associated with their black-box approach to soil constitutive modelling.

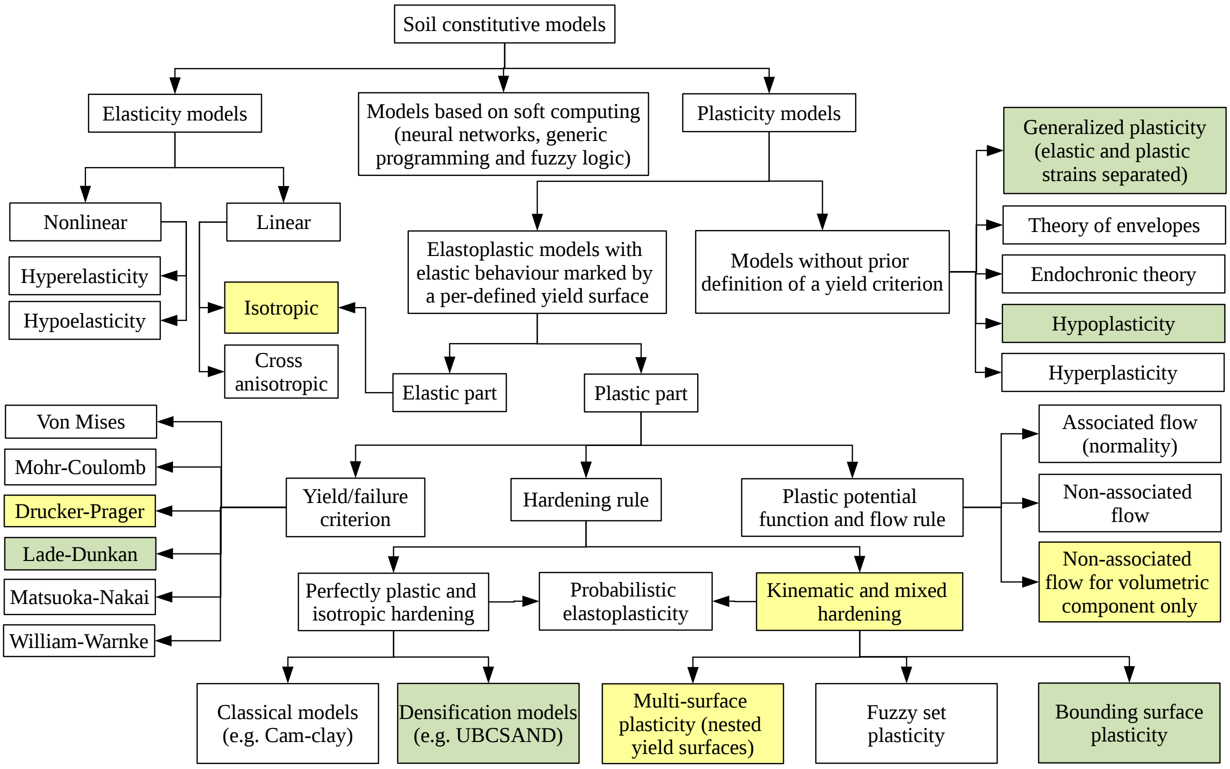

Figure 2.11: Soil constitutive modelling (green boxes are promising models for feasible modelling of sand under cyclic loading. Yellow boxes are the selected models for the PhD study)

2.4.2 Elastoplastic models with an explicit yield criterion

Plasticity models with a predefined yield criterion need to describe four aspects: (i) The elastic behaviour, (ii) The yield function, (iii) The hardening rule and (iv) The plastic potential function and the flow rule. In elastoplastic models, the elastic part can be considered with the assumption of isotropy. Anisotropy is introduced implicitly by the plastic part.

Several failure criteria (yield functions) are used for elastoplastic models (e.g. Tresca and von Mises). Nevertheless, granular material are more accurately modelled by pressure dependent criteria (e.g. Drucker-Prager). The Mohr-Coloumb criterion has been used for modelling sand with better results than Drucker-Prager. Other failure criteria that best represent granular material are Mohr-Coloumb like criteria with smoothed edges (e.g. Lade-Duncan). These models provide better results than the Drucker-Prager criterion, because they include the effect of the Lode angle. The Drucker-Prager criterion, nevertheless, provides a more convenient substitute for kinematic hardening models (especially multi-surface models).

a. Isotropic hardening and critical state models

It is a major disadvantage for classical elastoplastic models when all stress paths of a certain problem lie inside the yield surface. Thereby, the model is merely a linear elastic model. Classical models are also not capable of modelling hysteresis in loading-unloading cycles.

Several modifications were made to classical Cam-Clay models, most important modifications can be found in Gens and Potts (1988). Nevertheless, the Cam-Clay models suffer some major limitations such as the inability to properly model granular soils.

Existing Cam-Clay models fail to predict observed softening and dilatancy of dense sands and the undrained response of very loose sands. Although a number of double hardening sand models (e.g. Nova and Wood (1979); Vermeer (1978); Lade (1977)) have been available for many years, they have not been widely used in numerical analyses. This was due to the use of two separate yield surfaces for modelling hardening and softening, which may cause significant numerical difficulties. Another reason would be the large number of constants needed to be determined before a model can be applied (some of these constants have no clear physical meaning).

Soil failure induced by cyclic loading is due to either flow liquefaction or cyclic mobility. Liquefaction due to cyclic loading can be thought of as an accumulation of pore pressure with loading cycles, then liquefaction occurs in the last cycle as shear failure would happen under monotonic loading (due to shear strength reduction by pore pressure accumulation). Following this interpretation, the strain in the constitutive relation can be decoupled into a monotonic component and a densification component caused by cyclic loading (e.g. the model by Zienkiewicz et al. (1978), based on a non-associative Mohr-Coulomb model with zero dilatancy, as described in Zienkiewicz et al. (1999)).

The densification model is the only model that decouples the strain into a monotonic component and a cyclic component. The Zienkiewicz et al. (1978) model is only capable of modelling undrained soils until complete liquefaction or until the stress path reaches the phase transformation line. Nevertheless, to model cyclic mobility that occurs after the stress state reaches the phase transformation line, some modifications need to be introduced to the model (e.g. Shiomi and Tsukuni (1998)). In the Shiomi and Tsukuni (1998) model, the volumetric strain increment can be considered as a function which represents the limitation of the volumetric strain at a large damage parameter, which is a damage quantity that causes irreversible dilatancy. The damage quantity is dependent on the stress ratio and the accumulated shear strain.

Densification models are simple and provide relatively acceptable results for practical use. The UBCSAND model (Byrne et al., 1995; Beaty and Byrne, 1998; Byrne et al., 2004) is gaining wide acceptance for practical applications. This model uses the Mohr-Coulomb yield criterion and the Drucker-Prager function as a plastic potential function to maintain the assumption of stress-strain coaxiality. In this model, a simple procedure based on the mobilized friction angle is used to model responses for load reversal and change of direction. Densification models can be used with empirical models for relating excess pore pressure change with number of load cycles to account for excess pore pressure buildup under cyclic loading.

b. Kinematic hardening models

Classical soil elastoplastic models, which define only one yield surface, suffer from the sudden change from elastic to plastic behaviour, whereas in natural soils the transition is gradual. These models often overestimate the elastic domain and are not suitable for situations where unloading occurs. Furthermore, they fail to model cyclic loading. As shown earlier, perfectly plastic as well as isotropic (volumetric) hardening models are capable of modelling phenomena associated with cyclic mobility only if special care of densification and plastic unloading is considered. Another approach is reviewed herein which allows for liquefaction, cyclic mobility and plastic unloading to be simulated with more accuracy.

Mroz (1967) and Iwan (1967) introduced the concept of multiple yield surfaces to modelling metals. This was further extended to modelling geomaterials (Prévost, 1977, 1978; Mroz et al., 1978, 1979, 1981). The hardening in these models is established mainly by changing the position of yield surfaces (kinematic/anisotropic hardening) or changing both their position and size (mixed hardening), as opposed to changing only its size (isotropic hardening). A single yield surface defines the change of soil behaviour from highly stiff in elastic region to softer behaviour in plastic region. Multiple loading (yield) surfaces in this regard approximate soil behaviour (stress-strain relationship) to smaller line segments that better match the actual behaviour. The outmost yield surface represents a failure surface, beyond which neither stress states nor inner loading surfaces can lie. The multi-surface plasticity models are able to reproduce most of the basic features of soils under cyclic loading, such as memory of past events and plastic deformation during unloading. They have been shown to perform well in modelling liquefaction and other cyclic loading phenomena (Ghaboussi and Momen, 1982; Hirai, 1987; Aubry et al., 1982). However, the computation costs are quite high.

Based on the original multi-surface plasticity theory for frictional non-cohesive soils (Prévost, 1985), another constitutive model was developed with the emphasis on simulating mechanism of shear strains due to (non-flow) liquefaction in clean non-cohesive soils with special attention given to dilation under cyclic loading which causes cyclic mobility (shear stress and volumetric strain coupling), Elgamal et al. (2003). The model basically focuses on situations where no flow (complete) liquefaction occurs. Therefore, it is better suited for medium-dense to dense sands. Nevertheless, in experimental observations (e.g. Ishihara (1985); Arulmoli et al. (1992); Boulanger and Seed (1995); Sture (1999)), shake-table, and centrifuge tests (Dobry et al., 1995; Dobry and Abdoun, 1998; Balakrishnan et al., 1997), relatively loose soils with relative density of (D_r = 37%) may exhibit cyclic mobility rather than flow liquefaction (especially under asymmetric loading). Regarding the behaviour of seabed soil in the experiments by Kudella and Oumeraci (2004a), it is evident that cyclic mobility is the relevant soil phenomenon, due to asymmetric load conditions inherited from the nature of caisson response to breaking wave loads. Although the sandy seabed was loose (D_r = 21%), the maximum achieved residual pore pressure ratio ($p_r/\sigma_v^{'}$) was 0.25 (25% of the critical value for liquefaction initiation) with no potential for flow liquefaction in natural conditions. The multi-surface model was developed to allow for the simulation of (observed) sand behaviour in the triaxial stress plane ($p^{'}$-q) relative to the phase transformation line. Further, Yang and Elgamal (2004, 2008) used the Lade-Duncan failure criterion in their model (for which the Lode angle effect is considered) which compared well to discrete element model of granular materials (Thornton, 2000) and also to experimental results as well. Multiple yield surfaces models were used in several Engineering applications, in which these models showed a good agreement with experimental results of centrifuge tests (e.g. Yang and Elgamal (2001); Yang et al. (2003b); Zhang et al. (2003)).

Due to the long computational time required by multi-surface plasticity, simplified versions were developed. The bounding surface plasticity models utilize only two explicitly defined surfaces, the outer (or consolidation) surface and the inner (or yield) surface, unlike multi-surface models for which all surfaces must be previously defined. On the bounding surface, plastic strain develops according to classical plasticity theory through material hardening or softening properties. Nevertheless, a field/continuum of intermediate loading surfaces is implemented to transfer the stress state between both explicit surfaces (interpolation rules). Thereby, the bounding surface models provide a smooth transition from elastic to plastic behaviour, as observed for real soils. This feature is considered as an advantage of bounding surface models over multi-surface models. Only the relative location of the inner and outer surfaces completely describes the distribution of all intermediate surfaces. Manzari and Dafalias (1997) developed a critical state bounding surface model for sands, for which the loading surfaces resemble a rounded Mohr-Coulomb criterion in the deviatoric plane.

Elastoplastic fuzzy set models for sand plasticity were introduced to address sharp transition of plastic moduli in multi surface models (Klisinski, 1988; Klisinski et al., 1991). Further, probabilistic elastoplastic models address the uncertainty in soil parameters arising from spatial variation and from testing of soils directly by increasing emphasis on probabilistic characterization of soil continuum, and hence introduce probabilistic constitutive relations. Fenton and Griffiths (2003) introduced a probabilistic simulation of spatially random ($c - \phi$) soil using Monte Carlo technique. It was shown that due to uncertainty in yield function (stress), there is always a possibility, depending upon the magnitude of uncertainty that a plastic behaviour starts at very low strain and influence of elastic behaviour continues far into plastic domain (at large strains) and hence, the ensemble average (mean) of all the possibilities or the most probable (mode) possibility differs from deterministic behaviour. In addition, a very realistic, smooth transition between elastic and plastic domains was observed even for elastic-perfectly plastic models. Furthermore, nonlinear behaviour was observed even for linear hardening models. A realistic cyclic material behaviour could be obtained even with the simple elastic-perfectly plastic probabilistic model. It was also shown that considering either an isotropic or a kinematic hardening rule did not significantly improve the qualitative nature of the simulated cyclic soil response. These findings support the probabilistic micromechanical simulation results by Einav and Collins (2008).

Other models that implement kinematic hardening include the constitutive models for frictional (granular) geomaterials based on a micromechanical approach (e.g. Nemat-Nasser and Zhang (2002)). This type of models satisfies non-coaxiality of soil plasticity, which means that the principle axes of stress and plastic strain-rate are not coincident. This concept is experimentally evident for granular materials. Another concept is the rotational kinematic hardening (Lade and Inel, 1997). This alternative approach incorporates rotation and intersection of yield surfaces to achieve a better fit with experimental data.

2.4.3 Plasticity models without a predefined yield criterion

In these models, the yield function and the plastic potential function are a product of the formulation rather than being explicitly defined.

a. Generalized plasticity

Generalized plasticity is one of the most established approaches to elastoplastic modelling without a predefined yield criterion. A first important step for formulation of the generalized plasticity theory was the idea, suggested by Eisenberg and Phillips (1971), of a plasticity model where, as opposed to classical plasticity, loading and yielding surfaces are not explicitly defined. Then Lubliner proposed some simple generalized plasticity models which are able to represent some observed experimental behaviour of metals (Lubliner, 1974; Lubliner et al., 1993).

Zienkiewicz et al. (1985) applied both bounding surface theory for modelling loading phase and generalized plasticity theory for modelling unloading phase to establish a model to analyze soil behaviour under static and transient loads. They used critical state yield surface and a modified plastic modulus. They defined the plastic modulus as the product of a function of derivative of yield surface with respect to plastic strain and a nonlinear function of distance between current yield surface and bounding surface. The same method for the analysis of sand in Pastor et al. (1985) was used. Chen and Baladi (1985) expressed stress-strain relation in terms of the hydrostatic and deviatoric components of strain and stress. Therefore, these relations can be used simply if there are components of the flow rule vector and the plasticity modulus. Pastor et al. (1990) proposed a plastic modulus and a flow rule dependent on soil dilatancy without using special yield and potential surfaces. They defined components of the flow rule in the directions of volumetric and shear deformations.

b. The theory of envelopes

Chandler (1985) presented a plasticity theory which starts with a dilatancy rule and a function of plastic strain rates which represents the energy dissipated during plastic deformation. Yield functions and flow rules are then derived from energy conservation and the mathematical theory of envelopes. Unlike the critical state soil mechanics approach, the method proposed by Chandler does not assume a universal validity of the associated flow rule.

The theory of envelopes approach has enabled a physically based understanding of the material behaviour to be encapsulated within the mathematical formulation of material models. Investigations by (Chandler, 1985; Collins and Houlsby, 1997) have shown that the flow is non-associative because frictional dissipation (i.e. dissipation that is dependent on the current state of stress carried by the assembly) is present. Models based on such an approach are used to simulate the behaviour of granular materials and are able to capture many of the features of granular material behaviour that have been demonstrated experimentally (Chandler, 1990; Chandler and Sands, 2007).

Due to the limitations of the theory of envelopes approach, reasonable choices of dissipation functions and dilation rules do not always result in analytical expressions for the yield surface, which is limiting progress in this area. Therefore, Chandler and Sands (2010) extended the framework by introducing optimization to assist the numerical rather than the mathematical establishment of the yield function. An optimization approach to the formulation of constitutive equations confirms earlier results found using the theory of envelopes. These show the pivotal role of the theory of optimization in providing an insightful structure for both associated and non-associated plasticity.

c. The endochronic theory

The endochronic theory of plasticity is a special case of the theory of viscoplasticity originated by Valanis (1970, 1975) and based on the concept of intrinsic time. The endochronic theory builds on the principle of thermo-dynamics and internal variables and is a direct extension of viscoelastic theories. The theory has undergone development and modification with the aim of modelling soil stress-strain behaviour (e.g. Valanis and Read (1982); Dangar and Nuh (1980). It is shown by Valanis (1970, 1975) that the endochronic theory is unifying in the sense that many existing theories of viscoelasticity, plasticity (e.g. perfect plasticity, theories with isotropic hardening, kinematic hardening, combined hardening, bounding surface or multi-surface plasticity) can be obtained as special cases by imposing suitable constraints on the material parameters involved. In addition, it does not make use of the idea of a yield surface to start off the model formulation.

The theory is found to be very capable of simulating unloading-reloading behaviour of soils Imai and Xie (1990); Yu (2006). Nevertheless, this theory is not very popular in geotechnical modelling due to inherent difficulties in mathematical formulation and existence of other rather straightforward models that focus more on modelling specific soil phenomena.

d. Hypoplasticity

Hypoplastic constitutive models assume a general incremental stress-strain relationship, which follows as a result of a (numerical) integration over time; thus the relationship depends on the load history. Hypoplastic models are formulated by a heuristic process considering the essential mechanical properties of soil (which includes trial and error to establish a suitable relation). Hypoplastic models differ from hypoelastic models in that the constitutive equation is incrementally non-linear rather than linear. Hypolplastic models need no definition a yield or any plastic potential function or a plastic flow rule, and no separation between elastic and plastic strains is made. Hypoplastic models are regarded by Zienkiewicz et al. (1999) to be the most promising framework for direct formulation of a stress-strain relationship. One of the first of such models was introduced by Darve and Labanieh (1982). Since then, it has been considerably improved (Desrues and Chambon, 1993). The model proved to reproduce well the behaviour of soils under both monotonic and cyclic loading. Dafalias and co-workers presented extensions of the bounding surface model within the framework of hypoplasticity (e.g. Dafalias (1986); Wang et al. (1990)). Hypoplastic models have been introduced also in Karlsruhe by (Wu and Kolymbas, 1990; Kolymbas, 1991; Kolymbas and Wu, 1993) who provided general expressions for the constitutive tensor. In France, hypoplastic models were introduced by Darve and Labanieh (1982); Desrues and Chambon (1993). A comparative review of the German and French approaches is given by Tamagnini et al. (2000). Hypoplastic models were formulated by a heuristic process considering the essential mechanical properties of granular materials undergoing homogeneous deformations.

Hypoplastic models are capable of describing a number of significant properties of granular materials: non-linear stress–strain relationship, dilatant and contractive behaviour, pressure dependence, density dependence and material softening. A further feature of hypoplastic models is the inclusion of critical states, i.e. states in which a grain aggregate can deform continuously at constant stress and constant volume. The distinctive characteristic of these models is their simple formulation and procedure for determining material parameters with standard laboratory experiments. The material parameters are related to granular material properties, i.e. size distribution, shape, angularity and hardness of grains (Herle and Gudehus, 1999). A further advantage lies in the fact that one single set of material parameters is valid for a wide range of pressures and densities. An exhaustive review of the development of hypoplasticity can be found in Wu and Kolymbas (2000) and Tamagnini et al. (2000). To increase the application range, a hypoplastic constitutive law has been extended for an elastic strain range (Niemunis and Herle, 1997), anisotropy (Tejchman et al., 2007) and for viscosity (, Niemunis; Gudehus, 2006). Hypoplastic models have diverse applications in granular material modelling. Unlike other models, the hypoplastic models are successful in reproducing the mechanical behaviour of sand rather than clay. The hypoplastic equations were modified to account for soils with low friction angle (Herle and Kolymbas, 2004) and also for clay.

e. Hyperplasticity

Hyperplasticity is a thermo mechanical approach to material behaviour. This theory may be regarded as an extension of hyperelasticity. A specific free energy function and a specific dissipation function are assumed for the material. The first ensures that the material obeys the first law of thermodynamics, whereas the second, a positive dissipation function, ensures that the material complies with the second law.

Houlsby (1982) shows that the formulation of an elastic-perfectly plastic material with a von Mises yield criterion and an associated flow rule can be derived by considering a free energy expression and a dissipation function which were also defined. Houlsby (1981) was the first to show that it is possible to derive critical state models using the thermo-mechanical approach, although a more general and extensive treatment was given by Collins and Kelly (2002). For example, a critical state model, almost identical to the modified Cam-Clay model, was obtained. Houlsby and Puzrin (2000) present a hyperplastic (thermo-mechanical) framework for the modeling of kinematic hardening of plastic materials. The advantage of this approach is that it allows for a compact development of plasticity theories that are guaranteed to obey thermodynamic principles. The study started with a single then multiple yield surfaces. The case of infinite yield surfaces was presented. Interpretation of hyperplastic models in terms of conventional plasticity is presented together with the link between hyperplasticity and conventional plasticity. Thermo-mechanical approaches to constitutive models for unsaturated soils are also reported in the literature (Hutter et al., 1999; Coussy, 2007; Coussy et al., 2010).

The use of a thermomechanical framework enables the geotechnical modeller to incorporate more fundamental physics into the basic concepts of the model than in most of the currently available modelling procedures. Despite some important advantages, the thermo-mechanical approach is apparently indirect in the sense that, for a given material, appropriate specific free energy and dissipation functions may be more difficult to determine than appropriate yield surfaces. Houlsby (1981) noted that for simple models, the thermo-mechanical approach may not offer any significant advantages over the conventional plasticity of assuming yield functions.

Implication 9 (Soil Constitutive Model) *1. The spectrum of theoretical models available to account for soil plasticity is very broad. A selection of a proper soil constitutive model that can successfully capture the most relevant aspects of soil behaviour under caisson breakwaters is crucial for the performance of the entire model system.*

2. Models based on soft computing are easily and conveniently able to simulate soil behaviour for various conditions. Nonetheless, their black-box nature makes it very difficult to draw any insight into the physical processes underlying the behaviour of the soil considered.

3. Classical (perfect-plasticity or isotropic hardening) elastoplastic models cannot capture soil behaviour under cyclic loads.

4. Soil constitutive models that can properly and practically (i.e. with less mathematical complications and more focus on essential physics) simulate sandy soil response to cyclic loading include: densification models, multi surface plasticity models, generalized plasticity models and hypoplasticity models.

5. Other sophisticated models (e.g. the endochronic theory and theory of envelopes) may be able to capture soil *behaviour under transient loading. However, their mathematical complications and indirect formulations hinder their wide use in geotechnical modelling.*

6. Densification models are implemented in some commercial software; however, for this study, satisfactory results are not likely to be provided, because such models can simulate soil behaviour only until liquefaction occurs or until the stress path reaches the phase transformation line but not beyond. Moreover, modelling cyclic mobility that occurs after the stress state reaches the phase transformation line is not possible.

7. Generalised plasticity models are capable of simulating the behaviour of soils under monotonic and transient loads including liquefaction and cyclic mobility. However, the model parameters must be selected to best fit experimental results which in turn may need much more time for calibrating the model.

8. Hypoplastic models are very promising. They are simple to formulate and also include a procedure to retrieve the model parameters using standard laboratory experiments. Unlike most models, they are more successful in reproducing the behaviour of sands rather than that of clay.

9. Multi surface plasticity models are capable of conveniently modelling the cyclic mobility behaviour of sands. Cyclic mobility, as highlighted in this chapter, is the most relevant soil phenomenon when modelling soil behaviour underneath caisson breakwaters. A trade-off between computational expense and accuracy of the model is possible by configuring the number of loading surfaces.

10. Multi surface plasticity has already been implemented in the OpenSees framework, supported by NEES, in a $u - p$ *approximate fully coupled Biot's formulation with a Drucker-Prager failure criterion. Validation of the multi surface plasticity for modelling sands under cyclic loading is widely available with guidance on reasonable assumptions of model parameters.*

11. In conclusion, multi surface plasticity models have been identified as the most suitable soil constitutive models for this study. It is also important to note that considering one of the rounded Mohr-Coulomb criteria for loading surfaces provides the best fit to sand behaviour as retrieved from experiments. Moreover, a cap for the yield surface as generally used for monotonic loading is not important for modelling cyclic loading.

2.5 Wave-Structure-Foundation Interaction Models

A review of models for wave-structure-foundation interaction that can be found in the literature is herein presented. In this section, both experimental and theoretical models used to study seabed response to water waves in the presence of a marine structure are considered.

Jeng (2003b) reviewed, extensively, developments in dynamic interaction between waves, seabed and coastal structures, including studies until 2003. Jeng's major conclusion is that further research regarding theoretical wave-structure-foundation interaction should consider a more sophisticated fully coupled approach applying more advanced poro-elastoplastic soil models that are capable of simulating large deformations caused by phenomena such as liquefaction and scour. Furthermore, he suggested to study the link between liquefaction and scour, which he refers to as another challenging task. Finally, he stated the need for a generally more realistic theoretical approach for the protection of the seafloor around coastal structures. The following sub-sections discuss more recent and more relevant models of the problem starting with physical models, and then analytical and numerical models.

2.5.1 Physical models

The large-scale physical model set up in Hannover constructed under the EU project LIMAS (Liquefaction around Marine Structures) substationally contributed to understand several aspects of wave-structure-foundation interaction (Oumeraci and Kudella, 2004; Kudella and Oumeraci, 2004a,b, 2006; Kudella et al., 2006). The model was used to study the generation of transient/instantaneous and residual pore water pressure in a seabed underneath a caisson breakwater subject to both pulsating and breaking wave loads. Unfavourable drainage conditions are considered in the model via considering impermeable sheets that surround the seabed under the caisson The considered drainage conditions are most convenient for liquefaction to take place. For that purpose also, the seabed was considered to consist of loose sand. Nevertheless, even under sever breaking wave loads, total liquefaction of the seabed was not achieved; only one fourth of the critical residual pore pressure ratio ($p_r/\sigma'_{v0} = 1.0$) for total residual liquefaction could be achieved, i.e. $p_r/\sigma'_{v0} = 0.25$.

The study singled out the processes that most likely result in total or, most probably, partial liquefaction of a sandy seabed beneath a caisson breakwater under poor drainage conditions. It was found that caisson motion is the primary reason for (residual) excess pore pressure to develop in the seabed underneath the caisson. It was also found that only caisson motions with large magnitude and high frequency can generate residual pore pressure and that only severe breaking wave impacts are capable of generating such motions that can consequently induce residual pore pressures in the seabed. Finally, a very close correlation was found between residual pore pressure and residual soil deformation, Fig. 1.1. The research concluded that a detailed study of the balance between the generation and dissipation of pore water pressure represents the key to finally understand/quantify the correlation between residual pore pressure and residual soil deformation, and hence to allow for design guidelines to be developed based on allowable soil deformations.

Other large-scale model tests were performed earlier by Oumeraci et al. (1992) in the large wave flume (GWK). Horizontal impact force, uplift forces and the related overturning moments were determined. The experiments included pendulum impact tests to determine the eigenfrequency of the caisson breakwater system and its foundation. The added mass of water and the added geodynamic mass oscillating with the structure, the stiffness of the foundation and the damping ratio were evaluated as well. Both masses were found to increase with the amplitude of oscillation of the structure. Oumeraci et al. (1992) found, experimentally, that there is some threshold value above which permanent displacement of caisson was initiated. They also found that successive permanent displacement may accumulate and lead to the collapse of the structure.

Following the results of the large-scale physical model (Kudella et al., 2006), Sumer et al. (2008) developed another physical model for the study of residual pore pressure in silty subsoil of an estimated $D_r = 0.38 \pm 0.01$ underneath a caisson breakwater due to its rocking motion. In their model the caisson was modelled as a rectangular plate slightly buried in soil (to prevent separation of plate from soil during rocking action) that is submerged in a wave flume. The model is considered to complement the Kudella et al. (2006) model in providing a wider spectrum of results for validating/testing advanced numerical models. The test setup, as mentioned earlier, does not account for large initial effective normal stresses from the caisson own weight and the asymmetry of the caisson rocking motion.

Centrifuge studies of caisson breakwaters include (Rowe et al., 1976) and (Rowe, 1981), who reported excess pore pressure generation in loose sandy seabed zones. In their tests, seaward tilt of caisson was observed, which agrees with field observations reported by Oumeraci (1994). Their explanation for the seaward tilt of the caisson is that when caisson is under positive wave pressure the seaside toe of the caisson unloads the subsoil and water inflow underneath is initiated. Consequently, soil swells. Thereafter, the heel reloads the 'softened' subsoil causing an increase in excess pore pressure and the initiation of plastic failure (cyclic mobility or ultimately liquefaction). Van der Poel and De Groot (1998) illustrated the significance of load pattern on caisson response in centrifuge tests. Lee et al. (2005) , Zhang et al. (2009a) and Zhang et al. (2009b) conducted centrifuge model tests at 100g. The model set-up and wave loading equipment are described by Lee et al. (2005) and Zhang (2006). In their model, they followed the approach in earlier studies in which the impulsive wave load was applied directly to the caisson using an actuator rather than water waves.

In Zhang et al. (2009b), the significance of load reversal to caisson breakwater behaviour in centrifuge tests is highly stressed. They report that seaward tilting of the caisson, as observed in field and centrifuge tests, is due to other mechanisms in addition to that reported by Rowe (1981). They found that excess pore pressure generation only occurs for load reversal; non-reversal load will produce neither liquefaction nor cyclic mobility. This finding contradicts the earlier explanation of soil liquefaction underneath the caisson toe due to water inflow when caisson is rocking, as being the sole mechanism of the seaward tilt phenomenon. They also report that in reversal load tests with loose sand bed, (i) pore pressure beneath the caisson heel is higher than beneath the shorewrd toe and (ii) soil liquefaction initiates at around the mid-depth of the sand layer and then propagates upward, which suggests that the cyclic behaviour of the sand also plays an important role. Moreover, the failure mechanisms due to reversal load can be hindered by densifying the seabed.

In their explanation for the seaward tilt of caissons, Zhang et al. (2009b) added to the earlier explanation by Rowe (1981) that after wave impact and as the caisson settles, it is embedded further in the subsoil at its seaward toe, causing a seaward tilt and a transfer of the bearing pressure from the toe. This further reduces the effective stress beneath the caisson toe and reduces soil strength (partial liquefaction). This may explain the larger liquefied zone on the seaward side of the caisson as compared to the shoreward side; despite the lower excess pore pressure. Owing to the larger extent of liquefaction on the seaward toe, the caisson continues to tilt seaward.

Implication 10 (Physical Wave-Structure-Foundation Interaction Models) *1. Results from physical models agree relatively well with field observations. However, a complete satisfactory explanation of caisson behaviour (e.g. seaward tilt) is still missing. Developing and applying a more advanced numerical model will contribute to substantially improve the knowledge of the many less understood aspects of caisson breakwater behaviour.*

2. From the observations of the behaviour of the soil underneath a caisson breakwater subject to breaking wave load (through physical models), it is evident that cyclic mobility is the relevant soil phenomenon (buildup of pore pressure until equilibrium whereas shear deformation of the soil continues). The multiple yield surfaces soil constitutive model in this regard is expected to successfully reproduce physical experiments in the large wave flume.

3. Seaward tilt of caisson breakwaters was observed in many cases of their failure. Many explanations of such behaviour were presented in the literature. However, all explanations are not quite satisfactory. In the course of this study, a more appropriate explanation of such phenomenon will be presented.

2.5.2 Analytical models

Based on the boundary-layer approximation, Mynett and Mei (1982) investigated the wave induced stresses and pore pressure in a saturated seabed beneath a rectangular caisson. Their analytical solution provides a simple analytical tool for engineering applications, although it was limited to the case of only a caisson lying directly on a saturated seabed (no rubble foundation). Tsai et al. (1990) applied the boundary layer approximation to investigate composite breakwaters (caisson and rubble base) and incorporated the theory for contact problems. They considered three different problems in their model: heave, pitch and surge.

Hsu et al. (1993) studied analytically the wave-induced soil response in front of a vertical wall. A closed-form of the 2D analytical solution for an infinite thickness was derived, in which a new parameter combining hydraulic anisotropy and wave obliquity was introduced. The framework was extended to a seabed of finite thickness (Hsu and Jeng, 1994; Jeng and Hsu, 1996) as well as a layered seabed (Hsu et al., 1995). Tsai (1995) extended the analytical solution of Hsu et al. (1993) to a partially reflected short-crested wave system and predicted the liquefaction potential. Tsai and Lee (1995) measured the standing wave-induced pore pressure in a sandy bed fronting a breakwater. They found that the reduced two-dimensional form of the analytical solution proposed by Hsu et al. (1993) agreed well with the experimental results for most cases, except for larger wave heights, for which the solution of Jeng and Hsu (1996) and Hsu and Jeng (1994) should be used.

Jeng (1997) further investigated the wave induced seabed instability in front of a breakwater, which includes the liquefaction potential and shear failure. The liquefaction criterion proposed by Zen and Yamazaki (1990) was modified by including the lateral deformation. The difference between wave-induced liquefaction and shear failure in a porous seabed was clarified in Zen et al. (1998). Tsai et al. (2000) further investigated the effects of wave non-linearity on the standing wave-induced liquefaction potential in front of a breakwater. They attempted to link scour and liquefaction.

Kumagai and Foda (2002) proposed an analytical solution for the sinusoidal standing wave-induced soil response around a composite breakwater. Their analytical solution requires less computation time than a numerical model, while providing a physical insight into the interaction between wave, caisson, mound and seabed. Also, the model can provide the relative contribution of the radiation and scattering modes to the response. More information on the aforementioned and further analytical models can be found in Jeng (2010).

Implication 11 (Analytical Wave-Structure-Foundation Interaction Models) *Although analytical models provide a much faster alternative compared to numerical models, they are not particularly suitable for problems with high complexities such as non-linearities and strong interactions found in the problem of the PhD study.*

2.5.3 Numerical models

From reviewing a wide spectrum of wave-structure-foundation interaction models, they can be classified in five main groups based on the coupling approach between the fluid and the soil domains:

- Models that are completely uncoupled with focus on the fluid domain (CFD models). For CFD models the porous media (soil and/or rubble foundation) is considered as a non-deformable body that has added resistance to fluid flow.
- Models that are completely uncoupled with focus on the soil-structure domain (CSD models). The structural models focus on soil-structure interaction under wave loads computed analytically or empirically.
- Model systems that are semi coupled; output of CFD models from the first group is used as input for CSD models from the second group
- Fully integrated models; coupling is established between two solvers for two domains that advance with the same time step. Feedback between both models is established for purpose of updating the domain. The strength or weakness of coupling depends on the approach for solvers communication and domains update
- Monolithically coupled models which works on a unified domain for fluid and solids with unified set of equations. Models of this type are not yet applied to Coastal Engineering applications

a. Uncoupled CFD models

Following the same philosophy of the VARANS model (COBRAS), Hur et al. (2010) developed a numerical model of wave-composite breakwater-foundation interaction to study wave induced pore pressure and flow changes inside rubble mound and seabed. The model was validated against experimental results and was further used to study stability of composite breakwaters. This model is an extension of an earlier model developed by Hur and Mizutani (2003). The model considers the rubble base and seabed as fixed matrix (non-deformable porous media). Other similar studies include Van Gent et al. (1995); Liu et al. (1999); Hsu et al. (2002); Hur and Mizutani (2003); Cheng et al. (2009) These models are based on the same concept, i.e. that the flow outside and inside the porous media are governed by the same set of equations, which (i) account for flow resistance inside the porous media and (ii) reduce to free flow equations outside the porous media. The model uses finite difference to solve both free and porous flows with no need to define an interface between both continua; however, the pressure at the boundary is always the same for both.

The major advantage of the single-domain approach in solving the governing equations is that this formulation avoids the explicit introduction of the boundary conditions at the interface free surface/porous flow regions in the entire domain.

Validating the results from the Hur et al. (2010) model against experimental data, the model reproduces better results than previous model by Hur and Mizutani (2003). Moreover, it reproduces a phase difference between porous flow and free surface flow which is a feature that was not simulated by the previous model. Hence, the direction of the flow inside the seabed upward under the wave trough and downward under the wave crest. In addition, the flow inside the seabed is directed toward the leeside under the wave crest and toward the seaside under the wave trough. Furthermore, clockwise and anticlockwise vortices are observed in the vicinity of the seaside corner of the rubble. In addition, such vortices become clearer as wave steepness, H/L, increases on a rubble mound with the same width, B/L.

Hur et al. (2010) also found found that the wave period rather than its height affects the position of the maximum non-dimensional uplift pressure acting beneath the rubble foundation. On the other hand, uplift pressure on the caisson is found to exponentially decrease after the peak value at the seaward toe of the caisson, then ensues until levelling at about $0.31B$ to the leeside with respect to caisson width (B), and then a linear decrease occurs.

b. Uncoupled CSD models

Jeng et al. (2001) and Jeng (2003a) developed a general FEM model for wave- seabed-structure interaction the model is referred to in Jeng (2010) as PORO-WSSI. The model uses Biot (1941) poro-elastic model governing equations with introduction of orthotropic (cross anisotropic) elastic seabed. The model is similar to a model presented by Mase et al. (1994); nevertheless, as all wave-induced soil response parameters were to fluctuate periodically in time domain, in the GFEM-WSSI model they were expressed in a real part and an imaginary part.

Introducing the complex soil response into the Biot's equations and applying the Galerkin method, a finite element formulation was achieved. This model was reported to have been used in two applications: the wave-seabed-pipe interaction and the wave-seabed-caisson interaction problems.

Jeng and Li (2006) developed a 3D model for wave-induced residual pore pressure in a porous seabed around the head of a breakwater. In their model, the pore pressure was decomposed into transient and residual components. The transient component and associated soil stresses are calculated according to Jeng and Li (2006). For the residual component, the Biot's one-dimensional consolidation equation, as in Sumer and Fredse (2002) in which a source term of the pore pressure generation associate with surface water waves is defined, was extended to three dimensions.

Ou (2009); Jeng and Ou (2010) developed another three dimensional model for elastoplastic behaviour of seabed around a vertical breakwater head. In their model, the pore pressure is not decoupled; instead the seabed is treated as a porous medium according to the $u - p$ approximation of the Biot's equations utilizing the generalized plasticity model of Pastor et al. (1990) via PORO-WSSI II. In their model, the poro-elastoplastic model is capable of capturing both mechanisms of pore pressure development (instantaneous and residual) simultaneously. They found that the poroelastic models underestimate liquefaction depth as opposed to poro-elastoplastic models.

A parametric study using this model shows that the effect of soil parameters as well as cross anisotropy on wave induced pore pressure is more significant in fine sands than it is for coarser sands. Therefore, the finer the seabed material, the more important it is to consider the effect of the cross anisotropy of seabed on pore pressure.

The effect of the degree of saturation of the seabed was also studied via this model. The results show a trend at S=0.95 which is due to a significant phase change occurring at unsaturated seabed, as reported by Okusa (1985) and Hsu and Jeng (1994). The occurrence of phase lag comes from the flow transfer between different media (solid and fluid). The study also included a parametric study of the effect of caisson's geometry and rubble mound on the wave-induced pore pressure in seabed.

Stickle (2010) developed a dynamic structural model (ADÍNDICA, within Matlab) to study cohesive soil seabed underneath a rubble foundation of caisson breakwater. The $u-p$ approximation of the Biot formulation was used. The constitutive model used for the seabed is a combination of both a nonlinear elastic model (hyperelasticity according to Mira et al. (2009)) and a generalized plasticity model (according to Pastor et al. (1990). A hyperelastic constitutive model is used for the rubble foundation.

ADÍNDICA succeeds in producing seaward tilt of caisson subject to regular impulsive wave action. Nevertheless, the generated pore pressure underneath the shoreward edge is less than that generated beneath the seaward edge. This is in contradiction with centrifuge model results by Zhang et al. (2009b). In reviewing figures provided by Stickle (2010), it apparently seems that the model has succeeded in reproducing large-scale experiments in GWK (Kudella et al., 2006). Nonetheless, the compared wave characteristics from experiments and numerical model are different. Another controversial aspect is that the seabed material used in both models has not only different properties but also a different behaviour. Although Kudella et al. (2006) used sandy seabed enclosed by impermeable sheets, which provides an approximation of a sandy seabed covered by a thin clay layer, Stickle (2010) considered clayey seabed. From well known differences between the behaviour of sand and clay, one expects different response. Therefore, no further analysis of the results of this model is herein pursued.

Nazem et al. (2008) and Nazem et al. (2009) presented an ALE (Arbitrary Lagrangian–Eulerian) formulation for solving consolidation problems in geomechanics. They showed the efficiency and robustness of the ALE method by solving some classical problems such as consolidation of footings and cavity expansion. The ALE method can successfully solve rigid footing and indentation problems involving relatively large deformations as well as dynamic loads. Thus, the ALE method may be applied in solving other important geotechnical problems. Nonetheless, no report of ALE being used for wave-structure-foundation problems can be found in the literature.

With a two-dimensional finite element model, Mase et al. (1994) investigated the wave-induced pore pressure and effective stresses in the vicinity of a composite breakwater based on the consolidation equations (Biot, 1941) with Hooke's law for an isotropic elastic seabed. The pore pressure distribution within a rubble foundation is one of the main concerns in their study. The lateral boundary condition used in their model is the analytical solution of Yamamoto et al. (1978), which limits their model to an isotropic and homogeneous seabed. For a more realistic case, such as an anisotropic and non-homogeneous seabed, their model is not applicable. They also considered an analytical approach for caisson-seabed interaction and they applied analytical water pressure based on the small amplitude wave theory to the wave-seabed interface neglecting uplift pressure on the caisson.

Meshless methods for solid dynamics have been applied to some geotechnical applications. These methods include coupled DEM-FEM (e.g. Bierawski et al. (2002)), the Material Point Method (MPM) (Sulsky et al., 1994; Sulsky, 2002; Bardenhagen et al., 2000; Vermeer et al., 2008), the Element-Free Galerkin (EFG) Method (Belytschko et al., 1994) and the Meshless Local Petrov-Galerkin (MLPG) method (Atluri and Zhu, 1998). Vermeer et al. (2008) provide a range of interesting examples for the use of MPM for geotechnics. The MPM does not provide any computational advantage over the FEM as calculations for the particles are added to mesh calculations, although the mesh does not need to be updated. Although meshless methods appear very promising (especially for large deformations), they are quite premature due to unresolved basic issues (e.g. boundary conditions).

c. Semi-coupled CFD-CSD model systems

After conducting large-scale model tests, Kudella and Oumeraci (2008a) attempted to investigate the wave-structure-foundation interaction problem numerically in order to improve the understanding of the problem. The goal of their study was similar to that of the current study, which is the reproduction of the physical experiments by Oumeraci and Kudella (2004) and Kudella et al. (2006). The flow field was simulated by COBRAS, a 2D Volume-Averaged/Reynolds-Averaged Navier Stokes (VARANS) model (Lin and Liu, 1998; Hsu et al., 2002). The flow inside the rubble foundation was considered turbulent (Forchheimer), whereas the flow inside the seabed was neglected (impermeable seabed) due to problem configuration. The computational domain considered for COBRAS was a reduced equivalent to the domain of the physical model, in order to reduce the required computational time. The results obtained by COBRAS simulation were transferred to a structural dynamics model. The results are: Wave horizontal and vertical exerted pressures on the caisson as well as the wave induced pressure at seabed surface (covered by an impermeable sheet).

The COBRAS model was capable to reproduce the water surface relatively well for all wave types. Nevertheless, the water pressure exerted on caisson and seabed was of more significance to the studied problem. Comparing exerted horizontal and vertical loads on caisson from physical models to those reproduced by COBRAS, the results agree very well in case of pulsating waves; however, for breaking wave impacts the agreement was neither satisfactory for horizontal load nor for vertical load. The maximum horizontal load is well simulated, whereas its oscillation, after the peak, is not reproduced at all. This was concluded to be due to the inability of the applied COBRAS version to model the oscillations of entrapped air in the breaking wave during impact. The effect of entrained air on breaking wave impact is further explained in Bullock et al. (2007). For the wave-induced uplift force, the maximum value measured experimentally is much greater than numerically calculated. This might be due to the inability of the model to reliably simulate the Forchheimer flow in the rubble foundation beneath the caisson.

The 2-D FE-model DIANA-SWANDYNE II, introduced by Chan (1988), was used to simulate the response of both the caisson and seabed to wave action by considering soil structure interaction. A generalized plasticity type soil model was applied, for which yield and plastic potential surfaces need not be explicitly defined. The behaviour of sand is formulated with a non-associative model (Pastor et al., 1985; Zienkiewicz et al., 1999). It includes a hardening (softening) law, which considers the effect of pre-shearing and describes plastic deformations also during unloading.

An equivalent reduced computational domain was also used for the structural dynamic analysis in order to further reduce computational expense. Partially saturated sand was realized by adjusting the compressibility of the pore fluid. The frictional behaviour between caisson and rubble foundation was simulated by a “slip layer”, which additionally provides a zero-tension condition. The wave loads obtained by COBRAS were applied as a function of time and space at the seabed in front and underneath the caisson, while the resultant wave forces at the caisson are transferred into “pseudo”-pressures to account for the varying lever arm of the resulting force.

Beside the limitations of COBRAS, the general plasticity soil model requires the specification of complex parameters for which a proper methodology for their determination is still lacking. Therefore, the results matched the experimental results qualitatively rather than quantitatively. Furthermore, the solution was carried out with the approximate $u - p$ formulation, which was shown in section 2.3 to be (mostly) inappropriate for this specific problem.

The structural dynamics model was capable of reproducing pore pressure buildup until a saturation point (S), at which generation and dissipation of pore pressure equate. After this saturation point, pore pressure dissipation then dominates over pore pressure generation. Nevertheless, the saturation point was reached after only 140 seconds numerically compared to the physically measured 340 seconds.

Hur et al. (2007) studied the sand suction mechanism in a reclaimed sand area protected by a seawall by using a coupled VOF-FEM model. The VOF sub-model applies the NSE. However, the FEM model utilises the $u - p$ approximation of the Biot's formulation. The continuity of water particle velocity at the wave–sand interface is established by firstly calculating the fluid velocity and pressure in the wave field and inside both of the rubble mound and the sandy seabed. Then, the calculated velocities and pressures at the sand foundation interface were used as boundary conditions for the FEM sub-model. Thereafter, the FEM sub-model computes the displacements and pressures in the sandy soil simultaneously and consequently stresses and strains in sand are obtained. Nonetheless, there exists no feedback from the FEM sub-model to the VOF part. Many similar coupled VOF-FEM model studies for wave-seabed-structure interaction are published in Japanese and hence are not reviewed here.

Liu and García (2006) developed a semi-coupled CSD-CFD model based entirely on the finite volume method using the OpenFOAM framework. The CFD part is an Eulerian VOF-RANS model with a $(k - \epsilon)$ RANS turbulence model. The CSD part is an implementation of Biot's quasi-static poroelastic model (Biot, 1941) for an FVM discretisation. The coupled model system is in 3D. Nevertheless, the studied structure is so small to reduce reflection effects. The wave generation is carried out by providing a velocity profile at one boundary and imposing the wave surface (VOF value) and a beach is provided on the other side of the model to absorb waves. The wave maker does not provide any wave absorption. The model is verified by an analytical problem from Jeng and Hsu (1996).

The model gives good results as compared to analytical poroelastic solution. Nevertheless, the model is only applicable to transient liquefaction as only an isotropic elasticity soil constitutive model is implemented. The authors state that implementation of more sophisticated soil models should provide good results for predicting residual pore pressure/liquefaction.

Zhang et al. (2011) and Jeng et al. (2013) implemented the COBRAS model (Lin and Liu, 1998; Hsu et al., 2002) into the 2D PORO-WSSI II model (Jeng et al. (2013) and Jianhong (2012)). The new integrated model solves the VARANS equations, simultaneously, for the water free flow (wave domain) and porous flow throw a submerged porous breakwater separately then water pressure on the seabed surface and shear stresses are considered as an input for the seabed model, which is governed by the Biot (1941) poroelastic equations, the PORO-WSSI model (Jeng, 2010). The integrated model is, correspondingly, basically a one-way interaction model. The seabed sub-model is a fully implicit time finite difference model. Under-relaxation technique is used in iterative procedure to obtain convergence. The model can be thought to pursue the same approach as Kudella and Oumeraci (2008a). The computations, overall, agree rather well with experimental results (Mizutani et al., 1998); nevertheless, results from Hur et al. (2008) compare better against the experimental results for both wave profile and pore pressure inside the seabed. No validation was carried out for the poroelastic seabed model; however, a parametric study was directly carried out. The results of this model are of little interest as the studied problem was a submerged permeable breakwater.

Ye et al. (2013) extended the PORO-WSSI 2D model (also be referred as FSSI-CAS 2D) for one-way coupling between CFD and CSD. The hydro-geotechnical model solves the $u - p$ approximation of Biot's equations with the PZIII generalized plasticity model (Pastor et al., 1990). The model was validated using benchmark poroelastic problems and results from small scale models. Ye et al. (2014), Jianhong et al. (2014) and Ye et al. (2015) present applications of this model to composite breakwaters. However, the lack of proper (or any) modelling of soil-structure interaction in this model casts a great doubt on its applicability for such a problem. Additionally, although referred to it as an integrated model system in various publications, the coupling only takes place in one direction (CFD to CSD), without any feedback whatsoever. This means that linking both models on the time-step level results in redundancy in CFD calculations for different structural configurations. Therefore, according to the classification system adopted in this subsection, this model system is considered semi-coupled.

Bierawski and Maeno (2004) developed a coupled VOF-FEM numerical model for the analysis of submerged breakwaters on permeable bottoms. The VOF submodel was employed to model the wave field and porous flow through the rubble mound applying NSE. The FEM model is used to model the sandy seabed as a poroelastic material with a single fluid phase (water-air mixture). At the interface pressure fluctuations are fed from the VOF submodel to the FEM sub-model. The vertical velocity generated in the FEM submodel is fed back in the VOF sub-model. The model system was compared to results from small scale experiments. Nevertheless, only small part of information is fed back to the structural model which weakens the two models coupling appreciably.

d. Integrated CFD-CSD models

Mostafa et al. (1999) studied the nonlinear dynamic interaction among (nonlinear and non-breaking) water waves, composite breakwater and a sandy seabed of finite thickness, experimentally and numerically. In wave tank experiments, the water surface levels around the breakwater and the dynamic pore pressure inside its rubble base and seabed foundation were measured. Numerically, a coupled 2D BEM-FEM model system was used. A BEM model was used to model the free surface flow problem, while an FEM model was used to model porous flow. A poroelastic (Biot, 1941) FEM model, with identical mesh as for the porous flow model, was used to model the poroelastic behaviour of the rubble foundation and the seabed.

The free surface flow BEM model was based on the assumptions that the water is incompressible and that the flow is irrotational and inviscid. Green's theorem was used to integrate the governing Poisson's equation. The weighted residual method has been applied in order to integrate the dynamic boundary condition on the free surface using a weight function.

The FEM model used for the porous flow considered the pore-water to be viscous and incompressible and the flow may be rotational. The considered governing equations were of a modified Navier-Stokes type to account for resistance coefficients that represent the porous flow, proposed by Mccorquodale et al. (1978). The drag and added mass coefficients were estimated using experimental records for the wave forces acting on armour units in a submerged breakwater (Mizutani et al., 1998).

Along the interface between the rubble base and the seabed foundation, the continuity of pore-water pressure and normal velocity component is considered. The BEM-FEM iterates for the nonlinear water surface and computes the flow inside the rubble mound base and seabed foundation simultaneously at each time step in a time-marching scheme. The poroelastic FEM model for the soil followed the Biot's quasi-static approach (Biot, 1941); however, the pore fluid was considered compressible due to existence of air via a reduced water-air mixture bulk modulus (Verruijt, 1969).

The model was found to be a powerful tool for simulating non-breaking waves, the induced pressure on the caisson and the transmitted waves behind the caisson. The poroelastic FEM model could "fairly well" calculate pore pressure inside porous media, when the surface boundary pressure is computed by the BEM-FEM flow model. The study concluded that considering the rubble foundation and seabed as permeable changes the properties of the modelled water surface as well as the pressures induced on the breakwater. It was found that the solid particle displacement under the bottom slab of a caisson may be mostly vertical at its offshore side and mostly horizontal at its harbour side. Moreover, the dynamic shear stresses along the bottom slab of a caisson have been found to have a parabolic distribution with a peak at the midsection of the base. High dynamic vertical and shear stresses have been found to occur under the ends of the rubble foundation threatening its stability. Also, the seabed in front of the rubble base has been found to be vulnerable to liquefaction.

Implication 12 (Numerical Wave-Structure-Foundation Interaction Models) *The available numerical models for wave-structure-foundation interaction can be classified in five main groups in terms of coupling approach:*

(1) Flow models with non-deformable porous media (CFD): In these models, no structural behaviour is accounted for. Neither motions of the structure nor deformations of the foundation are considered. These models are essentially CFD models with the option of modelling both free surface flow and porous flow. These models include Hsu et al. (2002); Hur et al. (2010).

(2) Structural models (CSD): These numerical models consider only the structural dynamics. The fluid effect is accounted for analytically (e.g. Lu and Jeng (2007)) or empirically (e.g. Ülker et al. (2010)).

(3) Semi coupled CFD-CSD codes: Wave loads on the structure and their direct effect on pore pressures are described by a CFD model (similar to the first group). The results are then fed into a CSD code for structural analysis (similar to the second group). However, the link between both models is one-way direction, e.g. the geometry in the CFD model is not altered due to CSD model computations (e.g. Kudella and Oumeraci (2008a); Zhang et al. (2011)).

(4) Fully integrated coupling: This represents an advanced approach, but also a very expensive one. The CFD and the CSD models are solved simultaneously and the geometry as well as relevant parameters are updated from the CSD model into the CFD model. An interface, with proper matching conditions, between both fluid and solid domains is important to satisfy mass conservation of fluid inside and outside the soil. Applications of this approach are scarce in the literature. For vertical breakwaters, only one study was found (Mostafa et al., 1999) that can barely be considered to have provided a fully integrated coupled model system. However, this model system is based on considerable assumptions and simplifications which seriously limit its applicability.

(5) Monolithically coupled models: In these types of models, the coupling between the fluid and solid domains is established at the governing equations level. No application of such models in coastal engineering can be found in the literature.

2.5.4 Simplified models

A simple mathematical model for soil compaction and liquefaction (C/L model) was first developed by Sawicki (1987). This model considers a densification relation (like densification constitutive models of soils), for which material parameters should be obtained experimentally. The densification equation relates the densification increment ($d\Phi$), which is a function of irreversible volumetric strain and initial soil porosity, to the increment of the number of load cycles (dN), considering the number of cycles (N) as a continuous variable. Another relation is considered between the increment of pore water pressure and both densification increment and increment of number of load cycles (dN) for undrained conditions. From general relations of continuum mechanics and considered a constitutive relation between cyclic shear stress and strain amplitudes, which includes a shear modulus as a function of soil properties and mean effective stress, differential equilibrium equations are derived and solved for defined boundary conditions of the problem. Diffusion equations according to Verruijt (1969) are used for partially undrained conditions, which are solved simultaneously with equilibrium equations. The model was applied to the response of sandy soils to cyclic loads, to pore pressure generation and dissipation as well as re-solidification of saturated subsoil (Sawicki and Świdziński, 1989). Assessment of seismic-induced liquefaction was studied by Sawicki and Świdziński (2007) using the C/L model within the EU-LIMAS project to examine the capability of the model to numerically reproduce the effects of the 1999 Kocaeli earthquake. The model was calibrated using parameters retrieved from laboratory tests of soil samples from site. In their paper, they conclude that the method provides a realistic picture of soil liquefaction development and recommend it for practical applications due to its simplicity.

Based on their large-scale experiments (Oumeraci and Kudella, 2004), Kudella and Oumeraci (2008a) developed a simple and very approximate formula for the generation of pore pressure in sandy seabed underneath a caisson breakwater for the special case of a thin overlying impermeable layer (e.g. clay) as an analogy to their experimental setup. The decay of residual pore pressure in the experiments after the wave loading was found to fit an exponential function of the time duration normalised by a characteristic drainage period of soil (T_{Drain}). By considering the residual pore pressure as a superposition of generated and dissipated pore pressures, the residual pore pressure can be estimated from a simple formula. They found that the determination of the residual pore pressure approaches the undrained case only for storms with relatively low residual pore pressure generation and subsequent low compaction of the seabed. Significant compaction during the storm will simultaneously decrease the generation rate which will not occur in undrained situations. For these cases, the determination of generated pore pressure will underestimate the pore pressure development which will occur under undrained situations.

Kudella and Oumeraci (2008a) also found that the development of residual pore pressure is significantly influenced by the compaction density of the soil. Moreover, for regular impact wave loads and long drainage lengths the residual pore pressure may reach the condition for total liquefaction. However, irregular wave loads will not lead to such high residual pore pressures, not even for very long drainage lengths.

Noorzad et al. (2009) followed Rollins and Seed (1990) approach for correcting free-field seismic liquefaction potential to account for effects of the presence of a structure. They modified two methods for the evaluation of wave-induced liquefaction potential of sand deposits in free-field conditions (Rahman and Jaber, 1986; Chang et al., 2004) to account for the effects of a structure (both for vertical walls and rubble-foundation).

They found that wave-induced liquefaction analyses in a free field using either the Rahman and Jaber or the Chang methods yield relatively similar results. Moreover, the wave-induced liquefaction potential in a free field decreases with the increase in water depth and relative density of the sand deposit. According to their model, the presence of marine structures of both kinds – energy reflecting and energy dissipating – over sand deposits with different relative densities affects the safety factor against liquefaction of these soil deposits. For both types of structures, a structural presence over loose sand increases the liquefaction potential and decreases it in dense sand. The difference between energy “reflecting” structures such as caissons and energy “dissipating” structures such as rubble mound breakwaters is particularly important for waves propagating in transitional water depths and in deep water. In these cases the energy reflecting structure has a more pronounced effect on increasing the liquefaction potential of the underlying seabed sand deposit. Finally, the effect of a structural presence on the liquefaction potential of underlying loose or dense sand deposits is greater in regions where the shear stress from the structure is higher.

In order to provide a tool for the dynamic analysis of wave-caisson-foundation system, as opposed to prevailing quasi-static approaches, several discrete models were adopted (e.g. Goda (1994); Oumeraci and Kortenhaus (1994); Wang (2001); Wang et al. (2005). In their model, Oumeraci and Kortenhaus (1994) used results from large-scale experiments for calibration and validation (Oumeraci et al., 1992). The model by Oumeraci and Kortenhaus (1994) shows a relatively good agreement with experimental results. Nevertheless, the model suffers uncertainties regarding the damping coefficients. A tool for calculating equivalent static load, in special cases, is also presented. The study stresses the significance of experimental studies (especially large-scale) to reduce uncertainties in numerical modelling associated with both dynamic load history and components of the structural model itself. Several models of breaking wave load-time histories based on large-scale model tests are also discussed.

In another mass-spring-dashpot model, Wang et al. (2005) studied the effect of different breaking wave load histories, as defined by Oumeraci and Kortenhaus (1994), on the caisson response and found the sliding amplitude and displacements to differ for different wave load histories even if the wave loads have the same amplitude. Nonetheless, the overturning moment amplitudes are equal for equal load amplitudes. They also found that adding the uplift motion to the model does not add appreciably to the calculated overturning (rotational) response.

Zhang et al. (2009a) present a simplified analysis that employs a 2-DOF lumped mass-spring model

(Richart et al., 1970) for an elastic caisson response, which is similar to the model by Oumeraci and Kortenhaus (1994), but with the damping neglected. In addition, they accounted for permanent (plastic) caisson tilt by applying a slip circle solution. The slip circle is considered to pass through the shoreward edge (heel) of the caisson. By using a search algorithm, the critical slip surface, which offers the lowest resistance to rotational motion, as well as the limiting moment for incipient plastic tilting, are determined (radius and centre). An equation of motion for the dynamic plastic tilting of the caisson is established, based on the overturning and resisting moments as well as on the rotational inertia of the system. Time-step integration of this equation of motion allows permanent caisson tilt to be computed. In their analysis, plane-strain conditions are assumed to prevail and both elastic and plastic solutions are superposed to give the final tilt of the caisson. The results of this analysis were checked against the results of centrifuge model tests, showing a reasonably good agreement. A partial comparison was also made with field observations, for which the sliding displacement is calculated by Ling et al. (1999) and added to the calculated horizontal displacement. Nevertheless, their model does not provide a unified approach for response of caisson breakwaters. For example the effect of calculated permanent displacements is not accounted for further load cycles. Additionally, soil-structure separation and reattachment as well as soil densification caused by loading are not considered. Their model tends to be more suitable for permanent response from extreme events rather than the step-wise mechanism associated with relatively moderate wave action.

Cuomo et al. (2011) developed a 3-DOF mass-spring-dashpot model for caisson breakwaters. In their model, the caisson is supported by vertical and horizontal springs at the bottom of the caisson. The vertical springs are elastic but allow for soil-structure separation and reattachment. Only vertical dashpots are considered in their study. The stiffness of the horizontal springs is calculated based on horizontal displacement of the caisson. The model of Cuomo et al. (2011) cannot predict residual displacement (e.g. tilt) of the caisson breakwater.

Implication 13 (Simplified Wave-Structure-Foundation Interaction Models) *1. Some simplified numerical models for the dynamic response of the soil foundation of caisson breakwaters are available (e.g. Zhang et al. (2009a) and Sawicki and Świdziński (2007)). Nevertheless, none of them is satisfactory enough to be adopted as a standard for practical engineering purposes.*

2. Modified lump mass-spring-dashpot models alone or in conjunction with other methods for permanent displacement calculation seem promising for providing a practical tool for engineering use. However, further developments of such models is needed.

2.6 Specification of Objectives and Methodology

Based on the results of the previous sections, the objectives and the methodology of the PhD research study are specified more precisely.

2.6.1 Objectives and Requirements of Prospective Models

This PhD study primarily aims at developing a numerical model that can successfully reproduce the physical experiments carried out in the Large Wave Flume (GWK) in Hannover (Oumeraci and Kudella, 2004). The model should be able to simulate accurately the processes involved in the wave-structure-foundation interaction. More specifically, the stepwise failure (residual displacement) underneath caisson breakwaters, together with the associated generation and dissipation of residual pore pressure, is to be properly reproduced (Fig. 1.1). Hence, the observed correlation between residual pore pressure and residual soil deformation will be analysed. This will assist in the interpretation of the measured data as well as in building a better understanding of the phenomenon. Consequently, a parameter study will be performed using the new validated CFD-CSD model system in order to possibly develop a simplified model for the reliable prediction of residual displacements (stepwise failure) of monolithic breakwaters subject to wave attack. Finally, recommendations for the design of monolithic breakwaters and for future developments of the numerical CFD-CSD model system as well as the simplified model will be provided.

Based on the outcomes of the previous sections and their implications, the overall structure of the prospective numerical model system is illustrated by Fig. 2.13. More specifically, the prospective models as well as their coupling should fulfil the following requirements:

- The overall numerical model system should be developed within a reliable and open (transparent) numerical framework. OpenFOAM is determined as the most appropriate framework for this purpose.

- The CFD model for the free surface and porous flow should be developed based on the multiphase (*porousInterFoam*) CFD solver from OpenFOAM. It is essential to enhance to the capabilities of the code to reproduce the effect of entrapped air on breaking wave impact loads. Further, the porous flow should be extended to account for volume-averaging principles with different relevant seepage models. A systematic validation of the new developments is necessary.

- The CSD model should properly describe the fully dynamic behaviour of non-cohesive soils as fully coupled porous media with justified simplifications if needed, but without considerable accuracy loss. The highly dynamic soil-structure interaction of the study problem dictates the implementation of a frictional contact model to simulate sliding, separation and reattachment of the gravity structure from the underlying foundation. Also, the applied soil constitutive model should be elasto-plastic with the capability to reproduce soil behaviour with the ability to model cyclic mobility and possible sudden loss of strength due to soil liquefaction. Finally, all implemented modules should work together to reproduce properly the behaviour of non-cohesive soils underneath monolithic breakwaters subject to breaking waves.

- To focus on hydrodynamic and hydro-geotechnical processes separately and due to the constraints imposed by the time-frame of the PhD study, a one-way coupling of the CSD-CFD models will be sufficient, by which the CSD model uses the output of the CFD model as its input for wave dynamics. The new numerical CFD-CSD model system should be validated against large-scale experiments (called hereafter GWK tests). The overall structure of the numerical model system is illustrated in Fig. 2.12

- The validated CFD-CSD model should be used for a parameter study, together with the results from the GWK tests, to enhance the understanding of the response of foundations of monolithic breakwaters to wave attack. This includes an interpretation of stepwise failures and the relative importance of transient and residual excess pore pressure for the development of residual soil deformations (Fig. 2.12)

- Based on the results of the parameter study, a simplified model (with a related toolbox) that can account for residual settlement and tilt of monolithic breakwaters subject to wave attack should be developed, calibrated and validated in OpenFOAM. The simplified model can be used for preliminary analysis and engineering applications (Fig. 2.12)

2.6.2 Methodology

As indicated in Fig. 2.13, the methodology adopted for this PhD study includes five main stages:

(i) Review and analysis of the current knowledge and models related to the processes relevant to the wave loading and response of monolithic breakwaters and their soil foundations in order to specify more precisely the objectives and methodology of the PhD study (this chapter)

(ii) Development and validation of the semi coupled CFD-CSD model system; including separate and systematic validation of the hydrodynamic, the hydro-geotechnical and the coupled model system (chapters 3, 4 and 5 for CFD, CSD and coupled CFD-CSD model, respectively)

(iii) Analysis of monolithic breakwaters subject to wave attack, including stepwise failure mechanisms and the role of transient and residual pore pressure on residual displacements of monolithic breakwaters (chapter 5)

(iv) Development, calibration and validation of a simplified model for residual displacements of monolithic breakwaters (with the related toolbox) in OpenFOAM based on a 3-DOF mass-spring-dashpot model with elastoplastic springs (chapter 6)

(v) Discussion of the implications of the new models and the gained new knowledge for the design of monolithic breakwaters as well as outlook and recommendations for further research (chapter 7)

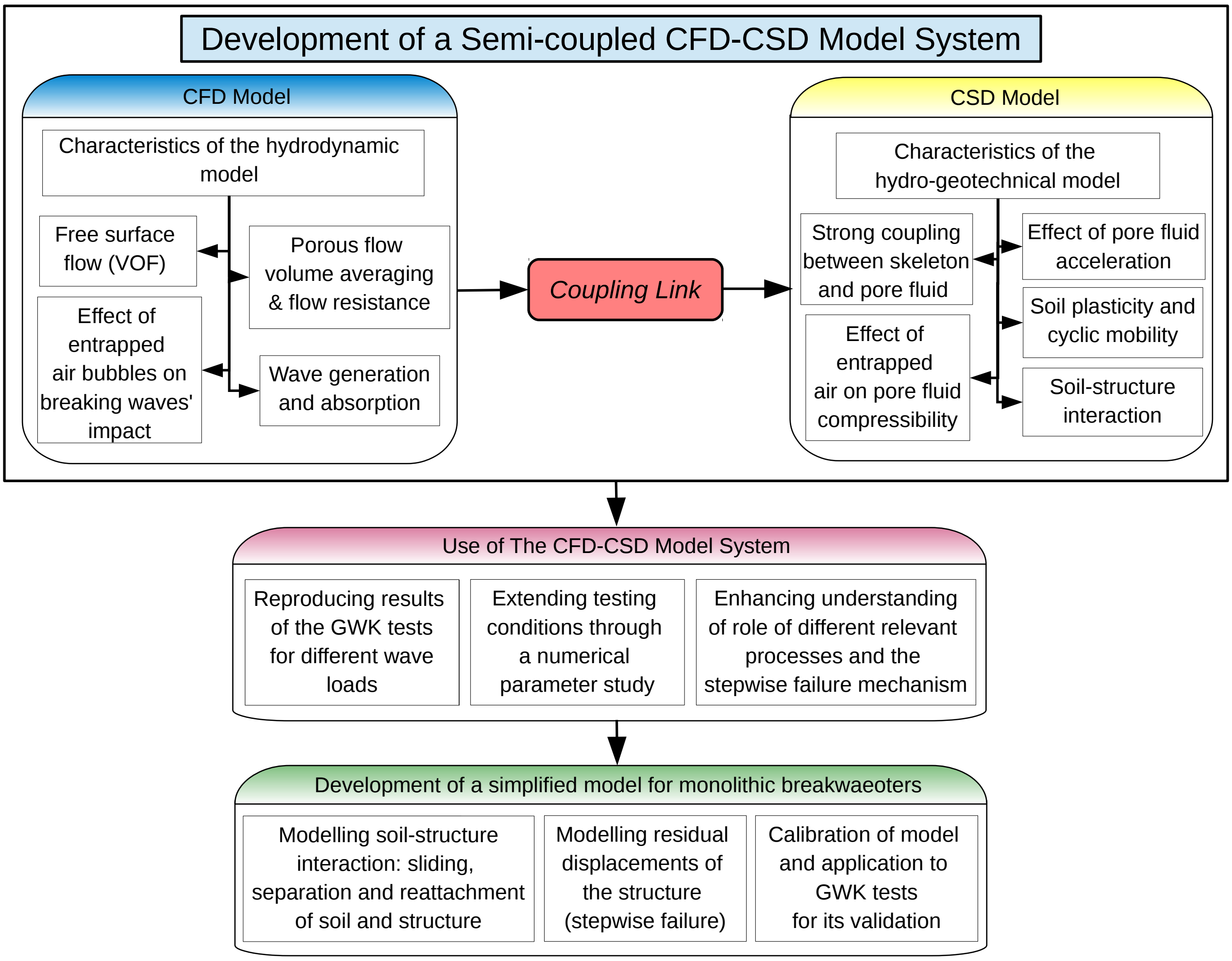

Figure 2.12: Overall structure of the PhD study: (i) Development of the numerical model system, (ii) validation of the model system using the GWK tests and extension of the testing conditions through a parameter study and enhancement of understanding of stepwise failure and (iii) development of a simplified model for monolithic breakwaters

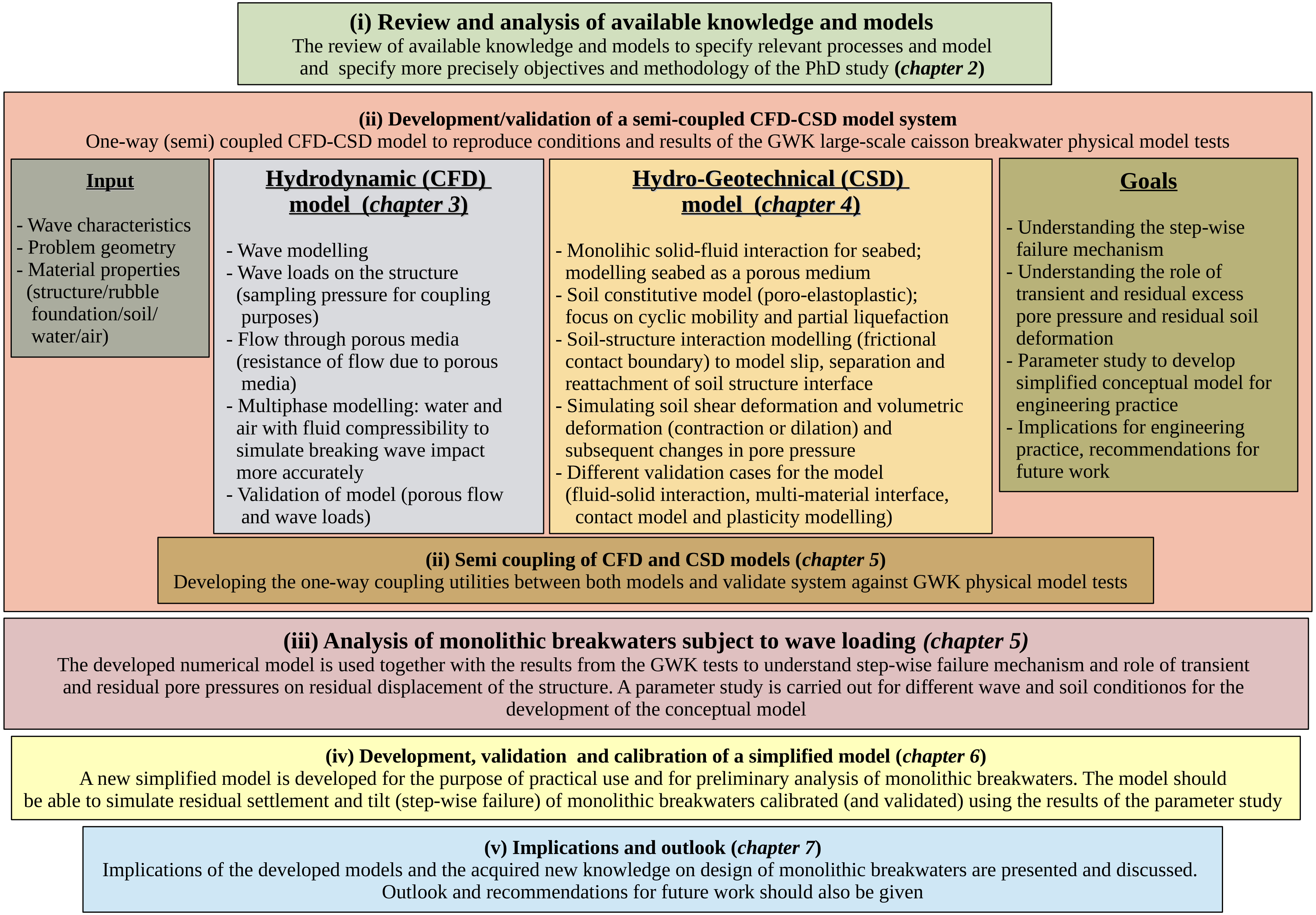

(i) Review and analysis of available knowledge and models

The review of available knowledge and models to specify relevant processes and model and specify more precisely objectives and methodology of the PhD study (***chapter 2***)

(ii) Development/validation of a semi-coupled CFD-CSD model system

One-way (semi) coupled CFD-CSD model to reproduce conditions and results of the GWK large-scale caisson breakwater physical model tests

Input

- Wave characteristics
- Problem geometry
- Material properties (structure/rubble foundation/soil/ water/air)

Hydrodynamic (CFD) model (*chapter 3*)

- Wave modelling
- Wave loads on the structure (sampling pressure for coupling purposes)
- Flow through porous media (resistance of flow due to porous media)
- Multiphase modelling: water and air with fluid compressibility to simulate breaking wave impact more accurately
- Validation of model (porous flow and wave loads)

Hydro-Geotechnical (CSD) model (*chapter 4*)

- Monolihic solid-fluid interaction for seabed; modelling seabed as a porous medium
- Soil constitutive model (poro-elastoplastic); focus on cyclic mobility and partial liquefaction
- Soil-structure interaction modelling (frictional contact boundary) to model slip, separation and reattachment of soil structure interface
- Simulating soil shear deformation and volumetric deformation (contraction or dilation) and subsequent changes in pore pressure
- Different validation cases for the model (fluid-solid interaction, multi-material interface, contact model and plasticity modelling)

Goals

- Understanding the step-wise failure mechanism
- Understanding the role of transient and residual excess pore pressure and residual soil deformation
- Parameter study to develop simplified conceptual model for engineering practice
- Implications for engineering practice, recommendations for future work

(ii) Semi coupling of CFD and CSD models (*chapter 5*)

Developing the one-way coupling utilities between both models and validate system against GWK physical model tests

(iii) Analysis of monolithic breakwaters subject to wave loading *(chapter 5)*

The developed numerical model is used together with the results from the GWK tests to understand step-wise failure mechanism and role of transient and residual pore pressures on residual displacement of the structure. A parameter study is carried out for different wave and soil conditionos for the development of the conceptual model

(iv) Development, validation and calibration of a simplified model (*chapter 6*)

A new simplified model is developed for the purpose of practical use and for preliminary analysis of monolithic breakwaters. The model should be able to simulate residual settlement and tilt (step-wise failure) of monolithic breakwaters calibrated (and validated) using the results of the parameter study

(v) Implications and outlook (*chapter 7*)

Implications of the developed models and the acquired new knowledge on design of monolithic breakwaters are presented and discussed. Outlook and recommendations for future work should also be given

Figure 2.13: Methodology of the PhD study

3 Hydrodynamic (CFD) Model

In this chapter, a numerical wave flume is developed for the problem of wave-structure-foundation interaction, as part of the semi-coupled CFD-CSD model system described in Chapter 5. First, the model development, as an extension to an existing CFD solver, is presented. The development include different seepage laws for flow through porous media as well as a simplified fluid compressibility model to enhance breaking wave impact without significant increase in computational time. Second, the validation of the developed model is presented for dam break flow through a porous obstacle and for large-scale caisson breakwater experiments (GWK tests). Finally, concluding remarks on the CFD model are given.

3.1 CFD Model Development

The model is developed using OpenFOAM® (Open Field And Operation Manipulation), a free and open source toolbox.

3.1.1 Governing Equations

The developed hydrodynamic solver (*waveVolAvgPorousInterFoam*) is based on the *interFoam* family of solvers of the multiphase incompressible Navier-Stokes equations in the OpenFOAM framework. The solver treats the air-water mixture as a single Eulerian fluid. The Volume-Of-Fluid (VOF) method is used for air-water interface capturing. The properties of the fluid are interpolated at each cell center according to the phase fraction (VOF function) value. The mixture continuity equation is:

$$\nabla \cdot \mathbf{U} = 0 \tag{3.1}$$

and the mixture momentum balance equation is:

$$\rho_f \left(\frac{\partial \mathbf{U}}{\partial t} + \mathbf{U} \cdot \nabla \mathbf{U} \right) = -\nabla p + \nabla \cdot (\boldsymbol{\tau} + \mathbf{R}) + \rho_f \mathbf{b} + \sigma_T \kappa_\gamma \nabla \gamma \tag{3.2}$$

Where ∇ is the *del* (Nabla) operator $\nabla = \hat{\mathbf{x}} \frac{\partial}{\partial x} + \hat{\mathbf{y}} \frac{\partial}{\partial y} + \hat{\mathbf{z}} \frac{\partial}{\partial z}$ where $\hat{\mathbf{x}}, \hat{\mathbf{y}}, \hat{\mathbf{z}}$ are the unit vectors in their respective directions. $\mathbf{U}$ is the fluid mixture velocity vector, p is the fluid mixture pressure, $\rho_f = \rho_{water}\gamma + (1-\gamma)\rho_{air}$ is the mixture density; where γ is the phase fraction (varies between unity for only water and zero for only air). $\mu = \gamma\mu_{water} + (1-\gamma)\mu_{air}$ is the mixture dynamic viscosity, $\boldsymbol{\tau} = \mu((\nabla\mathbf{U} + (\nabla\mathbf{U})^T) - \frac{2}{3}(\nabla \cdot \mathbf{U})\mathbf{I})$ is the deviatoric viscous stress tensor, $\mathbf{R} = \mu_t((\nabla\mathbf{U} + (\nabla\mathbf{U})^T) - \frac{2}{3}(\nabla \cdot \mathbf{U})\mathbf{I})$ is the additional stress tensor induced by the unresolved turbulence fluctuation (absent for laminar flow), μ_t is the eddy dynamic viscosity, $\mathbf{I}$ is the identity tensor and $\mathbf{b}$ is the body acceleration vector (mostly gravity). The last term on the right hand side represent surface tension force; where σ_T is the surface tension coefficient, $\kappa_\gamma = -\nabla \cdot \left(\frac{\nabla\gamma}{|\nabla\gamma|} \right)$ is the mean curvature (divergence of the unit normal vector to the air-water interface). The gradient of the phase fraction ($\nabla\gamma$) equals zero away from the water-air interface.

3.1.2 Water Surface Capturing

The phase fraction obeys a transport (advection) equation of the form:

$$\frac{\partial \gamma}{\partial t} + \nabla \cdot (\gamma \mathbf{U}) + \underline{\nabla \cdot (\gamma (1-\gamma) \mathbf{U}_r)} = 0 \tag{3.3}$$

The underlined term in Eq. 3.3 is an additional term in OpenFOAM (Weller (2008), as cited in Berberovic 2010) to compress the interface and hence make it sharper (i.e. reduce interface smearing). This term can be driven (from original VOF method) by defining the phase fraction advection equation for an individual phase (i.e. water) then substituting the water velocity with a phase weighted average velocity using the phase fraction:

$$\frac{\partial\gamma}{\partial t} + \nabla \cdot (\gamma \mathbf{U}_{water}) = 0 \tag{3.4}$$

and considering mixture velocity:

$$\mathbf{U} = \gamma \mathbf{U}_{water} + (1-\gamma)\,\mathbf{U}_{air} \tag{3.5}$$

The compression term in the phase fraction transport equation (Eq. 3.3) is equal to zero in cells with one phase present (i.e. $\gamma = 0$ or 1). $\mathbf{U}_r$ is the relative velocity vector $\mathbf{U}_r = \mathbf{U}_{water} - \mathbf{U}_{air}$ modelled as the compression velocity (compression in this context means shrinking the interface) that can be obtained as:

$$\mathbf{U}_c = \min\left[C_\gamma |\mathbf{U}|, \max\left(|\mathbf{U}|\right)\right] \frac{\nabla\gamma}{|\nabla\gamma|} \tag{3.6}$$

where the compression velocity is based on the maximum velocity in the interface region. $\mathbf{U}_c$ is limited using the largest value of the velocity in the domain as the worst possible case (Weller (2008), as cited in Berberovic 2010). The intensity of the interface compression is controlled by the constant C_γ, which yields no contribution if set to zero, a conservative compression if the value is one and an enhanced compression for values greater than one (OpenCFD Ltd., 2012). In order to ensure boundedness of the phase fraction, independence of the numerical discretisation schemes, the solution procedure utilizes the Multidimensional Universal Limiter for Explicit Solutions (MULES solver) of OpenCFD Ltd. (2012).

3.1.3 Turbulence Modelling

OpenFOAM treats turbulence in a generic manner. Incompressible CFD solvers in OpenFOAM have the ability to carry out direct numerical simulations, Reynolds averaged Navier-Stokes (RANS) equations or large eddy simulation (LES) for turbulence modelling. It is also possible to consider a detached eddy simulation (DES) where LES is considered away from walls while a RANS approach is considered near the walls (turbulent length scale is less than the maximum grid dimension). In this study, the RANS approach was initially considered for its faster performance as compared to other turbulence models, while providing results of acceptable accuracy. Nevertheless, it was found that LES has a better performance than the Reynolds-averaged model in terms of wave transformation especially for large domains where water waves have to travel over long distances. Additionally, LES gives better results for maximum breaking wave impact on walls (as shown later by the results in Subsection 3.2.2).

3.1.4 Reynolds-averaged turbulence modelling

For the current simulations, the $k-\omega-SST$ (Shear Stress Transport model) turbulence model was used in a RANS framework, where k is the turbulence kinetic energy, ϵ is the energy dissipation rate caused by the viscous effects and ω is the specific dissipation rate $\omega = \frac{\epsilon}{C_d k}$ with C_d being an empirical coefficient ($C_d = 0.09$). The $k-\omega-SST$ model has the advantages of using both the $k-\epsilon$ and the $k-\omega$ models. The $k-\omega$ model is considered in the boundary layer, while the $k-\epsilon$ model is applied elsewhere. A smooth switch between both models is ensured via a blending function F_1 that ranges from unity near solid surface and zero otherwise. This approach reaps advantages of both turbulence models. For the transition, the $k-\epsilon$ model is reformulated in terms of ω using the aforementioned $\omega-\epsilon$ relation, the total time derivative of ω becomes:

$$\begin{aligned}\frac{d\left(\mathbf{U}\omega\right)}{dt} &= \frac{d}{dt}\left(\mathbf{U}\frac{\epsilon}{C_d k}\right)\\ &= \frac{1}{C_d k}\frac{d\left(\mathbf{U}\epsilon\right)}{dt} - \frac{\epsilon}{C_d k^2}\frac{d\left(\mathbf{U}k\right)}{dt}\\ &= \frac{1}{C_d k}\frac{d\left(\mathbf{U}\epsilon\right)}{dt} - \frac{\omega}{k}\frac{d\left(\mathbf{U}k\right)}{dt}\end{aligned} \tag{3.7}$$

The k and ω are calculated by:

$$\frac{\partial\left(\rho_f k\right)}{\partial t} + \nabla\cdot\left(\rho_f \mathbf{U}k\right) = \tilde{P}_k - \beta^*\rho_f k\omega + \nabla\cdot\left[\left(\mu+\sigma_k\mu_t\right)\nabla k\right] \tag{3.8}$$

$$\begin{aligned}\frac{\partial\left(\rho_f \omega\right)}{\partial t} + \nabla\cdot\left(\rho_f \mathbf{U}\omega\right) = \alpha\rho_f S_s^2 - \beta\rho_f\omega^2 + \nabla\cdot\left[\left(\mu+\sigma_\omega\mu_t\right)\nabla\omega\right]\\ + 2\left(1-F_1\right)\rho_f\sigma_{\omega 2}\frac{1}{\omega}\nabla k\cdot\nabla\omega\end{aligned} \tag{3.9}$$

The blending function F_1 is defined as:

$$F_1 = \tanh\left[\left(\min\left[\max\left(\frac{\sqrt{k}}{\beta^*\omega L_w}, \frac{500\nu}{L_w^2\omega}\right), \frac{4\rho_f\sigma_{\omega 2}k}{CD_{k\omega}L_w^2}\right]\right)^4\right] \tag{3.10}$$

$$CD_{k\omega} = \max\left[2\rho_f\sigma_{\omega 2}\frac{1}{\omega}\nabla k\cdot\nabla\omega, 10^{-10}\right] \tag{3.11}$$

Where L_w is the distance to the nearest wall. Finally, the eddy viscosity is calculated as:

$$\nu_t = \frac{k}{\tilde{\omega}} \tag{3.12}$$

For:

$$\tilde{\omega} = \max\left[\omega, \frac{S_s F_2}{a_1}\right] \tag{3.13}$$

Where F_2 is a second blending function defined as:

$$F_2 = \tanh\left(\left[\max\left(\frac{2\sqrt{k}}{\beta^*\omega L_w}, \frac{500\nu}{L_w^2\omega}\right)\right]^2\right) \tag{3.14}$$

A production limiter is used in the SST model to prevent the buildup of turbulence in stagnation regions:

$$\tilde{P}_k = \min\left(P_k, c_1\beta^*\rho_f k\omega\right) \tag{3.15}$$

Where:

$$P_k = \mu_t S_s^2 \tag{3.16}$$

And S_s is the magnitude of the strain rate tensor $\dot{\varepsilon}$, defined as:

$$S_s = \sqrt{2\dot{\varepsilon}:\dot{\varepsilon}} \tag{3.17}$$

The strain rate tensor is defined as:

$$\dot{\varepsilon} = 1/2\left(\nabla \mathbf{U} + (\nabla \mathbf{U})^T\right) \tag{3.18}$$

The model constants (i.e. α, β, σ_k and σ_ω) are calculated using the first blending function F_1 as:

$$\phi = F_1\phi_1 + (1 - F_1)\,\phi_2 \tag{3.19}$$

where ϕ is any model constant (e.g. α); Eq. 3.19 is applied for each model constant.
The model constants are:

$$\begin{gathered}\alpha_1 = 5/9, \alpha_2 = 0.44, \beta_1 = 3/40, \beta_2 = 0.0828, \beta^* = 0.09, a_1 = 0.31,\\ \sigma_{k1} = 0.85, \sigma_{k2} = 1.0, \sigma_{\omega 1} = 0.5, \sigma_{\omega 1} = 0.856, c_1 = 10\end{gathered} \tag{3.20}$$

3.1.5 Large eddy simulation

In the Reynolds averaging (RANS) approach the turbulences at all scales are modelled by the turbulence model and only mean flow is resolved by the CFD simulation. On the other hand, the LES technique is based on the notion that large eddies are geometry dependent and not numerically expensive, and should therefore be simulated directly by the Navier-Stokes equations. However, small scale turbulences (scales smaller than Δ (Sub-Grid Scale (SGS)) are universal (independent of geometry) and expensive to resolve by simulation and therefore should be modelled by the turbulence model. A filtering operation is applied to extract large scale components. Further, small scales are modelled using the same concept of eddy viscosity (similar to Reynolds-averaged models). The mean filter size Δ is related to the mesh size, hence when the mesh becomes too dense (Δ approaches zero) the modelled turbulences approach zero and the solution returns to a direct numerical simulation (DNS) of the Navier-Stokes equation. In this study, a one-equation eddy-viscosity Sub-Grid Scale (SGS) model is used. In which the SGS eddy viscosity is calculated as:

$$\nu_t = \nu_{SGS} = C_k \Delta \sqrt{k} \tag{3.21}$$

Where $C_k = 0.094$ and k is the turbulence kinetic energy (same as defined in Reynolds-averaged models). The k field is calculated by a transport equation:

$$\frac{\partial\left(\rho_f k\right)}{\partial t} + \nabla \cdot \left(\rho_f \mathbf{U} k\right) = \nabla \cdot \left[\left(\mu + \mu_t\right) \nabla k\right] - \frac{\rho_f C_\epsilon k^{3/2}}{\Delta} - 2\mu_t S_s^2 \tag{3.22}$$

Where $C_\epsilon = 1.048$ and S_s is as defined in Eq. 3.17.

3.1.6 Wave Generation and Absorption

The *waves2Foam* toolbox (Jacobsen et al., 2012) is implemented in the hydrodynamic solver to allow for generation/dissipation of water waves inside the domain. For this purpose, the library uses two combined approaches: A boundary condition is introduced for inlet of waves according to different wave theories. This boundary condition distinguishes three types of cell faces: dry, wet and interface cell faces. At interface cells, the VOF value is calculated rather than simply considering all boundary cells wet or dry. A relaxation zone is defined in which the required wave profile is imposed (to generate or to diminish waves) through a relaxation function. The velocity and fluid phase fraction (VOF) are imposed as:

$$f = \alpha_R f_{computed} + (1 - \alpha_R)\, f_{target} \tag{3.23}$$

Where (f) is the velocity or the (VOF) phase fraction (γ) and α_R is the relaxation function. The relaxation zones are located at the inlet and outlet of waves into and out of the domain. Several wave theories are optionally available in the *waves2Foam* toolbox. For regular waves, the proper wave theory is selected according to Le Méhauté et al. (1976).

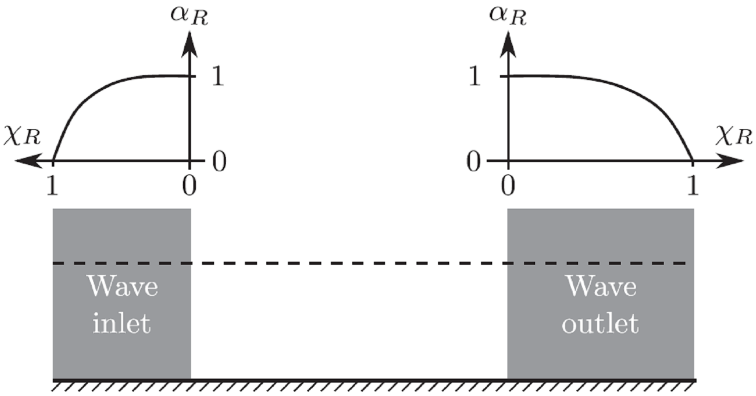

Figure 3.1: A sketch of variation of the relaxation function for both inlet and outlet zones (Jacobsen et al., 2012)

3.1.7 Flow in Porous Media

As presented earlier, OpenFOAM original implementation for modelling flow through porous media uses a sink (vector) term **S** in the momentum balance equation (Eq. 3.24) to model flow resistance and attenuation of the velocity time derivative by the porosity n. Both measures are applied for porous media zones only.

$$\rho_f \left(\frac{\partial n\mathbf{U}}{\partial t} + \mathbf{U} \cdot \nabla \mathbf{U} \right) = -\nabla p + \nabla \cdot (\boldsymbol{\tau} + \mathbf{R}) + \rho_f \mathbf{b} + \sigma_T \kappa_\gamma \nabla \gamma - \mathbf{S} \tag{3.24}$$

To extend the original solver, volume averaging is introduced to the governing equations in the solver similar to Masuoka and Takatsu (1996); Nakayama and Kuwahara (1999); Hsu et al. (2002); Lin (2008), the governing equations become:

$$\nabla \cdot \overline{\mathbf{U}} = 0 \tag{3.25}$$

$$\rho_f \left(\frac{(1 + c_A)}{n} \frac{\partial \overline{\mathbf{U}}}{\partial t} + \frac{1}{n^2} \overline{\mathbf{U}} \cdot \nabla \overline{\mathbf{U}} \right) = -\nabla p + \frac{1}{n} \left(\nabla \cdot \left(\boldsymbol{\tau} + \frac{\mathbf{R}}{n} \right) \right) + \rho_f \mathbf{b} + \sigma_T \kappa_\gamma \nabla \gamma - \mathbf{S} \tag{3.26}$$

Where $\overline{\mathbf{U}}$ is the fluid ensemble average (Darcy's) velocity vector ($\overline{\mathbf{U}} = n\mathbf{U}$; where $\mathbf{U}$ is the fluid intrinsic velocity vector and n is the porosity), p is the (intrinsic) fluid pressure, where n equals unity outside zones of porous media.

The added mass coefficient c_A is calculated as:

$$c_A = C_M \frac{(1 - n)}{n} \tag{3.27}$$

where C_M is the virtual mass coefficient, also called the inertial coefficient. In many studies (e.g. Van Gent (1995); Hsu et al. (2002); Lin and Karunarathna (2007)) is set to $C_M = 0.34$. The volume averaging approach enables the use of the same set of governing equations for the flow inside and outside the porous media. The resistance of the porous media (the sink term) is calculated using a seepage model (e.g. Darcy or Darcy-Forchheimer). The Darcy-Forchheimer model (Forchheimer, 1901) describes the hydraulic gradient ($I = \frac{1}{\rho g} \nabla p$) by two components: a viscous loss component and an inertial loss component. The viscous (linear) part represents laminar flow while the inertial (nonlinear) part represents turbulent flow. For transient flow, Kochina (1962) added a time-dependent term to the formula. Lin and Karunarathna (2007) have introduced another term to represent transitional flow (e.g. $10 < Re_p < 1000$). The pore (grain size related) Reynolds number is defined as $Re_p = \frac{D_{50} |\overline{\mathbf{U}}|}{\nu}$; where D_{50} is the equivalent mean diameter of the porous media particles, ν is the kinematic viscosity and $\overline{\mathbf{U}}$ is a typical velocity scale. The final seepage model is defined as:

$$I = -\frac{1}{\rho g}\nabla p = \underbrace{a\overline{\mathbf{U}}}_{\substack{\text{viscous}\\\text{(laminar)}}} + \underbrace{c\overline{\mathbf{U}}\sqrt{|\overline{\mathbf{U}}|}}_{\text{(transitional)}} + \underbrace{b\overline{\mathbf{U}}\,|\overline{\mathbf{U}}|}_{\substack{\text{inertial}\\\text{(turbulent)}}} + \underbrace{\frac{(1+c_A)}{ng}\frac{\partial\overline{\mathbf{U}}}{\partial t}}_{\text{transient}} \tag{3.28}$$

In this study, the last term (transient term) in the hydraulic gradient (Eq. 3.28) definition is merged with the momentum balance equation (Eq. 3.26).

For the original OpenFOAM Darcy-Forchheimer model, the sink term in the momentum balance equation is expressed as:

$$\mathbf{S} = \left(\mu\mathbf{d} + \frac{\rho}{2}\mathbf{f}|\overline{\mathbf{U}}|\right)\overline{\mathbf{U}} \tag{3.29}$$

where $\mathbf{d}$ is the Darcy coefficient (symmetric) tensor and $\mathbf{f}$ is the Forchheimer coefficient (symmetric) tensor. In OpenFOAM, $\mathbf{d}$ and $\mathbf{f}$ are input as vectors (instead of tensors) and the code calculates the average value for their elements to introduce isotropic porous media ($\mathbf{d}$ and $\mathbf{f}$ are reduced to scalars). A new class *volAvgPorousZone* was developed to implement different (Darcy/Darcy-Forchheimer) seepage models, based on the original *porousZone* class of OpenFOAM. A new tensor $\mathbf{e}$ is introduced, in the same manner as $\mathbf{d}$ and $\mathbf{f}$, for the transitional term in Eq. 3.28. For the Lin and Karunarathna model, the sink term is defined as:

$$\mathbf{S} = \rho g\left(a + c\sqrt{|\overline{\mathbf{U}}|} + b|\overline{\mathbf{U}}|\right)\overline{\mathbf{U}} = \left(\mu\mathbf{d} + \rho^{1/2}\mu^{1/2}\mathbf{e}\sqrt{|\overline{\mathbf{U}}|} + \frac{\rho}{2}\mathbf{f}|\overline{\mathbf{U}}|\right)\overline{\mathbf{U}} \tag{3.30}$$

where:

$$\begin{aligned}\mathbf{d} &= \frac{\rho g a}{\mu}\mathbf{I}\\ \mathbf{e} &= \frac{gc}{\nu^{1/2}}\mathbf{I}\\ \mathbf{f} &= 2gb\mathbf{I}\end{aligned} \tag{3.31}$$

where $\mathbf{I}$ is the identity tensor. The parameters a, b and c are given by several expressions for different seepage models in the literature as shown in Table 3.1, where D_{15} and D_{50} are the sieve size at which 15% and 50% particles pass. D_{EQ} is the equivalent diameter of porous media particles, ρ_s is the density of the solid phase, M_{50} is the average mass of a rock grading, determined by the 50% value on the mass distribution curve.

The stress due to turbulence is modelled by a modified turbulence eddy viscosity model:

$$\frac{\mathbf{R}}{n} = \frac{\mu_t}{n}\left(\left(\nabla\overline{\mathbf{U}} + \left(\nabla\overline{\mathbf{U}}\right)^T\right) - \frac{2}{3}\left(\nabla\cdot\overline{\mathbf{U}}\right)\mathbf{I}\right) \tag{3.32}$$

The turbulence model (e.g. $k-\epsilon$ or $k-\omega$) should be modified to account for volume averaging of the velocity. Nevertheless, this is outside the scope of this study. Original turbulence models from OpenFOAM are used directly by dividing the eddy viscosity by the porosity (Eq. 3.32).

The original *porousZone* classes was extended to *volAvgPorousZone* classes to provide automatic calculation of different seepage model parameters and the flow resistance sink term for these models. Finally, the call to the VOF-MULES solver is modified to account for the fact that water only fills the pores of porous media and not the total size of cells. Therefore, fluctuations of the water surface (air-water) interface change accordingly.

Table 3.1: Parameters of different seepage models, Eqs. 3.30 and 3.31 (modified from Van Gent (1993) and Lin (2008))

Author	a [s/m]	$\mathbf{d}$ [m^{-2}]	b [s^2/m^2]	$\mathbf{f}$ [m^{-1}]	$\mathbf{e}$ [m$^{-1.5}$]
Carman (1937)	$180\frac{(1-n)^2}{n^3}\frac{\nu}{gD_{50}^2}$	$180\frac{(1-n)^2}{n^3}\frac{1}{D_{50}^2}\mathbf{I}$	0	0	0
Ergun (1952)	$150\frac{(1-n)^2}{n^3}\frac{\nu}{gD_{50}^2}$	$150\frac{(1-n)^2}{n^3}\frac{1}{D_{50}^2}\mathbf{I}$	$1.75\frac{1-n}{n^3}\frac{1}{gD_{50}}$	$1.75\frac{1-n}{n^3}\frac{2}{D_{50}}\mathbf{I}$	0
Engelund (1953)	$\alpha\frac{(1-n)^3}{n^2}\frac{\nu}{gD_{EQ}^2}$ $\alpha = 780 - 1500$ $D_{EQ} = \left(6M_{50}/\pi\rho_s\right)^{1/3}$	$\alpha\frac{(1-n)^3}{n^2}\frac{1}{D_{EQ}^2}\mathbf{I}$	$\beta\frac{1-n}{n^3}\frac{1}{gD_{EQ}}$ $\beta = 1.8 - 3.6$	$\beta\frac{1-n}{n^3}\frac{2}{D_{EQ}}\mathbf{I}$	0
Koenders (1985)	$\alpha\frac{(1-n)^2}{n^3}\frac{\nu}{gD_{15}^2}$ $\alpha = 290\,(250 - 330)$	$\alpha\frac{(1-n)^2}{n^3}\frac{1}{D_{15}^2}\mathbf{I}$	$\beta\frac{1}{n^5}\frac{1}{gD_{15}}$ $\beta = 1.4$	$\beta\frac{1}{n^5}\frac{2}{D_{15}}\mathbf{I}$	0
Den Adel (1987)	$\alpha\frac{(1-n)^2}{n^3}\frac{\nu}{gD_{15}^2}$ $\alpha = 160\,(75 - 350)$	$\alpha\frac{(1-n)^2}{n^3}\frac{1}{D_{15}^2}\mathbf{I}$	$\beta\frac{1}{n^2}\frac{1}{gD_{15}}$ $\beta = 2.2(0.9 - 5.3)$	$\beta\frac{1}{n^2}\frac{2}{D_{15}}\mathbf{I}$	0
Shih (1990)	$\alpha\frac{(1-n)^2}{n^3}\frac{\nu}{gD_{15}^2}$ $\alpha = 1684 + 3.12 \cdot 10^{-3}\left(\frac{g}{\nu^2}\right)^{2/3} D_{15}^2$	$\alpha\frac{(1-n)^2}{n^3}\frac{1}{D_{15}^2}\mathbf{I}$	$\beta\frac{1-n}{n^3}\frac{1}{gD_{15}}$ $\beta = 1.72 + 1.57e^{\left[-5.10\cdot 10^{-3}\left(\frac{g}{\nu^2}\right)^{1/3} D_{15}\right]}$	$\beta\frac{1-n}{n^3}\frac{2}{D_{15}}\mathbf{I}$	0
van Gent (1995)	$1000\frac{(1-n)^2}{n^3}\frac{\nu}{gD_{50}^2}$	$1000\frac{(1-n)^2}{n^3}\frac{1}{D_{50}^2}\mathbf{I}$	$1.1\frac{1-n}{n^3}\frac{1}{gD_{50}}$	$1.1\frac{1-n}{n^3}\frac{2}{D_{50}}\mathbf{I}$	0
Liu et al. (1999) Hsu et al. (2002)	$200\frac{(1-n)^2}{n^3}\frac{\nu}{gD_{50}^2}$	$200\frac{(1-n)^2}{n^3}\frac{1}{D_{50}^2}\mathbf{I}$	$1.1\frac{1-n}{n^3}\frac{1}{gD_{50}}$	$1.1\frac{1-n}{n^3}\frac{2}{D_{50}}\mathbf{I}$	0
Lin and Karunarathna (2007)	$126\frac{(1-n)}{n^3}\frac{\nu}{gD_{50}^2}$	$126\frac{(1-n)}{n^3}\frac{1}{D_{50}^2}\mathbf{I}$	$1.02\frac{1-n}{n^3}\frac{1}{gD_{50}}$	$1.02\frac{1-n}{n^3}\frac{2}{D_{50}}\mathbf{I}$	$c = 4.5\frac{1-n}{n^3}\frac{\nu^{1/2}}{gD_{50}^{3/2}}$ $\mathbf{e} = \frac{gc}{\nu^{1/2}}\mathbf{I}$

3.1.8 Fluid Compressibility

For applications where thermal changes are insignificant, fluid compressibility can be defined as changes in fluid volume (and subsequently density) due to variations of the applied pressure. Generally, compressibility of pure water is very low so that pure water can generally be considered as incompressible. Air compressibility, on the other hand, is four orders of magnitude higher than pure water compressibility. Nevertheless, air compressibility, typically, has insignificant effects for subsonic flows.

As shown in Subsection 2.1.1, when breaking waves approach a vertical wall, the water in front of the wall has a high content of entrapped air and can be regarded as a bubbly-mixture between the wave front and the wall or as a large air pocket underneath the tongue of the breaking wave which is then entrapped at the wall. This entrapped air results in oscillations of wave-induced pressure just after the wave impact. This is due to the high air compressibility. This process cannot be reproduced numerically unless fluid compressibility is taken into account.

As shown in Fig. 3.2, using a single-phase-fluid (only water) RANS-CFD model (COBRAS) to simulate wave impact does not reproduce pressure or force oscillations after the impact caused by the volume oscillations of the entrapped air pocket. Therefore, a multiphase CFD model is needed (i.e. water and air) with the proper account of compressibility.

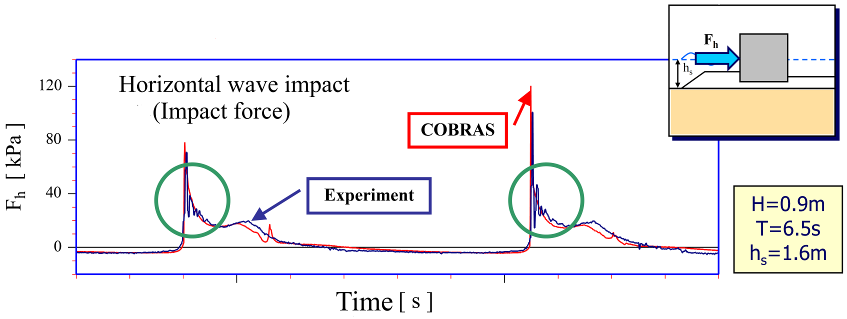

Figure 3.2: Experimental wave impact versus simulated incompressible single-phase-fluid RANS-CFD (Kudella and Oumeraci, 2008b)

Typically, fluid compressibility is considered by adding a term to the mass balance equation to account for the time derivative of the fluid density:

$$\nabla \cdot (\rho \overline{\mathbf{U}}) + \frac{\partial \rho}{\partial t} = 0 \tag{3.33}$$

Due to mass conservation, the rate of density change is equal in magnitude to the rate of change in fluid volume:

$$-\frac{\partial \forall}{\partial t} = \frac{\partial \rho}{\partial t} \tag{3.34}$$

Further, a state law is needed to calculate the rate of fluid density change. For simplicity, an effective barotropic relation can be considered for the fluid (air-water) mixture. This means that fluid density is considered as a function of only the fluid pressure:

$$\rho = \rho(p) \tag{3.35}$$

Considering an elastic model for the fluid response, the rate of fluid volume change can be expressed as:

$$-\frac{\partial \forall}{\partial t} = \frac{1}{Q}\frac{\partial p}{\partial t} \tag{3.36}$$

where:

$$\frac{1}{Q} = \frac{n}{K_f} \tag{3.37}$$

The porosity (n) is considered unity outside zones of porous media and is multiplied by the rate of fluid volume change to account for the reduction of the volume of cells located in zones of porous media because fluid occupies only the pores:

$$\underset{actual}{\rlap{-}V} = n\,\rlap{-}V \tag{3.38}$$

The fluid bulk modulus K_f is calculated based on the phase fraction (γ) as:

$$\frac{1}{K_f} = \frac{\gamma S}{K_w} + \frac{(1-\gamma S)}{K_a} \tag{3.39}$$

where $K_w = 2200 MPa$ is the bulk modulus of pure water, K_a is the bulk modulus of air, equal to fluid absolute pressure ($K_a = 0.101$ MPa, at atmospheric pressure). and S is the degree of saturation in the porous media.

$$S = \frac{\rlap{-}V_w}{\rlap{-}V_v} \tag{3.40}$$

where $\rlap{-}V_v$ is the volume of voids in the porous media. The final fluid continuity equation, the mass balance, is considered for volume balance instead, and reads:

$$\nabla \cdot \overline{\mathbf{U}} + \frac{1}{Q}\frac{\partial p}{\partial t} = 0 \tag{3.41}$$

3.2 CFD Model Validation

3.2.1 Dam Break Flow Through a Porous Vertical Barrier

The validation of the hydrodynamic model is herein presented for the transient flow through a porous vertical barrier. The simulations is run on multiple processors using OpenMPI via domain decomposition, which is a generic implementation in OpenFOAM.

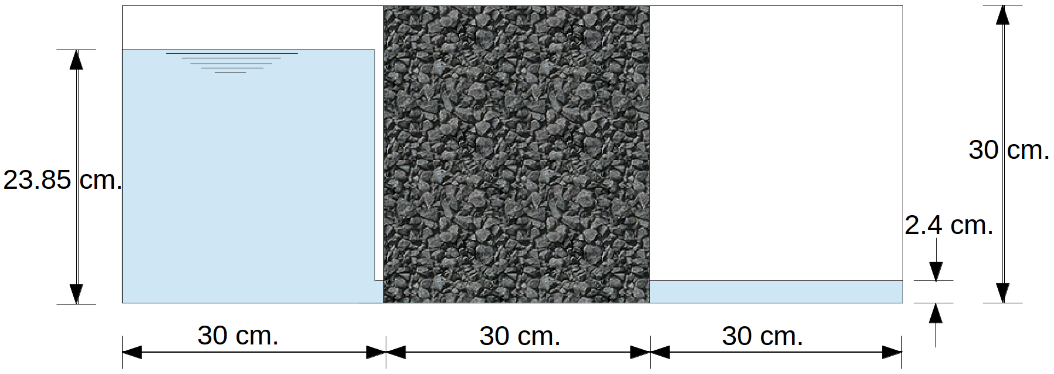

Figure 3.3: A sketch of the benchmark case of transient flow through a vertical porous barrier

The used validation case is the dam break in front of a vertical column of rocks or beads presented by Liu et al. (1999) as explained in Lin (2008). This case is considered as a benchmark for models similar to the one presented in this chapter. This case is used, here, to validate and test the different implemented seepage models. The relative effect of different model parameters and of the applied turbulence models on the results are also tested.

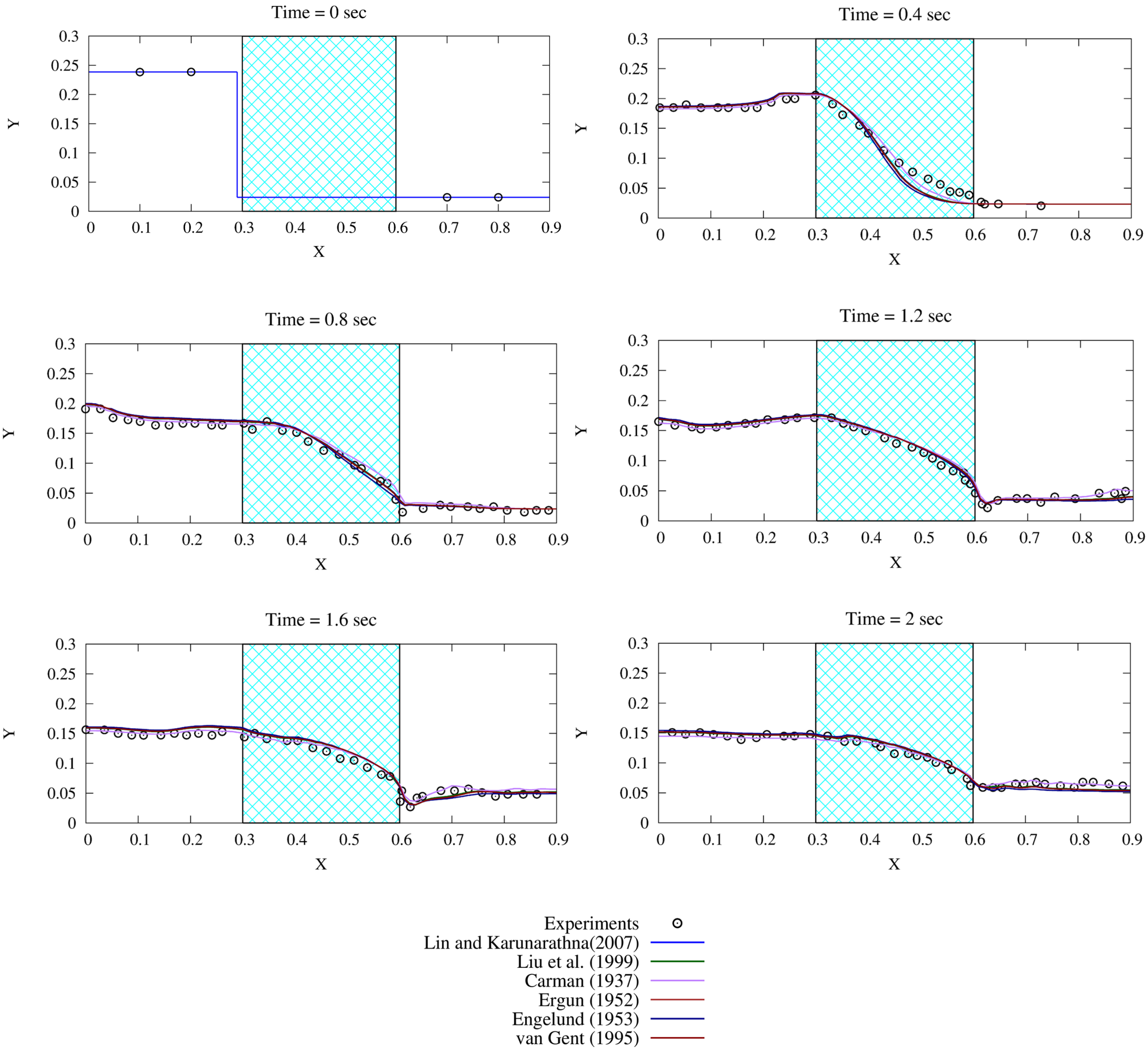

Figure 3.4: Porous dam break for different seepage models without turbulence modelling (porous media hatched)

This case consists of a vertical column of crushed stones of 30 cm breadth in the middle of a fish tank. Water is retained on the left basin by a vertical gate for a head of 23.85 cm then the gate is lifted to unleash the water to hit the crushed stone and flow through to the other side, Fig. 3.3. The fish tank extends 30 cm on both sides of the crushed stones barrier. Results from the numerical simulations using *waveVolAvgPorousInterFoam* for different seepage models without turbulence modelling are shown in Fig. 3.4.

From these results, it is obvious that no noticeable difference is observed for the use of different seepage models and that the use of the Lin and Karunarathna (2007) model without any modification (values of the parameters as given in Table 3.1) is acceptable; i.e. no calibration of the model parameters is needed.

A comparison of the solution using the seepage model of Lin and Karunarathna (2007) with and without turbulence modelling (the $k-\omega-SST$ RANS model and the one- equation eddy-viscosity SGS large eddy simulation model) is given in Fig. 3.5. As shown, the RANS turbulence model yields less accurate water surface. The large eddy simulation on the other hand yields results similar to direct numerical simulation (without turbulence modelling) with enhancement of the simulation time. The use of the $k-\epsilon$ turbulence model for this case takes more time to converge than the $k-\omega-SST$ model and generally offers less accurate solution and therefore is not considered in this study. Further, the large eddy simulation will be considered for the rest of the study (i.e. simulating monolithic breakwaters).

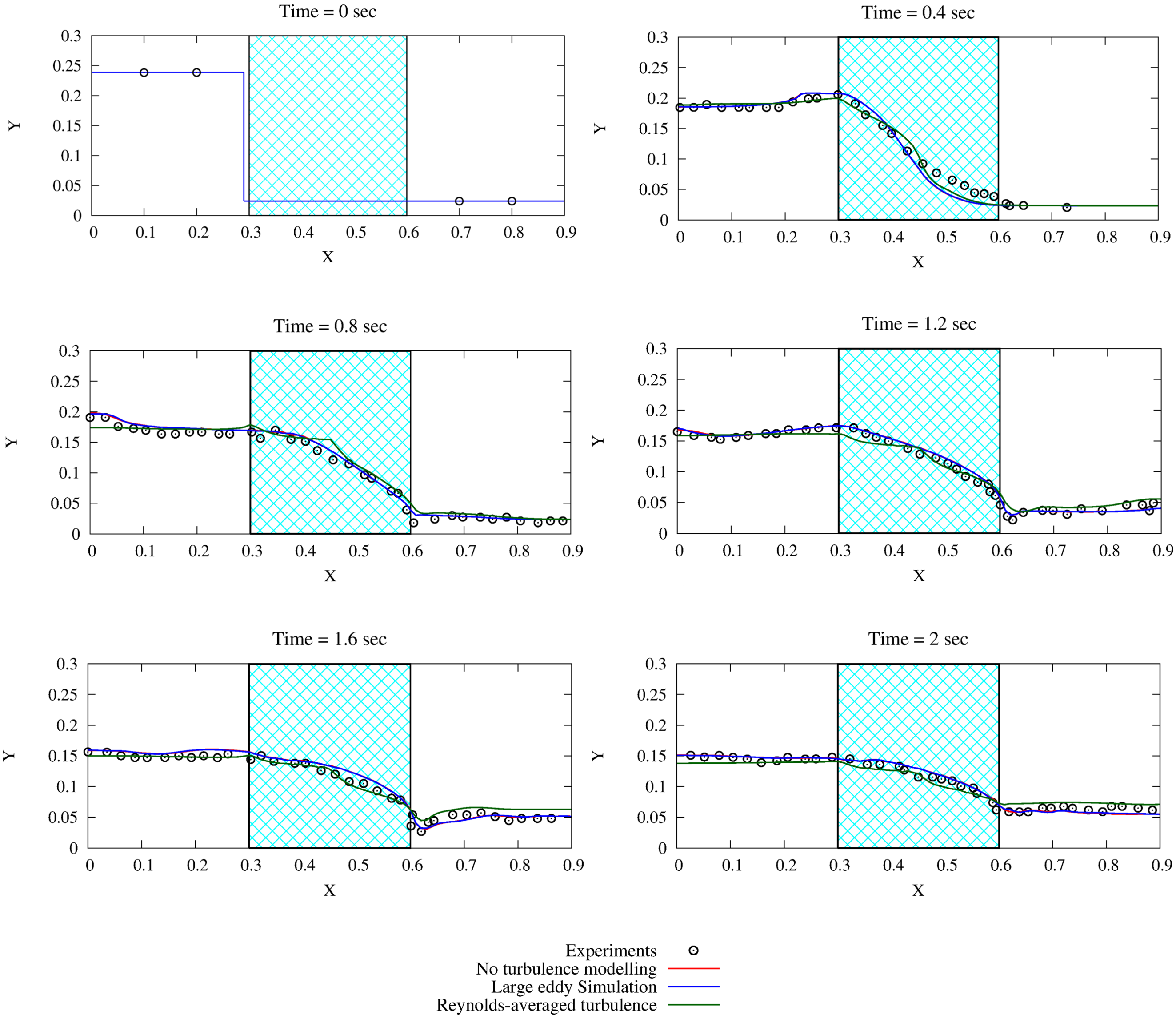

Figure 3.5: Porous dam break: without turbulence modelling (red), large eddy simulation (blue) and $k - \omega - SST$ RANS model (green) using Lin and Karunarathna (2007) seepage model (porous media hatched)

It is very important to avoid using tetrahedron or prism elements in regions where the water-air interface is expected. Generally, increasing the mesh density at the interface region is advisable. Special care to the selection of the numerical solvers/parameters is needed for the solution not to diverge and the water-air interface not to explode.

The turbulence models should also be modified for volume averaged velocity (closure terms). Nevertheless, original turbulence models from OpenFOAM have been used with satisfactory results.

3.2.2 Large-Scale Caisson Breakwater Experiments in GWK

a. Model setup and testing programme

The model tests were performed in the Large Wave Flume (GWK) in Hannover (Fig. 3.6). The effective length of the flume is about 307 m., the width 5 m and the depth 7 m. After a horizontal bottom of 250 m. the flume is limited by an impermeable embankment with a slope of 1:6. The investigated model construction includes the sand body (1:25 slope starting at 170 m. to level +2.45) beneath the breakwater, the rubble foundation with a seaward berm and the caisson breakwater (Oumeraci and Kudella, 2004). The locations of wave pressure transducers, pore pressure transducers and displacement meters are shown in Fig. 3.7. The numbering of the measuring channels for the transducers deployed in the near field of the structure is shown in Fig. 3.8.

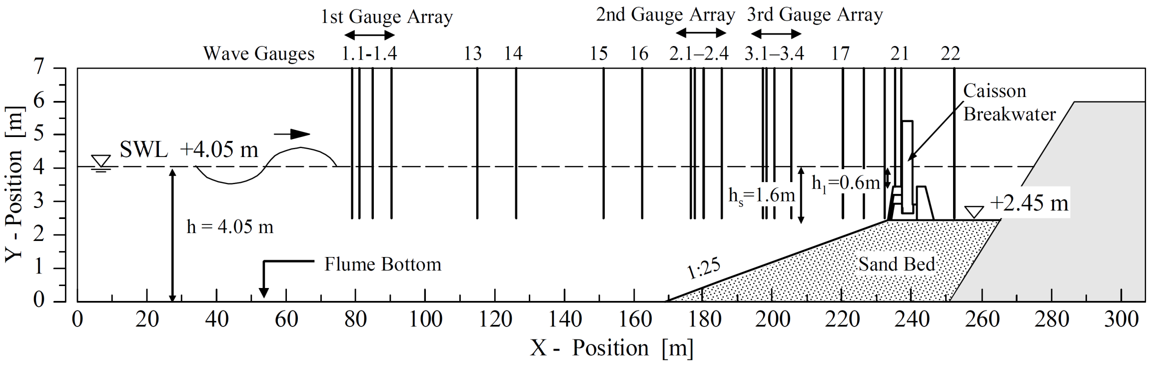

Figure 3.6: Caisson breakwater model with position of wave gauges in the Large Wave Flume (GWK) (Oumeraci and Kudella, 2004)

The PE-sheet is treated as an impervious boundary. Geotextiles are neglected in the model because they are assumed to have similar hydraulic properties as underlying soil. Different conditions tested in the Large-Wave Flume (GWK) are presented in Table 3.2. According to Subsection 3.1.6, the most appropriate wave theory for reproducing different tested regular wave conditions in the far field is Stokes II (Table 3.4).

The geometry of the computational domain is constructed using the free mesh generator *Gmsh* (Fig. 3.9, Fig. 3.10). The inlet and outlet zones of the wave generation are given in (Fig. 3.11). The properties of the porous media are given in (Table 3.3). An example view of the field of the VOF function is given in Fig. 3.12.

The domain is reduced by 90 m. and the start of the wave domain is considered at wave gauge 1.4 (see Fig. 3.6). The inlet relaxation zone has a length of 50 m and a smaller relaxation zone of 15 m is considered behind the caisson to prevent reflection of small waves that may be caused by overtopping.

For the presentation of the validation results, three cases of regular waves are selected: non-breaking waves with H = 0.4 m and T = 5.5 s, slightly breaking waves with H = 0.5 m and T = 6.5 s and breaking waves with H = 0.7 m and T = 6.5 s. The three wave conditions could be reproduced by Stokes II theory (as mentioned earlier) in the far field (Table 3.4).

For comparison, numerical and experimental results are shown for water surface elevation for selected wave gauges, pressure transducers for wave pressure and pore pressure (including uplift) results. Unfortunately, no experimental results were recorded for pressure transducer No. 61 because it was damaged during installation. For pore pressure inside rubble foundation away from caisson, pressure transducer 62 is used.

It is important to note that the noise in the measured signals from experiments were not removed (no signal filtering). It is also important to recognize how the water surface elevation is calculated in the *waves2Foam* library to better understand some of the differences of the measured versus calculated water surface elevation near the structure.

The *waves2Foam* library provides a wave gauge class that calculates the water surface elevation via integrating the volume-of-fluid (phase fraction) function over a column of fluid and divides the result by the column height instead of searching for the highest position with an interpolated phase fraction value of 0.5 (for example). The former method is adopted in this study as it is more convenient to implement than the latter (already implemented in *waves2Foam*). Nevertheless, the calculated surface elevation is only accurate in absence of tongues and splashes. If splashes or tongues are present, the given water surface elevation is simply an accumulation of height of water filled cells and is therefore smaller than the actual highest

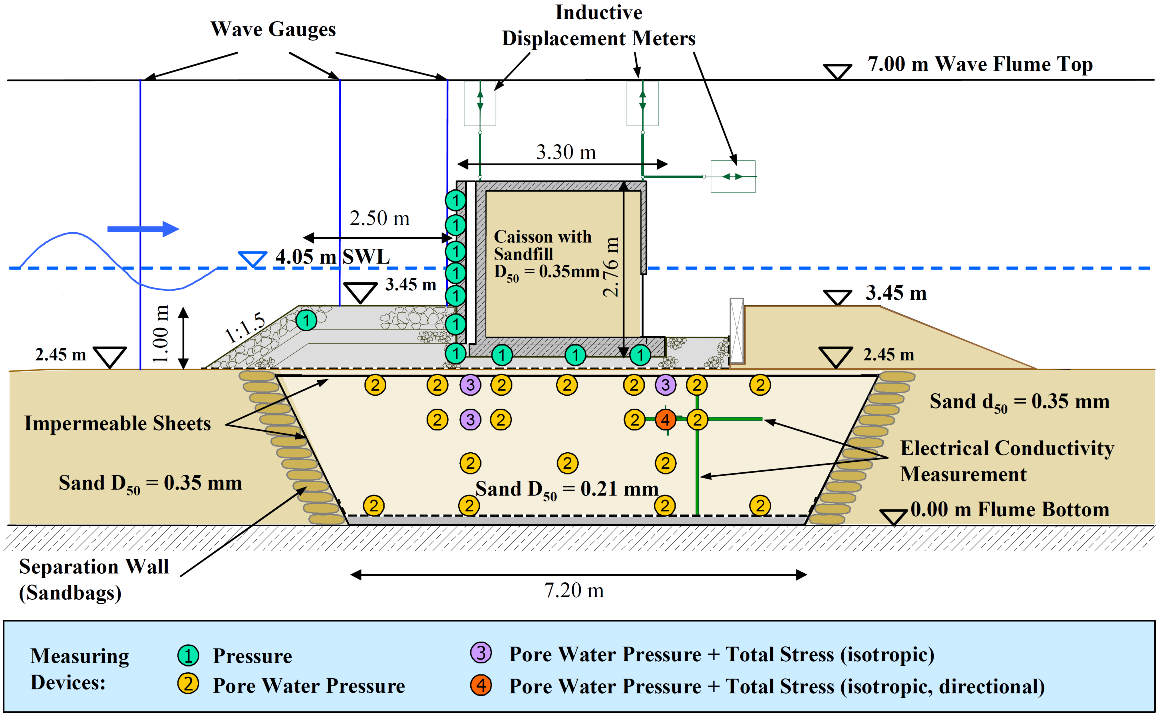

Figure 3.7: Wave pressure transducers, pore pressure transducers and displacement gauges (Oumeraci and Kudella, 2004)

reach of water recorded in the lab. This method is also not accurate for air-water mixture with a high air content. Despite these limitations, the used method provides an excellent tool for wave gauges near the wave generation source.

b. Model validation for water surface elevation and pressure

The water surface elevations obtained from the numerical simulations (Figs. 3.13, 3.16 and 3.19) agree well with the measured signals from the wave gauges that are located far from the structure (e.g. wave gauge No. 14). However, for wave gauges near the structure, the agreement is not obvious. This is (as mentioned earlier) due to the way by which the *waves2Foam* toolbox calculates the water surface elevation at a wave gauge position (integration of the phase fraction divided by the sampled height). Adopting a different way for calculating the water surface elevation (e.g. highest point with a phase fraction value of 0.5) is expected to enhance the numerical results of wave gauges near the structure.

For the pressure transducers located on the caisson front, the numerically calculated pressures agree very well with the measured pressures from the physical experiments for all three wave types (Figs. 3.14, 3.17 and 3.20). The good agreement extends to pore pressure inside the rubble mound (Figs. 3.15d, 3.18d and 3.21d).

However, the uplift pressure calculated numerically (Figs. 3.15, 3.18 and 3.21) is of higher amplitude than the measured in GWK tests. This is partially due to the fact that uplift pressure on a caisson structures is affected by the structure motion (Oumeraci et al., 2001). This effect is magnified under the very specific conditions of these experiments because of the impermeable sheet underneath the caisson. This sheet is non-deformable in the hydrodynamic model (confinement effect) while, actually, it is flexible so that it responds to changes in pore pressure. It is anticipated that introduction of mesh motion (caisson motion and PE-impermeable sheet deformation) to the hydrodynamic model (as feedback from the structural model) would enhance the results and reduce computed uplift pressure amplitude. However, accounting for fluid compressibility reduces the difference noticeably.

The difference between the calculated and measured uplift amplitude is highest for pressure transducer No. 59 and hardly noticeable for transducer No. 58, which supports the aforementioned interpretation.

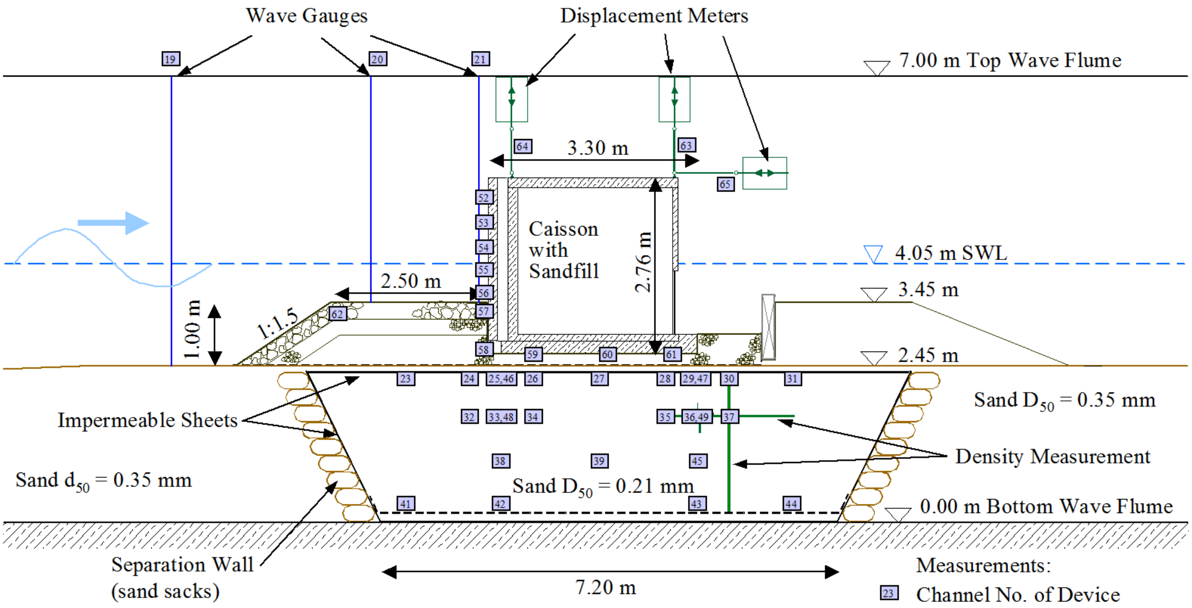

Figure 3.8: Channel numbering for wave pressure transducers, pore pressure transducers and displacement gauges (Oumeraci and Kudella, 2004)

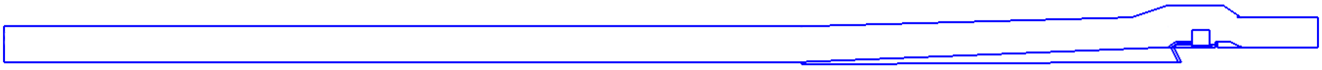

Figure 3.9: Geometry of (reduced) problem domain for numerical simulations

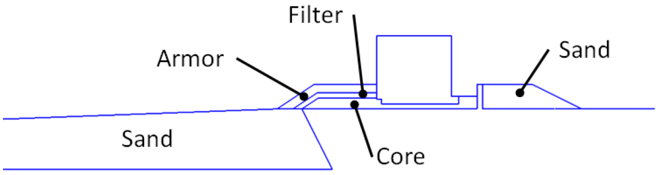

Figure 3.10: Enlarged geometry of the problem showing different defined porous media zones

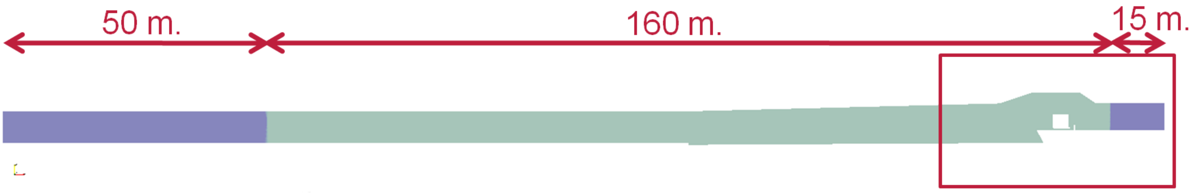

Figure 3.11: Inlet and outlet (relaxation) zones for wave generation and absorption

Unfortunately, transducer No. 61 was damaged and cannot be used here.

Figure 3.12: The VOF function for a regular wave train of height 0.4 m. and period 5.5 s.

Table 3.2: Test program with regular waves (R) and irregular waves (S) used during the first and second test phases (Oumeraci and Kudella, 2004)

		Test phase	Wave period T or T_p [s]				
			4.5	5.5	6.5	7.0	8.0
Wave height H or H_s [m]	0.4	1		R			
		2	R/S	R/S	R/S		
	0.5	-					
		2	R/S	R/S	R/S		R/S
	0.6	1	R	R			
		2	R/S	R/S	S		
	0.7	-					
		2	S	R/S	R/S		
	0.8	1	R				
		2	S	R/S	R/S		
	0.9	-					
		2		S	R	R	
		Water depth $h_s = 1.6m.$, $h_1 = 0.6m.$					

Table 3.3: Material properties for the test program (Oumeraci and Kudella, 2004)

	Sand	Core	Filter	Armour
Porosity	0.45946	0.411	0.411	0.411
Diameter [m]	2.1×10^{-5}	35×10^{-3}	50×10^{-3}	0.206
$W_{50} [kg]$	-	-	-	26.6
Density [kg/m^3]	1700	2000	2000	2000

Table 3.4: Nonlinearity of regular waves used in tests

Test	H [m]	T [s]	d/gT^2	H/gT^2	L [m]	$L_{MaxStokes}$ [m]	Wave theory
Non-breaking	0.4	5.5	0.01364	0.00134	31.554	72.39	Stokes II
Slightly breaking	0.5	6.5	0.00977	0.00120	38.341	69.12	Stokes II
Breaking	0.7	6.5	0.00977	0.00168	38.341	63.02	Stokes II

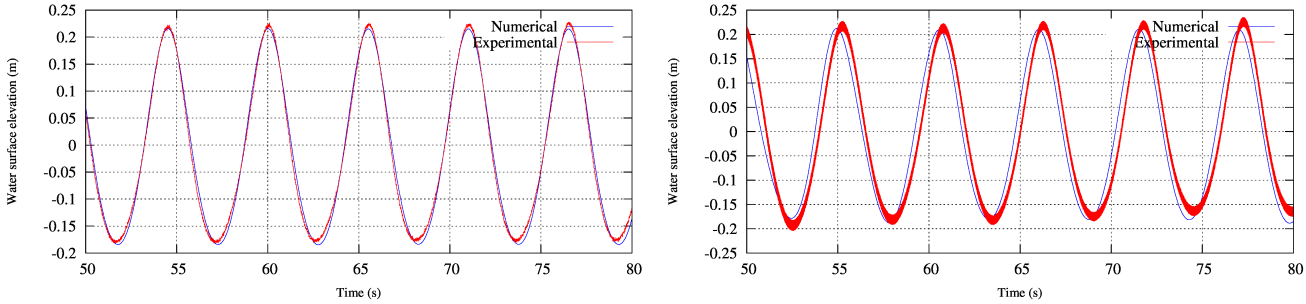

(a) Wave gauge 1.4 (b) Wave gauge 14

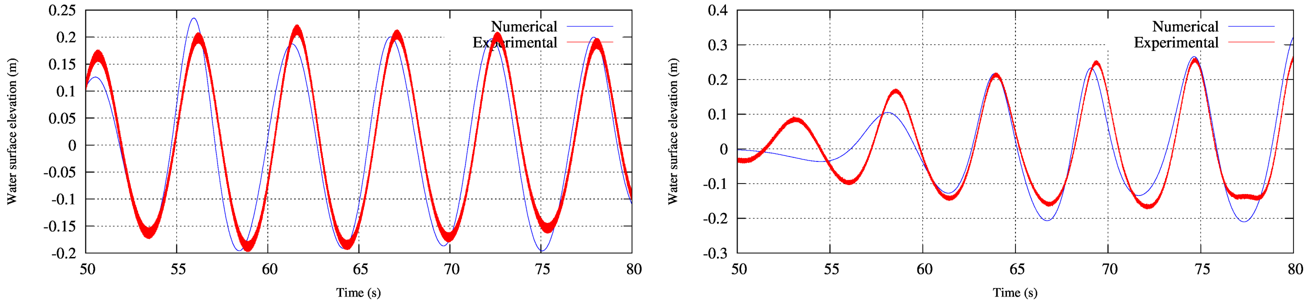

(c) Wave gauge 16 (d) Wave gauge 3.4

Figure 3.13: Wave surface elevation for a regular non-breaking wave train of height 0.4 m. and period 5.5 s.

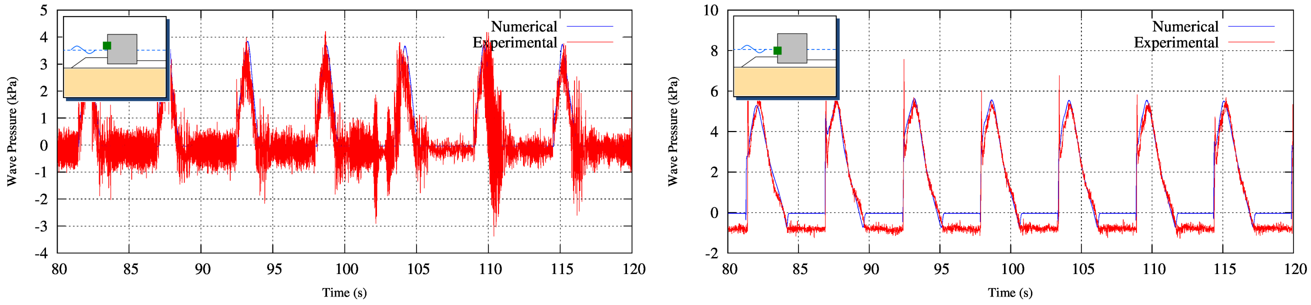

(a) Pressure transducer 54 (b) Pressure transducer 55

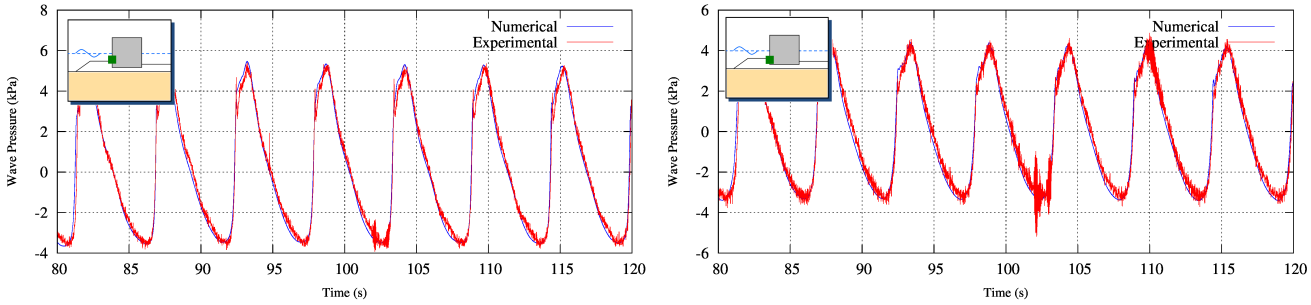

(c) Pressure transducer 56 (d) Pressure transducer Wave 57

Figure 3.14: Wave pressure on the caisson breakwater for a regular non-breaking wave train of height 0.4 m. and period 5.5 s.

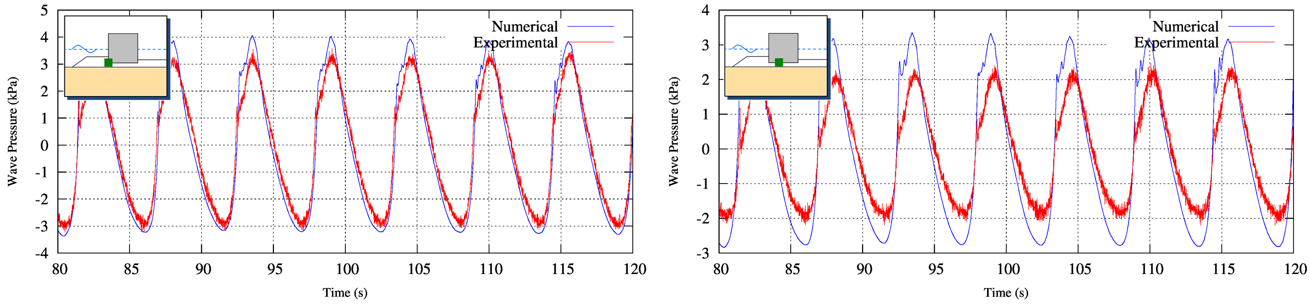

(a) Pressure transducer 58

(b) Pressure transducer 59

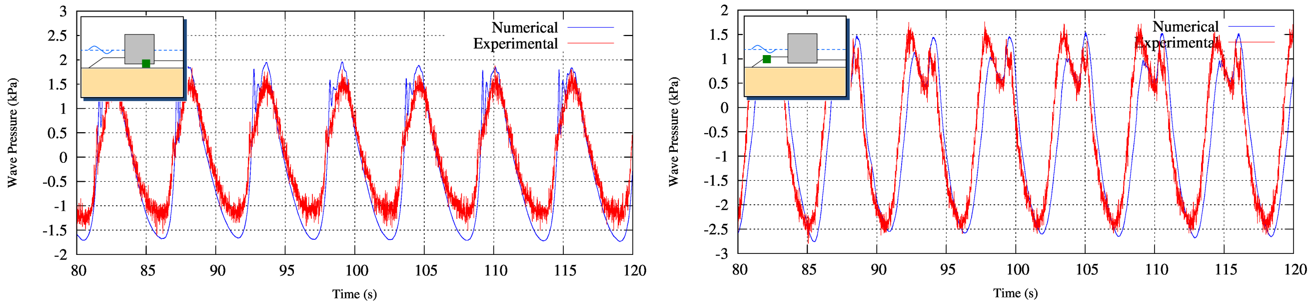

(c) Pressure transducer 60

(d) Pore pressure inside rubble foundation from channel No. 62 for a regular non-breaking wave train of height 0.4 m. and period 5.5 s.

Figure 3.15: Uplift pressure on the caisson breakwater and pressure inside the rubble foundation for a regular non-breaking wave train of height 0.4 m. and period 5.5 s.

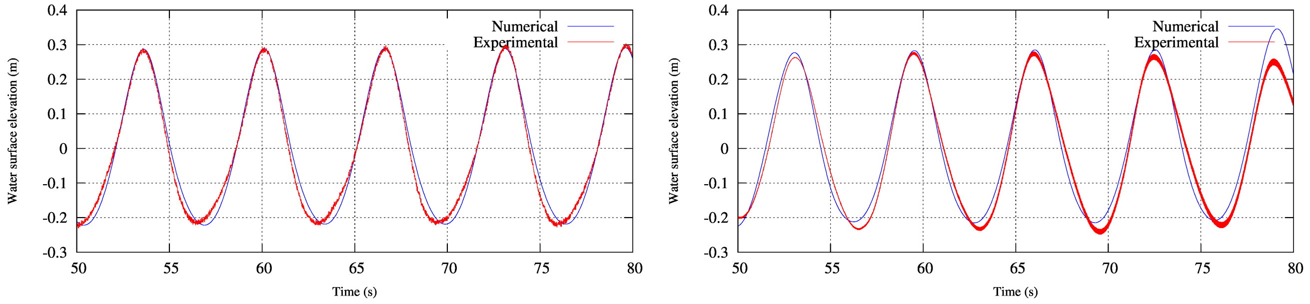

(a) Wave gauge 1.4

(b) Wave gauge 14

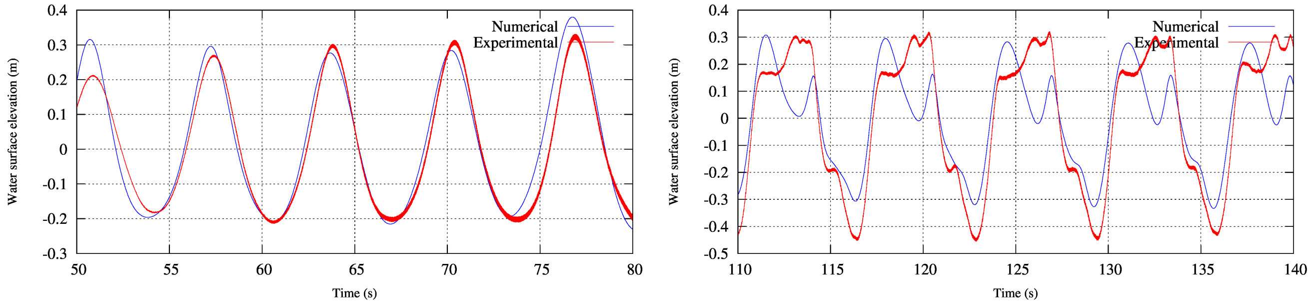

(c) Wave gauge 15

(d) Wave gauge 3.4

Figure 3.16: Wave surface elevation for a regular slightly breaking wave train of height 0.5 m. and period 6.5 s.

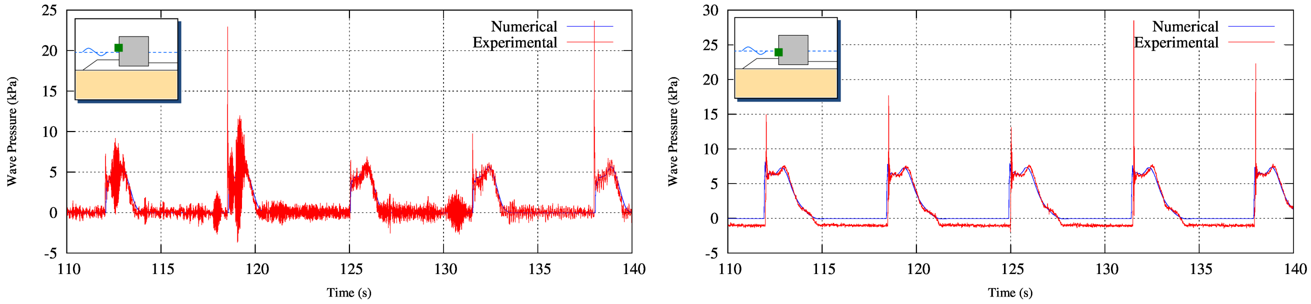

(a) Pressure transducer 54

(b) Pressure transducer 55

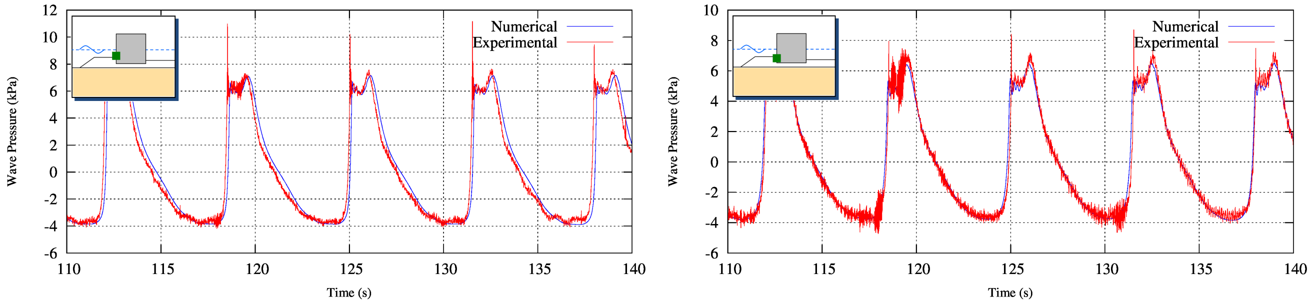

(c) Pressure transducer 56

(d) Pressure transducer Wave 57

Figure 3.17: Wave pressure on the caisson breakwater for a regular slightly breaking wave train of height 0.5 m. and period 6.5 s.

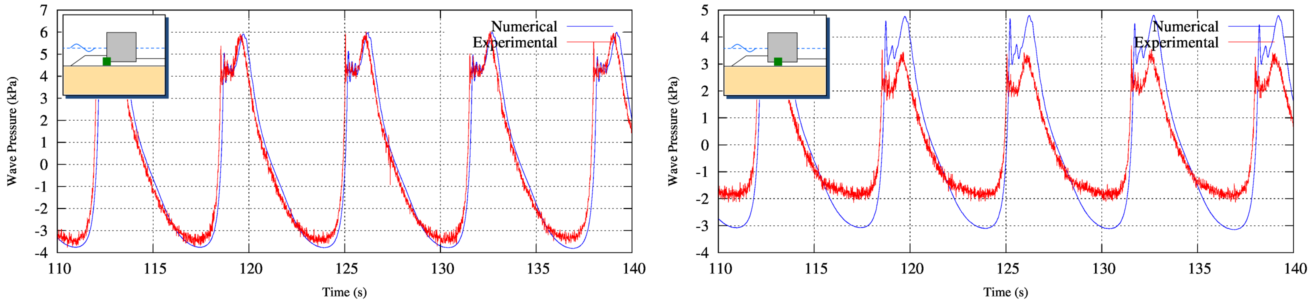

(a) Pressure transducer 58

(b) Pressure transducer 59

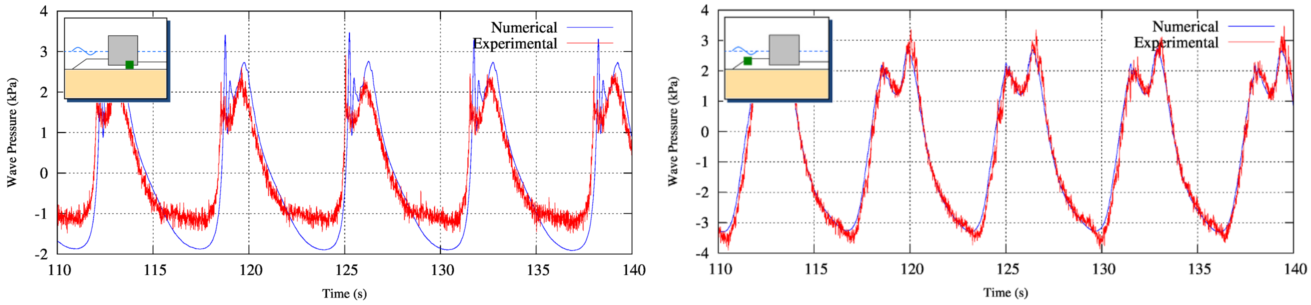

(c) Pressure transducer 60

(d) Pore pressure inside rubble foundation from channel No. 62 for a regular slightly breaking wave train of height 0.5 m. and period 6.5 s.

Figure 3.18: Uplift pressure on the caisson breakwater and pressure inside the rubble foundation for a regular slightly breaking wave train of height 0.5 m. and period 6.5 s.

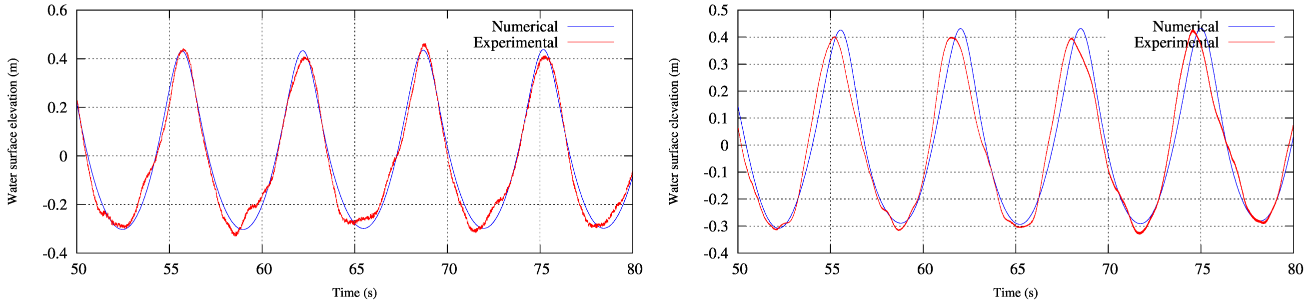

(a) Wave gauge 1.4

(b) Wave gauge 14

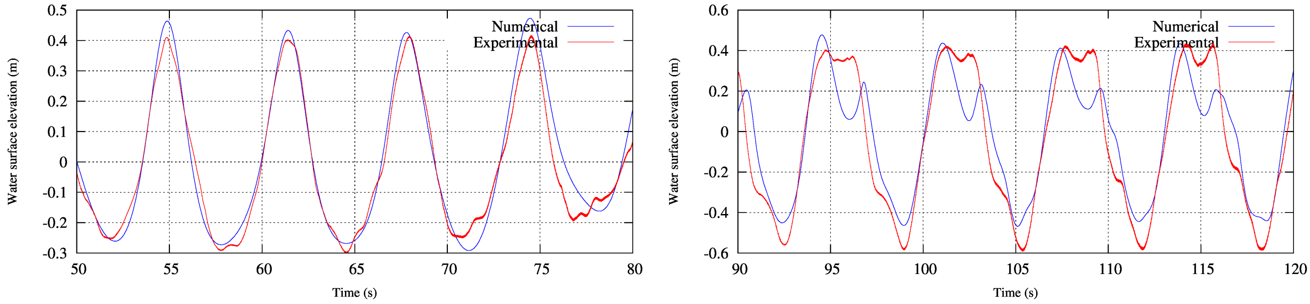

(c) Wave gauge 16

(d) Wave gauge 3.4

Figure 3.19: Wave surface elevation for a regular breaking wave train of height 0.7 m. and period 6.5 s.

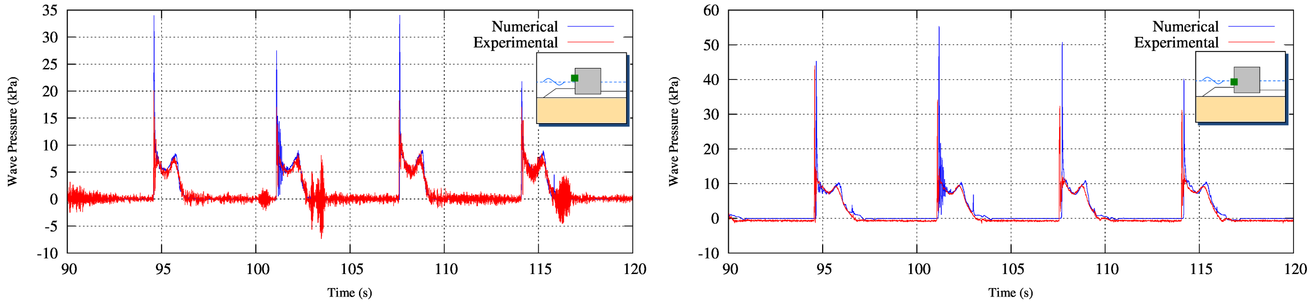

(a) Pressure transducer 54

(b) Pressure transducer 55

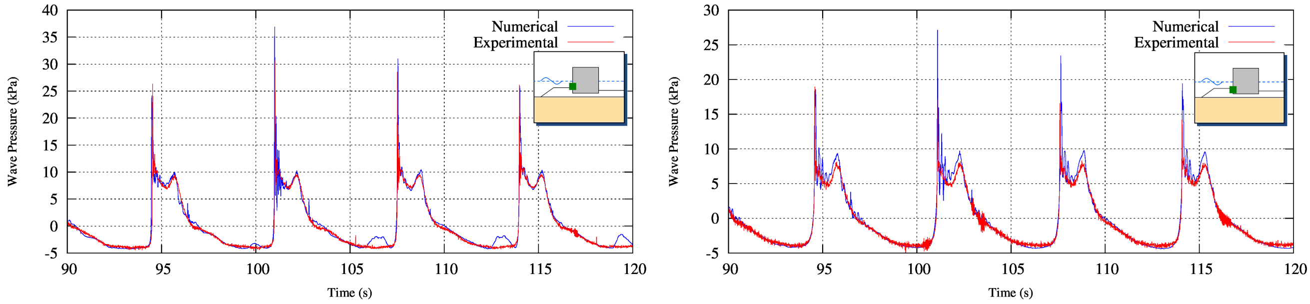

(c) Pressure transducer 56

(d) Pressure transducer Wave 57

Figure 3.20: Wave pressure on the caisson breakwater for a regular breaking wave train of height 0.7 m. and period 6.5 s.

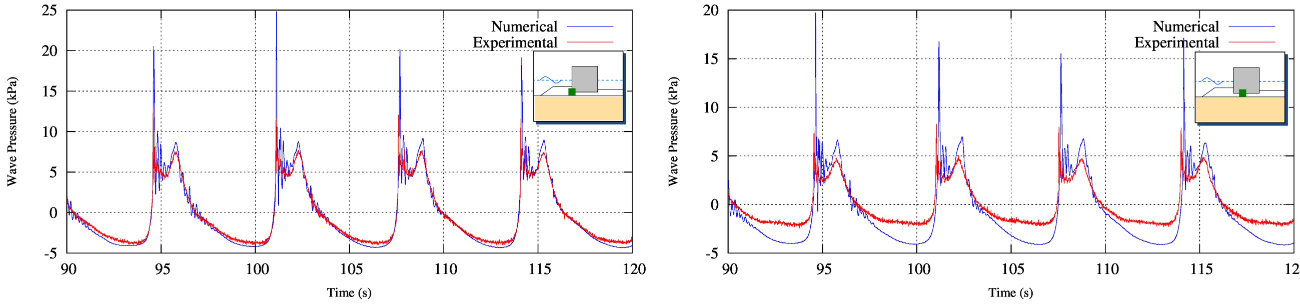

(a) Pressure transducer 58

(b) Pressure transducer 59

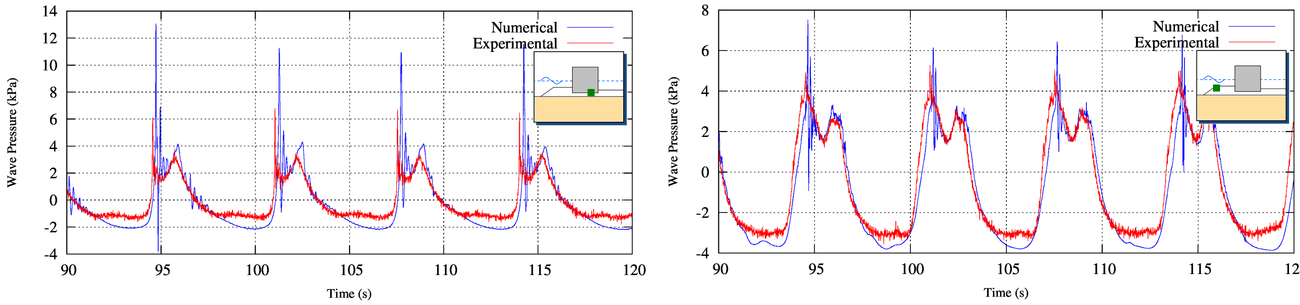

(c) Pressure transducer 60

(d) Pore pressure inside rubble foundation from channel No. 62 for a regular breaking wave train of height 0.7 m. and period 6.5 s.

Figure 3.21: Uplift pressure on the caisson breakwater and pressure inside the rubble foundation for a regular breaking wave of height 0.7 m. and period 6.5 s.

c. Effect of turbulence modelling

Using RANS turbulence modelling provides the fastest alternative to solve the Navier-Stokes equations. Nevertheless, for large domains, in which water waves have to travel a long distance, RANS causes the wave height to dampen along the flume. LES on the other hand does not appear to suffer from this shortcoming.

In Fig. 3.22, it is shown that (for a dense mesh) RANS and LES simulations give the same wave height at generation. However, for wave-induced pressure on a caisson (Fig. 3.23 and 3.24), the peak impact pressure is better reproduced by LES.

Additionally, one should select the numerical schemes carefully. Some of the more stable numerical schemes (e.g. *upwind*) could cause the reduction of impact pressure for breaking waves.

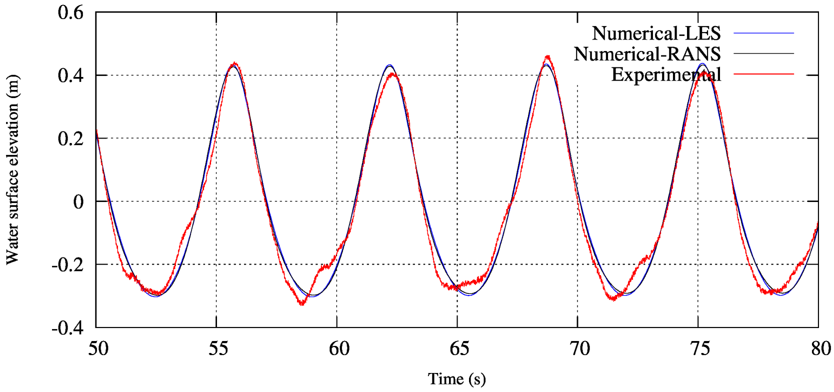

(a) Wave gauge No. 1.4

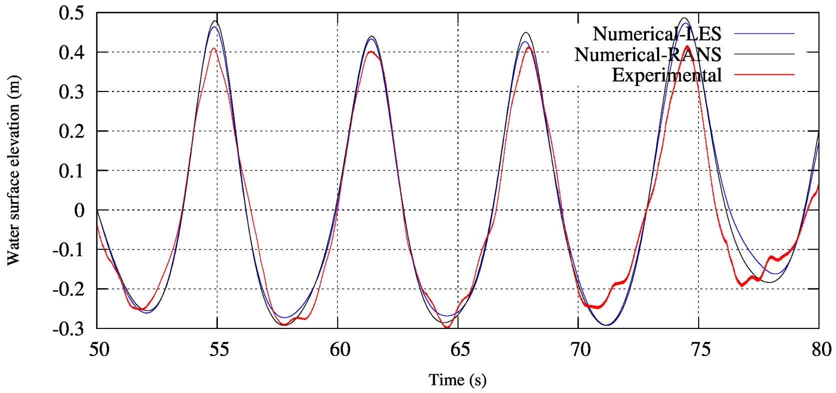

(b) Wave gauge No. 16

Figure 3.22: Comparison of turbulence modelling effect; water surface elevation for a regular wave of height 0.7 m. and period 6.5 s.

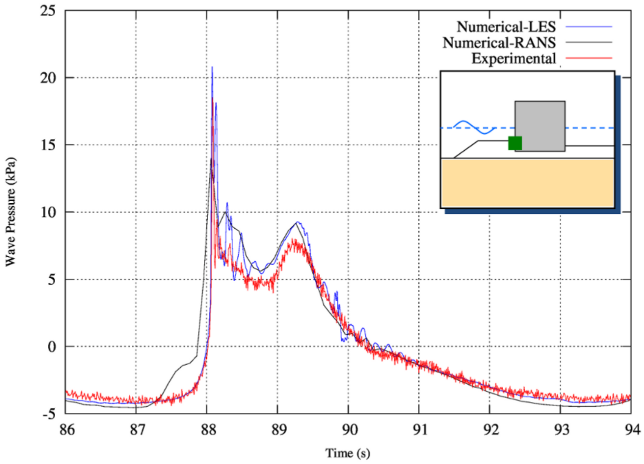

Figure 3.23: Comparison of turbulence modelling effect; wave pressure on the caisson breakwater (channel No. 57) for a regular breaking wave of height 0.7 m. and period 6.5 s.

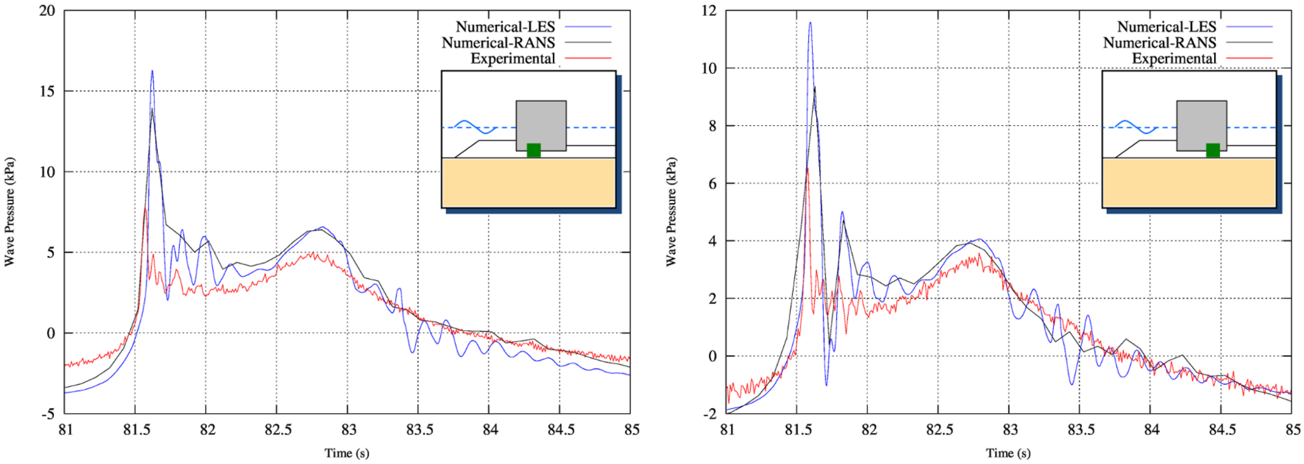

(a) Pressure transducer 59

(b) Pressure transducer 60

Figure 3.24: Comparison of turbulence modelling effect; uplift pressure on the caisson breakwater for a regular breaking wave of height 0.7 m. and period 6.5 s.

d. Effect of fluid compressibility on breaking wave impact

The effect of fluid compressibility in the simulation is obvious in locations where air is present. Although, pure water can be safely considered as incompressible, water-air mixtures especially with high air content cannot be considered incompressible in case of breaking wave impact. As shown in Fig. 3.25, when a wave breaks just in front of the structure, a cushion of air is trapped between the wave front and the wall. This air cushion increases the air content in the water body hitting the wall. The vertical rise of water is subsequently followed by the fall of a splash of water. This splash is a mixture of water and air, which also increases the air content in the water body in front of the caisson.

In Fig. 3.25, the development of a high air content is shown by tracking the colour of phases: Blue for water and light grey for air. The water-phase velocity vectors are plotted in red to provide a description of the development of breaking wave attack.

From the pressure calculated with and without considering fluid compressibility, Fig. 3.26, it is obvious that considering fluid compressibility enhances the result of pressure post impact. After the breaking wave impact, the pressure oscillates due to oscillation of trapped air cushion volume. The oscillation is absent in case the fluid compressibility is neglected.

The pressure oscillation from the numerical model has higher amplitude than oscillations recorded from the GWK experiments. This could be due the inability of the multiphase CFD model of properly reproducing the escape of air bubbles from the water phase, which may in turn accumulate the air content in the water-air mixture in front of the wall. Simulation of the air phase as a dispersed phase in the water phase (simulating inter-phase momentum transfer) can enhance the simulation of behaviour of air bubbles in water and hence may enhance the simulation of pressure oscillation after impact.

Supporting the aforementioned explanation are the results from studying depressurized wave impact (Lugni et al., 2010a,b). In a depressurized environment, the trapped air does not escape the surrounding water in the same manner like under normal conditions. In Fig. 3.27, typical results for pressure on a wall exerted by a breaking wave in depressurized conditions are shown. The results show obvious pressure oscillations after the impact (region *B*) that is similar to results calculated by the numerical model at hand.

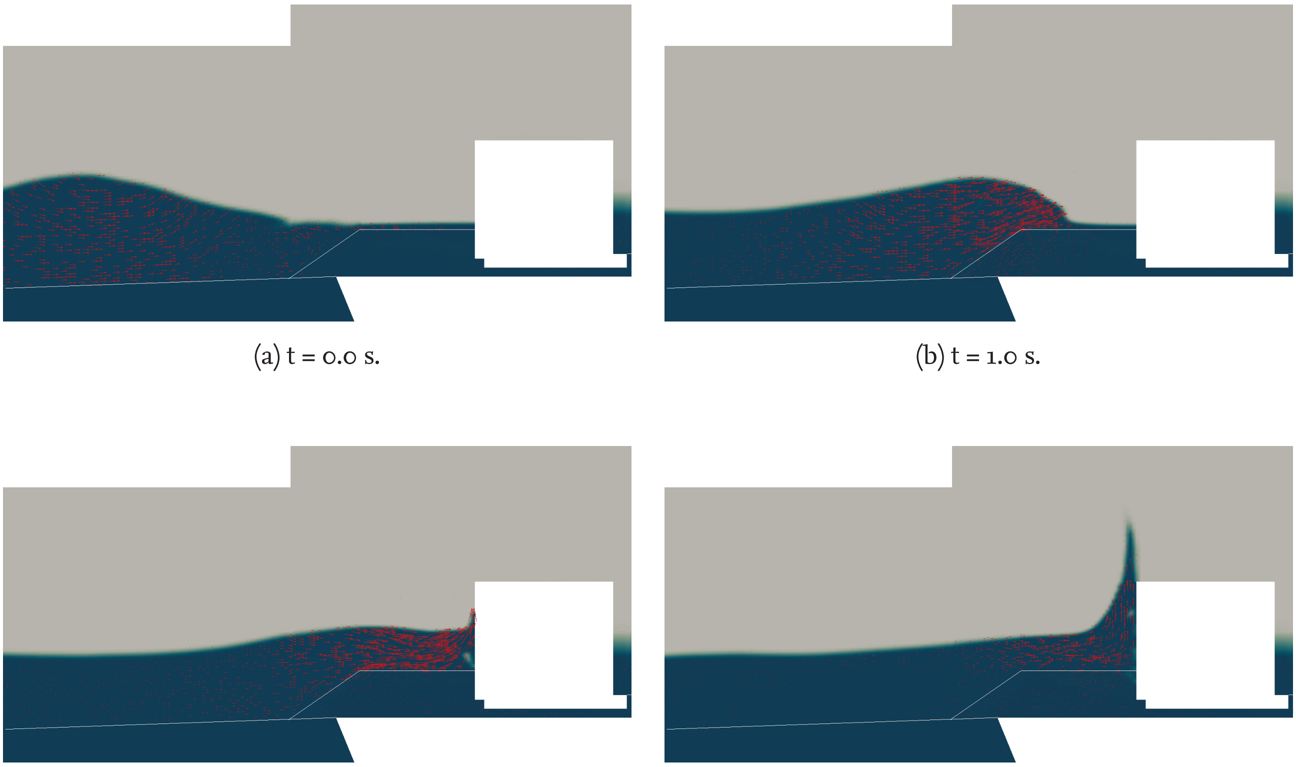

(a) t = 0.0 s.

(b) t = 1.0 s.

(c) t = 1.5 s.

(d) t = 2.0 s.

(e) t = 2.5 s.

(f) t = 3.0 s.

Figure 3.25: Breaking wave hitting the caisson breakwater (value of the VOF function) height 0.7 m. and period 6.5 s. with velocity vectors

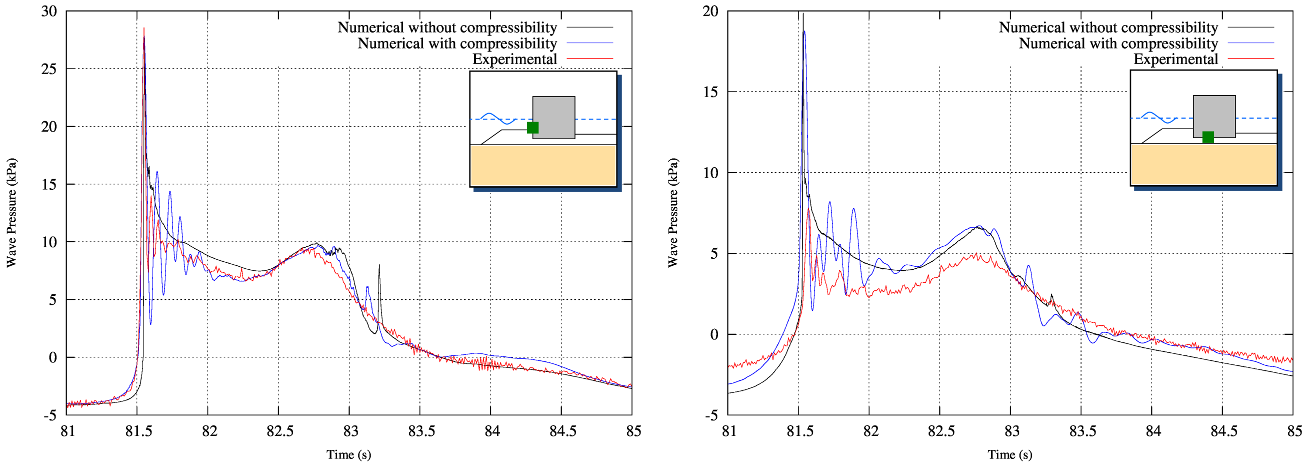

(a) Wave pressure; transducer No. 56

(b) Uplift pressure; transducer No. 59

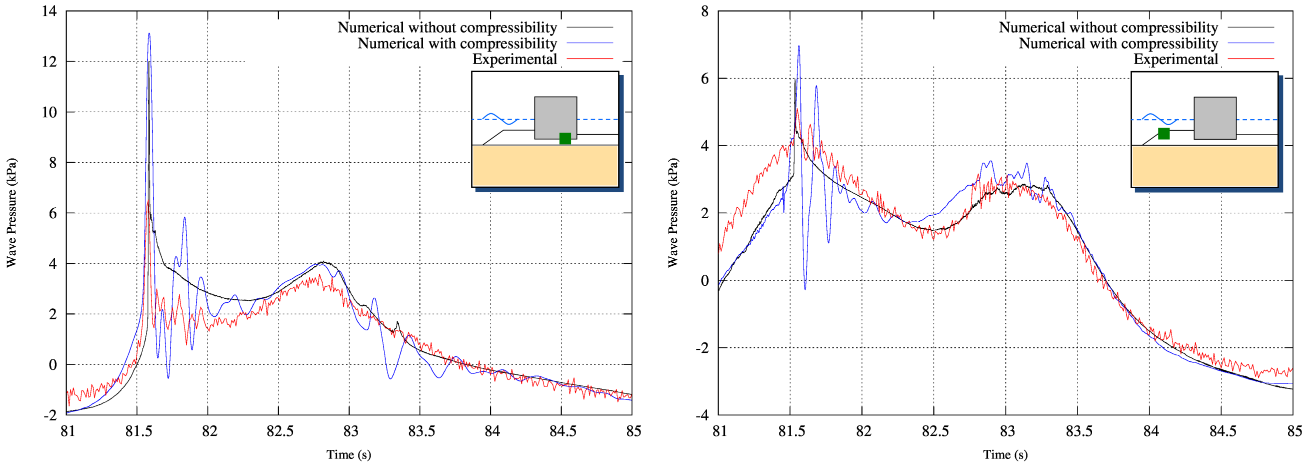

(c) Uplift pressure; transducer No. 60

(d) Pore pressure; transducer No. 62

Figure 3.26: Significance of fluid compressibility; wave/uplift pressure from a regular breaking wave of height 0.7 m. and period 6.5 s.

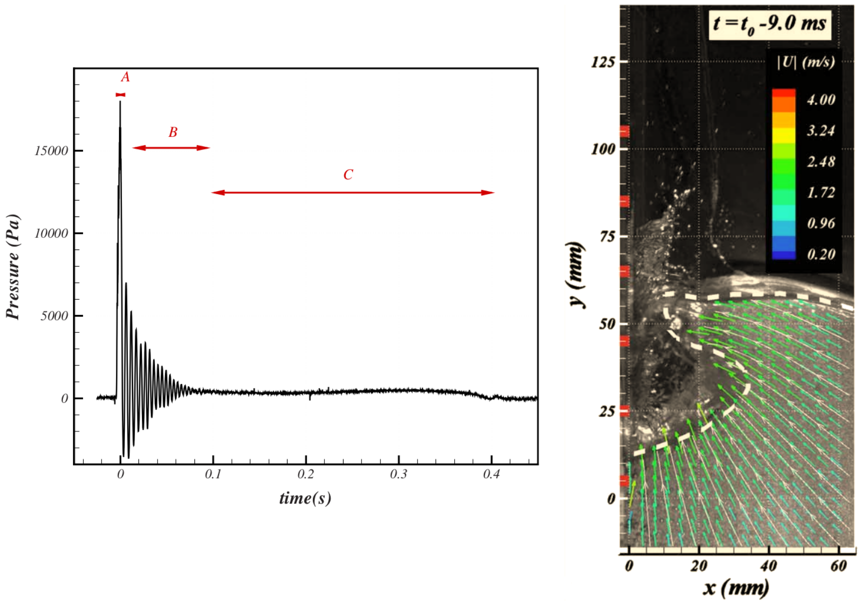

Figure 3.27: Depressurized wave impact (Lugni et al., 2010a,b)

e. Total wave loads on the caisson breakwater

The total wave loads exerted on caisson breakwaters are the resultant vertical force, the resultant horizontal force and resulting moment acting at the center of gravity of the caisson due to both vertical and horizontal forces. The latter are directly obtained from the integration of the wave-induced pressure at the caisson boundaries. Tangential forces and (consequently) exerted moments, caused by fluid viscous effects, are not considered in the calculations as they are negligible in comparison to the forces and moments caused by the fluid exerted pressures.

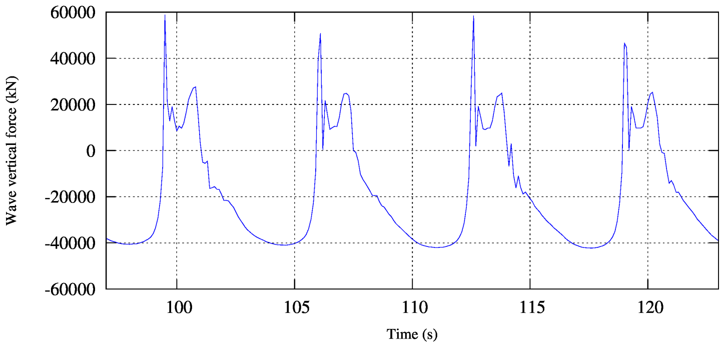

(a) Vertical force

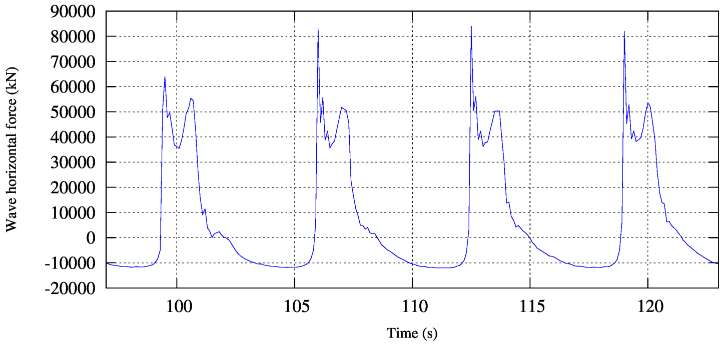

(b) Horizontal force

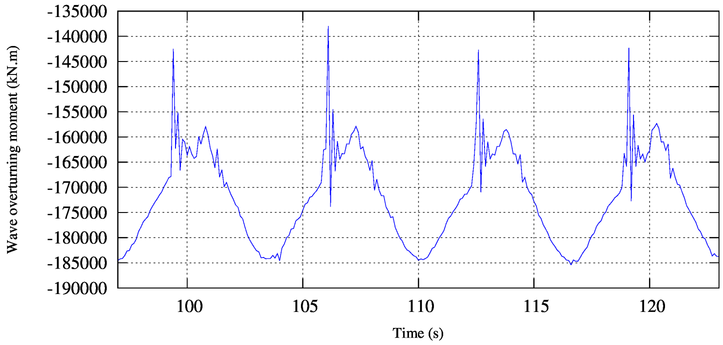

(c) Moment

Figure 3.28: Forces and moment exerted on a caisson breakwater from regular breaking waves with height 0.7 m. and period 6.5 s.

The forces time history is considered for developing the simplified model that is introduced later in this study. An example of forces time history for the case of regular waves of $H = 0.7$ m. and $T = 5.5$ s. is presented in Fig. 3.28. Considering the fluid compressibility enhances the produced forces time history by reproducing the oscillations in force time history after the wave impact. Fig. 3.29 shows a colour map for the dynamic pressure map at the impact multiplied by the VOF function.

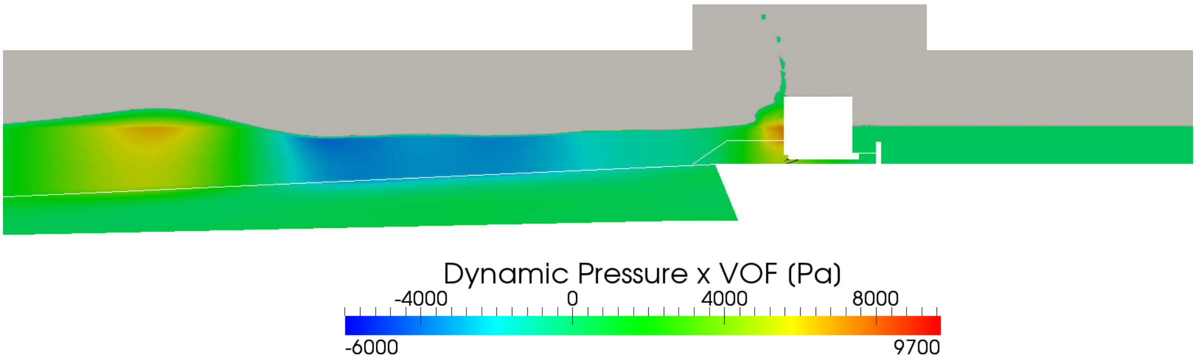

Figure 3.29: Dynamic fluid pressure (multiplied by the VOF function value) for water phase of a test of regular breaking waves with height 0.7 m. and period 6.5 s.

3.3 Remarks on the CFD Model

In this chapter, the development of a CFD model (*waveVolAvgPorousInterFoam*) for the study of monolithic breakwaters is presented. The model is an extension of OpenFOAM incompressible Eulerian multiphase VOF solver. The original porous media treatment in OpenFOAM was modified according to the volume-averaged model from Liu et al. (1999), with the inclusion of several seepage laws that account for viscous, inertial, transitional and transient flow. The fluid compressibility was introduced in a simplified manner by considering linear elastic changes in fluid volume rather than its density (to reduce computational time). The fluid bulk modulus is computed according to the phase fraction value at each cell. The implementation of fluid compressibility has succeeded in reproducing the oscillation of pressure/force after initial breaking wave impact.

The model is validated against the benchmark test for dam break through a vertical porous barrier. For this test, different seepage and turbulence models are compared. Additionally, the hydrodynamic model is used successfully to reproduce the large-scale GWK tests, for non-breaking, slightly breaking and breaking waves.

Essential conclusions of using the hydrodynamic model for simulating caisson breakwater subject to wave attack are:

- The difference among different seepage models implemented for modelling porous media resistance to water flow is small, as observed in the dam break through a porous column validation case.
- The hydrodynamic model can successfully reproduce the maximum horizontal impact. Nevertheless, the uplift force amplitude is overestimated by numerical computations. This is due to the effect of caisson rocking motion on the uplift pressure and due to the existence of a deformable impermeable sheet underneath the rubble foundation, which is simulated as a non-deformable entity (similarly is the underlying sand foundation) in the CFD model.
- Turbulence modelling is introduced via the turbulence eddy viscosity concept. Using OpenFOAM Reynolds-Averaged turbulence model (k-ω-SST) can dampen water waves for long domains (e.g. the GWK). However, using a Large-Eddy-Simulation LES turbulence model, has produced better results as validated against experimental results (wave impact) with acceptable speed-up of simulations against omitting turbulence modelling.
- A multiphase hydrodynamic model can reproduce the effects of entrapped/entrained air on the breaking wave impact only if the fluid compressibility is considered. By considering a linear elastic fluid compressibility model (bulk modulus calculated according to the VOF function) that considers only volume change rather than density change, the pressure fluctuations after the wave impact was reproduced successfully by the numerical model.

Based on the results of this model, the following is suggested for future research:

- The numerical simulation of entrapped/entrained air effect on breaking wave impact may be further enhanced by considering a computational model that treats air as a dispersed phase. In this manner, the effects of the simulated air compressibility will be more realistic
- Although, introducing two-way coupling between the CFD and the CSD models will be more computationally expensive, it will yield far better results overall and especially for uplift loads on caisson breakwaters. Further, better validation against the GWK test configurations (e.g. impermeable sheet) can be achieved

4 Hydro-Geotechnical (CSD) Model

In this chapter, the development of a computational structural dynamics model (CSD) for the problem of wave-caisson-soil interaction is presented. The model is developed, similar to the hydrodynamic model, utilizing the finite volume method through the OpenFOAM toolbox.

First, the model development is presented with a discussion of the interaction between the pore fluid and the solid skeleton of the soil as a porous medium, an outline of the different formulations the governing equations and their discretization, multi-material interface correction, soil-structure interaction, solver algorithm, plasticity modelling and organisation of the newly developed *geotechFoam* solver. Further, the validation of the model is presented using several benchmark problems as well as physical experiments. Finally, a summary and concluding remarks are given.

4.1 CSD Model Development

The model is developed using OpenFOAM. Although OpenFOAM is essentially a CFD toolbox, it provides a general framework for computational continuum mechanics. The flexibility provided by OpenFOAM for numerical model developers stems from its advanced programming features like the high use of modularity/abstraction that enables convenient reuse of developed code.

A new solver named *geotechFoam* is developed to model strong pore fluid-solid skeleton interaction for the soil foundation as well as to model strong soil-structure interaction. These interactions are considered at the governing equations level (monolithic coupling).

In this model, three formulations of Biot's governing equations are implemented: (i) the fully coupled-fully dynamic formulation, in which the accelerations of both pore fluid and solid skeleton are included, (ii) a dynamic formulation, in which the acceleration of the solid skeleton is included but only the local (temporal) acceleration of the pore fluid is considered (the convective acceleration of the pore fluid is neglected) and (iii) the $u - p$ approximation (also referred to as the partially dynamic formulation), in which only the acceleration of the solid skeleton is included (pore fluid acceleration is completely neglected). Additionally, a switch is provided to neglect the solid-pore fluid coupling and to solve only the equation of motion.

Soil constitutive modelling for the sand foundation is based on a nested yield surfaces elastoplastic model utilizing the Drucker-Prager failure criterion. An associated deviatoric flow rule is considered, whereas a non-associated flow rule is considered for the volumetric component of strain. A pure kinematic hardening rule is considered for the multiple yield surfaces.

Soil-structure interaction is accounted for by implementing a frictional non-adhesive contact model. This allows for modelling separation/rejoining and slip of soil structure adjacent faces. The model is established to regenerate experiments from the large wave flume (GWK). The wave load is considered by coupling the structural model with the hydrodynamic model in Chapter 3.

4.1.1 Pore fluid-solid skeleton interaction

Conventional geotechnical theoretical models consider soil to be either in a fully drained ($\delta p = 0$) or a fully undrained ($\delta p = \delta\sigma$) condition, and hence treating soil as a single-phase continuum. Nevertheless, modelling time-dependent drainage is essential for modelling the interaction between the pore fluid and the solid skeleton of the soil. Moreover, soil needs to be modelled as a multi-phase material to realize such a strong interaction and to model, properly, relevant soil phenomena such as liquefaction and cyclic mobility. Analysis of porous media is quiet a novel physical notion introduced by Biot (1941) to solve consolidation of soils, based on Terzaghi's work. Nevertheless, his theory is, currently, widely utilized in several Engineering disciplines including biomechanical research.

An approximation to avoid the modelling of fluid-soil skeleton interaction is the use of *empirical models*, which are simplified models that treat a porous medium as single-phase medium. The generation of excess pore pressure and strain are related to the number of load cycles until complete liquefaction is reached. These empirical relations are derived using triaxial and simple shear tests for soils. These models are used with densification soil constitutive models, which treat effects of cyclic loading (densification) as an addition to conventional elastoplastic constitutive models suitable for modelling monotonic loading. These combined models (empirical relations + densification models) are implemented in undrained formulations (no dissipation of pore pressure) or in a Biot consolidation model, by which the pore pressure dissipation is accounted for. The pore pressure dissipation can also be accounted for in a consolidation equation relating to the soil characteristic drainage period. The residual pore pressure is then obtained as the subtraction of dissipation from generation of pore pressure. The main principle behind the densification models is to consider a damage parameter that describes the reduction of soil strength due to cyclic loading. Nevertheless, the constitutive model is basically more suitable for monotonic loading.

For the modelling of porous media as multi-phase continua, two approaches are generally followed to start formulation from: (i) A *macroscopic* level approach and (ii) a *microscopic* one. The work of Biot (1941) and its extensions belong to the first category. This is also the case for mixture theory formulations, which in practice offer no practical advantage over Biot's formulation (Detournay and Cheng, 1993). The macroscopic approach adopts the principle of overlapping continua that fills the total volume of matter, (Fig. 4.1). On the other hand, averaging theories (hybrid mixture theories), transforming the porous media into overlapping equivalent continua with reduced densities obtained through volume fractions, belong to approaches starting with a microscopic viewpoint (Lewis and Schrefler, 1998). An extensive discussion on the modelling theories of porous media and their history can be found in the literature (e.g. Lewis and Schrefler (1998); Zienkiewicz et al. (1999); Boer (2005)). Regardless of the method used for the derivation of the equations, based on appropriate assumptions and correct application, they all yield the same governing equations (Zienkiewicz et al., 1999; Lewis and Schrefler, 1998).

The seabed can be considered as a three-phase medium; the solid phase (skeleton continuum), the water phase and the air phase (fluid continua). For simplicity, one may consider the seabed to have a single-phase fluid continuum; i.e. only water (fully saturated). For many purposes, the effect of air bubbles inside pore water can be implicitly introduced as a reduced fluid bulk modulus (compressible pore fluid). Nonetheless, the kinematics of the involved continua are, in fact, similar to kinematics of a single continuum.

If the soil *solid to fluid* interaction is neglected, e.g. the solid phase is considered as a fixed (non-deformable) matrix, the pore pressure can be separately calculated in time and space domains (e.g. using the VARANS model or a diffusion equation) so that the stress field equilibrium can be achieved using calculated values. This approach is referred to as the uncoupled approach (Wang, 2000).

Basically, the difference between considering a soil medium as a single-phase or as a bi-phase continuum is the necessity to introduce interaction terms to the governing equations of both continua. In Fig. 4.1, the general framework of poromechanics, from a macroscopic point of view, is outlined. A compatibility condition is imposed by the simultaneous solution of system equations (strong coupling).

The complete governing equations can be conveniently implemented in an explicit scheme (e.g. Hwang et al. (1971); Ghaboussi and Wilson (1972); Chan (1988)). For the fully coupled approaches, approximations can be introduced based on an assumption of the dynamicity of the modelled system in order to reduce

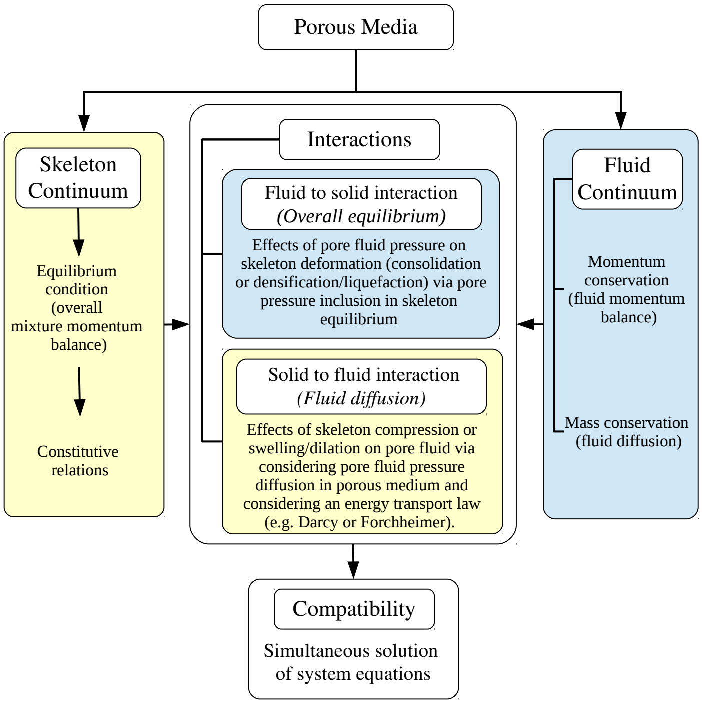

Figure 4.1: Framework of poromechanics from a macroscopic point of view

computational expense and model complexity. A fully dynamic solution considers inertial effects of both solid and fluid phases (e.g. (Ülker et al., 2012)). A partially dynamic approach considers inertial effects of the solid phase only (Zienkiewicz et al., 1980; Elgamal et al., 2003). A quasi-static approach neglects all inertial terms (Biot, 1941; Zhang et al., 2011; Liu and García, 2006). Fig. 4.2 illustrates the framework for theoretical geotechnical modelling from a macroscopic point of view. Boxes highlighted in orange indicate the path chosen for this study, while the box highlighted in yellow indicates the method included for comparison.

Zienkiewicz et al. (1980) analysed the validity of different simplifications of the governing equations, alongside the consideration of fully drained or undrained soil behaviour, to model soil accurately. They considered a one-dimensional system for all cases under an applied periodic surface load, for which exact solutions of the problem can be derived. The solutions were compared against the complete formulation and validity regions of these solutions were outlined using two non-dimensional parameters.

4.1.2 Governing equations

OpenFOAM has a transient solver of linear-elastic, small-strain deformation of a solid body, with optional thermal diffusion/stresses (*solidDisplacementFoam*). This solver was the basic start for the new solver (*geotechFoam*). The developed solver is capable of geotechnical analyses by modification of the solid momentum balance equation (equation of motion) and adding new equations for pore fluid pressure and velocity based on the *icoFoam* solver, with required interaction terms. The thermal capabilities of the original solver have been removed as they are irrelevant to geotechnical analysis in this study.

a. Fully dynamic formulation

The fully coupled-fully dynamic governing equations of porous media (Biot, 1962) are arranged in the manner proposed by (Zienkiewicz et al., 1999). An overall equilibrium equation (momentum balance) for the solid-fluid mixture, considering a control volume $dV = dx \cdot dy \cdot dz$, can be written in a Lagrangian framework as proposed by (Zienkiewicz et al., 1999):

$$\nabla \cdot \sigma - \rho \frac{\partial^2 \mathbf{u}}{\partial t^2} - c \frac{\partial \mathbf{u}}{\partial t} - \rho_f \left(\frac{\partial \overline{\mathbf{U}}}{\partial t} + \underline{\overline{\mathbf{U}} \cdot \nabla \overline{\mathbf{U}}} \right) + \rho \mathbf{b} = 0 \tag{4.1}$$

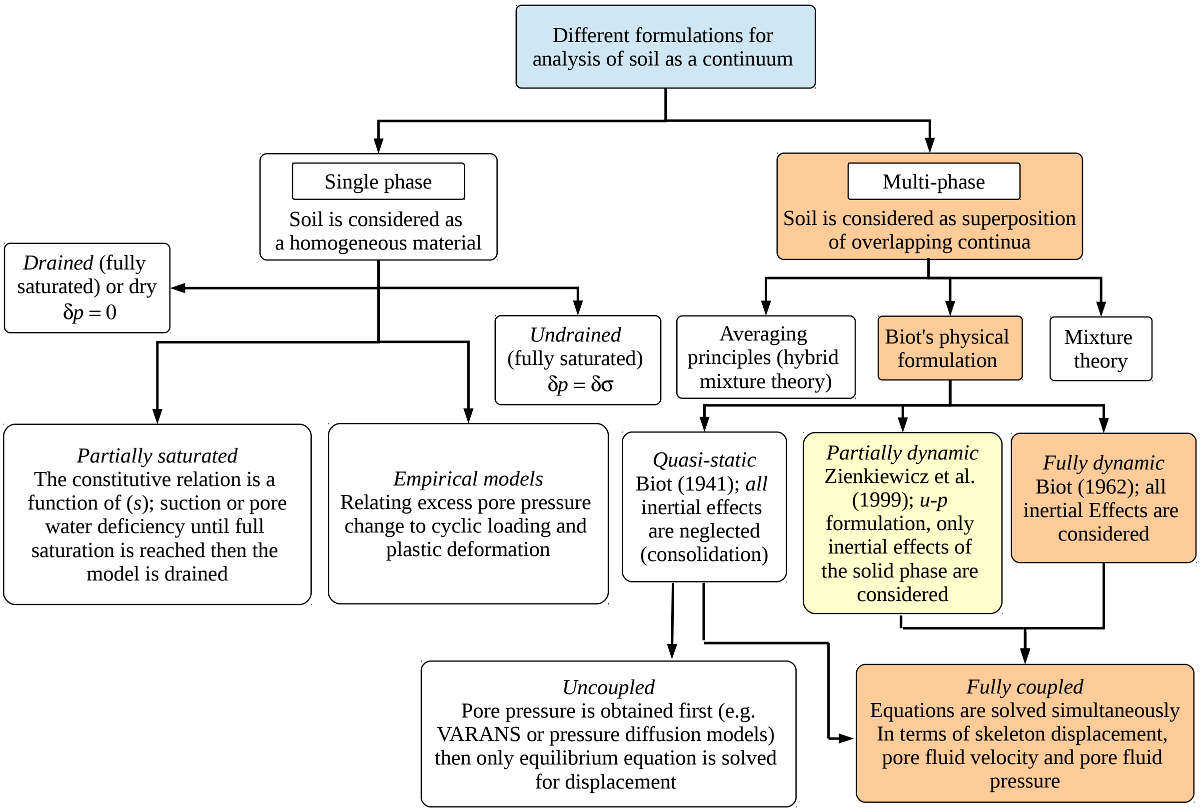

Figure 4.2: Different formulations for geotechnical theoretical modelling from a macroscopic point of view: Boxes highlighted in orange indicate the path chosen for this study, while the box highlighted in yellow indicates the method included for comparison

Where σ is the total stress tensor, $\mathbf{u}$ is the displacement vector and $\overline{\mathbf{U}}$ is the average (Darcy's) velocity of the percolating fluid, c is the damping coefficient. The fourth term in the Left Hand Side (LHS) of the above equation represents pore fluid acceleration relative to the solid phase. The underlined part represents convective pore fluid acceleration. Further, ρ_f is the density of the fluid, $\mathbf{b}$ is the body force per unit mass tensor (mostly gravity) and ρ is the (fully saturated) density of the solid-fluid mixture defined as:

$$\rho = n\rho_f + (1-n)\rho_s \tag{4.2}$$

Where ρ_s is the density of the solid particles and n is the porosity. In Eq. 4.1, the stress is defined in a generic incremental fashion that permits later implementation of any material constitutive model as:

$$\sigma = \sigma' - p\mathbf{I} \tag{4.3}$$

and:

$$d\sigma' = \mathbf{E} : d\varepsilon^e \tag{4.4}$$

σ' is the effective stress tensor, $\mathbf{I}$ is the identity tensor. Unlike in conventional soil mechanics, tensile stresses are considered positive in continuum mechanics and therefore the relation between total and effective stresses is different from that found in classical soil mechanics textbooks. $\mathbf{E}$ is the fourth order tangent (elastic stiffness modulus) tensor. Generalised Hooke's law is valid for the incremental stress-elastic strain ($d\varepsilon^e$) relationship. Strain-displacement relationship is considered for the assumption of small-strain (further extension to large strain conditions is feasible) as:

$$\varepsilon = \frac{1}{2}\left(\nabla \mathbf{u} + (\nabla \mathbf{u})^T\right) \tag{4.5}$$

Another equation is required for the momentum balance of the fluid phase alone considering the same control volume in an Eulerian framework and assuming that the solid phase is the reference (the considered element moves with the solid phase) (Zienkiewicz et al., 1999):

$$\rho_f \left(\frac{\partial \overline{\mathbf{U}}}{\partial t} + \underline{\overline{\mathbf{U}} \cdot \nabla \overline{\mathbf{U}}} \right) / n = -\nabla p - \rho_f \frac{\partial^2 \mathbf{u}}{\partial t^2} + \rho_f \mathbf{b} - \mathbf{S} \tag{4.6}$$

where p is the pore (fluid) pressure and $\mathbf{S}$ is a sink term representing the viscous drag force vector (resistance). The viscous drag force can be defined according to the Darcy seepage law assuming an isotropic medium as:

$$\mathbf{S} = \frac{\overline{\mathbf{U}} \rho_f g}{k} \tag{4.7}$$

where k is the isotropic hydraulic conductivity (m/s), originally a symmetric permeability tensor reduced to a scalar for isotropic permeability. The seepage relation can be extended to a Darcy/Forchheimer seepage law (or any other porous flow resistance model).

Finally, mass conservation of the fluid flow is achieved as (Zienkiewicz et al., 1999):

$$\nabla \cdot \overline{\mathbf{U}} + \frac{\partial \varepsilon_v}{\partial t} + \frac{1}{Q}\frac{\partial p}{\partial t} = 0 \tag{4.8}$$

Where $\varepsilon_v = tr(\boldsymbol{\varepsilon})$ is the volumetric strain of the solid skeleton, and:

$$\frac{1}{Q} = \frac{n}{K_f} \tag{4.9}$$

$$\frac{1}{K_f} = \frac{S}{K_w} + \frac{1-S}{K_a} \tag{4.10}$$

where K_f, K_w (2200 MPa) and K_a (under atmospheric pressure = 0.101 MPa) are the bulk moduli for pore fluid, pure water and air, respectively. $S = {}^{V_w}/_{V_v}$ is the degree of saturation, V_w and V_v are the volumes of pore water and voids, respectively. Considering the entrapped air content of 1% (e.g. $S = 0.99$) produces a bulk modulus (9.95 MPa) roughly 200 times less than the bulk modulus of pure water (Verruijt and Van Baars, 2007).

The mass balance of fluid flow is achieved by equalizing the flow divergence to the change in pore volume due to: (1) Change in skeleton volumetric strain ($d\varepsilon_v$); (2) Pore fluid compression ($n\,{}^{dp}/_{K_f}$); (3) Change in solid grains strain due to change in pore pressure $(1-n)\,{}^{dp}/_{K_s}$; (4) Change in solid grains strain due to change in intergranular effective contact stresses $[-{}^{K}/_{K_s} \cdot (d\varepsilon_v + {}^{dp}/_{K_s})]$. In the former equation, K is the average bulk modulus of the solid skeleton, K_s is the bulk modulus of the solid grains material. Volume changes caused by compression of the solid particles are neglected because of their insignificance compared to volume changes caused by rearrangement of solid particles. Terms that correspond to strain due to thermal changes are irrelevant to the study and hence are not considered.

As the soil strain is mostly due to the rearrangement of solid grains rather than to the compression of the solid grains themselves, it is convenient in all the aforementioned equations to consider rate of change in porosity equal to rate of change in volumetric strain (Coussy, 2004):

$$\frac{\partial n}{n} = \frac{\partial \varepsilon_v}{\varepsilon_v} \tag{4.11}$$

As change in porosity is generally accompanied by change in permeability, it is possible to retrieve a relationship between porosity and permeability for a specific soil sample, and consequently update permeability of the soil foundation according to changes in volumetric strain. Nevertheless, due to the unavailability of such relationship (for the tested seabed soil), the permeability is considered constant throughout the simulation.

b. The $u-p$ approximation

To reduce the computational effort, one can neglect the pore fluid acceleration relative to the solid phase, $\frac{\partial\overline{\mathbf{U}}}{\partial t}=0$ (Zienkiewicz et al., 1999), the equations reduce then to two sets of equations (merging equations 4.6 and 4.8), the solid skeleton momentum balance and pore fluid continuity become (Zienkiewicz et al., 1999):

$$\nabla\cdot\sigma-\rho\frac{\partial^2\mathbf{u}}{\partial t^2}-c\frac{\partial\mathbf{u}}{\partial t}+\rho\mathbf{b}=0 \tag{4.12}$$

$$\nabla\cdot\left(\frac{k}{\rho_f g}\left(-\nabla p-\rho_f\frac{\partial^2\mathbf{u}}{\partial t^2}+\rho_f\mathbf{b}\right)\right)+\frac{\partial\varepsilon_v}{\partial t}+\frac{1}{Q}\frac{\partial p}{\partial t}=0 \tag{4.13}$$

where Q is as defined in Eq. 4.9.

This approximation to the solution, the $u-p$ formulation, is accurate for static/quasi-static as well as dynamic cases with relatively low frequencies. Nevertheless, for high frequency oscillations the solution would suffer inaccuracies. Although the pore fluid velocity has been purged from the governing equations, the pore fluid velocity vector field can be calculated explicitly as:

$$\overline{\mathbf{U}}=\frac{k}{\rho_f g}\left(-\nabla p-\rho_f\frac{\partial^2 u}{\partial t^2}+\rho_f\mathbf{b}\right) \tag{4.14}$$

Because the momentum balance equation is not (explicitly) solved for the fluid phase, the submerged density of the soil should be considered instead of the fully saturated density to account for fluid uplift pressures on the solid phase grains (buoyancy effect). The density becomes:

$$\rho=(1-n)\left(\rho_s-\rho_f\right) \tag{4.15}$$

c. The $u-u_w$ approximation

In Zienkiewicz et al. (1999), another formulation is introduced (for compressible pore fluids) by considering the approximate total (not relevant to skeleton) true (intrinsic, i.e. not averaged) pore fluid displacement ($\mathbf{u_w}$) instead of fluid velocity as:

$$\mathbf{u_w}=\mathbf{u_w^r}+\mathbf{u} \tag{4.16}$$

where $\mathbf{u}$ is the displacement of the solid skeleton and $\mathbf{u_w^r}$ is the (intrinsic) water displacement relative to the solid skeleton, defined as:

$$\frac{\partial\mathbf{u_w^r}}{\partial t}=\frac{\overline{\mathbf{U}}}{n} \tag{4.17}$$

The pore pressure can be expressed as:

$$p=-Q\left(tr\left(\varepsilon\right)+n\nabla\cdot\mathbf{u_w^r}\right) \tag{4.18}$$

The system of equations is reduced to two equations as in (Zienkiewicz et al., 1999):

$$\begin{aligned}\nabla\cdot\sigma'+(1-n)^2Q\nabla\left(\nabla\cdot\mathbf{u}\right)+n\left(1-n\right)Q\nabla\left(\nabla\cdot\mathbf{u_w}\right)\\-\left(1-n\right)\rho_s\left(\mathbf{b}-\frac{\partial^2\mathbf{u}}{\partial t^2}\right)+\frac{n^2}{k\rho_f\mathbf{b}}\left(\frac{\partial\mathbf{u_w}}{\partial t}-\frac{\partial\mathbf{u}}{\partial t}\right)=0\end{aligned} \tag{4.19}$$

$$\begin{aligned} n\left(1 - nQ\nabla\left(\nabla \cdot \mathbf{u}\right) + n^2 Q \nabla\left(\nabla \cdot \mathbf{u_w}\right)\right. \\ + n\rho_f \left(\mathbf{b} - \frac{\partial^2 \mathbf{u_w}}{\partial t^2}\right) - \frac{n^2 \rho_f \mathbf{b}}{k}\left(\frac{\partial \mathbf{u_w}}{\partial t} - \frac{\partial \mathbf{u_w}}{\partial t}\right) = 0 \end{aligned} \tag{4.20}$$

This formulation is not applicable for long-term studies leading to steady state conditions, as the water displacement $\mathbf{u_w}$ then increases indefinitely (Zienkiewicz et al., 1999). For all the aforementioned formulations, reducing the number of governing equations to be solved implies penalties. The momentum balance for the fluid phase is accounted for in the continuity equation rather than being solved. This causes the absence of hydrostatic pressure ($\rho_f gh$) inside the domain (only excess pore pressure is calculated). To overcome this setback, the submerged (rather than the saturated, Eq. 4.15 instead of Eq. 4.2) density is considered for all materials positioned underneath the ground water table.

d. Biot's original quasi-static model

Biot's original model for soil as porous media (Biot, 1941) was developed for quasi-static conditions and for soil as elastic media. Hence, the model is often referred to as the poro-elastic model. Nevertheless, Biot's quasi-static model can be generalized for other soil constitutive models in the same manner adopted in the aforementioned formulations.

By completely neglecting solid and fluid inertial effects, the solid skeleton momentum balance equation reads:

$$\nabla \cdot \sigma + \rho \mathbf{b} = 0 \tag{4.21}$$

The pore fluid continuity equation reads:

$$\nabla \cdot \left(\frac{k}{\rho_f g}\left(-\nabla p + \rho_f \mathbf{b}\right)\right) + \frac{\partial \varepsilon_v}{\partial t} + \frac{1}{Q}\frac{\partial p}{\partial t} = 0 \tag{4.22}$$

Biot's quasi-static model is more suitable for static problems. The velocity vector field can be calculated explicitly as:

$$\overline{\mathbf{U}} = \frac{k}{\rho_f g}\left(-\nabla p + \rho_f \mathbf{b}\right) \tag{4.23}$$

In a sense, Biot's original quasi-static model can be thought of as a further simplification of the $u - p$ approximation; where all accelerations are neglected (for both solid and fluid phases).

4.1.3 Discretisation of the computational domain

Discretisation of the computational domain is done in two folds; First, the time duration of the simulation is divided into small intervals (Δt), and hence the transient solution marches time steps. Further, the spatial domain is then filled with non-overlapping control volumes/cells (CVs). The CVs are polyhedra that has shared faces with other CVs (i.e. internal faces). Some CVs have some faces that are not shared with other CVs (i.e. boundary faces). The computational mesh (i.e. CVs) is arbitrarily unstructured, which means different CV shapes can be conveniently combined in the same mesh giving great flexibility in mesh generation. Additionally, unlike the FEM, there is no need for a priori postulate of a topology-dependent shape function.

In Fig. 4.3, a CV of volume V_P is shown. The computations are carried out at the CV centroid P. The CV is fully defined by defining the volume verticies and hence the faces. A shared face (f) with a neighboring CV of centroid (N) has a face area S_f and a unit normal vector $\mathbf{n}_f$. The surface area of a CV (S_P) is the sum of areas of internal (S_f) and boundary faces (S_b), Eq. 4.24.

$$S_P = \partial V_P = \sum_f S_f + \sum_b S_b \tag{4.24}$$

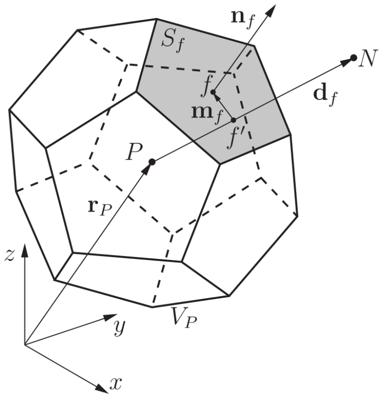

Figure 4.3: Polyhedral control volume (a cell) (Tuković et al., 2013)

4.1.4 Equations discretisation

The finite volume method discretisation utilizes an integral form of the governing equations. Using the Gauss' (divergence) theorem, the fully coupled-fully dynamic governing equations (Eqs. 4.1, 4.6 and 4.8) are expressed as given in Eqs. (4.25, 4.26 and 4.27). In the integral form of the momentum balance equation of the solid-fluid mixture (Eq. 4.25), $\mathbf{q}$ is the mass flux through the face, $\mathbf{q} = S_f \cdot (\rho_f \overline{\mathbf{U}})_f$. The mass flux must satisfy continuity conditions.

$$\begin{aligned} &\oint_{S_P} \mathbf{n}_f \cdot \sigma \, \mathrm{d}S - \int_{V_P} \rho \frac{\partial^2 \mathbf{u}}{\partial t^2} \, \mathrm{d}V - \int_{V_P} c \frac{\partial \mathbf{u}}{\partial t} \, \mathrm{d}V - \int_{V_P} \rho_f \frac{\partial \overline{\mathbf{U}}}{\partial t} \, \mathrm{d}V \\ &\quad - \underline{\oint_{S_P} \mathbf{q} \left(\mathbf{n}_f \cdot \overline{\mathbf{U}} \right) \mathrm{d}S} + \int_{V_P} \rho \mathbf{b} \, \mathrm{d}V = 0 \end{aligned} \tag{4.25}$$

$$\int_{V_P} \frac{\rho_f}{n} \frac{\partial \overline{\mathbf{U}}}{\partial t} \, \mathrm{d}V + \underline{\oint_{S_P} \frac{\mathbf{q}}{n} \left(\mathbf{n}_f \cdot \overline{\mathbf{U}} \right) \, \mathrm{d}S} = - \int_{V_P} \nabla p \, \mathrm{d}V - \rho_f \frac{\partial^2 \mathbf{u}}{\partial t^2} + \int_{V_P} \rho_f \mathbf{b} \, \mathrm{d}V - \int_{V_P} \mathbf{S} \, \mathrm{d}V \tag{4.26}$$

$$\oint_{S_P} \mathbf{n}_f \cdot \overline{\mathbf{U}} \, \mathrm{d}S + \int_{V_P} \frac{\partial \varepsilon_v}{\partial t} \, \mathrm{d}V + \int_{V_P} \frac{1}{Q} \frac{\partial p}{\partial t} \, \mathrm{d}V = 0 \tag{4.27}$$

For the $u - p$ approximation, Eqs. 4.26 and 4.27 are replaced with Eq. 4.28.

$$\oint_{S_P} \left(\frac{k}{\rho_f g} \right)_f \mathbf{n}_f \cdot p \, \mathrm{d}S + \oint_{S_P} \mathbf{n}_f \cdot \left(\rho_f \frac{\partial^2 \mathbf{u}}{\partial t^2} - \rho_f \mathbf{b} \right) \mathrm{d}S - \int_{V_P} \frac{\partial \varepsilon_v}{\partial t} \, \mathrm{d}V - \int_{V_P} \frac{1}{Q} \frac{\partial p}{\partial t} \, \mathrm{d}V = 0 \tag{4.28}$$

The governing equations are solved in a segregated manner. In this approach the governing equations are uncoupled iteration-wise. Each equation is solved for one variable and terms from other variables are updated explicitly from the previous iteration. Further, terms of the variable in a governing equation are either *implicitly* or *explicitly* discritised.

The segregated approach extends to each component of the displacement and velocity vectors. The equations are solved separately for each component of an unknown vector and the inter-component coupling is treated explicitly. The result of this approach is well-structured diagonally dominant sparse matrices ideally suited for iterative solvers. The segregated approach is also adopted in original OpenFOAM linear elastic solver for considering thermal stresses (Jasak and Weller, 2000a).

The displacement is calculated from equation 4.1 or 4.21, divided as shown in Eq. 4.29.

$$\begin{aligned}&\underbrace{\rho\frac{\partial^2\mathbf{u}}{\partial t^2}+c\frac{\partial\mathbf{u}}{\partial t}-\nabla\cdot\left(\left(2G+\lambda\right)\nabla\mathbf{u}\right)}_{\text{Implicit}}\\&+\underbrace{\rho_f\left(\frac{\partial\overline{\mathbf{U}}}{\partial t}+\underline{\overline{\mathbf{U}}\cdot\nabla\overline{\mathbf{U}}}\right)-\nabla\cdot\left(\sigma'-\left(2G+\lambda\right)\nabla\mathbf{u}-p\mathbf{I}\right)-\rho\mathbf{b}}_{\text{Explicit}}=0\end{aligned}\tag{4.29}$$

The discretization of the temporal derivatives is calculated using two old-times values of the calculated parameter (Eq. 4.30). This form of discretisation is bounded, but only first-order accurate in time and causes a certain amount of numerical dissipation, dependent on the Courant number (based on the speed of sound). This first-order discretisation ensures boundedness of the differential form of the operator. Other methods of discretisation may cause unphysical stress peaks or even solution instability (Jasak and Weller, 2000a).

$$\int_{V_P}\rho\frac{\partial^2\mathbf{u}}{\partial t^2}\,\mathrm{d}V=\rho\frac{\mathbf{u}\left(t+\Delta t\right)-2\mathbf{u}\left(t\right)+\mathbf{u}\left(t-\Delta t\right)}{\Delta t^2}V_P\tag{4.30}$$

A second-order accurate approximation in space is obtained by assuming a linear variation of a variable (e.g. **u**) over the control volume as illustrated in Eq. 4.31 (Jasak and Weller, 2000a).

$$\mathbf{u}\left(\mathbf{x}\right)=\mathbf{u}_P+\left(\mathbf{x}-\mathbf{x}_P\right)\cdot\left(\mathbf{u}\right)_P\tag{4.31}$$

The volume integrals are evaluated using the mid-point rule (Jasak and Weller, 2000a). For example the body force term is calculated as shown in Eq. 4.32.

$$\int_{V_P}\rho\mathbf{b}\,\mathrm{d}V=\rho_P\mathbf{b}_P V_P\tag{4.32}$$

The divergence of the stress tensor is discretised as shown in Eq. 4.33. The discretisation is summed over internal faces, interfaces between different material zones and boundary faces (Tuković et al., 2013).

$$\oint_{S_P}\mathbf{n}_f\cdot\sigma\,\mathrm{d}S=\underbrace{\sum_f\mathbf{t}_f^n S_f}_{\substack{Internal\\faces}}+\underbrace{\sum_i\mathbf{t}_i^n S_i}_{\substack{Multi-material\\interfaces}}+\underbrace{\sum_b\mathbf{t}_b^n S_b}_{\substack{Boundary\\faces}}\tag{4.33}$$

The traction from the boundary faces is discussed in Sec. 4.1.6 and the traction at different material interfaces is discussed in Sec. 4.1.5. To treat the material stress (traction at faces) as an explicit term is convenient to allow for the introduction of different material constitutive models in the domain. Nevertheless, a discretisation in this manner will result in a system that is at best only marginally convergent. The explicit terms carry more information than their implicit counterparts and the convergence can be achieved only with extensive under-relaxation (slow convergence). An alternative is to use an approach similar to that used by Jasak and Weller (2000a). As illustrated in Eq. 4.34

$$\mathbf{t}=\nabla\cdot\sigma=\underbrace{\nabla\cdot\left(\left(2G+\lambda\right)\nabla\mathbf{u}\right)}_{\text{Implicit}}-\underbrace{\nabla\cdot\left(\sigma'-p\mathbf{I}\right)+\nabla\cdot\left(\left(2G+\lambda\right)\nabla\mathbf{u}\right)}_{\text{Explicit}}\tag{4.34}$$

The face normal derivative of displacement (the Div-Grad term) is discretised two times in Eq. 4.34, implicitly and explicitly, implicit discretisation is given in Eq. 4.35, (Tuković et al., 2013).

$$\begin{aligned}\nabla\cdot\left(\left(2G+\lambda\right)\nabla\mathbf{u}\right) &= \oint_{S_P}\left(2G+\lambda\right)_f\mathbf{n}_f\cdot\nabla\mathbf{u}\,\mathrm{d}S\\ &= \left(2G+\lambda\right)_f\left(\underbrace{|\boldsymbol{\Delta}_f|\frac{\mathbf{u}_N-\mathbf{u}_P}{|\mathbf{u}_f|}}_{\text{Orthogonal contribution}}+\underbrace{\left(\mathbf{n}_f-\boldsymbol{\Delta}_f\right)\cdot\left(\nabla\mathbf{u}\right)_f}_{\text{Non-orthogonal contribution}}\right)\end{aligned}\tag{4.35}$$

where $\boldsymbol{\Delta}_f = \frac{\mathbf{u}_f}{\mathbf{u}_f\cdot\mathbf{n}_f}$, Fig. 4.3. The orthogonal contributions are considered implicitly in the equations, whereas the non-orthogonal contributions are considered explicitly (calculated from last iteration's displacement field; it will contribute to the right-hand side of the resultant linear algebraic equation).

Explicit discretisation of the face normal derivative of displacement (the Div-Grad term) is calculated by interpolation gradients, which are given by Eq. 4.36

$$\left(\nabla\mathbf{u}\right)_f = f_x\left(\mathbf{u}\right)_P\left(1-f_x\right)\left(\mathbf{u}\right)_N\tag{4.36}$$

where $f_x = \overline{fN}/\overline{PN}$ is the interpolation factor. The gradient of displacement at cell-centre is calculated using discretised Gauss integral theorem as in Eq. 4.37.

$$\left(\nabla\mathbf{u}\right)_P = \frac{1}{V_P}\sum_f\mathbf{n}_f\mathbf{u}_fS_f\tag{4.37}$$

where $\mathbf{u}_f$ is the face-centre displacement, which is calculated by linear interpolation of the neighbouring cell-centre values. Eq. 4.37 gives a second-order accurate approximation of cell-centre gradient if face-centre displacement is calculated with second-order accuracy. Simple linear interpolation Eq. 4.36 will give second-order approximation of variable in face centre only if line $\overline{PN}$ intersects face f in its centroid. Otherwise, linear interpolation with 'skewness' correction must be applied, that is given in Eq. 4.38.

$$\mathbf{u}_f = f_x\mathbf{u}_P+\left(1-f_x\right)\mathbf{u}_N+\mathbf{m}_f\cdot\left(\nabla\mathbf{u}\right)_f\tag{4.38}$$

where $\mathbf{m}_f$ is the skewness correction vector, which points from the intersection point between the line $\overline{PN}$ and the face f to the face centre, as shown in Fig. 4.3.

The cell-centre displacement gradient needed for skewness and non-orthogonal correction and all other explicit terms in the discretised momentum equation are used from previous outer iteration.

For the $u-p$ approximation, the first term of the explicit part is completely neglected. However, for the fully dynamic solution without pore fluid convection, only the underlined part in Eqs. 4.1 and 4.6 (also underlined in following equations) is ignored. After calculating the displacement of the solid skeleton, the pore pressure is calculated directly for the $u-p$ formulation from the following equation, assuming a scalar (isotropic) value for the permeability:

$$\underbrace{\frac{1}{Q}\frac{\partial p}{\partial t}-\nabla\cdot\left(\frac{k}{\rho_f g}\nabla p\right)}_{\text{Implicit}}+\underbrace{\frac{\partial\left(\nabla\mathbf{u}\right)}{\partial t}+\nabla\cdot\left(\frac{k}{\rho_f g}\left(-\rho_f\frac{\partial^2\mathbf{u}}{\partial t^2}+\rho_f\mathbf{b}\right)\right)}_{\text{Explicit}}=0\tag{4.39}$$

In the case of considering the pore fluid acceleration, other unknown needs to be calculated (namely the pore fluid velocity relative to the solid skeleton, $\overline{\mathbf{U}}$). Nevertheless, using equations 4.6 and 4.8 in their original format presents two problems.

First, the pore pressure cannot be calculated from any of both equations. Therefore, the PISO (Pressure Implicit with Splitting of Operators) algorithm is used to resolve the pressure-velocity coupling of both equations as the case with solving the Navier-Stokes equations for transient CFD solvers (e.g. within the OpenFOAM standard solvers). The pore fluid velocity is first calculated from equation 4.6.

Second, the velocity convection term in Eq. 4.40 is a non-linear term because it implies that velocity is being transported by itself (Jasak, 1996). The convection term is linearised as shown in Eq. 4.41. The fluid mass flux, $\mathbf{q}$, is calculated from velocity from earlier time steps/iterations.

$$\underbrace{\frac{\rho_f}{n}\left(\frac{\partial \overline{\mathbf{U}}}{\partial t} + \underline{\overline{\mathbf{U}} \cdot \nabla \overline{\mathbf{U}}}\right) + \frac{\rho_f g}{k}\overline{\mathbf{U}}}_{\text{Implicit}} + \underbrace{\rho_f \frac{\partial^2 \mathbf{u}}{\partial t^2} - \rho_f \mathbf{b} + \nabla p}_{\text{Explicit}} = 0 \tag{4.40}$$

$$\rho_f\left(\overline{\mathbf{U}} \cdot \nabla \overline{\mathbf{U}}\right) = \oint_{S_P} \mathbf{q}\left(\mathbf{n}_f \cdot \overline{\mathbf{U}}\right) \, \mathrm{d}S = a_P \overline{\mathbf{U}}_P + \sum_N a_N \overline{\mathbf{U}}_N \tag{4.41}$$

where P and N (as mentioned earlier) represent centroids of current CV and neighboring CVs, respectively; where a_P and a_N are functions of $\overline{\mathbf{U}}$.

The underlined term in Eq. 4.40 is not considered when convective acceleration is neglected. Afterwards, to calculate the pressure using the PISO algorithm, the momentum balance equation 4.6 is rewritten in a semi-discretised manner, pressure gradient is not discretised at this stage (Jasak, 1996):

$$a_P \overline{\mathbf{U}}_P = \mathbf{H}\left(\overline{\mathbf{U}}\right) \nabla p \tag{4.42}$$

Equation 4.42 is obtained from the integral form of the momentum equation. The parameters a_P (the central coefficient) and $\mathbf{H}\left(\overline{\mathbf{U}}\right)$ (a vector including the transport part and source part of the momentum balance equation) are functions of the velocity $\overline{\mathbf{U}}$. The velocity from 4.42 is:

$$\overline{\mathbf{U}}_P = \frac{\mathbf{H}\left(\overline{\mathbf{U}}\right)}{a_P} - \frac{1}{a_P}\nabla p \tag{4.43}$$

Substituting the velocity from Eq. 4.43 into the continuity equation, Eq. 4.8:

$$\underbrace{\nabla \cdot \left(\left(\frac{1}{a_P}\right)_f \nabla p\right) - \frac{1}{Q}\frac{\partial p}{\partial t}}_{\text{Implicit}} \underbrace{- \frac{\partial\left(\nabla \mathbf{u}\right)}{\partial t} - \nabla \cdot \left(\frac{\mathbf{H}\left(\overline{\mathbf{U}}\right)}{a_P}\right)_f}_{\text{Explicit}} = 0 \tag{4.44}$$

The parameters $\left(\frac{1}{a_P}\right)_f$ and $\left(\frac{\mathbf{H}\left(\overline{\mathbf{U}}\right)}{a_P}\right)_f$ are face interpolates at cell faces. Eq. 4.44 is solved to get the pore pressure.

The segregated approach provides a convenient approach for introducing several ways for approximating the governing equations. In this manner, two approximations are compared to the fully dynamic equations; the $u - p$ approximation, in which the fluid acceleration is neglected. Another approximation considers neglecting only the convective part of the pore fluid accelerations.

The plasticity part of the material behaviour is introduced explicitly to the first governing equation, where the plastic part of the stress is updated based on calculations of the material constitutive model. An explicit elastic predictor-return mapping approach is used for numerical integration of the constitutive equations (in which the deviatoric component obeys radial return), with an automatic strain sub-incrementation algorithm to improve accuracy (Elgamal et al., 2003).

4.1.5 Multi-material interface

a. Traction at multi-material interface

The traction vector at internal cell faces coinciding with multi-material interface ($\mathbf{t}_i^n$, in Eq. 4.33) should be approximated in a different manner compared to internal faces of the same material, as the normal derivative of displacement is discontinuous across the interface. Considering the fact that displacement and traction must be continuous across the interface, approximation of the traction will be derived to ensure physically realistic solution near the interface and reasonable convergence properties of the solution procedure (according to Tuković et al. (2013)).

In Fig. 4.4, two CVs are shown; the primary of volume V_P and centroid P and a neighbouring cell (from another material) of volume V_{N_i} and centroid N_i. The common interface i is situated between two different elastic materials. The material properties on both sides of the interface are given subscripts ia and ib for cells P and N_i, respectively. Derivation of traction approximation at the centre of the face i is carried out separately for the normal and tangential component.

Normal component of the traction is discretised separately at the left and right sides of the interface as shown in Eq. 4.45 and Eq. 4.46, with the assumption of mesh orthogonality at face i.

$$(\mathbf{t}_n)_{ia} = (2G_{ia} + \lambda_{ia}) \frac{(\mathbf{u}_n)_i - (\mathbf{u}_n)_P}{\delta_{an}} + \lambda_{ia} \mathbf{n}_i \left(\nabla_t \mathbf{u}_t\right)_{ia} \tag{4.45}$$

$$(\mathbf{t}_n)_{ib} = (2G_{ib} + \lambda_{ib}) \frac{(\mathbf{u}_n)_{N_i} - (\mathbf{u}_n)_i}{\delta_{bn}} + \lambda_{ib} \mathbf{n}_i \left(\nabla_t \mathbf{u}_t\right)_{ib} \tag{4.46}$$

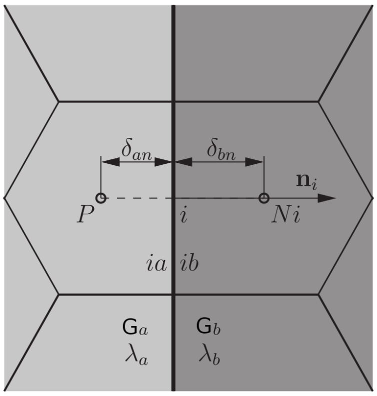

Figure 4.4: Control volumes V_P and V_{N_i} sharing face i at the multi-material interface (Tuković et al., 2013)

Considering continuity of traction across the interface, $(\mathbf{t}_n)_{ia} = (\mathbf{t}_n)_{ib}$, one can express the normal component of displacement vector at face i by combining Eq. 4.45 and Eq. 4.46 as given in Eq. 4.47.

$$\begin{aligned}(\mathbf{u}_n)_i = &\frac{(2G_{ia} + \lambda_{ia})\delta_{bn}(\mathbf{u}_n)_P + (2G_{ib} + \lambda_{ib})\delta_{an}(\mathbf{u}_n)_{N_i}}{(2G_{ia} + \lambda_{ia})\delta_{bn} + (2G_{ib} + \lambda_{ib})\delta_{an}} \\ &+ \frac{\delta_{an}\delta_{bn}[\lambda_{ib}\mathbf{n}_i \mathrm{tr}(\nabla_t \mathbf{u}_t)_{ib} - \lambda_{ia}\mathbf{n}_i \mathrm{tr}(\nabla_t \mathbf{u}_t)_{ia}]}{(2G_{ia} + \lambda_{ia})\delta_{bn} + (2G_{ib} + \lambda_{ib})\delta_{an}}\end{aligned} \tag{4.47}$$

where δ_{an} and δ_{bn} are distances between cell centres of CVs V_P and V_{N_i} and common face, respectively, as shown in Fig. 4.4.

Substituting Eq. 4.47 into Eq. 4.45, a final expression for the approximation of the normal traction is obtained in Eq. 4.48.

$$\begin{aligned}(\mathbf{t}_n)_i = &\ \overline{(2G + \lambda)}_i \frac{(\mathbf{u}_n)_{N_i} - (\mathbf{u}_n)_P}{\delta_{in}} \\ &+ \frac{(2G_{ia} + \lambda_{ia})\delta_{bn}\lambda_{ib}\mathbf{n}_i \mathrm{tr}(\nabla_t \mathbf{u}_t)_{ib} + (2G_{ib} + \lambda_{ib})\delta_{an}\lambda_{ia}\mathbf{n}_i \mathrm{tr}(\nabla_t \mathbf{u}_t)_{ia}}{(2G_{ia} + \lambda_{ia})\,\delta_{bn} + (2G_{ib} + \lambda_{ib})\,\delta_{an}},\end{aligned} \tag{4.48}$$

where $\delta_{in} = \delta_{an} + \delta_{bn}$, and $\overline{(2G + \lambda)}_i$ is the mathematical property at the interface obtained by harmonic interpolation, Eq. 4.49.

$$\overline{(2G + \lambda)}_i = \frac{(2G_{ia} + \lambda_{ia})\,(2G_{ib} + \lambda_{ib})}{\frac{\delta_{bn}}{\delta_{in}}\,(2G_{ia} + \lambda_{ia}) + \frac{\delta_{an}}{\delta_{in}}\,(2G_{ib} + \lambda_{ib})} \tag{4.49}$$

Applying the same procedure for the tangential component of traction, expressions Eq. 4.50 and Eq. 4.51 for the tangential displacement and traction are obtained.

$$\begin{aligned}(\mathbf{u}_t)_i =& \frac{G_{ia}\delta_{bn}\left(\mathbf{u}_t\right)_P + G_{ib}\delta_{an}\left(\mathbf{u}_t\right)_{N_i}}{G_{ia}\delta_{bn} + G_{ib}\delta_{an}} \\ &+ \frac{\delta_{an}\delta_{bn}\left[G_{ib}\left(\nabla_t u_n\right)_{ib} - G_{ia}\left(\nabla_t u_n\right)_{ia}\right]}{G_{ia}\delta_{bn} + G_{ib}\delta_{an}},\end{aligned} \tag{4.50}$$

$$\begin{aligned}(\mathbf{t}_t)_i =& \overline{G}_i \frac{\left(\mathbf{u}_t\right)_{N_i} - \left(\mathbf{u}_t\right)_P}{\delta_{in}} \\ &+ \frac{G_{ia}G_{ib}\delta_{bn}\left(\nabla_t u_n\right)_{ib} + G_{ib}G_{ia}\delta_{an}\left(\nabla_t u_n\right)_{ia}}{G_{ia}\delta_{bn} + G_{ib}\delta_{an}},\end{aligned} \tag{4.51}$$

Similar to the aforementioned procedure, the shear modulus at the interface is obtained by harmonic interpolation, Eq. 4.52.

$$\overline{G}_i = \frac{G_{ia}G_{ib}}{\frac{\delta_{bn}}{\delta_{in}}G_{ia} + \frac{\delta_{an}}{\delta_{in}}G_{ib}} \tag{4.52}$$

By summing Eq. 4.48 and Eq. 4.51, the final expression for the interface traction is obtained as given in Eq. 4.53.

$$\begin{aligned}\mathbf{t}_i =& \overline{(2G+\lambda)}_i \frac{\mathbf{u}_{N_i} - \mathbf{u}_P}{\delta_{in}} - \left[\overline{(2G+\lambda)}_i - \overline{G}_i\right] \frac{\left(\mathbf{u}_t\right)_{N_i} - \left(\mathbf{u}_t\right)_P}{\delta_{in}} \\ &+ \frac{\left(2G_{ia}+\lambda_{ia}\right)\delta_{bn}\lambda_{ib}\mathbf{n}_i \operatorname{tr}\left(\nabla_t \mathbf{u}_t\right)_{ib} + \left(2G_{ib}+\lambda_{ib}\right)\delta_{an}\lambda_{ia}\mathbf{n}_i \operatorname{tr}\left(\nabla_t \mathbf{u}_t\right)_{ia}}{\left(2G_{ia}+\lambda_{ia}\right)\delta_{bn} + \left(2G_{ib}+\lambda_{ib}\right)\delta_{an}} \\ &+ \frac{G_{ia}G_{ib}\delta_{bn}\left(\nabla_t u_n\right)_{ib} + G_{ib}G_{ia}\delta_{an}\left(\nabla_t u_n\right)_{ia}}{G_{ia}\delta_{bn} + G_{ib}\delta_{an}},\end{aligned} \tag{4.53}$$

where the first term on the right-hand side is treated as implicit while the remaining terms are explicit. In this manner, when two similar materials exist at the two sides of the interface, the relations derived for multi-material interface reduce to those of an internal interface.

b. Calculation of tangential gradient of displacement at the interface

The evaluation of the tangential gradient of the displacement at the interface is needed for the application of Eqs. 4.47, 4.50 and 4.53. Three different approaches are proposed in Tuković et al. (2013).

The simplest approach is based on the application of already calculated gradients in the neighbouring cell centres. In that sense, two different procedures can be used. In the first procedure, tangential gradient of displacement at the interface is extrapolated from the neighbouring cell centres, Eqs. 4.54 and 4.55.

$$\left(\nabla_t \mathbf{u}\right)_{ia} = \left(\mathbf{I} - \mathbf{n}_i\mathbf{n}_i\right) \cdot \left(\nabla \mathbf{u}\right)_P, \tag{4.54}$$

$$\left(\nabla_t \mathbf{u}\right)_{ib} = \left(\mathbf{I} - \mathbf{n}_i\mathbf{n}_i\right) \cdot \left(\nabla \mathbf{u}\right)_{N_i}, \tag{4.55}$$

and the procedure is referred to as the *extrapolated* method. Using this procedure, discontinuity of the tangential gradient is present across the interface, but it tends to zero with the mesh refinement.

In the second procedure, tangential gradient is calculated using linear interpolation of the neighbouring cell values, representing the *interpolated* method, Eq. 4.55.

$$\left(\nabla_t \mathbf{u}\right)_{ia} = \left(\nabla_t \mathbf{u}\right)_{ib} = \left(\mathbf{I} - \mathbf{n}_i\mathbf{n}_i\right) \cdot \left[f_x\left(\nabla \mathbf{u}\right)_P + \left(1 - f_x\right)\left(\nabla \mathbf{u}\right)_{N_i}\right]. \tag{4.56}$$

This procedure forces the continuity of the tangential gradient across the interface, but the use of linear interpolation is dubious because the normal derivative of tangential gradient is discontinuous across the interface.

The third approach is to calculate the tangential gradient of displacement directly at the interface. Let the interface be represented by the surface mesh consisting of the arbitrary polygonal control areas (faces). In this approach, one has to calculate the face-centre tangential gradient of displacement using face-centre displacements given by Eqs. 4.47 and 4.50. For this purpose, the surface Gauss' integral theorem is used, which, for a displacement $\mathbf{u}$ defined on surface S bounded by closed line ∂S , Eq. 4.57.

$$\int_S \nabla_t \mathbf{u} \, dS = \int_{\partial S} \mathbf{m}\mathbf{u} \, dL - \int_S \kappa \mathbf{n}\mathbf{u} \, dS, \tag{4.57}$$

where $\mathbf{n}$ is the unit normal vector on the surface S, $\mathbf{m}$ is the unit bi-normal vector perpendicular to a line ∂S and tangential to surface S, and κ is the mean curvature of the interface.

Approximation of the face-centre tangential gradient of displacement is obtained by discretising Eq. 4.57 on the control area S_i (Fig. 4.5) using basic principles of the finite volume discretisation procedure. Thus, the tangential gradient of displacement at the centroid of control area S_i is calculated using the following expression:

$$(\nabla_t \mathbf{u})_i = \frac{1}{S_i} \sum_e \mathbf{m}_e \mathbf{u}_e L_e - \kappa_i \mathbf{n}_i \mathbf{v}_i, \tag{4.58}$$

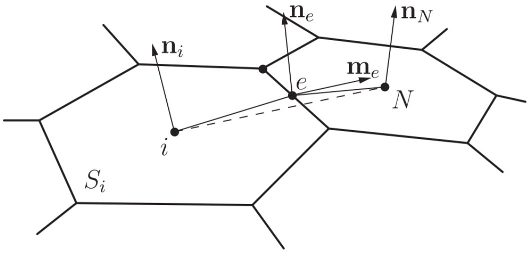

Figure 4.5: Control area S_i at the interface (Tuković et al., 2013)

where surface integrals over the control area S_i and line integrals over the control area edge e of length L_e are approximated using the mid-point rule. Subscript e implies the value of the variable in the middle of the edge e, and summation is performed over all edges closing the face i. The mean curvature at the control-area centre is calculated as follows:

$$\kappa_i = \frac{1}{S_i} \sum_e \mathbf{m}_e L_e. \tag{4.59}$$

The edge-centre displacement $\mathbf{u}_e$ is calculated using the following linear interpolation formula:

$$\mathbf{u}_e = \left(\mathbf{T}_e^T \right) \cdot \left[e_x \mathbf{T}_P \cdot \mathbf{u}_P + (1 - e_x) \, \mathbf{T}_N \cdot \mathbf{u}_N \right], \tag{4.60}$$

where e_x is the interpolation factor calculated as the ratio of geodetic distances $\overline{eN}$ and $\overline{PeN}$, Fig. 4.6:

$$e_x = \frac{\overline{eN}}{\overline{PN}}, \tag{4.61}$$

and $\mathbf{T}_P$, $\mathbf{T}_N$ and $\mathbf{T}_e$ are the tensors of transformation from the global Cartesian coordinate system to the edge-based local orthogonal coordinate system, as defined in Fig. 4.6. The previously described finite volume discretisation procedure intended for discretisation on curved surface mesh is referred to as the finite area method (FAM).

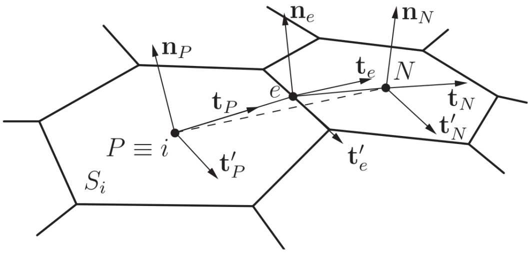

Figure 4.6: Edge-based local orthogonal coordinate system whose axes are aligned with orthogonal unit vectors **n**, **t** and $\mathbf{t}^{'}$, where vector **t** is tangential to the geodetic line $\overline{PeN}$ (Tuković et al., 2013)

4.1.6 Boundary conditions

The boundary conditions available in OpenFOAM include fixed value (Dirichlet) and fixed gradient (Neumann) boundary conditions. The traction boundary condition is a Neumann type boundary condition, in which the gradient is calculated from force balance on the boundary face considering an external force, **F**, as:

$$\mathbf{F} = \mathbf{t} + \mathbf{n}P = \mathbf{n} \cdot \sigma^{'} \tag{4.62}$$

F is the external force vector, **t** is the traction, **n** is the vector of outward-pointing boundary face area and P is any external pressure (traction acting perpendicular to the boundary face). The displacement gradient is calculated from:

$$\mathbf{n} \cdot \nabla \mathbf{u} = \frac{\mathbf{F} + (2G + \lambda)\, \nabla \mathbf{u} - \mathbf{n} \cdot \sigma^{'}}{2G + \lambda} \tag{4.63}$$

A new boundary condition (*timeVaryingMappedTractionFvPatch*) was developed to allow for interpolating time-series of traction/pressure values given for a scatter of points on the boundary. The new boundary condition is based on the *tractionDisplacementFvPatch* and the *timeVaryingMappedFixedValueFvPatch*.

For consideration of solid-fluid coupling effects, only the dynamic effect of fluid pressure is considered at traction boundaries. This means that Eq. 4.62 is modified as:

$$\mathbf{F} = \mathbf{t} + \mathbf{n}P + \mathbf{n}p_{dynamic} = \mathbf{n} \cdot \sigma^{'} \tag{4.64}$$

Eq. 4.64 is used for all solid-fluid coupling formulations. As illustrated in Fig. 4.7, a soil element at the mud line is analysed for the hydrostatic and the hydrodynamic cases. It is necessary to recall that the effect of hydrostatic pressures (water column weight + uplift) is already accounted for by considering the submerged soil density in the $u - p$ formulation. While the fully saturated density of the soil is used in the fully coupled formulation, the effect of hydrostatic pressure is considered implicitly by solving the fluid momentum balance equation and considering the body forces effects of the gravitational acceleration (uplift). Additional uplift pressures on the mud line resulting from dynamic fluid pressures (wave motion) are introduced in the solution to the solid phase by the solid-fluid coupled governing equations, which yields the total upward pressure. Nevertheless, the dynamic pressure acting on the mud line still need to be (explicitly) considered in the boundary condition of the solid phase and not just for the fluid phase.

For the fluid pressure boundary, the dynamic pressure is considered for the $u - p$ formulation, while the total fluid pressure is considered for the fully coupled-fully dynamic solution because of the consideration of the body forces from the gravitational acceleration and the solution of the fluid momentum balance equation.

Because less attention has been dedicated to contact problems of porous media, the solid-fluid coupling at the soil-structure interface is considered by providing two thin layers on both sides of the interface with

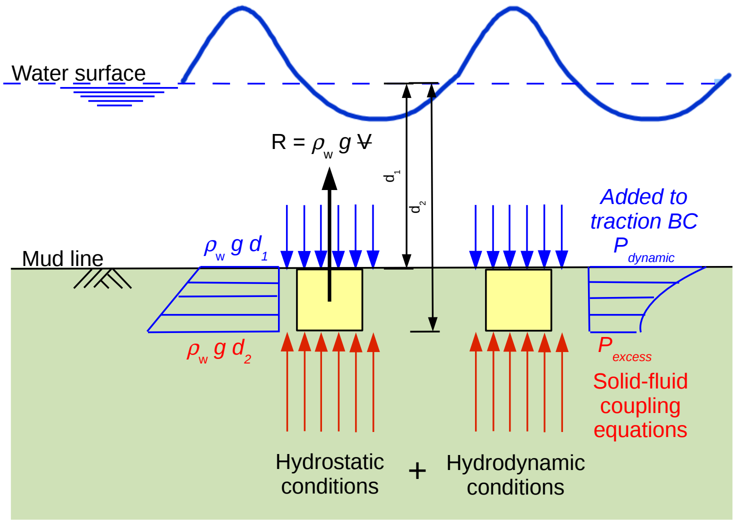

Figure 4.7: A sketch showing difference between hydrostatic and hydrodynamic fluid pressure at mud line

high permeability. In this way it is possible to develop uplift pressures on the structure just after this thin layer by means of the coupled solid-fluid governing equations.

4.1.7 Soil-structure interaction

Several strategies are available for modelling soil-structure interaction. These methods include the introduction of special springs or special elements at the interface. These simplifications are acceptable for small and continuous relative displacements of the interface. Nevertheless, the introduction of realistic contact constrains (boundary conditions) is essential for highly dynamic conditions. For the structure-soil interface, a contact model is implemented (in this study), which can simulate the separation and reattachment of soil and structure adjacent surfaces, using the coupling algorithm.

The method applies second-order accurate discretisation and unstructured meshes in a segregated framework with explicit update of the contact condition, which allows for geometric flexibility and efficient treatment of non-linearity. The contact also accounts for friction between caisson surface and sand foundation. The non-linearity of the system is caused by the fact that the boundary condition is solution-dependent.

A mixed boundary condition (Dirichlet-Neuman) is defined for the displacement at the contact boundary. A fixed value (Dirichlet) is used for displacement component normal to contact surface while a fixed displacement gradient (Neumann) is used for tangential components (friction). This mixed boundary condition is defined for the surface normal. Three values are defined: the displacement, the displacement gradient and the value-fraction to define which part of the boundary is in contact and consequently which fraction of the displacement value and gradient is assigned to the calculation.

Different (potential) pairs of contact surfaces are defined by the user. One of them is assigned a mixed boundary condition and the other is assigned a fixed-gradient boundary condition. Both boundaries are updated together when the contact surfaces overlap, during iterations (Jasak and Weller, 2000b).

A generalised procedure is used to find the overlapping parts of the contact surfaces according to Jasak and Weller (2000b). Consider two surfaces in partial contact, Fig. 4.8. First, an "equivalent" point is found for each vertex of side **A**, e.g. P and Q. The dot-product of $\overline{PQ}$ and the local normal $\mathbf{n}_P$ gives the indication and contact distance for every vertex of **A**.

Several ways can be used to assemble equivalent point pairs, the simplest of which is normal projection, Fig. 4.8. In order to improve the monotonicity of interpolation for curved surfaces with variable gaps, the Jasak and Weller (2000b) method constructs the sphere of minimum radius which passes through P and

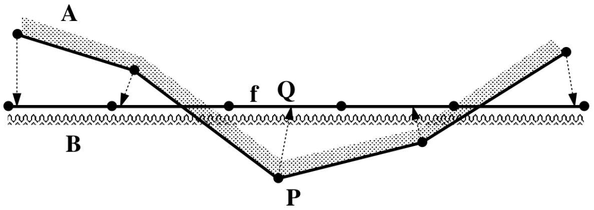

Figure 4.8: Surfaces in contact (Jasak and Weller, 2000b)

is tangential to both surfaces, Fig. 4.9. For a point P, the unit normal $\mathbf{n}_1$ and the opposite surface defined by an arbitrary point R and unit normal $\mathbf{n}_2$, the radius of the sphere is given according to Eq. 4.65.

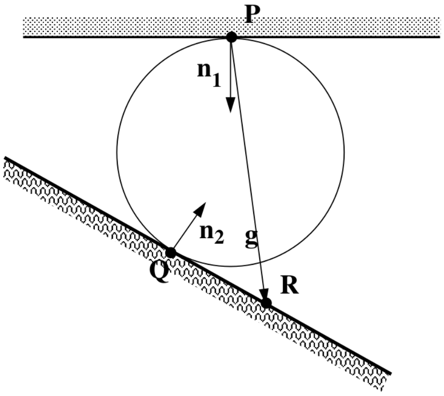

Figure 4.9: Contact sphere (Jasak and Weller, 2000b)

$$r = \frac{\mathbf{g} \cdot \mathbf{n}_2}{\mathbf{n}_1 \cdot \mathbf{n}_2 - 1} \tag{4.65}$$

where $\mathbf{g} = \overline{PR}$ and negative r denotes overlapping surfaces. The equivalent point on the opposite surface is provided by Eq. 4.66.

$$Q = P + r\left(\mathbf{n}_1 - \mathbf{n}_2\right) \tag{4.66}$$

To determine the contact area for a general polygon, given the surface gap in all its vertices, Fig. 4.10. The contact area fraction is the area ratio of the "contact polygon" (shaded) and the complete face. If all the gaps are of the same sign, no further calculation is necessary. For partial contact, a sub-polygon is constructed from all vertices with negative gap values and edge intersections where the gap changes the sign along the edge, e.g. G in Fig. 4.10. The surface area of both polygons is calculated using triangular decomposition (Jasak and Weller, 2000b).

The transfer of face-based data between patches is carried out via a two-step inverse distance weighting, in which data is first interpolated into the vertices of the master patch, then transferred via the equivalent point pairs onto the slave vertices, where the face values are reassembled. The area in contact is calculated separately for each direction (Jasak and Weller, 2000b).

The normal contact constraint can be represented as (Sheng et al., 2007):

$$\mathbf{g_n} = 0, \text{ when } \sigma_n^{'} > 0; \mathbf{g_n} > 0, \text{ when } \sigma_n^{'} = 0; \mathbf{g_n}\sigma_n^{'} = 0 \tag{4.67}$$

Where $\mathbf{g_n}$ is the relative displacement in normal direction (separation). The contact adopts Coulomb's law of friction for tangential constrains (Sheng et al., 2007), as:

$$\mathbf{g_t} = 0, \text{ when } \mu\sigma_n^{'}|\sigma_t^{'}| > 0; |\mathbf{g_t}| > 0, \text{ when } \mu\sigma_n^{'}|\sigma_t^{'}| = 0; \mathbf{g_t}\left(\mu\sigma_n^{'}|\sigma_t^{'}|\right) = 0 \tag{4.68}$$

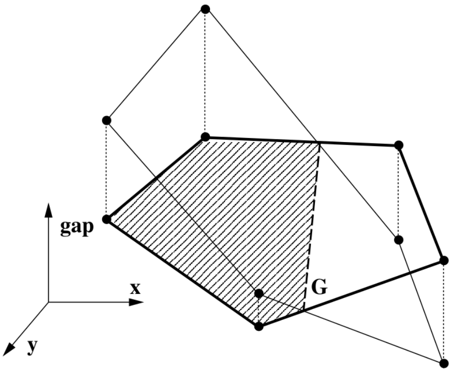

Figure 4.10: Polygonal area in contact (Jasak and Weller, 2000b)

Where $\mathbf{g_t}$ is the relative displacement in tangent direction (slide). The tangential effective stress at contact is σ_t' and the coefficient of friction is μ. No adhesion is simulated by the contact.

4.1.8 CSD solver algorithm

For each variable, the discretisation procedure given in Sec. 4.1.4 is used to transform its governing equation to a linear algebraic equation assembled for each cell. The displacement equation at a cell centroid P is given as:

$$a_P \mathbf{u}_P + \sum_N a_N \mathbf{u}_N + \sum_{N_i} a_{Ni} \mathbf{u}_{Ni} = \mathbf{r}_P \tag{4.69}$$

where a distinction should be made between ordinary neighbouring cells N and neighbouring cells N_i sharing faces at multi-material interface with the considered cell P. Diagonal coefficient a_P , neighbour coefficients a_{Ni} and source term $\mathbf{r}_P$ are defined by assembling discretisations from Sec. 4.1.4 and they contain contributions from boundary conditions. Finally, the equations for all control volumes are assembled for the whole domain, Eq. 4.70.

$$[A]\,[\mathbf{u}] = [\mathbf{r}] \tag{4.70}$$

where $[A]$ is the sparse square matrix with coefficients a_P on the diagonal and $a_{N(i)}$ off the diagonal, $[\mathbf{u}]$ is the displacement vector consisting of displacements for all computational points, and $[\mathbf{r}]$ is the right-hand side vector consisting of $\mathbf{r}_P$ terms for all control volumes. The preceding system is solved for the three components of $\mathbf{u}$ in a segregated manner.

Matrix $[A]$ from Eq. 4.70 is symmetric and diagonally dominant even in the absence of the transient term, which is important for steady-state calculations. It has to be mentioned that the discretised system described previously includes explicit terms, depending on the variables (e.g. displacement) from the previous iteration. Therefore, it would be unnecessary to converge the solution of Eq. 4.70 to a very tight tolerance, as the new solution will only be used to update the explicit terms. Only when the solution changes less than some predefined tolerance is the system considered to be solved. In transient calculations, this is done for every time step, using the previously available solution as the initial guess.

For the $u - p$ approximation, the same approach is considered to compute the pore pressure, Eq. 4.71 and Eq. 4.72. Both forms of the algebraic equations are also used for solving for the pressure in the PISO (Pressure Implicit with Splitting of Operator) algorithm for the fully coupled-fully dynamic equations.

$$a_P p_P + \sum_N a_N p_N = r_P \tag{4.71}$$

$$[A]\,[p] = [r] \tag{4.72}$$

The pore fluid velocity (for the PISO algorithm) is discretized to the forms in Eqs. 4.73 and 4.74.

$$a_P \overline{\mathbf{U}}_P + \sum_N a_N \overline{\mathbf{U}}_N = \mathbf{r}_P \tag{4.73}$$

$$[A]\,\left[\overline{\mathbf{U}}\right] = [\mathbf{r}] \tag{4.74}$$

The solution procedure consists of the following steps (Fig. 4.11):

1. Switch to the new time step and initialize the value of the dependent variable with the value from the previous time step
2. For the fully coupled-fully dynamic equations, assemble and solve the pore fluid momentum predictor equation with the available face fluxes
3. Go through the PISO loop until the tolerance for pressure-velocity system is reached. At this stage, pressure and velocity fields for the current time-step are obtained, as well as the new set of conservative fluxes (for next time step)
4. For the $u - p$ approximation, the pressure equation is solved for pore pressure
5. Calculate face-centre displacement for the internal faces using linear interpolation and for the faces at the multi-material interface
6. Calculate cell-centre gradient with face-centre displacement obtained in the previous step
7. Calculate face-centre gradient using linear interpolation (or using special procedure for the faces at the interface)
8. Assemble and solve discretised equation for displacement $\mathbf{u}$
9. Update effective stresses from constitutive model
10. Return to step 1 if converged solution is reached, otherwise return to step 2 (or step 4)

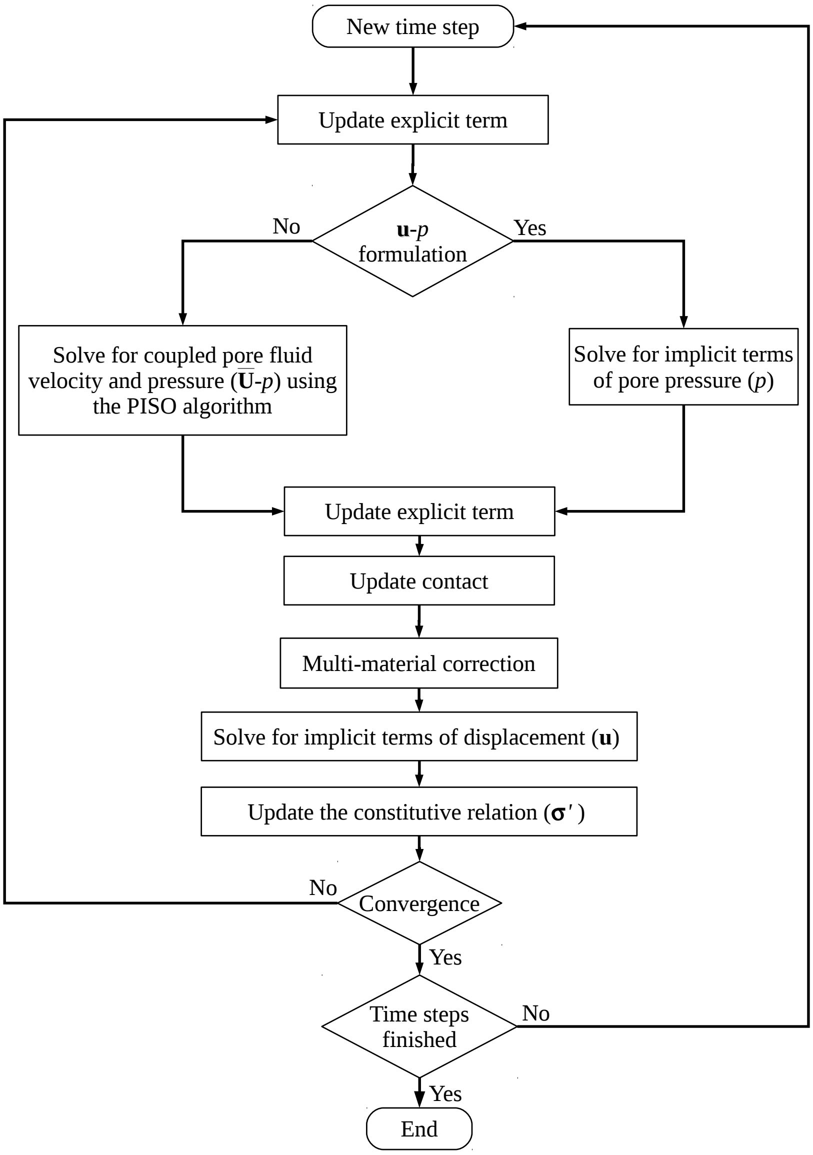

Figure 4.11: Algorithm for *geotechFoam*

4.1.9 Soil constitutive model

In this subsection, the implementation of the selected soil constitutive model discussed in Section 2.4 is presented. For elastoplastic material constitutive models, the total strain can be conveniently decomposed into elastic (ε^e) and plastic (ε^p) components:

$$\varepsilon = \varepsilon^e + \varepsilon^p \tag{4.75}$$

Therefore, Eq. 4.4 can be expressed as:

$$d\sigma' = \mathbf{E} : (d\varepsilon - d\varepsilon^p) \tag{4.76}$$

Where $d\varepsilon$ is the strain rate tensor and $d\varepsilon^p$ is the plastic strain rate tensor. Anisotropy is considered to be due to plasticity; therefore, any elastic anisotropy is omitted. Consequently, the former relation is simplified to:

$$d\sigma' = 2G\left(d\varepsilon - d\varepsilon^p\right) + \left(K - \frac{2G}{3}\right)\left(tr\left(d\varepsilon\right) - tr\left(d\varepsilon^p\right)\right)\mathbf{I} \tag{4.77}$$

Where G is the shear modulus and K is the bulk modulus. Nonlinear elasticity can be introduced by considering elastic parameters to be functions of confinement (Prévost, 1985):

$$G = G_r \left(\frac{tr\left(\sigma'\right)/3 + p_0}{p^r + p_0} \right)^a \tag{4.78}$$

$$K = K_r \left(\frac{tr\left(\sigma'\right)/3 + p_0}{p^r + p_0} \right)^a \tag{4.79}$$

Where (G_r) and (K_r) are the reference shear modulus and reference bulk modulus, which correspond to the reference effective mean normal stress (p^r). The parameter a equals 0.5 for most cohesion-less soils. A multi-yield surface plasticity model is considered, in which the plastic strain rate tensor is calculated as:

$$d\varepsilon^p = \mathbf{P}\langle L \rangle \tag{4.80}$$

P is a symmetric second-order tensor which defines the direction of plastic deformation, $\langle\rangle$ are MacCauley's brackets, so $\langle L \rangle$ (the plastic loading function) is set to zero if it has a negative value. L is calculated as:

$$L = \frac{1}{H'} \left(\mathbf{Q} : d\sigma' \right) \tag{4.81}$$

$H^{'}$ is the plastic modulus and **Q** is a symmetric second-order tensor that denotes the outer normal to yield surfaces. **P** and **Q** are decomposed into deviatoric (**P** and **Q**) and volumetric (P and Q) parts, as:

$$P^{''} = \frac{tr\left(\mathbf{P}\right)}{3} \tag{4.82}$$

$$\mathbf{P}^{'} = \mathbf{P} - P^{''}\mathbf{I} \tag{4.83}$$

$$Q^{''} = \frac{tr\left(\mathbf{Q}\right)}{3} \tag{4.84}$$

$$\mathbf{Q}^{'} = \mathbf{Q} - Q^{''}\mathbf{I} \tag{4.85}$$

The **Q** tensor is normalized as follows:

$$\mathbf{Q} = \frac{\partial f_m / \partial \sigma'}{||\partial f_m / \partial \sigma'||} \tag{4.86}$$

Where (f_m) is the yield function of the m^{th} surface, and $\frac{\partial f_m}{\partial \sigma'}$ is its gradient in the effective stress space.

a. Yield function

The soil constitutive model implemented in the *geotechFoam* solver utilizes the Drucker-Prager yield function (f_m), Fig. 4.12a. The Drucker-Prager criterion (Prévost, 1985; Elgamal et al., 2003; Yang et al., 2003a) reads:

$$f_m = 3/2 \left(\mathbf{s} - \left(tr\left(\sigma'\right)/3 + p_0^{'} \right) \boldsymbol{\alpha}^m \right) : \left(\mathbf{s} - \left(tr\left(\sigma'\right)/3 + p_0^{'} \right) \boldsymbol{\alpha}^m \right) - M_m^2 \left(tr\left(\sigma'\right)/3 + p_0^{'} \right)^2 \tag{4.87}$$

For which:

$$\frac{\partial f_m}{\partial \sigma} = 3 \left(\mathbf{s} - \left(tr\left(\sigma'\right)/3 + p_0^{'} \right) \boldsymbol{\alpha}^m \right) + \left(\left(tr\left(\sigma'\right)/3 + p_0^{'} \right) \left(\boldsymbol{\alpha}^m : \boldsymbol{\alpha}^m - 2/3 M_m^2 \right) - \mathbf{s}\boldsymbol{\alpha}^m \right) \mathbf{I} \tag{4.88}$$

The deviatoric stress tensor **s** is calculated as $\mathbf{s} = \boldsymbol{\sigma}' - \boldsymbol{p}'\mathbf{I}$. A small positive constant $(p_0^{'})$ is considered for numerical convenience (Elgamal et al., 2003). $\boldsymbol{\alpha}^m$ is the kinematic deviatoric tensor defining coordinates of the m^th^ yield surface's centre in stress subspace (stress deviatoric plane/view) and M_m is a scalar that defines the m^th^ surface size. It is therefore a material parameter for the most outer surface (failure surface) and is obtained for inner surfaces from piece-wise linearization of the octahedral shear stress-strain curve (triaxial-stress plane) retrieved from lab experiments.

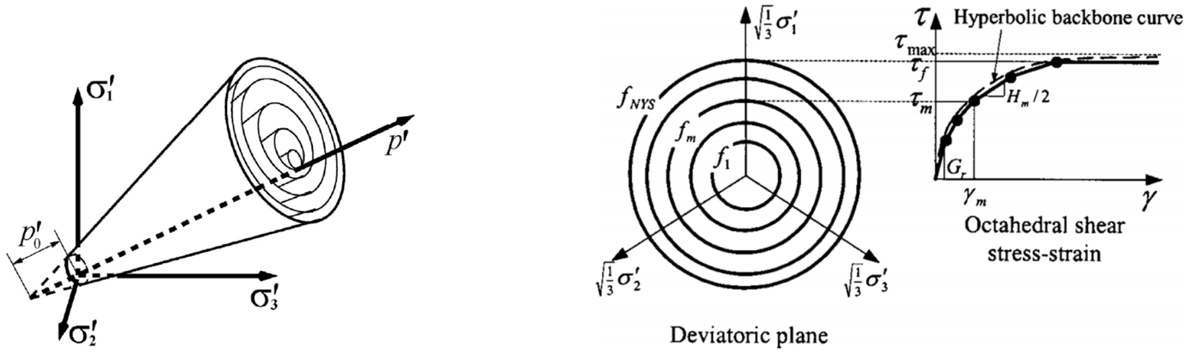

(a) The Drucker-Prager yield surfaces

(b) Piecewise-linear approximation of nonlinear shear stress-strain backbone curve (monolithic drained compression) for Drucker-Prager yield surfaces

Figure 4.12: Piecewise-linear approximation of nonlinear shear stress-strain backbone curve (monolithic drained compression) for Drucker-Prager yield surfaces (Yang et al., 2003a)

The shear stress-strain curve (backbone curve from drained monolithic compression tests) is approximated by several line segments (Fig. 4.12b). Each segment has its slope (H_m):

$$H_m = 2\frac{\tau_{m+1} - \tau_m}{\gamma_{m+1} - \gamma_m} \tag{4.89}$$

For the final surface $H_{NYS} = 0$ (NYS is the number of yield surfaces).The parameter (M_m) can be calculated as:

$$M_m = \frac{3\tau_m}{\sqrt{2}\left(tr\left(\sigma'\right) + p'_0\right)} \tag{4.90}$$

The parameter M_f for the failure (outer) surface can be related to the friction angle as:

$$M_f = \frac{6\sin\phi}{(3 - \sin\phi)} \tag{4.91}$$

b. Flow rule

The flow rule determines how the outer normal to the plastic potential function **P** is calculated. Generally, a non-associative flow rule is considered for cohesionless soils to better model shear-volumetric strain interaction. In this model, the deviatoric part of the flow rule is associative ($\mathbf{P}' = \mathbf{Q}'$) while the volumetric part ($P'' \neq Q''$) is nonassociative (Prévost, 1985). Consequently, the flow rule as a whole is nonassociative; $\mathbf{P} \neq \mathbf{Q}$. The flow rule from Yang et al. (2003a) with Yang and Elgamal (2008) modification is used. According to the stress state position (in the effective principal stress space) relative to the phase-transformation surface (soil phase), defined by soil properties, three expressions are used to calculate P''.

The phases are recognized by comparing the stress ratio η to the stress ratio at the phase transformation surface (η_{PT}) and also by the sign of the stress ratio increment $d\eta$. For ($\eta < \eta_{PT}$) and ($\eta > \eta_{PT}$ and $d\eta < 0$), soil is in the contractive phase. For ($\eta > \eta_{PT}$ and $d\eta > 0$), soil is in the dilative phase. Finally, soil is in a neutral phase when ($\eta = \eta_{PT}$). The stress ratio (η) is the ratio of the (triaxial) deviator stress to the mean effective normal stress/hydrostatic stress) ($\eta = \frac{q}{p'}$). Therefore, the stress ratio is calculated as:

$$\eta = \frac{q}{p'} = \frac{\sqrt{3/2\mathbf{s}:\mathbf{s}}}{tr\left(\sigma'\right)/3} \tag{4.92}$$

In Fig. 4.13, a sketch of undrained ($\partial\varepsilon_v = 0$ and $\partial p' = -\partial p$; $p' = tr\left(\sigma'\right)/3$) effective stress path and corresponding shear stress-strain response are shown. For the contractive phase of soil, the excess pore pressure builds-up (paths 0-1 and 4-5), P'' is calculated by (Yang et al., 2003a):

$$P'' = \left(1 - \sin\left(d\eta\right)\frac{\eta}{\eta_{PT}}\right)\left(c_1 + c_2\varepsilon_c\right)\left(\frac{tr\left(\sigma'\right)/3}{p_{atm}}\right)^{c_3} \tag{4.93}$$

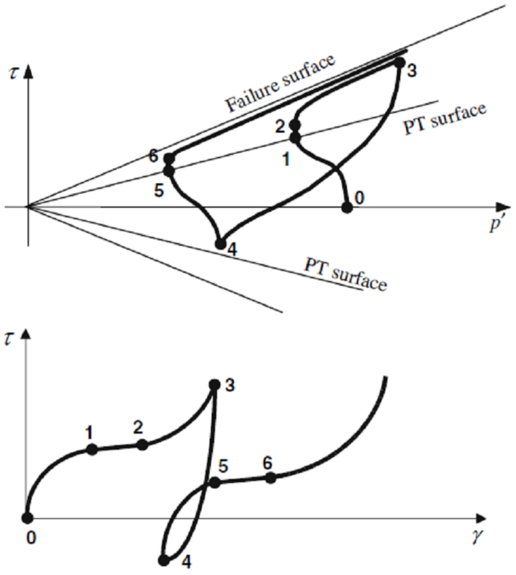

Figure 4.13: Sketch showing the model undrained effective stress path and shear stress–strain response (Yang and Elgamal, 2008)

The parameters c_1 and c_2 are positive calibration constants that dictate the rate of contraction (or excess pore pressure increase). The parameter c_3 is introduced to represent the dependence of pore pressure buildup on confinement. Atmospheric pressure (p_{atm}) is used for normalization of the confinement pressure. A non-negative scalar (ε_c) is governed by the following rate (incremental) equation:

$$d\varepsilon_c = \begin{cases} -d\varepsilon_v^p & \left(\varepsilon_c > 0 \text{ or} - d\varepsilon_v^p > 0\right) \\ 0 & \text{otherwise} \end{cases} \tag{4.94}$$

For the dilative soil behaviour, dissipation of pore pressure (e.g. path 2-3 in Fig. 4.13), soil regain stiffness and strength, P is:

$$P'' = \left(1 - \frac{\eta}{\eta_{PT}}\right) d_1\left(\gamma_d\right)^{d_2}\left(\frac{tr\left(\sigma'\right)/3}{p_{atm}}\right)^{d_3} \tag{4.95}$$

The parameters d_1, d_2 and d_3 are calibration constants. The parameter d_3 is included to represent dependence of pore pressure dissipation (and dilatancy) on confinement. (γ_d) is the octahedral shear strain accumulated during a current dilation phase. Therefore, dilation increases with accumulated shear strain (as observed experimentally). This model lacks expressions for P'' through the neutral phase and the critical state. Nevertheless, it is logical to consider $P'' = 0$, which allows for shear strain without change in confinement (or pore pressure). The critical state occurs at very low confinement (e.g. less than 10 kPa), at which considerable permanent shear strain may accumulate with minimal change in shear stress.

c. Hardening rule

The hardening rule is a pure deviatoric kinematic one. Consequently, all surfaces do not change size. They do, however, translate except for the outermost surface which is considered as a failure surface (the stress state cannot lie outside it). The direction of translation is selected independently of any formal plasticity constraints to ensure no overlapping between yield surfaces (Elgamal et al., 2003; Prévost, 1985; Mroz, 1967) To translate the active surface (f_m), in Fig. 4.14, so that the new (deviatoric) stress state (**S**) lies on its new position, a conjugate stress state ($\mathbf{S^T}$) that lies on the outer yield surface (f_{m+1}) and thus satisfies its yield function (Eq. 4.96). In Eq. 4.96, the unknown is (x). Solving for (x) yields a quadratic equation if the Lode angle effect is neglected (e.g. Drucker-Prager criterion).

$$\mathbf{s}^T = x\left(\mathbf{s} - \frac{tr\left(\sigma'\right)}{3}\boldsymbol{\alpha}^m\right) + \frac{tr\left(\sigma'\right)}{3}\boldsymbol{\alpha}^m \tag{4.96}$$

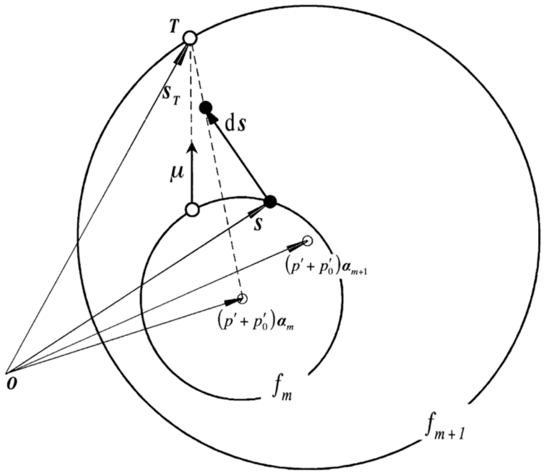

Figure 4.14: Deviatoric hardening rule (after Parra-Colmenares (1996))

The direction of surface translation is given by:

$$\mu = \left(\mathbf{s}^T - \frac{tr\left(\sigma'\right)}{3}\boldsymbol{\alpha}^m\right) - \frac{M_m}{M_{m+1}}\left(\mathbf{s}^T - \frac{tr\left(\sigma'\right)}{3}\boldsymbol{\alpha}^{m+1}\right) \tag{4.97}$$

4.1.10 The CSD model *geotechFoam* solver

The *geotechFoam* solver was developed through the study at hand. The solver is developed, as mentioned earlier, within the OpenFOAM framework. The development started as a modification of the *solidDisplacementFoam* solver with added features from *icoFoam*, *porousZones*, the *solidMechanics* branch from the OpenFOAM-Extend project (The OpenFOAM-Extend Project, 2014) and the OpenSees framework (McKenna et al., 2014).

The modules outline and organization structure of the *geotechFoam* solver are illustrated in Fig. 4.15. The solver is developed in a main C++ source code file *geotechFoam.C*. In this file, use of standard libraries of the OpenFOAM toolbox through inclusion of several header files (e.g. *createTime.H* and *createMesh.H*). Three libraries were developed for the *geotechFoam* solver.

The first library is the *libsoilZones.so*, which enables the division of the spatial domain into different zones with not only different material properties, but also different material models. Each material has a *soilZone* object with a single *soilZones* object for the whole domain that acts as a collection class for different *soilZone* objects.

The second library is the *libmaterialConstitutiveModel.so*, which is developed for the use of different material models for different *soilZones* across the domain. The *libmaterialConstitutiveModel.so* library contains an abstract *materialConstitutiveModel* class for different material constitutive models. Using this approach, several material models can be later implemented within the solver. Two material models have been implemented through this study; the elastic model (the *Elastic* class) for isotropic linear elasticity, and the kinematic hardening anisotropic multi-surface material constitutive model with the Drucker-Prager failure criterion (the *KH_AN_MS_DruckerPrager* class).

The third library, *libcontactModel.so*, encloses the contact model classes. A *contactPair* object is instantiated for each pair of surfaces that have the potential to get in contact. The *contactModels* class is developed as a collection class for the *contactModel* class.

The standard boundary conditions from OpenFOAM are used (e.g. *fixedValue*). A new boundary condition (*timeVaryingMappedTraction*) was developed to enable introduction of variable traction along a boundary that can be interpolated in both time and space with independence from domain's time and space discretisation. This boundary condition is derived from both the *tractionDisplacement* and the *timeVaryingMappedFixedValue* boundary conditions.

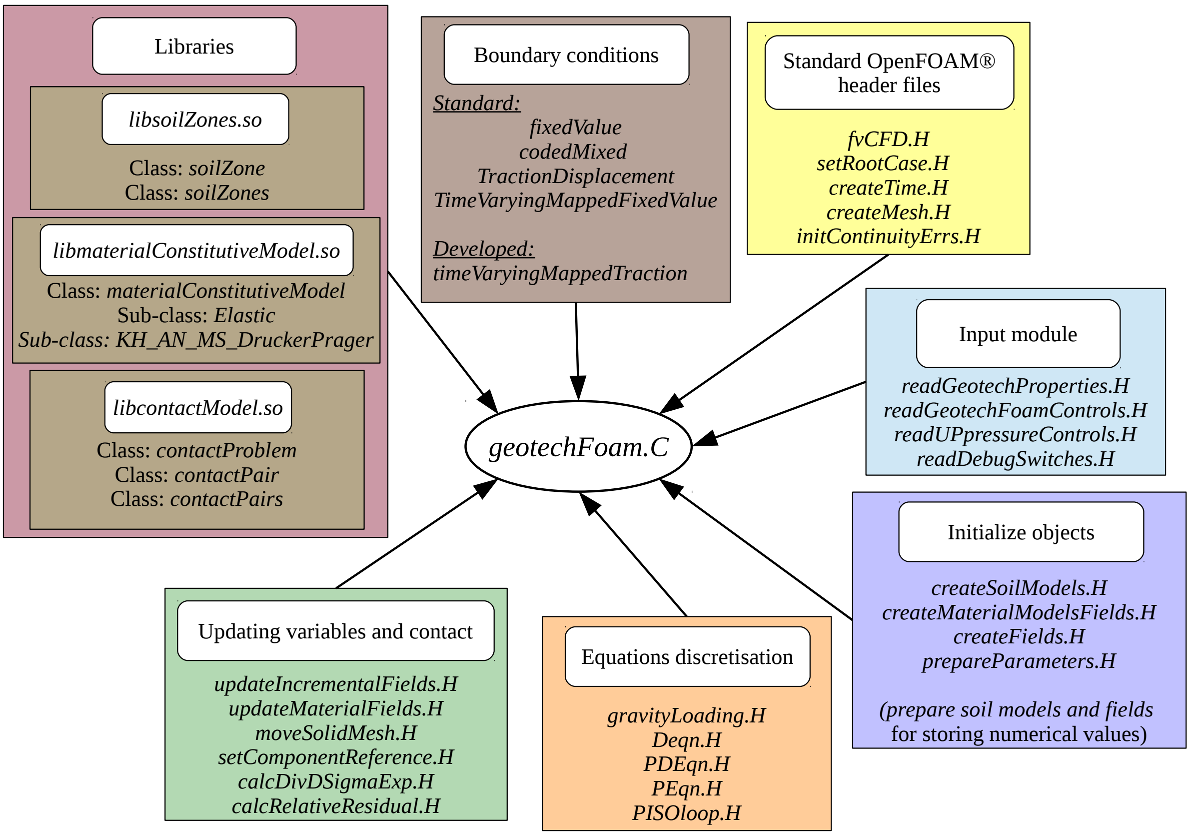

Figure 4.15: Outline and organization of *geotechFoam* development

The solver can be considered to consist of several modules. Nevertheless, these modules are often interdependent and clear distinctions are not in all cases possible. The input module consists of code needed to read user input for control of the simulation's attributes (e.g. material models and properties).

The object initialization module is responsible for initializing objects for soil zones and models and initializing fields for domain variables (e.g. displacement) and material model variables. This module is responsible for preparing the objects for a new simulation or a simulation continued from a previous one.

Both equation discretisation module and update variables module are executed interchangeably. In the equations discretisation module, the equations are discretised according to the method selected by the user for the simulation. The update variables module is responsible for updating fields, contact and variables between iterations and time steps. The output is also calculated for each output time. Finally, the output of variables and fields and further post-processing are carried out by the standard utilities of OpenFOAM.

4.2 CSD Model Validation

In this section, the developed *geotechFoam* solver is tested against theoretical benchmark problems as well as physical experiments. *For the solid-fluid coupling* verification, three poro-elastic problems are considered: (i) The 1D (one-dimensional) consolidation of a saturated soil column under uniform loading, (ii) sudden loading of a soil layer surface by fluid (also one-dimensional) and (iii) the 2D (two-dimensional) response of a poro-elastic seabed with finite thickness to direct wave action (without any structure). *For the contact problem* verification, a 3D ball-brick frictionless contact problem and an elastic cylinder-block frictional contact problem are considered. *For the multi-material interface correction*, a validation is performed against numerical solution by the boundary element method. *For the elasto-plastic soil constitutive model*, a validation is performed using physical centrifuge tests of a soil embankment on a liquefiable soil layer subject to base shaking. Finally, the complete model capabilities are assessed by reproducing physical tests of a rocking plate on a sand box, which resembles caisson rocking motion on the foundation underneath.

4.2.1 One-dimensional soil consolidation

The first benchmark problem is Terzaghi's 1D soil consolidation problem (under external stress). This 1D problem represents the dissipation of pore pressure in soil. The problem has an analytical solution based on uncoupled and quasi-static conditions, which are justified for the problem conditions.

For uniaxial strain conditions, only the stress in the same direction as the strain in question is relevant. Considering a linear elastic material model, the constitutive relation is reduced to:

$$\sigma = \frac{2G\left(1-\nu\right)}{1-2\nu}\varepsilon - p \tag{4.98}$$

Where σ is the total stress (tension is +ve), p is the pore pressure and the first term on the RHS is the effective stress. Neglecting all body forces and considering a time-independent traction (surface load), the static equilibrium equation is:

$$\nabla \cdot \sigma = 0 \tag{4.99}$$

$$\frac{2G\left(1-\nu\right)}{1-2\nu}\frac{\partial^2 u_z}{\partial z^2} - \frac{\partial p}{\partial z} = 0 \tag{4.100}$$

And substituting Eq. 4.98 in Eq. 4.99: Assuming Darcy's law, the pore pressure diffusion equation reduces to that (uncoupled form) given by Terzaghi's consolidation theory:

$$\frac{\partial p}{\partial t} - c_v \frac{\partial^2 p}{\partial z^2} = 0 \tag{4.101}$$

Where c_v is the consolidation coefficient calculated as:

$$c_v = \frac{k}{\rho_w g\left(m_v + {}^{n}/_{K_f}\right)} \tag{4.102}$$

Where m_v is soil's compressibility coefficient (inverse of the $P - wave$ modulus):

$$m_v = \frac{\left(1+\nu\right)\left(1-2\nu\right)}{E\left(1-\nu\right)} \tag{4.103}$$

And K_f is the fluid bulk modulus defined as the inverse of the fluid compressibility (β). The bulk modulus of pure water K_w constant equals 2200 MPa. For air content in the pore fluid, K_f can be calculated as:

$$\frac{1}{K_f} = \frac{S}{K_w} + \frac{1-S}{K_a} \tag{4.104}$$

The degree of saturation (S) is the ratio of volume of water to total volume of voids ($^{V_w}/_{V_v}$) and K_a is the air bulk modulus, which is equal to the absolute fluid pressure (K_a = 101 kPa at atmospheric pressure). For the problem of one-dimensional consolidation of a soil layer of height (h), the boundary conditions are defined as:

$$\begin{aligned} p &= 0 \quad \text{at} \quad z = h \quad \text{(at soil surface)} \\ \frac{\partial p}{\partial z} &= 0 \quad \text{at} \quad z = 0 \quad \text{(impermeable layer underneath soil)} \end{aligned} \tag{4.105}$$

The initial condition of the pore pressure field is calculated by considering an undrained initial condition. The pore pressure is uniform for the whole domain and equal to:

$$p_i = \frac{q}{1 + {}^{n\beta}/_{m_v}} \qquad \text{at} \qquad t = 0 \tag{4.106}$$

Where q is the uniform load on the soil surface. For incompressible pore fluid the initial condition would be $p = q$. Using the Laplace transform method, the solution is given in Verruijt and Van Baars (2007) as:

$$p = p_i \times \frac{4}{\pi} \sum_{j=1}^{\infty} \frac{(-1)^{j-1}}{2j-1} \cos\left[(2j-1)\,\frac{\pi}{2}\frac{z}{h}\right] \exp\left[-\,(2j-1)^2\,\frac{\pi^2}{4}\frac{c_v t}{h^2}\right] \tag{4.107}$$

Once the pore pressure is calculated, the vertical displacement at the top surface of the soil layer (Δh) can be calculated from the relation:

$$\varepsilon = -m_v\,(\sigma + p) \tag{4.108}$$

The initial displacement just after loading is:

$$\Delta h_0 = -m_v h q \frac{{}^{n\beta}/_{m_v}}{1 + {}^{n\beta}/_{m_v}} \tag{4.109}$$

The initial displacement will equal zero for incompressible pore fluid. The displacement after a large period of time (when $p \rightarrow 0$) is:

$$\Delta h_\infty = -m_v h q \tag{4.110}$$

Defining the degree of consolidation (D_c) as:

$$D_c = \frac{\Delta h - \Delta h_0}{\Delta h_\infty - \Delta h_0} \tag{4.111}$$

The degree of consolidation is calculated as:

$$D_c = 1 - \frac{8}{\pi^2} \sum_{j=1}^{\infty} \frac{1}{(2j-1)^2} \exp\left[-\,(2j-1)^2\,\frac{\pi^2}{4}\frac{c_v t}{h^2}\right] \tag{4.112}$$

The geometry of the soil column and boundary conditions are illustrated in Table 4.1. The domain is a 3D column with sides (patches) defined as empty patches to achieve a 1D solution. The soil properties used are given in Table 4.2. The pore pressure computed by *geotechFoam* is shown in Fig. 4.16, which shows the results from different formulations as compared to Terzaghi's analytical solution. Results are shown as pressure ratio (p / p_i) along depth ratio (z / h) for different dimensionless times ($^{c_v t}/_{h^2}$). The fluid bulk modulus (implicit in c_v) is considered for pure water (2200 MPa) because Terzaghi's model assumes incompressible fluid. It is worth stressing that the degree of saturation ($S = {}^{V_w}/_{V_v}$) has a crucial effect on the numerical model results (implicitly present in the fluid bulk modulus). An applicable value of $S = 98.83\%$ is considered, which best compares to the analytical solution and causes a reduction of K_f by a factor ≈ 260 from that of pure water ($S = 100\%$). As shown in Fig. 4.16, the three formulations compare very well to the 1-D Terzaghi's consolidation model.

Table 4.1: Configurations of the consolidation and loading by fluid 1-D problems (boundary and initial conditions)

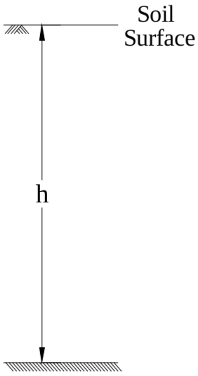

Consolidation			Loading by fluid		
u_z	p	$\overline{\mathbf{U}}_z$	u_z	p	$\overline{\mathbf{U}}_z$
$T_z = p_i$	$p = 0$	$\frac{\partial \overline{\mathbf{U}}_z}{\partial z} = 0$	$T_z = 0$	$p = p_i$	$\frac{\partial \overline{\mathbf{U}}_z}{\partial z} = 0$
Initial conditions					
$p = \frac{p_i}{1+\frac{n}{K_f m_v}}$			$p = 0$		
$u_z = 0$	$\frac{\partial p}{\partial z} = 0$	$\overline{\mathbf{U}}_z = 0$	$u_z = 0$	$\frac{\partial p}{\partial z} = 0$	$\overline{\mathbf{U}}_z = 0$

Table 4.2: Seabed properties for the consolidation and loading by fluid 1-D problems

Layer thick. (h)	10 m
Arbitrary pressure (p_i)	variable
Saturated density (ρ_{sat})	2000 kg/m^3
Submerged density (ρ_{sub})	1000 kg/m^3
Fluid density (ρ_f)	1000 kg/m^3
Porosity (n)	0.42
Hydraulic conductivity (k)	10^{-5} m/s
Elasticity modulus (E)	15 MPa
Poisson's ratio (ν)	0.3
Degree of saturation (S)	0.9883
Fluid bulk modulus (K_f)	8.514 MPa

4.2.2 One-dimensional fluid injection

The analytical solution of the 1D loading by fluid problem is a modification of Terzaghi's consolidation. The loading by fluid (fluid injection) problem resembles the buildup (accumulation) of pore pressure inside a soil layer.

If the soil layer is loaded by a fluid instead of a uniform load, only the pore pressure will be set to a given value (p^*) at the soil surface with zero external loads. The initial pore pressure of the whole domain is set to zero. Other boundary conditions are similar to the first case. The solution for this case is given by Verruijt and Van Baars (2007), as:

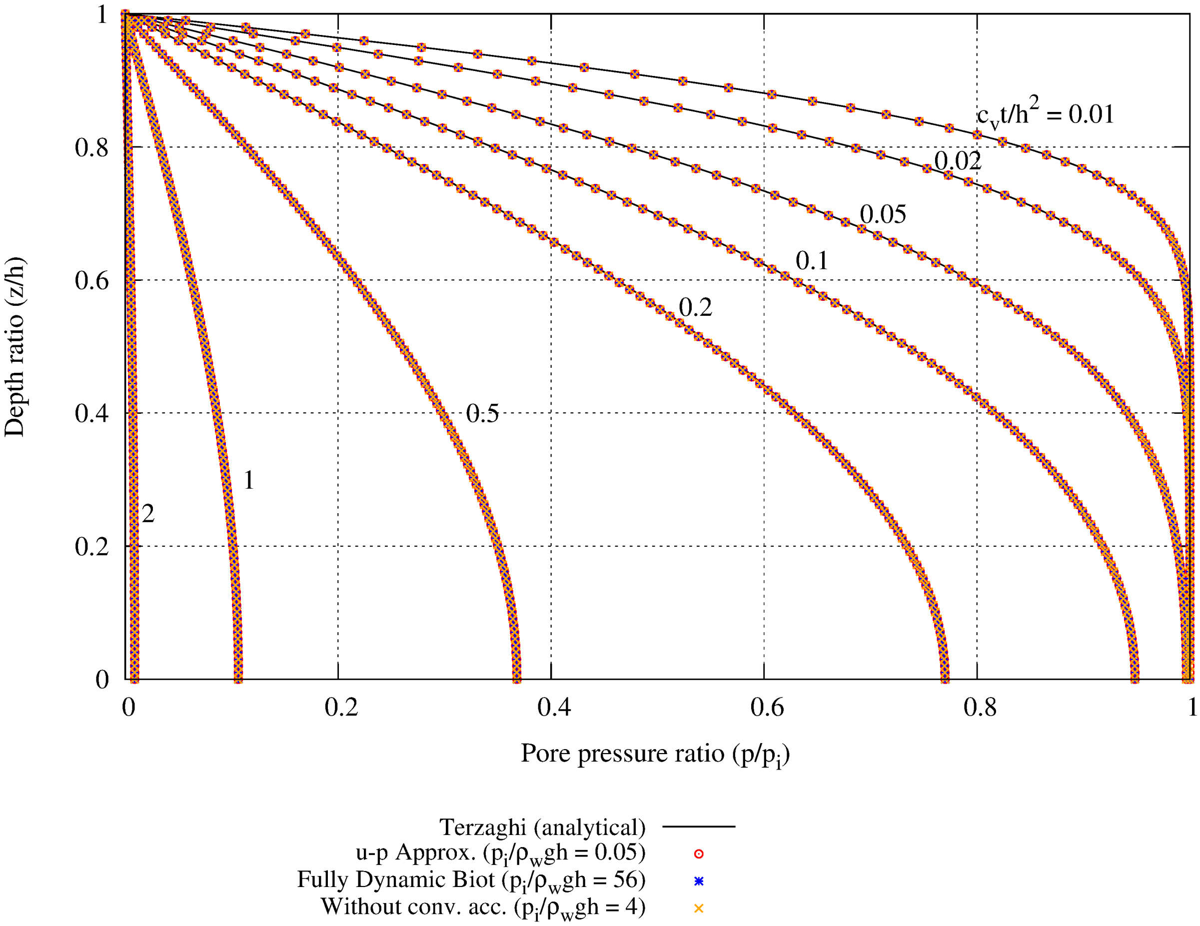

Figure 4.16: A Comparison of the three numerical approaches with Terzaghi's 1-D consolidation model (S = 98.83%)

$$p = p^* \times \left(1 - \frac{4}{\pi} \sum_{j=1}^{\infty} \frac{(-1)^{j-1}}{(2j-1)} \cos\left[(2j-1)\,\frac{\pi}{2}\,\frac{z}{h}\right] \exp\left[-\,(2j-1)^2\,\frac{\pi^2}{4}\,\frac{c_v t}{h^2}\right]\right) \tag{4.113}$$

The surface displacement is given by:

$$\Delta h = -\frac{1-2\nu}{2G\,(1-\nu)}\,p^* h \times \sum_{j=1}^{\infty} \frac{8}{j^2\pi^2}\left[1 - \exp\left(-j^2\pi^2\frac{c_v t}{4h^2}\right)\right] \tag{4.114}$$

The pore pressure computed by *geotechFoam* for the 1D loading by fluid problem, Table 4.2, is shown in Fig. 4.17. Similar to Terzaghi's consolidation problem, the three formulations compare very well to the the 1D loading by fluid.

It is observed that the fully dynamic Biot formulation (using the PISO algorithm) is affected by the ratio of the excess pore pressure to the hydrostatic pore pressure (more apparent for higher air content). The effect is significantly less apparent when the convective acceleration is neglected. At the beginning of the simulation, the dissipation and buildup agree with the analytical solution until the simulation reaches a certain time which depends on ratio of excess to total pore pressure. The dissipation and buildup of pore pressure are then reduced significantly. Therefore, higher value for the arbitrary pressure (p_i) was considered for the PISO algorithm based simulations. It was found that neglecting the pore fluid convective acceleration increases the time needed for convergence (because the convective term is in the implicit part of the momentum balance equations) and hence not favoured. The model is very sensitive to air content in the pore fluid (introduced to the fluid phase bulk modulus). The fluid momentum balance is solved in the PISO based model instead of being considered implicitly in the mass conservation equation

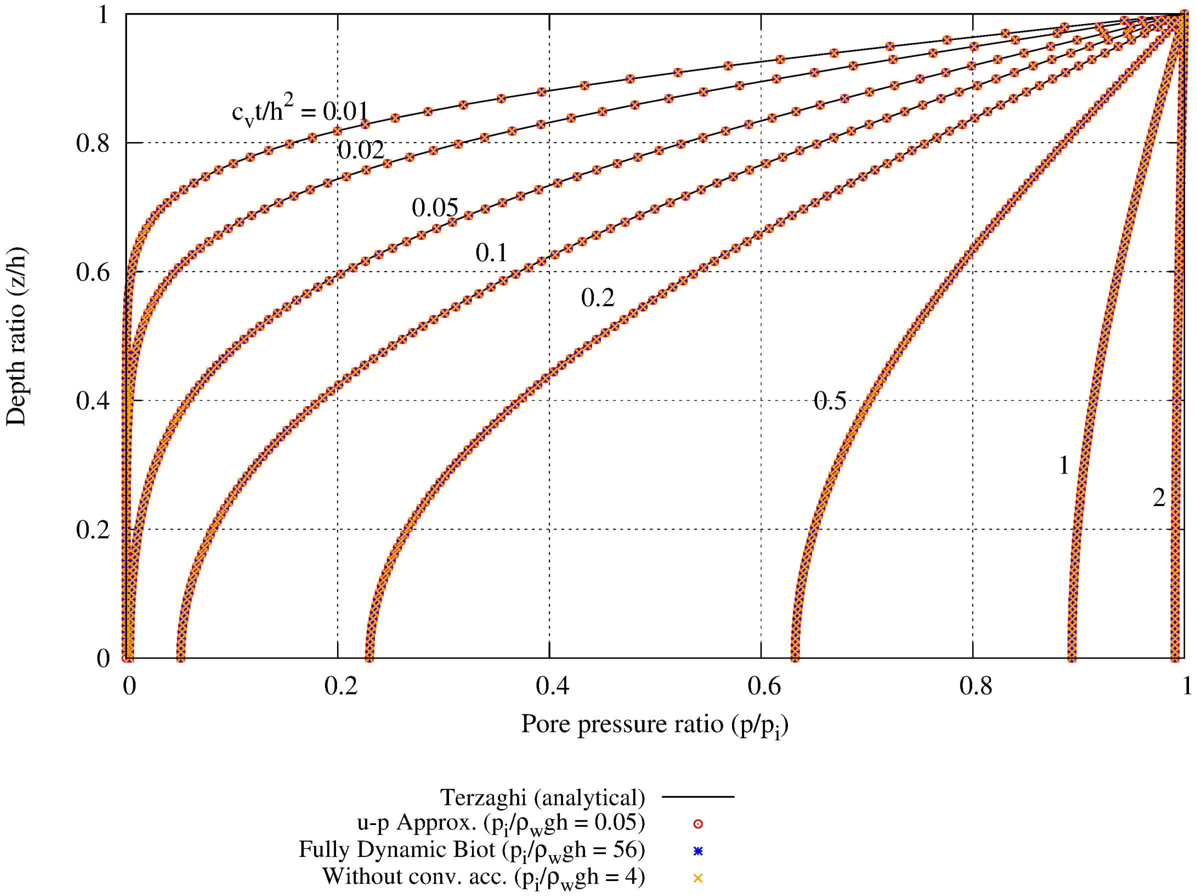

Figure 4.17: A Comparison of the three numerical approaches with the loading by fluid problem (S = 98.83%)

in the latter. Hence, the PISO based model calculates the total pore pressure as opposed to calculating the excess pore pressure in other approximations. It was observed that for the fully dynamic model the generation/dissipation of excess pore pressure is affected by the ratio of the excess pore pressure to total pore pressure (hydrostatic pressure included).

4.2.3 Wave-induced soil response

The effect of direct wave loading on an elastic seabed (without any structure) is studied using the three aforementioned approaches. The configuration of the problem is shown in Fig. 4.18. The considered wave conditions are given in Table 4.3. The excess pore pressure ratio (pore pressure to wave pressure amplitude (q_w)) in the horizontal section (A-A) is shown in Fig. 4.19. In Fig. 4.20, the excess pore pressure ratio for the vertical section (B-B) is presented. As shown in the results (Fig. 4.19 and Fig. 4.20), the three approaches give identical results for the pore pressure ratio. This means that direct seabed response is insensitive to dynamic effects of the pore fluid (as anticipated).

Table 4.3: Wave properties for wave-induced soil response validation case

Wave height (H)	1 m.
Wave length (L)	34.907 m.
Wave period (T)	5 s.
Water depth (d_w)	8 m.
Wave steepness. (H/L)	0.0286
Ratio of water depth to wave length (d_w/L)	0.2292

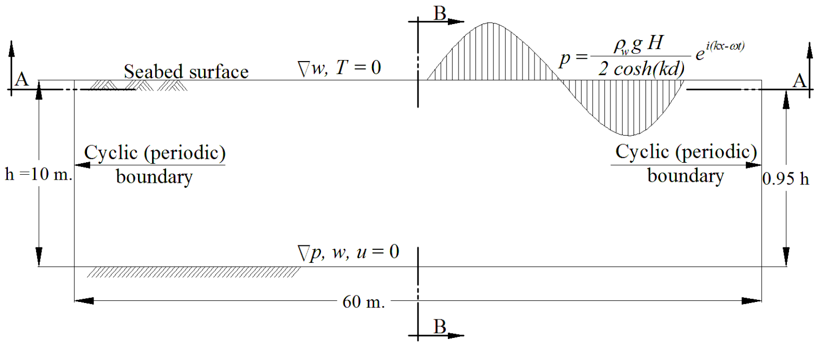

Figure 4.18: Computational domain of the elastic seabed subject to direct wave action (see results of corresponding sections A-A in Fig. 4.19 and section B-B in Fig. 4.20)

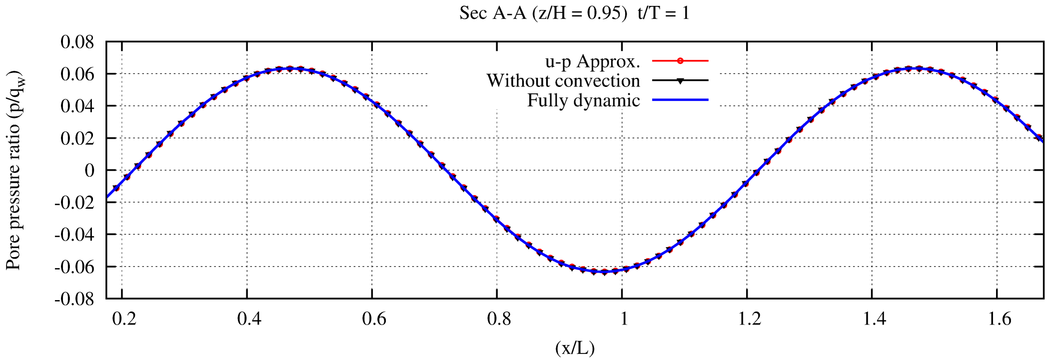

Figure 4.19: Pore pressure inside the seabed foundation (section A-A)

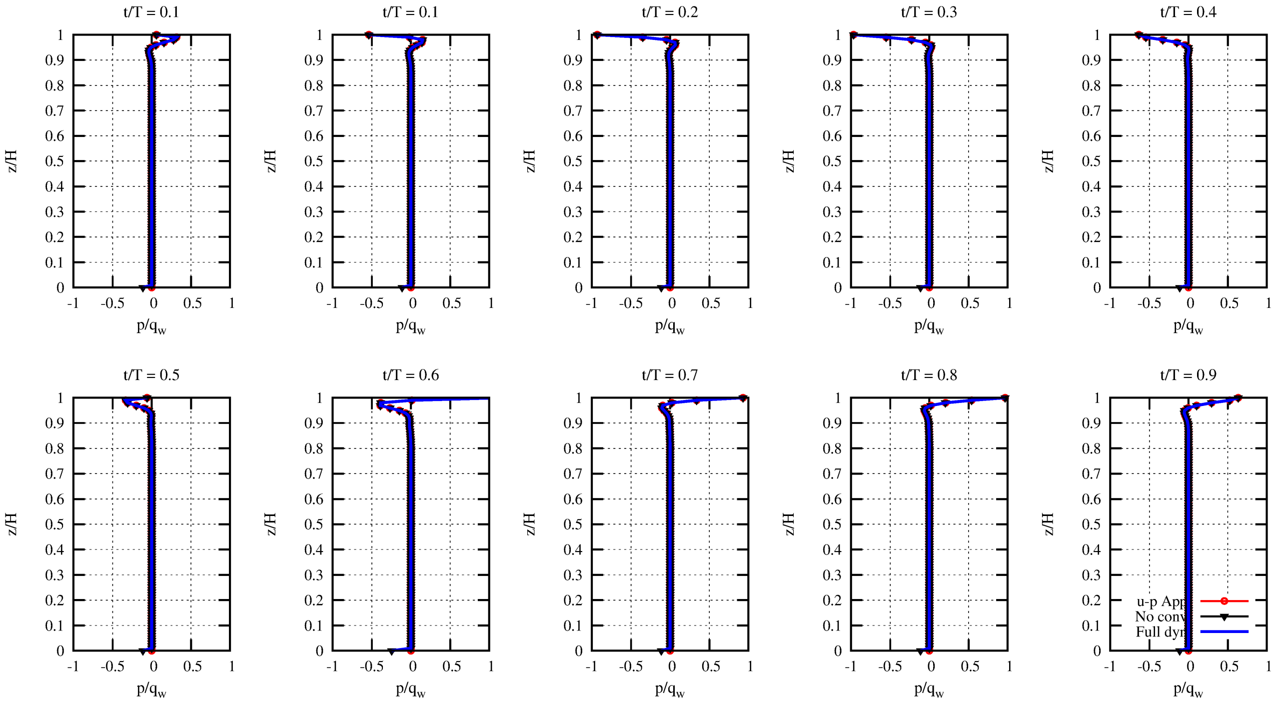

Figure 4.20: Pore pressure ratio to wave pressure amplitude (section B-B)

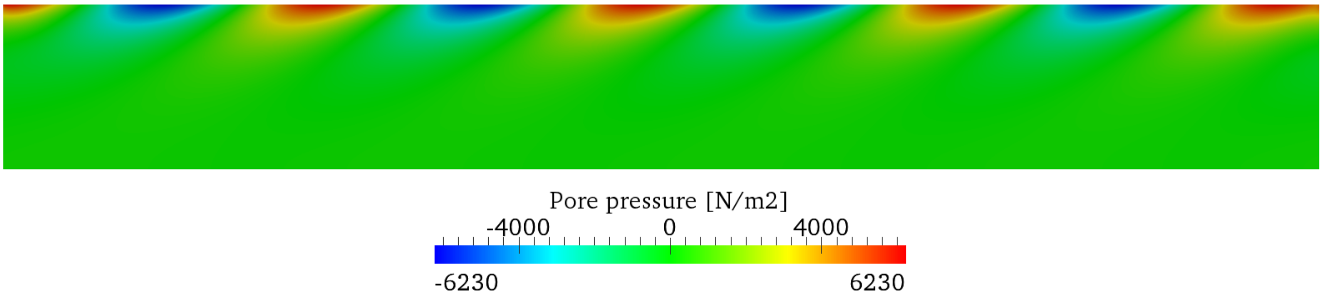

(a) Pore pressure in seabed loaded by direct wave action [N/m^2]

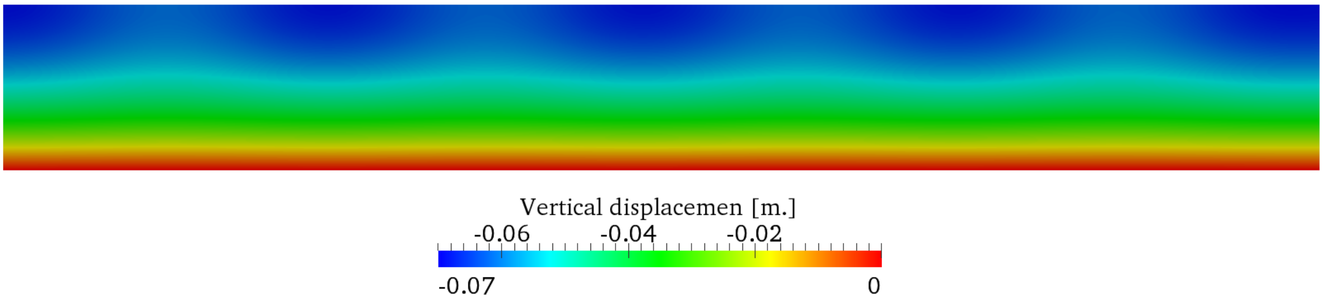

(b) Vertical displacement in seabed loaded by direct wave action [m]

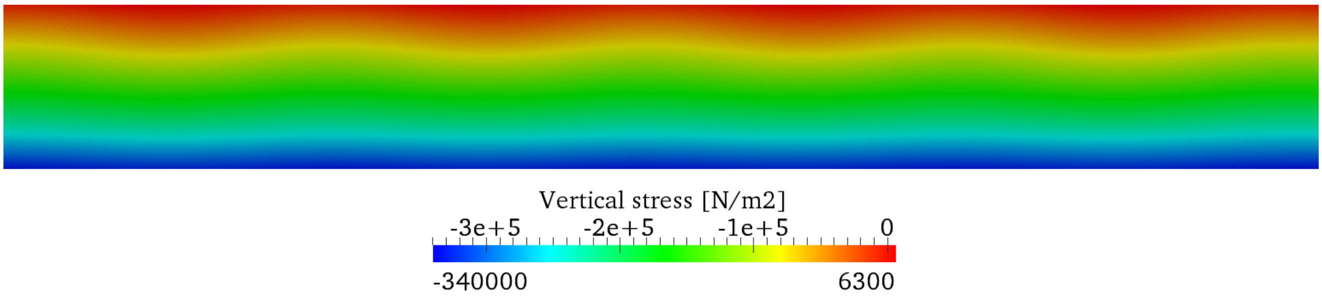

(c) Vertical stress in seabed loaded by direct wave action [N/m^2]

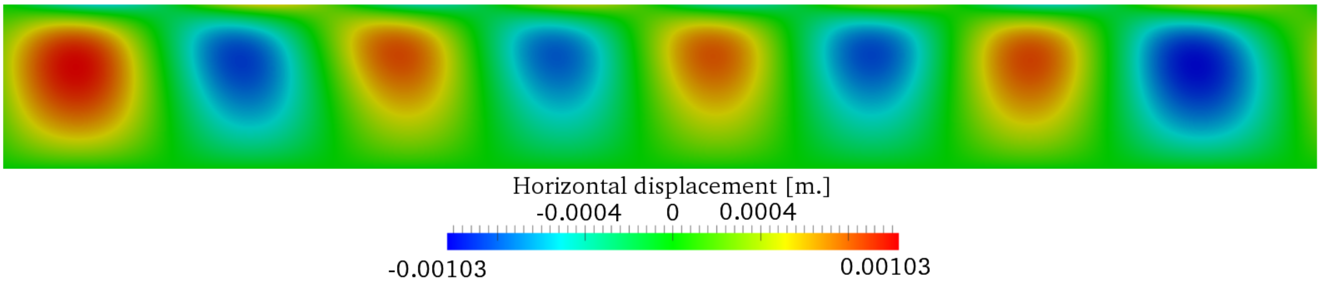

(d) Horizontal displacement in seabed loaded by direct wave action [m]

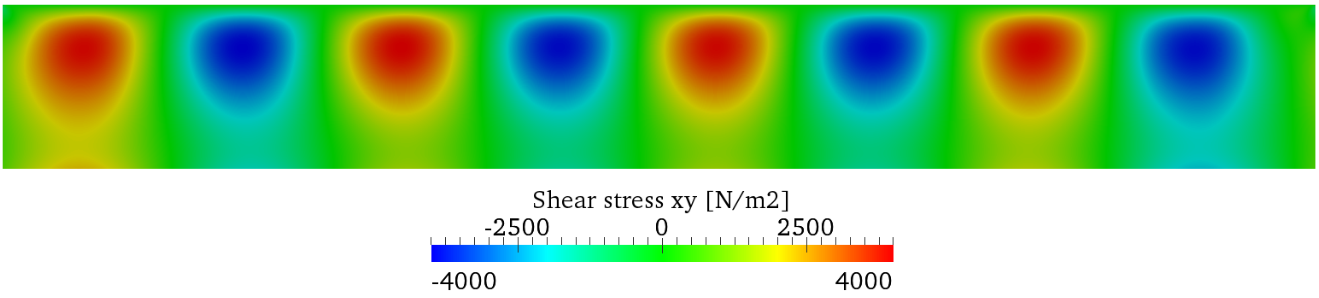

(e) Shear stress in seabed loaded by direct wave action [N/m^2]

Figure 4.21: Response of seabed to direct wave action

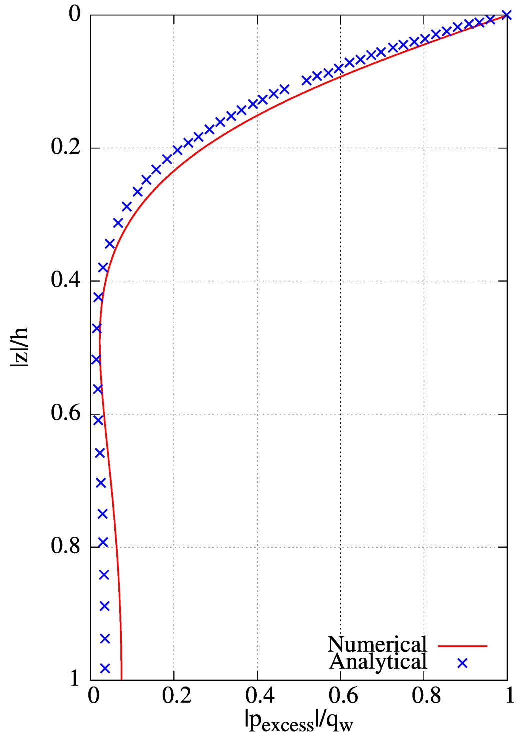

Figure 4.22: Validation of the pore pressure along the seabed depth against analytical solution by Jeng (1996)

An analytical solution to the problem of direct wave loading of elastic seabed has been introduced by Jeng (1996) based on Biot's poro-elastic (quasi-static) model. For validation, the configurations in Table 4.4 are used. The computed ($u - p$ approach) excess pore pressure profile, Fig. 4.22, compares well to the analytical solution by Jeng (1996). The results from this simulation are shown in Fig. 4.21 (excess pore pressure, vertical and horizontal displacement and vertical and shear stresses). In this figure, the solid-fluid coupling effects are obvious.

Table 4.4: Direct wave loading properties for validation case, Fig. 4.22

Wave height (H)	2.5 m.
Wave length (L)	48.382 m.
Wave period (T)	6 s.
Water depth (d_w)	10 m.
Wave steepness. (H/L)	0.0516
Ratio of water depth to wave length (d_w/L)	0.2067

4.2.4 Validation of multi-material interface correction

To test the implementation of the multi-material interface, a case is considered for applying a tensile stress (σ_0) to a plate consisting of three (or two) different elastic materials bonded together. The free-edge stress singularity near the interaction of the free surface and the interface of bonded materials is observed. The case geometry with associated mesh are shown in Fig. 4.23. The only variable geometry parameter is the mid-layer thickness, h, being 0, $0.002W$, $0.005W$ and $0.01W$, where $2W$ is the plate width. The used mesh densifies towards the multi-materials interface and the free edge with aspect-ratio progression in both directions.

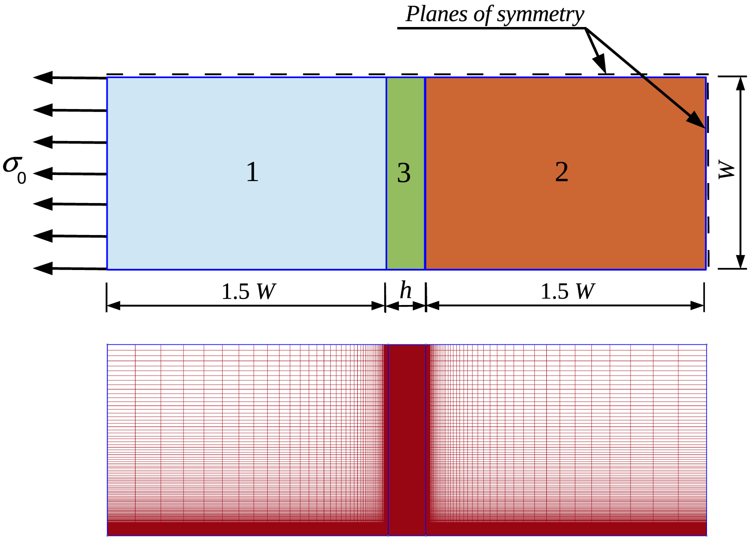

Figure 4.23: Multi-material plate in tension: geometry and mesh

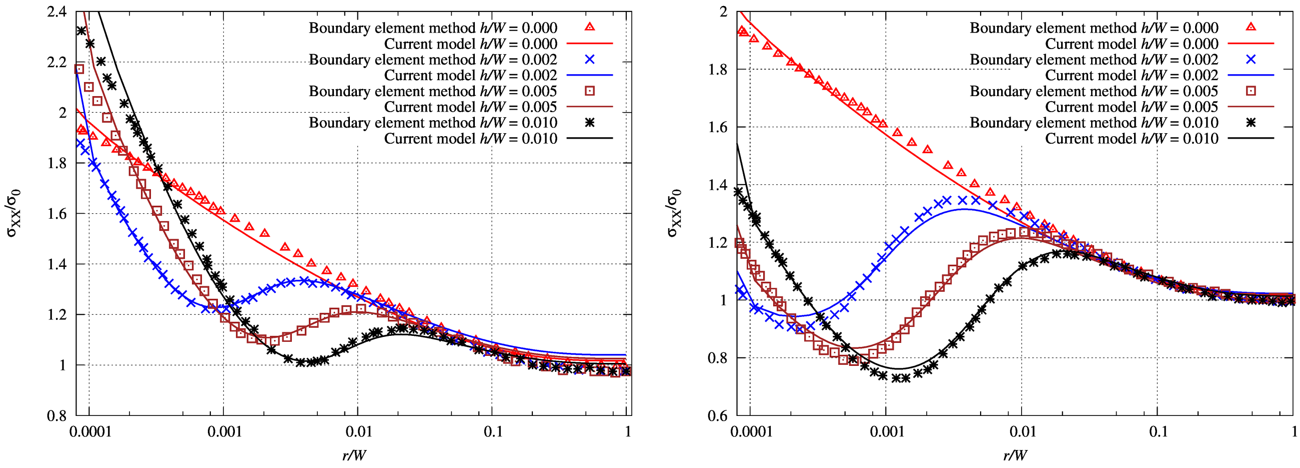

(a) Interface 2-3

(b) Interface 1-3

Figure 4.24: Normal stress distribution along multi-material interfaces: (a) interface 2-3 and (b) interface 1-3

The case is analyzed with a plane strain assumption. The tensile stress is applied at the left boundary, whereas the right boundary is modelled as symmetry plane. Because of symmetry, the upper boundary is also modelled as symmetry plane, whereas other boundaries are stress-free. The material properties used for this case are given in Table 4.5.

Table 4.5: Material properties used for the tension of a plate with different materials validation case

Property	Material 1	Material 2	Material 3
E, GPa	206.0	70.3	4.93
ν	0.3	0.345	0.33

The results from this case are compared to results from Ioka et al. (2007) (according to Tuković et al. (2013)). Ioka et al. (2007) studied the same problem using the boundary element method. Normal stresses, σ_{xx} , along interfaces between materials 1 and 3 (interface 1-3), and 2 and 3 (interface 2-3), are monitored for four different mid-layer thicknesses. Fig. 4.24 shows a comparison between calculated stress distributions with results from Ioka et al. (2007), as can be seen the results compare well. The validation of the multi-material interface correction is important to ensure correct transfer between the structure and the underlying foundation.

4.2.5 Validation of the contact problem

To verify the implementation of the contact model, the simple 2D cylinder-brick contact case from Jasak and Weller (2000b) is considered, Fig. 4.25. A constant traction is introduced at the top. A friction coefficient of 0.15 is considered. From the results in Fig. 4.26, it is apparent that the joining of the contact surfaces is achieved through iterations of the solution. The solution satisfies the symmetry although it was not imposed.

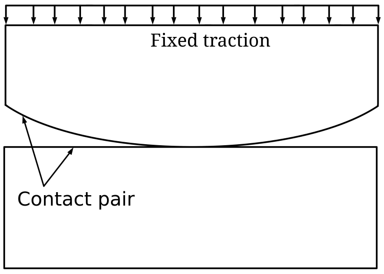

Figure 4.25: Geometry of the 2D elastic cylinder-half space contact from Jasak and Weller (2000b)

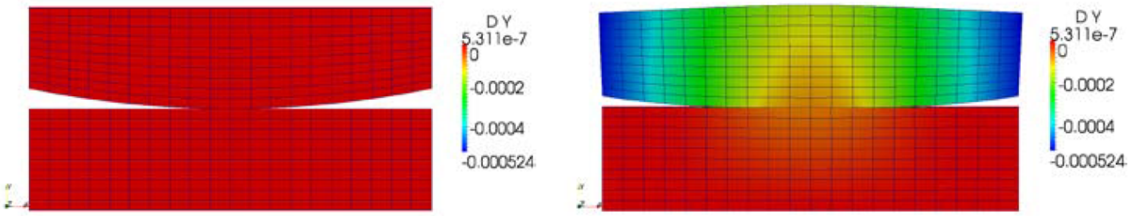

Figure 4.26: Development of the vertical displacement and the distorted mesh for the 2D elastic cylinder-half space contact case

To test the friction between both surfaces of the contact, the cylinder-brick case is considered with different configurations, in which the cylinder is forced to move horizontally (from left to right), Fig. 4.27, while subject to vertical traction. A friction coefficient ($\mu = 0.5$) was considered. As shown in Fig. 4.28, in the contact area the horizontal stress is roughly equal to the vertical stress multiplied by the coefficient of friction ($\mu = 0.5$ in this case), which implies that the friction implementation is working properly.

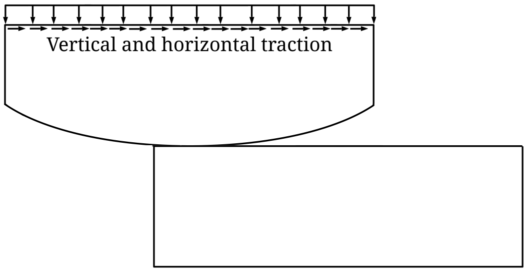

Figure 4.27: Configurations for a 2D elastic cylinder forced sliding over an elastic half-space

To validate the contact model, the 3D elastic frictionless contact between a sphere and a half-space is considered Fig. 4.29a. The Herzian analytical solution is used for comparison as in Cardiff et al. (2012). The block dimensions are 2mm × 2 mm with 1mm height. The ball radius is 1mm. Considering the results as shown in Fig. 4.29b, a comparison is given between analytically and numerically computed vertical, horizontal and Von Mises stresses. The Von Mises stress is a scalar value that is related to (and can be considered as a measure of) the deviatoric strain energy. The Von Mises stress is defined as:

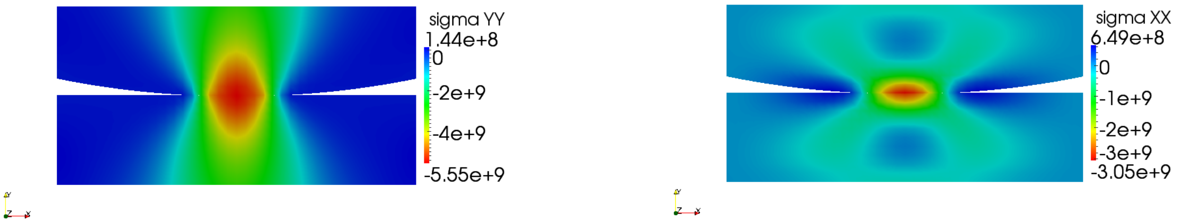

(a) σ_{yy}

(b) σ_{xx}

Figure 4.28: Vertical and horizontal stresses for a 2D elastic cylinder forced sliding over an elastic brick ($\mu = 0.5$)

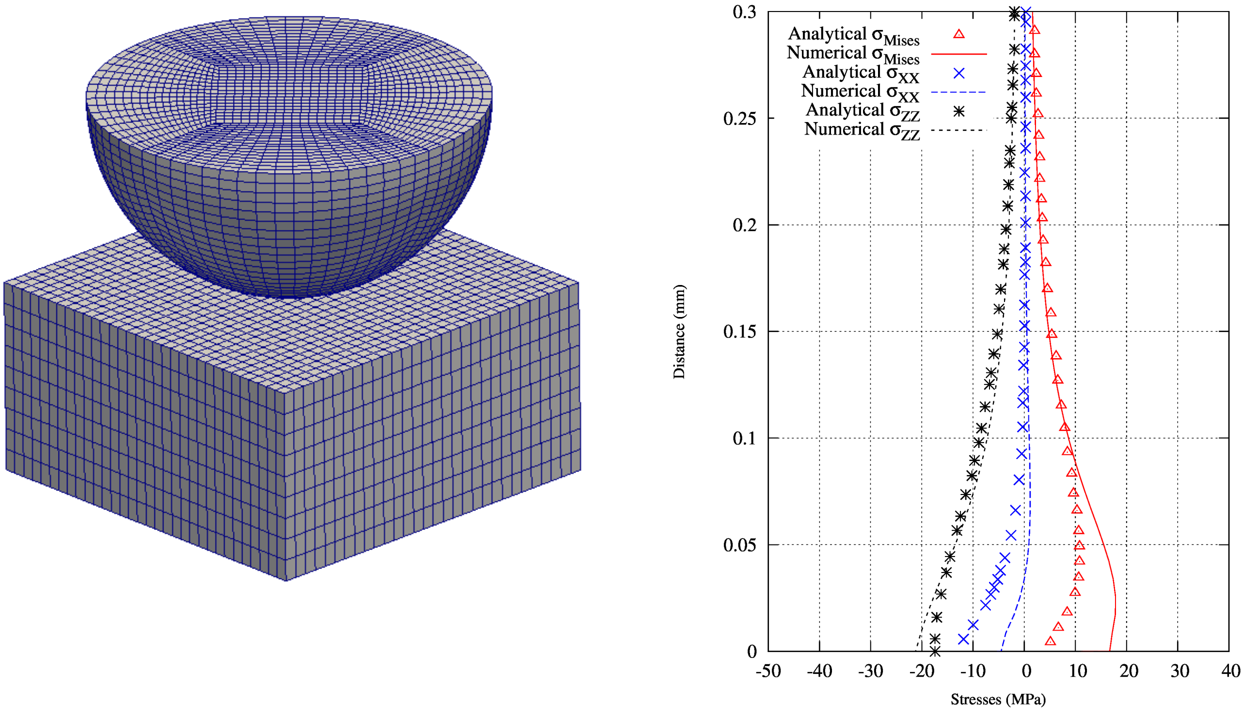

(a) Mesh of the 3D frictionless elastic sphere-brick contact case

(b) Stress distribution along y-axis in the center of the domain of the 3D frictionless elastic sphere-half space contact case

Figure 4.29: Stress distribution along y-axis in the center of the domain of the 3D frictionless elastic sphere-half space contact case

$$\sigma_{VM} = \sqrt{\frac{3}{2}\mathbf{s} : \mathbf{s}} \tag{4.115}$$

and the deviatoric strain energy is defined as:

$$W = \frac{1}{2}\mathbf{s} : \epsilon \tag{4.116}$$

It is shown that the contact model implementation in the solver yields relatively acceptable results.

4.2.6 Validation of the plasticity model

In this subsection, centrifuge tests are used for the validation of the plasticity constitutive model. The centrifuge tests were conducted mainly to assess the performance of liquefaction countermeasure techniques for a soil embankment resting on a liquefaction-prone foundation (Adalier et al. (1998). The used test data are retrieved from Elgamal et al. (2002). Only the test without any liquefaction countermeasure (basic configuration) is used for the validation.

As the tests are not completely described, they are used herein only to test the capability of the model to simulate buildup and dissipation of pore pressure induced by the dynamic excitation of the soil foundation underneath the embankment. The test setup is given in Fig. 4.30. The test was carried out under centrifuge-induced gravitational field of 75 g; where g is the gravitational acceleration. The embankment and the soil foundation beneath it are equipped with pore pressure transducers (PPT), accelerometers (ACC) and linear variable differential transducer (LVDT) to measure displacements.

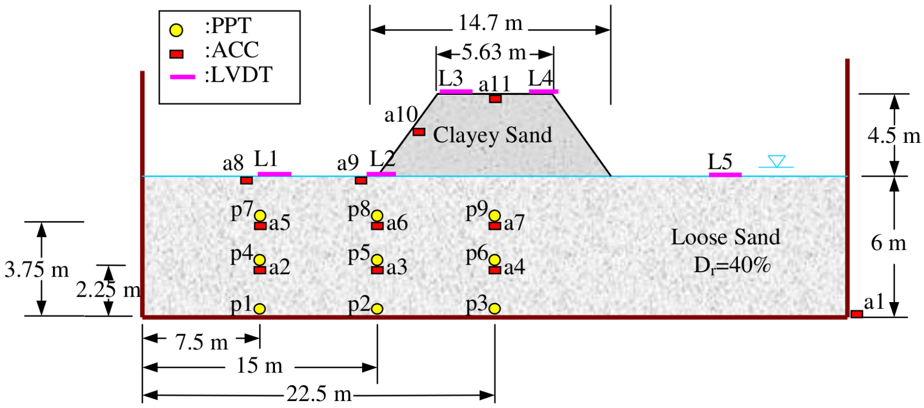

Figure 4.30: Centrifuge model setup (Adalier et al. (1998), PPT is Pore-Pressure Transducer, ACC is Accelerometer, LVDT is Linear Variable Differential Transducer to measure displacement)

The numerical model mesh for the test case is given in Fig. 4.31. In this figure, the position of the three points (S_1, S_2 and S_3) is given. Stress path and shear stress history are sampled from the numerical simulation for these points. Further, the boundary conditions are given in Fig. 4.31. Zero pore pressure is imposed at the top of the embankment and foundation, and zero pore pressure gradient (wall condition) at the bottom and sides of the soil foundation. For the displacement boundary condition, a zero load (free traction) boundary condition is set at the top of the embankment and soil foundation, while a predefined displacement history (according to shaking acceleration) is set at the bottom and the sides of the soil foundation.

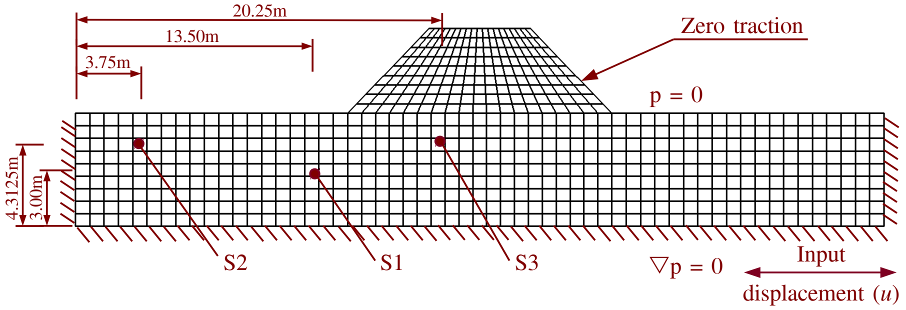

Figure 4.31: Numerical mesh, boundary condition and stress and strain sampling positions (S_1, S_2 and S_3)

The input signal of the shaking acceleration is given in Fig. 4.32a. Other numerically sampled accelerations at accelerometer positions a_7, a_9 and a_{11} are also shown in Fig. 4.32. The measured accelerations from

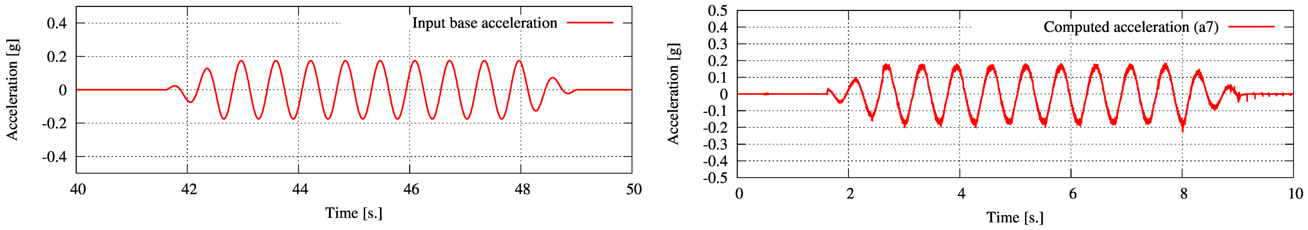

(a) Applied acceleration at base shaking

(b) a_7

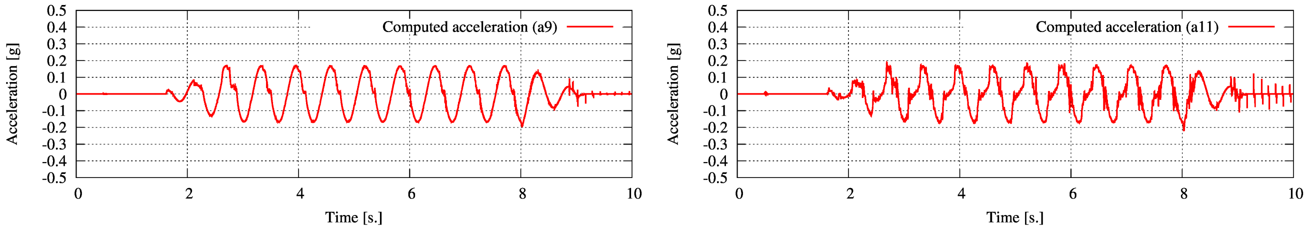

(c) a_9

(d) a_{11}

Figure 4.32: Horizontal input acceleration at base shaking and horizontal accelerations reproduced by the numerical hydro-geotechnical model at position of accelerometers (a_7, a_9 and a_{11})

the centrifuge test are shown in Fig. 4.33 (Elgamal et al., 2002).

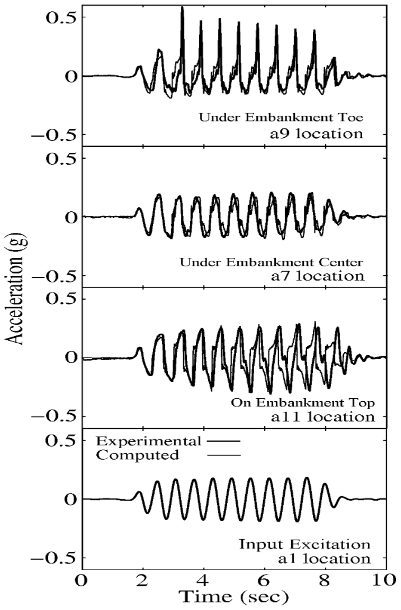

Figure 4.33: Computed and experimental lateral acceleration histories (Elgamal et al., 2002)

The pore pressure measured in the centrifuge tests for pore pressure transducers p_7, p_8 and p_9 is illustrated in Fig. 4.34 (Elgamal et al., 2002). The sampled pore pressure from the numerical model from different pressure transducers is shown in Fig. 4.35. As shown in Fig. 4.32 , 4.33, 4.35 and 4.34, although detailed soil properties of the embankment and the underlying foundation are not available, a very good agreement between the results from the numerical model and those from the centrifuge test could be achieved. The quality of the comparison between the numerical results and the measurements can be further enhanced, if detailed soil properties and test configurations were available.

The sampled horizontal displacement for different positions of the LVDT devices L_1, L_2 and L_3 are shown in Fig. 4.36. It is evident that at the end of the base shaking, residual (plastic) displacements are developed and LVDT devices cannot be retrieved to their original positions even with the dissipation of accumulated pore pressure.

Sampled shear stress history and effective stress path for the locations S_1, S_2 and S_3 are given in Fig. 4.37 and 4.38, respectively. These three locations are defined as follows: (i) Below the embankment toe (S_1), (ii) Below the embankment center (S_3) and (iii) Free field away from embankment (S_2). The deformation (shear strain, Fig. 4.37) and the stress path (Fig. 4.38) underneath the embankment toe shows the ability to simulate the cycle-by-cycle shear strain accumulation and the gradual loss of shear strength.

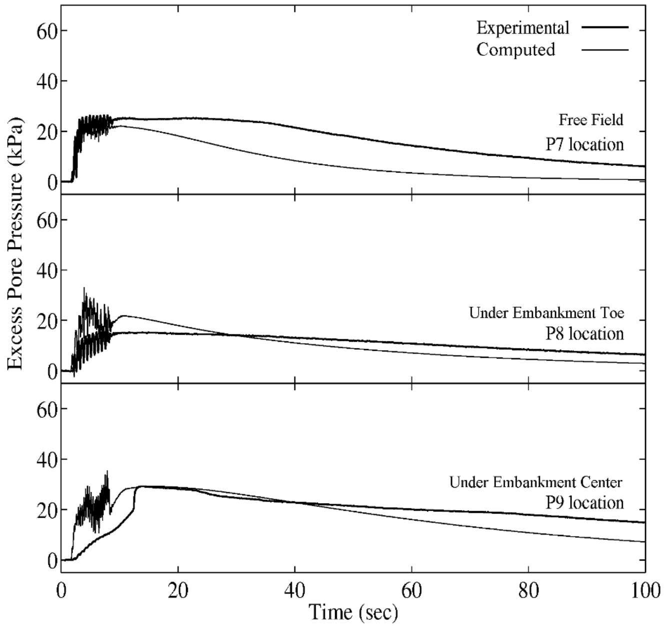

Figure 4.34: Computed and experimental excess pore-pressure histories (Elgamal et al., 2002)

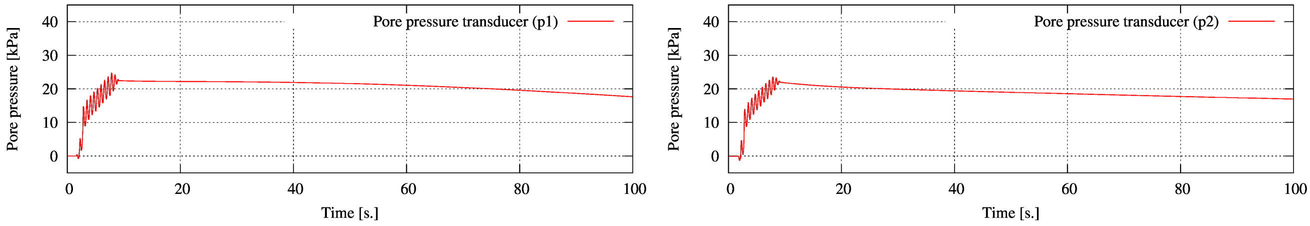

(a) p1 (b) p2

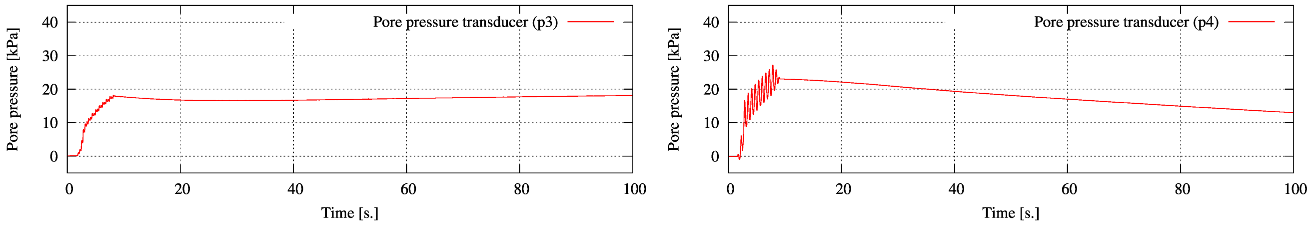

(c) p3 (d) p4

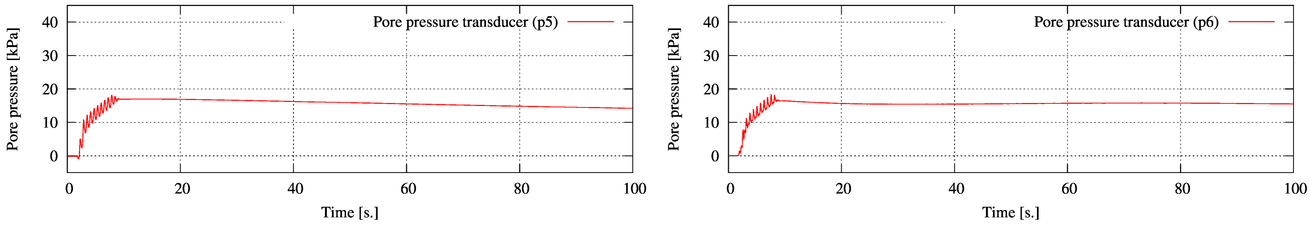

(e) p5 (f) p6

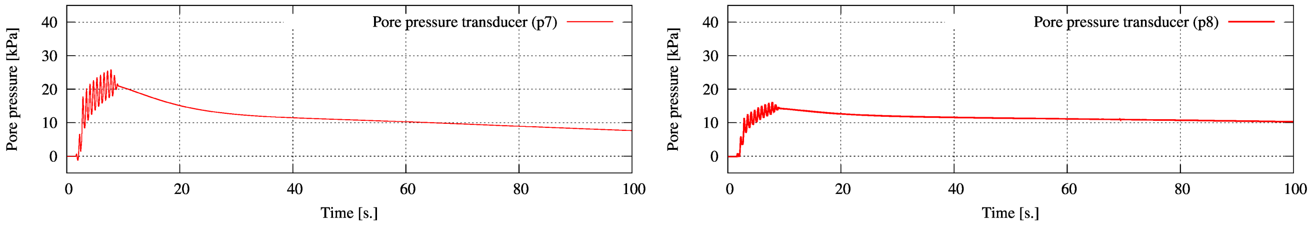

(g) p7 (h) p8

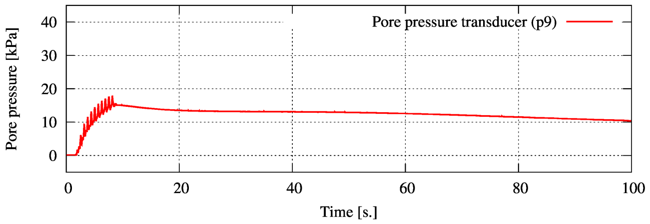

(i) p9

Figure 4.35: Pore pressure reproduced by the numerical hydro-geotechnical model at positions of different pressure transducers

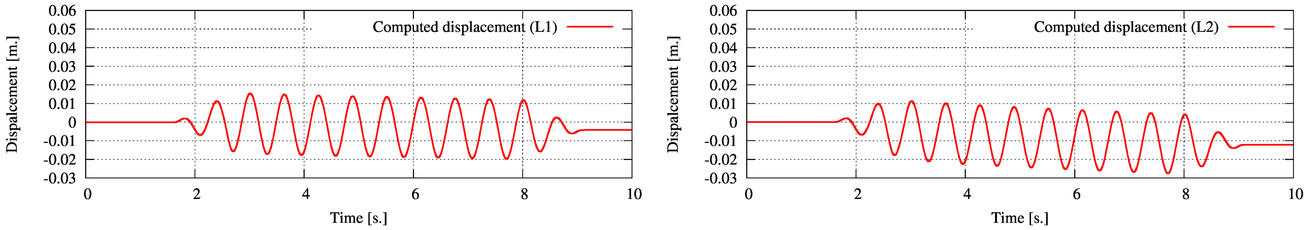

(a) L1 (b) L2

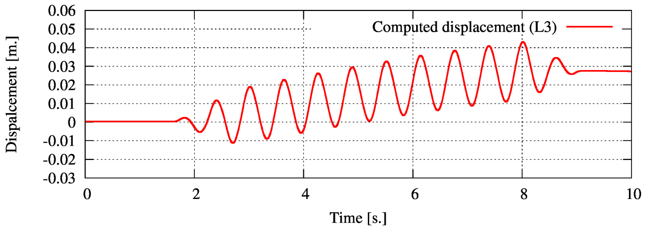

(c) L3

Figure 4.36: Displacements at positions of LVDT devices

Finally, the deformed geometry and residual pore pressure at the end of the base shaking are shown in Fig. 4.39. As presented in this subsection, the numerical model with the implemented soil constitutive model enables acceptable simulation of development of plastic deformations and pore pressure buildup and subsequent pore pressure dissipation due to dynamic excitation (base shaking).

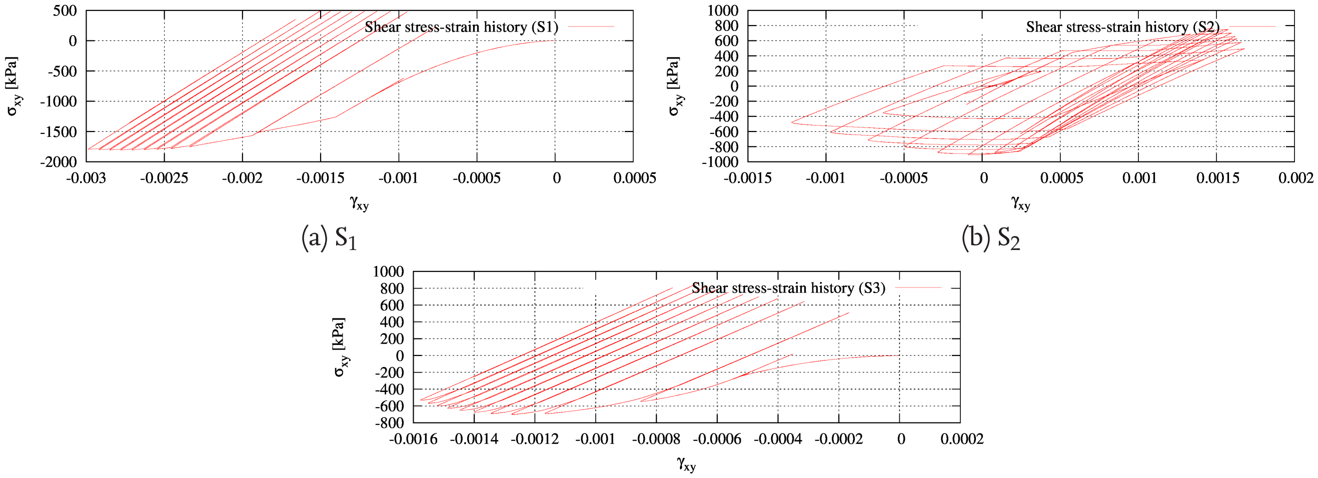

(a) S_1

(b) S_2

(c) S_3

Figure 4.37: Shear stress-strain history at positions (S_1, S_2 and S_3)

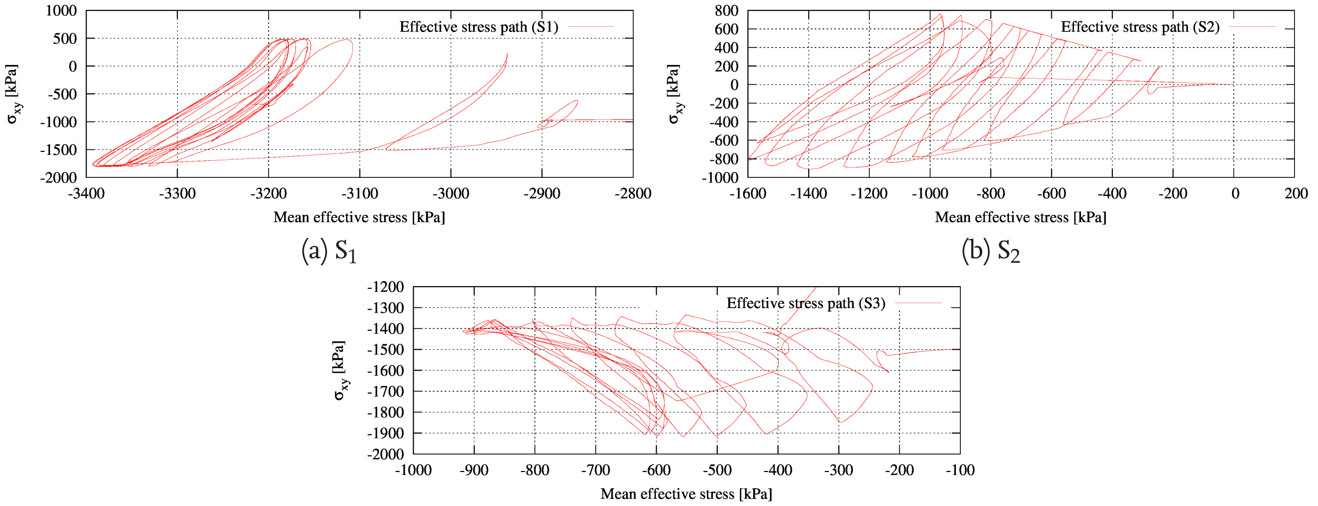

(a) S_1

(b) S_2

(c) S_3

Figure 4.38: Effective stress path at positions (S_1, S_2 and S_3)

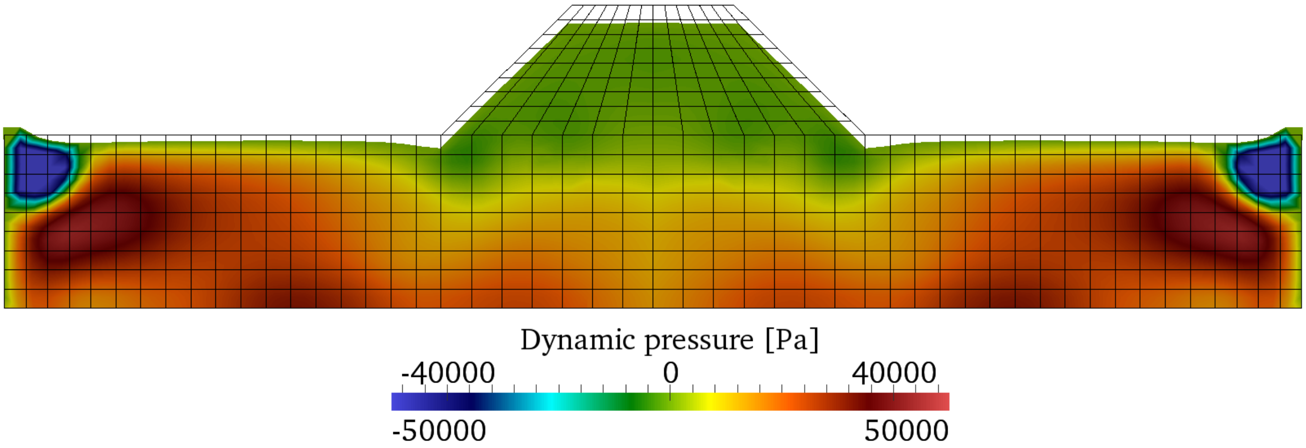

Figure 4.39: Deformed geometry and pore pressure at end of base shaking

4.2.7 Pore pressure buildup in the subsoil under a vibrating plate

Sumer et al. (2008) presented a simplified physical model to mimic the pore pressure buildup in the subsoil under a caisson breakwater. Based on the results of Kudella et al. (2006), Sumer et al. (2008) model isolates the caisson rocking motion (due to wave impact) as the main cause of pressure buildup in the seabed foundation. It is idealized as a rocking motion of a plate slightly buried in the seabed foundation, Fig. 4.40.

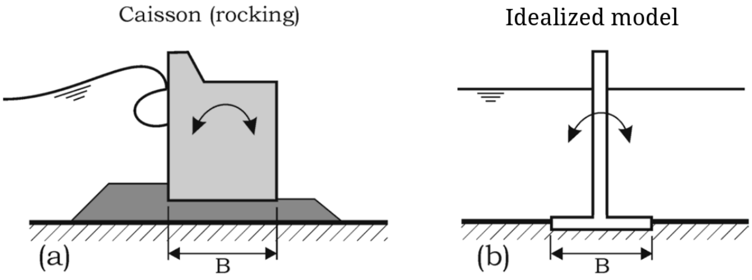

Figure 4.40: Idealization of caisson breakwater for laboratory experiments (Sumer et al., 2008).

The pore pressure inside the soil foundation was measured using transducers (mounted on pressure racks) distributed as shown in Fig. 4.41c. The objectives of the study by Sumer et al. (2008) were to examine the pore pressure buildup systematically; and to generate data that can be used to validate advanced numerical models as a benchmark case. In this regard, Sumer et al. (2008) acts with the study of Kudella et al. (2006) as a complementary source of information on the generation/accumulation and subsequent dissipation of pore pressure in the subsoil underneath a gravity marine structure (i.e. a caisson breakwater).

The seabed foundation is modelled as a soil box with 90 cm in length, 17 cm in depth and 57 cm in width (out-of plane). The soil box is immersed in water (placed in a wave flume), Fig. 4.41a. Experiments were carried out with the rocking-plate (plate A, in Fig. 4.41a) partially buried in the soil (the burial depth being 1.5cm). This was arguably to avoid for the plate to lose contact with the soil across one half of the plate when the other half was inside the soil during the course of the rocking motion. According to Sumer et al. (2008), this procedure was particularly important for larger rocking motions. The water depth inside the wave flume was 42 cm.

The seabed consists of silty soil, with d_{50} = 0.045 mm. The specific gravity of grains, $s = \rho_s \;/\; \rho_w$ = 2.65. The saturated density of soil, ρ_{sat} = 2054 kg/m^3, and the submerged density of the soil, $\rho_{sub} = \rho_{sat} - \rho_w$ = 1054 kg/m^3. The friction angle, $\phi = 36^o$. The coefficient of lateral earth pressure, k_0 = 0.41. The relative density of soil was estimated as D_r = 0.38 ± 0.01. Nevertheless, as described in Sumer et al. (2008), the soil properties were retrieved after the test, which justifies the unconventionally high values for soil density and angle of friction. The soil properties were measured after the soil has been densified throughout the test. Therefore, other more conventional values for a loose sand are assumed for the numerical simulations (Table 4.6).

The experimental procedure for soil placement is considered to ensure minimum air content in the soil, as the soil is placed in the water gently by hand, rubbing the soil between the fingers to get rid of air bubbles while placing it in the water, and crushing soil lumps, to ensure an even soil texture across the entire box.

The testing conditions included four different plate burial depths (including zero burring depth), five different rocking amplitudes and five different rocking periods. The plate was rocking according to a simple harmonic excitation, for which the vertical distance of the plate end (y) is described by:

$$y = A \sin\left(\omega t\right), \tag{4.117}$$

where A is the amplitude as defined in Fig. 4.41b, ω is the angular frequency ($\omega = 2\pi/T$), t is time and T is the rocking period.

Table 4.6: Considered soil properties for numerical simulation of rocking plate on an immersed sand box

Saturated density (ρ_{sat})	2054 kg/m^3
Angle of internal friction (ϕ)	30^o
Phase transformation angle (ψ)	27^o
Peak shear strain (γ_p)	0.1 [-]
Cohesion (c)	300 Pa
Modulus of elasticity (E)	48.382 Pa
Poisson's ratio (ν)	0.3 [-]
Porosity (n)	0.4 [-]
Hydraulic conductivity (k)	10e^{-05} m/s
Ratio of water depth to wave length (d_w/L)	0.2067 [-]

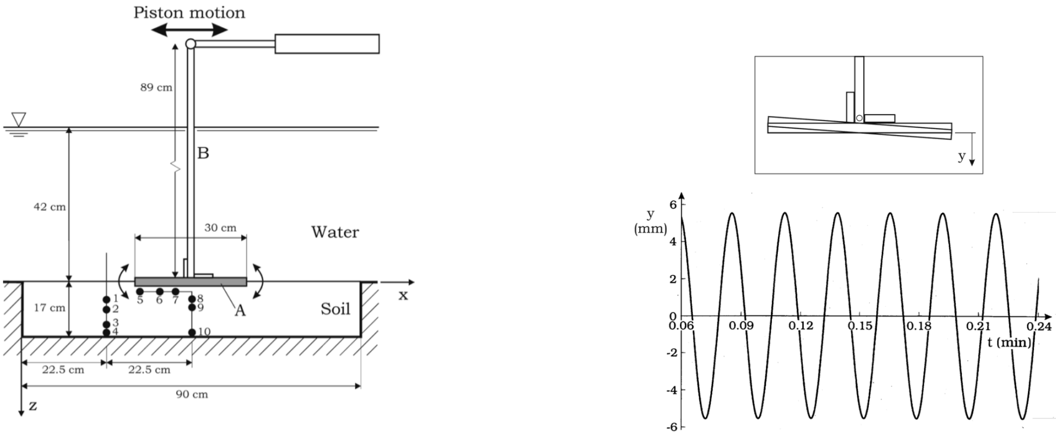

(a) Rocking-plate (caisson breakwater model), soil box, and pore pressure measurement positions

(b) Time series of the vertical displacement of the bottom corner (offshore/onshore) of the model structure

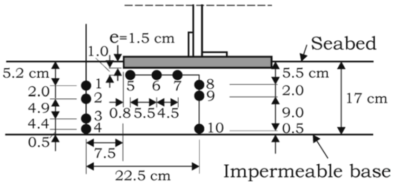

(c) Position of pore pressure transducers underneath rocking-plate (detailed)

Figure 4.41: Test setup for the rocking-plate physical experiments (Sumer et al., 2008)

Because accurate properties of the seabed soil before the test are not available, this test can also be used as a proof of model ability to reproduce the same behaviour as observed in the physical model qualitatively rather than quantitatively. Applying the plate rocking motion to the sand foundation, residual pore pressure develops across the soil foundation. This is shown in the excess pore pressure colour map given in Fig. 4.42 at the start of the simulation (after 1.02 s.) and after considerable loading time (38.85 s.).

Considering the sampled computed excess pore pressure at two different positions: p_1 and p_3, Fig. 4.43, the model is capable of reproducing the physically recorded behaviour of the sand foundation. The residual (excess) pore pressure is buildup during loading of the foundation until a peak of the pressure is reached (similar to the saturation point S described by Kudella et al. (2006)), then the residual pore pressure reduces with time to a minimum value (approaching zero), although the cyclic load is still applied. The behaviour is similar to the behaviour recorded in the physical large-scale breakwater experiments in the GWK (Kudella et al., 2006). The behaviour is associated with soil densification caused by cyclic loading, in which the pore

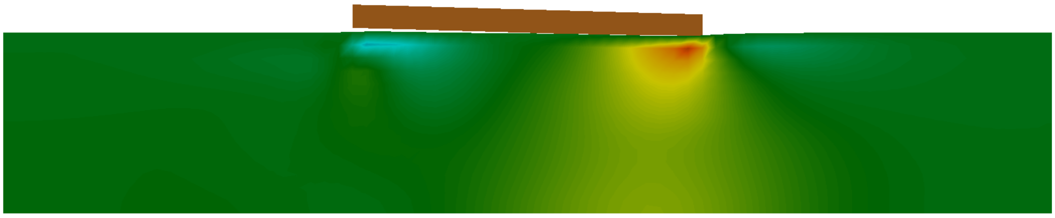

(a) 1.02 s.

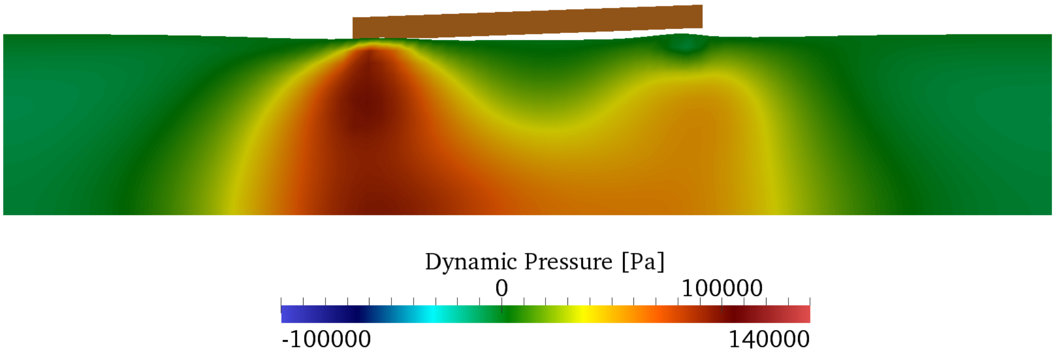

(b) 38.85 s

Figure 4.42: Numerical results of pore pressure for the rocking plate on sand box experiments (A = 1.4 mm and T = 1.6 s.); development of residual pore pressure

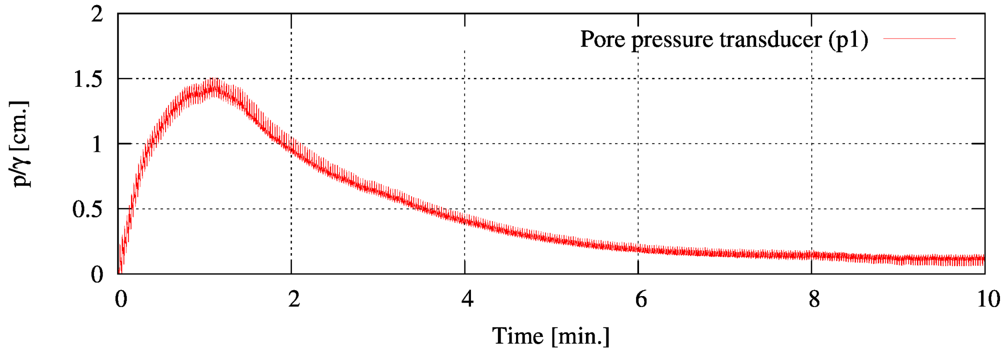

(a) p1

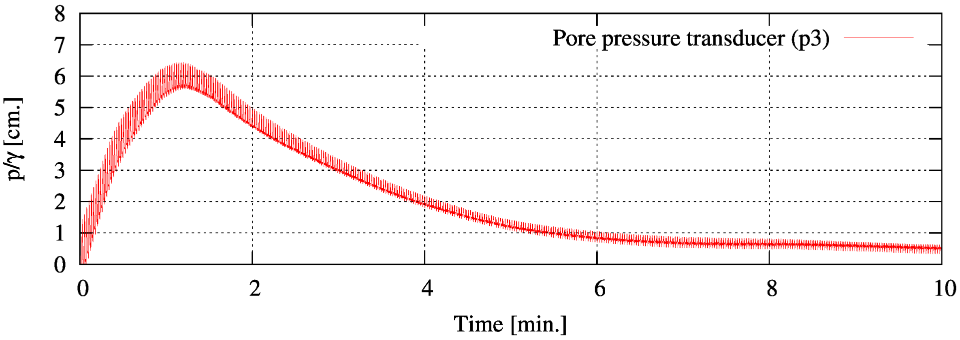

(b) p3

Figure 4.43: Pore pressure inside sand in the rocking plate on sand box experiments (A = 1.4 mm and T = 1.6 s.)

pressure generation surpasses its dissipation during the densification of soil (soil plastic contraction) until maximum densification (contraction) associated with the applied dynamic load is reached (the saturation point); then the pore pressure generation (from soil contraction) becomes less than the pore pressure dissipation (from diffusion/drainage).

4.3 Summary and Concluding Remarks for The CSD Model

In this chapter, a new numerical geotechnical model is developed to simulate the poromechanical behaviour of soil. The solver uses the finite volume method with a segregated algorithm to model the solid-skeleton pore fluid coupling. The *geotechFoam* solver has three options for solving the fully coupled Biot's equation:

1. Fully dynamic equations using the PISO algorithm to resolve the pressure-velocity coupling of the pore fluid
2. Fully dynamic equations, neglecting the pore fluid convection
3. The $u - p$ approximation, in which the pore fluid acceleration is fully neglected and the pore fluid momentum balance equation is implemented in the pore fluid mass balance equation rather than being solved explicitly

Different material constitutive models can be considered for different zones of the domain. Two models were implemented: a linear elastic and a multi-surface elastoplastic soil constitutive model. Additionally, a correction of traction at the interface of different materials was implemented. Further, a frictional contact model was implemented to model soil-structure interaction (i.e. soil-structure separation and reattachment and frictional sliding). The implementation in the OpenFOAM framework allows for three dimensional simulations with parallelization enabled through the domain decomposition approach.

The *geotechFoam* solver is validated using several test cases:

- **One-dimensional consolidation**: the results are validated against the theoretical solution of Terzaghi displaying ability of model to properly dissipate pore pressure
- **One-dimensional loading by fluid**: the results are validated against a theoretical solution adapted from Terzaghi's consolidation problem. This case displays the ability of model to properly accumulate pore pressure
- **Two-dimensional water wave loading on elastic seabed without a structure** in this validation case a two-dimensional seabed with periodic (cyclic) boundaries on both sides and linear wave theory used for input of fluid pressure on seabed. The results are validated against analytical solution from Jeng (1996)
- **Tension of a plate with different materials** to validate the implementation of multi-material interface traction correction (for adjacent materials of different properties, e.g. caisson and its foundation) against results using the boundary element method
- **Two-dimensional frictional cylinder-brick contact problem** to validate frictional contact, tangential and normal stresses comparison
- **Three-dimensional frictionless ball-brick contact problem** to validate implementation of (frictionless) contact model against the Herzian analytical solution
- **Centrifuge tests of embankment on liquefaction-prone soil foundation** to validate the ability of the implemented soil constitutive model to simulate buildup of pore pressure and plastic deformations

in sand foundations subject to base shaking (i.e. seismic action). The simulations are compared to results from the centrifuge model tests from Adalier et al. (1998)

- **Rocking plate on a sand box** to validate the ability of the model to simulate pore pressure buildup and subsequent densification of soil in response to loading similar to loading exerted by the caisson breakwater rocking motion. The simulations are compared to results from physical model tests from Sumer et al. (2008)

Main outcomes of the developed hydro-geotechnical (*geotechFoam*) model:

- The segregated algorithm used for the *geotechFoam* solver was implemented successfully for the fully coupled, fully dynamic poro-mechanical analysis. The segregated approach enables ease of adding or manipulating different parts of the model (e.g. soil constitutive model)
- The fluid momentum balance is solved in the newly proposed fully dynamic PISO based approach instead of being considered implicitly in the mass conservation equation in other approaches (e.g. $u - p$ approach). Hence, the PISO based model calculates the total pore pressure instead of calculating the excess pore pressure in other approximations. It is further observed that for the fully dynamic model the generation/dissipation of excess pore pressure is affected by the ratio of the excess pore pressure to the total (hydrostatic included) pore pressure.
- Neglecting pore fluid convection for the fully coupled, fully dynamic model did not increase the speed of the solution because the pore fluid convection is part of the implicit part of the mixture momentum balance equation. Therefore, it is not advised to neglect pore fluid convection for the presented model
- The $u - p$ approximation reduces the computational time significantly for quasi-static poroelastic problems without soil-structure interaction and should be considered when it is proper to neglect the pore fluid acceleration relevant to the soil skeleton
- Pore fluid compressibility plays a significant role in transient response of both soil phases (i.e. pore pressure and skeleton deformation).
- For most cases, a water content value of 98.83% was found to provide best fit against analytical and validation data
- The multi-surface plasticity sand constitutive model can successfully reproduce buildup of pore pressure in sand foundation underneath caisson breakwater and subsequent densification of the foundation

5 CFD-CSD Model System

In this chapter, the CFD and the CSD models developed respectively in chapters 3 and 4, are semi coupled. First, the one-way coupling procedure and the developed coupling utilities are outlined. The CFD-CSD model system is then validated by large-scale physical model tests for the response of a caisson breakwater and its foundation to wave loads (hereafter called GWK tests) with a particular focus on the response of the soil foundation. Using the validated model system, a numerical parameter study is carried out to extend the range of conditions considered in the GWK tests. Further, a concept of load eccentricity is introduced to describe the wave loads and the structural properties implicitly. Using this new concept, the results of the numerical tests are analysed. An interpretation of the stepwise failure mechanism and a classification of the response of the structure and its foundation based on the load eccentricity concept is proposed. Further, the relative contributions of the effect of transient and residual pore pressure as well as structural configurations and soil drainage conditions to residual displacement of caisson are then discussed. Based on this proposed interpretation, recommendations are drawn for the cross section of the caisson breakwater to enhance structure response to breaking wave impacts Finally, the capabilities and limitations of the numerical model system are discussed, including a brief outlook.

5.1 One-Way Coupling: Justification, Procedure and Utilities

The knowledge of the physical processes involved in the interaction between fluid flow (CFD model), response of the caisson and its soil foundation (CSD model) is a prerequisite for modelling the coupling of both CFD and CSD models. Though modelling is not about replicating exactly all actual aspects of the entire real behaviour, considering interaction properly is still important to reproduce reliably at least the processes, which are most relevant for the specific problem under study.

Marine structures such as caisson breakwaters represent one of the real life examples in civil engineering of how crucial the proper consideration of interactions in modelling may be. The modelling of the interaction problem consists of three components: waves, caisson and soil foundation. Nevertheless, the interaction links among the different constituents are not equally significant. Depending on the specific problem under study, it is therefore up to the model developer to decide which links have to be focused upon in the modelling process and which other links can be disregarded for convenience. Consequently, decisions are based on experiences from previous models or by a trial and error procedure. In Fig. 5.1, processes involved in wave-structure-foundation interaction (basic interaction links between the three components) are shown. It is clear that scour is out of the scope of the PhD study and hence not considered. Another insignificant link would be wave transformation due to seabed deformation. A (highly) significant aspect, that is not illustrated in Fig 5.1, is the strong interaction between the solid skeleton and the pore fluid, which constitute components of the seabed when modelled as a porous medium (a strongly coupled solution).

There are, mainly, two approaches to achieve coupled physics in numerical modelling; monolithic and partitioned coupling approaches. The *monolithic* coupling is implemented at the governing equations level (e.g. fully coupled solid-fluid governing equations for modelling porous media). In the *partitioned* coupling approach, two separate domains are considered; each solved with different governing equations. For the hydro-geotechnical model (as presented in chapter 4) full monolithic coupling is considered between solid and fluid for the porous media.

The response of the relatively stiff and massive caisson structure and its foundation to wave loads generally results in too small caisson motions to significantly affect the waves and the flow field in front of the structure. Therefore, the effect of the caisson motions on the wave load at the structure front may be assumed to be negligibly small under normal wave conditions. However, this assumption becomes questionable for the wave uplift force beneath the caisson. In fact, the uplift force was shown by Oumeraci et al. (2001) to be strongly affected by the rocking motions of the caisson under extreme wave loading conditions (see Fig. 2.3), so that this interaction can be only be reproduced properly by a two-way coupling of the model for the wave load and that of the response of the structure and its foundation.

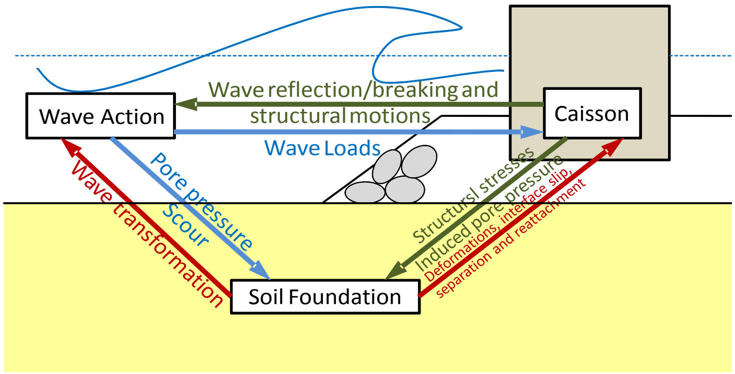

Figure 5.1: General concept and processes involved in wave-structure-foundation interaction

One-way coupling procedure is selected for the CFD-CSD model system, despite the aforementioned crucial issues and for the following reasons and considerations:

- The main objective of this study is to properly reproduce the stepwise failure mechanism in the soil foundation of caisson breakwaters, including the effect of transient and residual excess pore pressure generation on the residual soil deformations beneath the structure. This is achieved by the full coupling of solid-skeleton and pore fluid in the hydro-geotechnical model, which can describe both cyclic mobility and structure-foundation contact (see chapter 4)
- Using one-way coupling, the CFD and the CSD models are run separately; i.e. first, the CFD model is run and the results are then sampled to be used as input for the CSD model. Moreover, the aforementioned one-way coupling approach has the advantage of allowing the focus on different hydrodynamic and hydro-geotechnical processes involved separately without the need to rerun the CFD simulations for each run of the CSD model (no redundancies). This provides a faster means to develop and tune the CSD model and can be considered an acceptable approach for simulating monolithic concrete structures, which can be safely considered to pose only rigid body motion, it was not anticipated that updating the geometry of the problem in the CFD model will significantly change the results.
- Separate validation of the CFD and the CSD models as well as validation of the semi coupled model system furnish the way for the development of a two-way coupled model system, which will, unfortunately, not fit within the limited time frame of this PhD study

As shown in Fig. 5.2, results from the CFD model (as well as from the physical experiments) can be fed to the *geotechFoam* solver as input. The developed *data2TimeVaryingBC* utility can transfer output from the CFD model (or physical results processed by the developed *GWK2Plot* utility) into input for the boundary condition. The boundary condition can then do interpolation over time and space to meet discretisation of the domain for the *geotechFoam* solver. Another utility called *divideFile* was developed to divide the data files into several smaller files (of a given number of lines) to enable (otherwise impossible for some cases) or enhance the execution time and parallelization of use of the *data2TimeVaryingBC* utility. Fig. 5.3 shows the location of points used to sample the pressure in the CFD model for further use as input in the CSD model using the *data2TimeVaryingBC* utility.

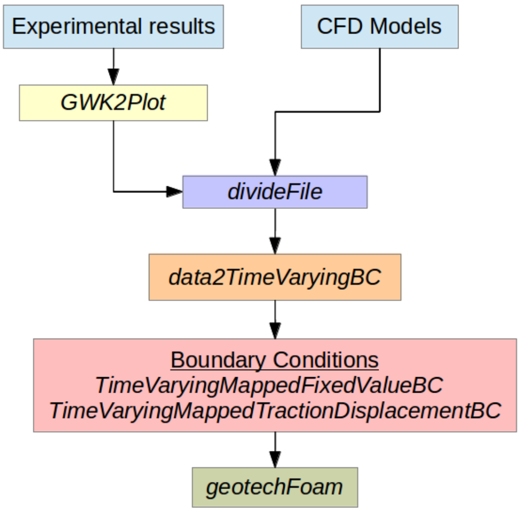

Figure 5.2: Linking utilities of the CFD-CSD model system

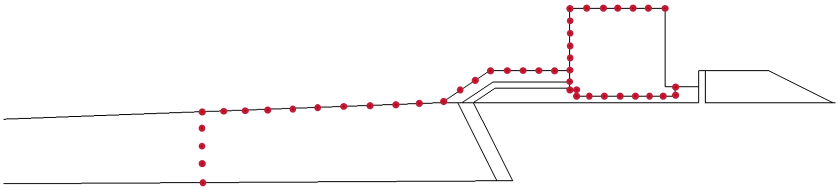

Figure 5.3: Sampling locations on shared interface surfaces between CFD and CSD model system used for the one-way coupling procedure

In summary, the coupling procedure between the CFD and the CSD models can be characterized by the following capabilities: (i) Each wave condition has to be simulated once for each structural configuration or material properties and (ii) Time and space discretization is performed independently in the CFD and CSD models. The coupling procedure has the following limitations: (i) It is less accurate than the two-way coupling approach (especially for uplift pressure) and (ii) It requires more intervention of the user (errors more likely).

5.2 CFD-CSD Model System Validation

In this section, the semi-coupled numerical model system is validated against GWK tests. In Subsection 3.2.2, the CFD mode was validated separately against the same physical model tests for the flow and pressures/forces on the structure. In Section 4.2, the CSD model was also systematically validated against benchmarking tests, analytical solutions, centrifuge tests as well as a simplified caisson breakwater physical model (rocking plate on a soil box). Herein, the validation is further extended to the CFD-CSD model system by testing the validity of the coupling procedure and the ability of the hydro-geotechnical model to reproduce the coupled soil-structure response.

The validation is performed for three load cases: (i) Non-breaking waves, (ii) slightly breaking waves and (iii) strongly breaking waves. Through the validation process, the results of the analysis of the structure response and comparison of the results from the fully coupled-fully dynamic implementation of Biot equations versus the $u-p$ approximation are presented.

5.2.1 Experimental Set-up and Soil Properties in the GWK Model

The experimental setup of the hydrodynamic part of the large-scale caisson breakwater physical model tests was already introduced in Subsection 3.2.2. The overall setup is given in Fig. 3.6. A cross section of the caisson breakwater mounted on top of the rubble and sand foundation instrumented with pore pressure transducers, stress measuring devices and displacement meters are illustrated in Fig. 3.7. The numbering of the measuring channels of pressure transducers and stress gauges are shown in Fig. 3.8. A cross section of the entire model used for the tests and the corresponding plan view are given in Fig. 5.4. In this subsection, more information is given on the construction procedure of the experimental setup and the properties of the used materials (e.g. soil properties) which may be relevant for the model implementation and validation.

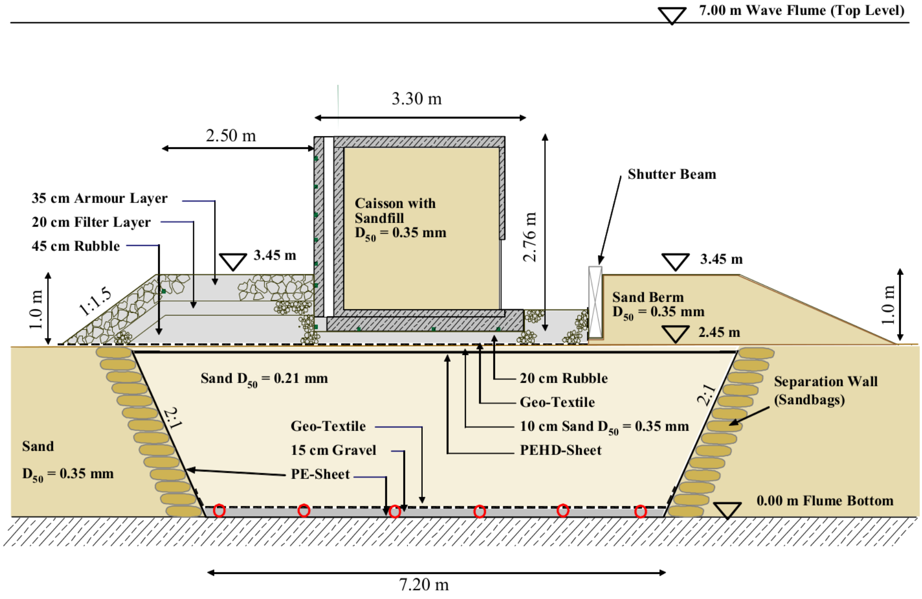

(a) Cross section elevation

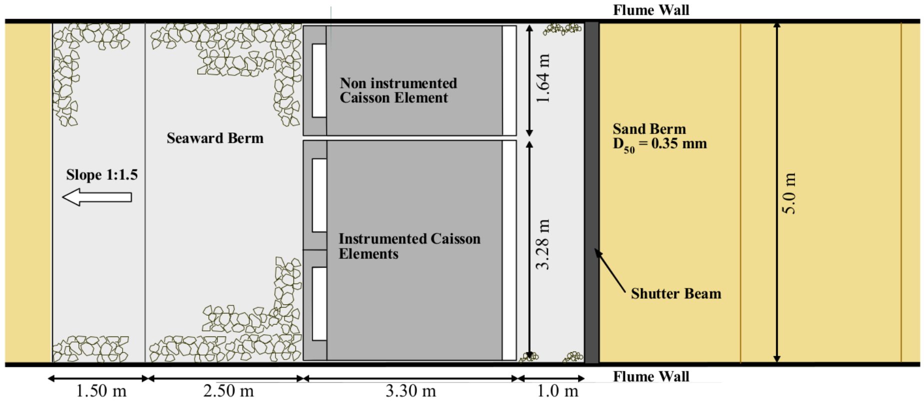

(b) Plan

Figure 5.4: (a) Cross section and (b) plan view of the caisson breakwater model (without measuring devices) (Oumeraci and Kudella, 2004)

a. Material properties

The soil foundation underneath the breakwater model consists of medium-fine sand with D_{50} = 0.21 mm and a uniformity coefficient $U = 1.69$. The medium fine sand was separated from the rest of the profile by two walls made of geotextile bags filled with sand. In addition, the part with the fine sand was separated from the adjacent profile with an impermeable PE-sheet on the bottom and at the sides. The impermeable sheets were used to prevent the drainage of pore fluid from underneath the structure, which was presumed to prevent dissipation of the expected buildup of excess pore pressure generated during the tests, and consequently to increase the risk of liquefaction. The properties of the used materials are given in Table 5.1.

The PE-sheet is 2.0 mm thick and weighs $1900g/m^2$ to sustain the locally expected high vertical loads and the subsequent deformations. The rough surface on both sides with a friction angle of 27° between sand and sheet ensures a safe transfer of the horizontal load from the breakwater to the sandy subsoil. Shear stress transmission was only ensured in the case of sand on both sides of the sheet. Therefore, a thin sand layer of 10 cm was applied on top of the PEHD-sheet, covered by a geo-textile separating the sand layer from the rubble foundation. The most relevant parameters of the used PE-sheet are also given in table 5.1. A 20 cm thin bedding layer made of crushed stones with an average diameter of D_{50} = 35 mm is installed on the 10cm thin sand layer and just beneath the caisson.

To prevent the risk of buckling of the sheet at the shore side of the caisson a sand berm (D_{50} = 0.35 mm) with 1 m height was installed thus providing enough overburden pressure on the sheet. The sand berm behind the caisson was separated against the rubble foundation by a shutter beam, which also served as to limit sliding of the caisson.

Table 5.1: Construction elements of the berm and the rubble foundation and their characteristics (Oumeraci and Kudella, 2004)

Element	Description/Parameter	Value
Armour layer	Thickness	35 cm
	Mean particle size (D_{50})	206 mm
	Mean weight (W_{50})	26.6 kg
Filter layer	Thickness	20 cm
	Mean particle size (D_{50})	50 mm
Rubble	Thickness	20 cm
	Mean Particle Size (D_{50})	35 mm
Geotextile	Thickness	6-7 mm
	Weight	828 g/m^2
	Permeability	3.8×10^{-3} m/s
PEHD-Sheet	Height of profile	0.4 mm
	Thickness	2 mm
	Weight	1900 g/m^2
	Density	0.942 g/m^3
	Yield stress	$\geq$ 15 N/mm^2
	Elongation at yield stress	$\geq$ 10 %
	Tear strength	$\geq$ 25 N/mm^2
	Elongation at break	$\geq$ 650 %

The entire caisson model consists of three adjacent single caissons elements. Two of them were fixed together to one monolithic block (Fig. 5.4b). The overall height of the caisson is 2.76 m while its width including the front wall is 3.30 m

After the first test phase (uncovered seabed, i.e. before installation of structure and impermeable sheet), the relative density of the medium-fine sand foundation was estimated using the Cone Penetration Test (CPT) at three different positions (only for sand underneath the structure). The method of Puech and Foray (2002) for the interpretation of shallow CPT's in saturated marine sands was applied to determine the relative density, Fig. 5.5 (Oumeraci and Kudella, 2004). The relative density D_r was estimated approximately from 12 to 17% before the second test phase, which means very loose sand. After the second test phase (at the end of the wave loads on the caisson structure), the relative density was estimated (in the same manner) as 50% (Oumeraci and Kudella, 2004).

The degree of saturation for the sand foundation beneath the caisson breakwater was estimated, based on the measurements of pore pressure inside the sand foundation during the first test phase and on the comparison to the analytical solution by Moshagen and Torum (1975). The analytical solution considers an isotropic seabed of finite thickness. The degree of saturation is crucial for the pore fluid compressibility. The degree of saturation was determined for a sand bed with porosity $n = 0.45$ and hydraulic conductivity $k = 10^{-4} m/s$

For the vertical distribution of the pore pressure over the entire depth of the sand foundation, four measuring locations were considered (Fig. 5.6). Nevertheless, it can be inferred that the degree of saturation increases with depth inside the sand foundation. The degree of saturation was estimated to be between 99% to 99.6% and considered to "fit" well with the 99.5% value (Oumeraci and Kudella, 2004), which is the universally acceptable maximum degree of saturation. Nonetheless, with closer examination of Fig. 5.6, at the top positions the degree of saturation may be below the 99% barrier. The variation in the estimated degree of saturation over the entire depth of the sand bed makes the feasibility of homogenizing the air content across the seabed questionable. At this point it is important to recall that a decrease of the degree of saturation from 100% to 99.5% reduces the calculated fluid bulk modulus by 200 times (Eq. 4.10).

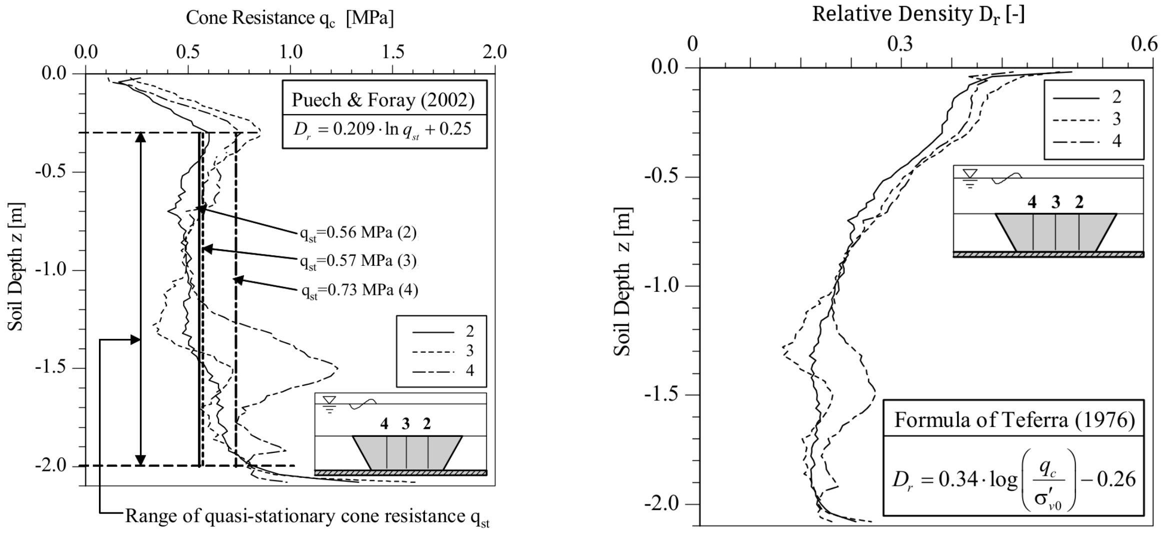

(a) (b)

Figure 5.5: Estimation of the relative density of the sand foundation underneath the caisson via CPT (Oumeraci and Kudella, 2004): (a) according to Puech and Foray (2002) and (b) according to Teferra (1976)

b. Model construction procedure

The physical model was built in two stages; first, the seabed was profiled and the prospective area beneath the planned breakwater model was carefully prepared. Sand bags were placed on both sides of the sand foundation underneath the caisson to form supporting walls to the high density impermeable polyurethane sheet (PE-sheet). On the bottom of the flume (on top of the placed PE-Sheet), perforated plastic pipes were placed, surrounded by a gravel filter and covered with geotextile. The pipes were used to flush the sand foundation from the bottom to increase the water content. On top of the geotextile, a wooden frame was installed, with all the measuring devices inside the sand fixed to it before sand was placed.

Afterwards, the sand foundation was placed in layers of 40 cm thickness each. First, a layer was filled

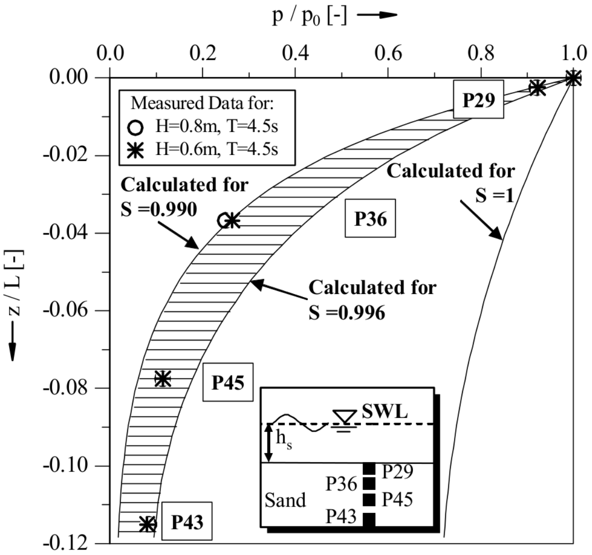

Figure 5.6: Estimation of the degree of saturation *S* by using the formula of Moshagen and Torum (1975) (Oumeraci and Kudella, 2004)

with water, then humid sand was poured from a container to fill the layer. This procedure was followed to reduce initial air content of the sand foundation. Flushing of the sand foundation was established from top and from underneath the sand layer to ensure lowest possible air content in the pores of the soil. Fig. 5.7 illustrates the key procedure for placement and saturation of the sand foundation. After completion of the first stage, a test series corresponding to a first test phase was performed. The objective of this first test phase was to investigate the response of the seabed to direct wave attack without any PE-sheet or breakwater and to compact the loose sand.

Afterwards, in the second stage the construction was completed by placing the PE-sheet on top of the sand bed, then the 20cm thin layer of crushed stones and the caisson units, and finally the rubble foundation (i.e. core, filter and armour layers) were placed. Further, a berm behind the caisson was constructed and the measuring devices related to the rubble foundation and the caisson were mounted. A second test phase was performed by subjecting the caisson breakwater to wave action.

c. Definition of caisson motions

Naturally, the final target of the structural design of a monolithic vertical (caisson) breakwater should not only be ensuring that the structure will survive extreme wave loads without catastrophic failure, rather the structure should also maintain acceptable displacements during its design service time (stepwise failure). Therefore, the measured displacements of the caisson breakwater from the large-scale physical tests are of high significance.

Three displacement meters were mounted at the top of the caisson (Fig. 3.7). The displacement meters measure the elongation of the rods connected to the caisson rather than providing direct measurements of the displacements. Therefore, the caisson motion needs to be calculated from the measurements of the displacement meters. The vertical and horizontal displacements of the top front and top back edges of the caisson are calculated from the displacement meters measurements (see Fig. 5.8).

Although it is safe to assume that the caisson will always undergo rigid body motion as long as none of its structural components have failed, the definition of the caisson motions is not a trivial task because the rotational pivot of the caisson cannot be identified in a straightforward manner. Additionally, the pivot changes position depending on soil-structure interaction during the wave loading. Therefore, the mid-point of the top-slab is used as a reference position for caisson motion. This is practically useful because the caisson's deck is of interest from a structural design point of view (to maintain acceptable use of the

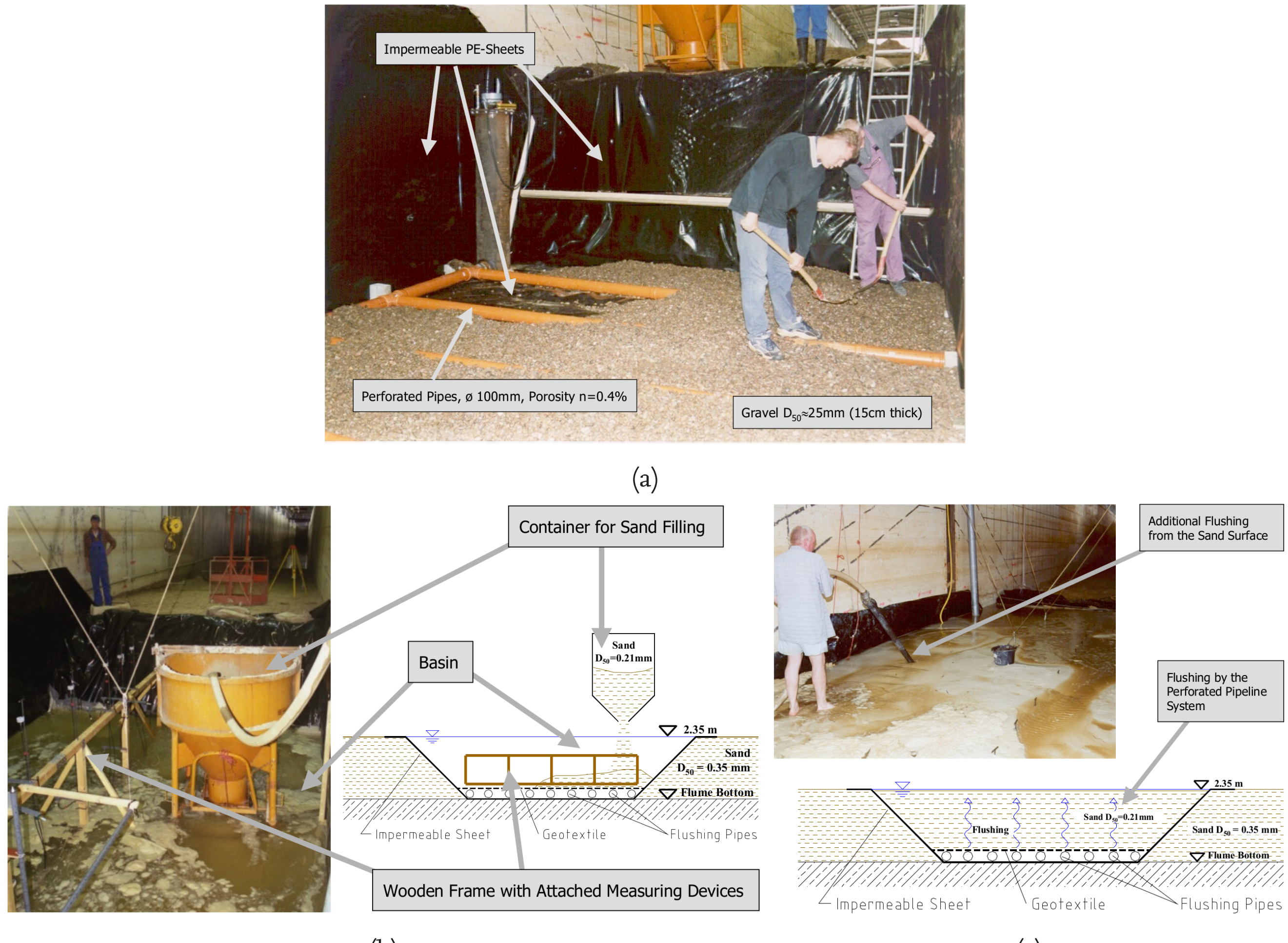

(a)

(b)

(c)

Figure 5.7: Preperation of the sand foundation underneath the caisson (Oumeraci and Kudella, 2004): (a) perforated pipes and gravel filter placement for flushing sand from underneath, (b) layer placement of sand and water and (c) dual flushing of the sand foundation

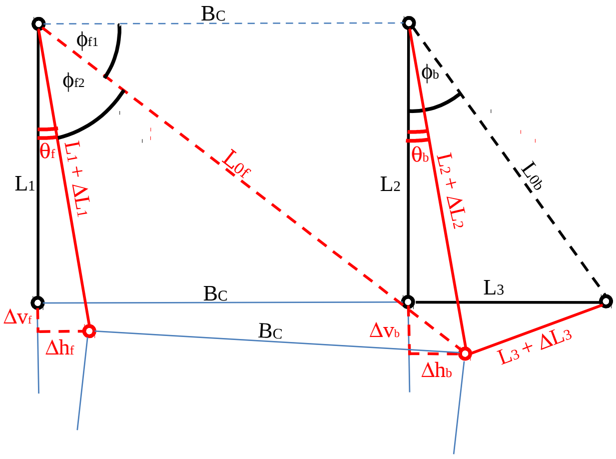

Figure 5.8: Calculation of caisson motion from measurements of displacement meters

breakwater deck). The caisson displacements are calculated as (see Fig. 5.8):

$$\begin{aligned}\Delta v &= \frac{(\Delta v_f + \Delta v_b)}{2}\\ \Delta h &= \frac{(\Delta h_f + \Delta h_b)}{2}\\ \theta &= \tan^{-1}\left(\frac{\Delta v_f - \Delta v_b}{B_c}\right)\end{aligned} \tag{5.1}$$

5.2.2 Idealisations for Numerical Tests

The CFD simulations for these tests were already presented in Subsection 3.2.2. Therefore, the main aim of this section is the presentation of the simulations of the CSD model within the semi-coupled CFD-CSD model system. In Fig. 5.9 and Table 5.2, the domain for the CSD simulations is shown with a description of the boundaries (e.g. contact surfaces) and material zones (e.g. sand foundation). Only the sand foundation underneath the caisson (enclosed by the impermeable PE-sheet) was simulated by the multi-surface plasticity model. Other material regions were assigned a linear elastic model. Two contact regions were considered; the contact between the caisson and the rubble foundation and the contact between the sand shutter-beam and surrounding materials. The sand shutter-beam is fixed from the top to simulate its fixation in the physical experiments to prevent excessive sliding of the caisson structure. The sand bags were averaged as a continuous sand layer. The high friction angle between sand and the PE-sheet combined with the procedure of the PE-sheet placement allows for the consideration of perfect transfer of shear stresses. Although the complete transfer of normal stresses (tensile stresses) is questionable, no separation between the impermeable PE-sheet and surrounding materials was simulated.

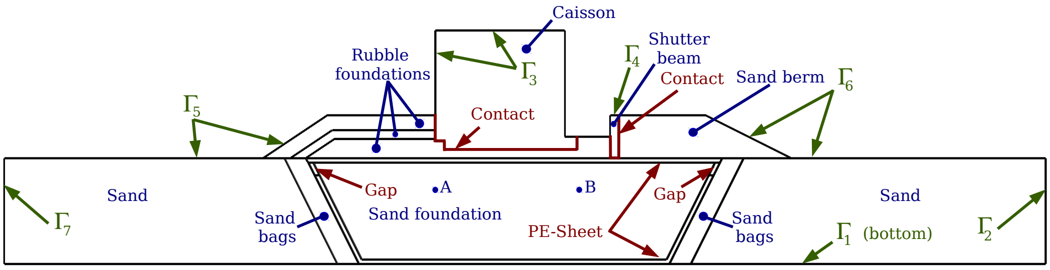

Figure 5.9: Domain of the GWK large-scale caisson breakwater tests for the CSD model *geotechFoam* solver with definition of boundary conditions

Table 5.2: Description of the boundary conditions for the CSD model domain of the GWK tests

	Description	$\mathbf{u}$	p	$\overline{\mathbf{U}}$
Γ_1	Bottom of geometry	$\mathbf{u} = 0$ "fixed bottom"	$\nabla p = 0$	$\overline{\mathbf{U}} = 0$
Γ_2	Right side of geometry	Mixed: allows vertical settlement	$\nabla p = 0$	$\overline{\mathbf{U}} = 0$
Γ_3	Caisson top and seaward side	Input traction (from CFD)	$p = 0$	$\overline{\mathbf{U}} = 0$
Γ_4	Sides of shutter beam	$\mathbf{u} = 0$	$p = 0$	$\nabla\overline{\mathbf{U}} = 0$
Γ_5	Rubble and seabed seaside	Zero traction	Value (from CFD)	$\nabla\overline{\mathbf{U}} = 0$
Γ_6	Other outer boundaries	Zero traction	$p = 0$	$\nabla\overline{\mathbf{U}} = 0$
Γ_7	Left side of geometry	Mixed: allows vertical settlement	Value (from CFD)	$\nabla\overline{\mathbf{U}} = 0$
	Contact	Contact boundary condition (mixed Drichilet-Neumann)	Value (from CFD)	$\nabla\overline{\mathbf{U}} = 0$

The permeability of caisson breakwater and the PE-sheet were set to small values to represent impermeable materials. A gap between the top and bottom PE-sheets was considered with different heights to simulate the effect of difference between top and bottom PE-sheet. However, for logical ranges of the gap height, it was found that there is no effect on the pore pressure underneath the caisson as they are located on relatively large horizontal distances from the caisson. A zero-gap was considered for the simulations. A small band adjacent to the contact surface of the caisson with the rubble foundation was assigned a relatively high permeability coefficient to allow for solid-fluid coupling near caisson contact to simulate uplift pressure on the caisson breakwater.

The boundaries on both sides of the domain (Γ_2 and Γ_7 in Fig. 5.9) are assigned mixed Dirichlet-Neumann boundaries to allow vertical displacement but no horizontal displacement. The boundaries used for the coupling with the hydrodynamic models are:

Γ_3	Neumann boundary of displacement
$\Gamma_{5,7}$ and contact surfaces	Dirichlet boundary of pore pressure

5.2.3 Pore pressure and displacement

The results from the CFD-CSD numerical model system are compared herein to the measurements from the GWK tests for three wave conditions: Non-breaking waves (H = 0.4 m. and T = 5.5 s.) in Fig. 5.10, slightly breaking waves (H = 0.5 m. and T = 6.5 s.) in Fig 5.11 and breaking waves (H = 0.7 m. and T = 6.5 s.) in Fig 5.10. The tests considered here are the same tests presented in chapter 3 for the validation of the hydrodynamic model.

The validation is carried out for the pore pressure in the sand foundation underneath both sea-side and shore-side edges of the caisson, the vertical displacements of both edges at the caisson top as well as horizontal and rocking motions of the caisson. The vertical displacement at the locations of the pressure transducers beneath both caisson breakwater edges are also presented.

The validation of the CFD-CSD model is carried out for both the $u-p$ approximation and the fully dynamic solution in the CSD model. A uniform compressibility of the pore fluid, which corresponds to a uniform water content of 98.83%, is considered over the entire computational domain in the seabed. From the results of the numerical model for all considered waves, it is obvious that the compressibility of the pore fluid in GWK tests is not the same under both caisson edges. The pore fluid is more compressible (i.e. larger air content) beneath the seaward edge of the caisson than beneath the shoreward edge. Therefore, the pore pressures obtained from the numerical model (with uniform pore fluid compressibility) are overestimated beneath the seaward edge and underestimated beneath the shoreward edge. This observation implies that the solid skeleton of the seabed beneath the seaward edge carries a higher portion of the dynamic stresses induced by caisson motions than the seabed skeleton beneath the shoreward edge. The most obvious interpretation of this observation would be a difference in water content in the seabed beneath both edges of the structure. Introduction of multiphase pore fluid modelling; water and air with air modelled as a dispersed phase can provide a better understanding for such difference in water content, and whether this behaviour is generic or related to configurations of the GWK tests (e.g. PE-sheet).

The computed vertical displacements compare well to the measured displacements also for the residual displacements generated stepwise by impact loads from regular breaking waves. It is noted that although good results were obtained using the semi coupled model system, a two-way coupling of both models will appreciably enhance the results by providing a higher resolution of the coupling (maximum values of response) and capturing processes such as caisson motion damping caused by water underneath (inertial effects) and enhance uplift pressure on caisson (as explained in validation of the hydrodynamic model).

The validation of both the fully dynamic and the $u-p$ approximation forms of the fully coupled Biot equations were carried out. The difference in computational time between both methods decrease significantly when considering plasticity and contact modelling (unlike for the long simulated consolidation problem used for the hydro-geotechnical model validation). The fully dynamic approach provides a more natural damping of elastic waves in the domain of the CSD solver. The fully dynamic solution provides better results for excess pore pressure, especially on both sides of the impermeable PE-sheet (Fig. 5.13) after wave loading of the structure. The solution with the $u-p$ approximation overestimates the residual tilt of caisson breakwater under breaking wave impact, Fig. 5.12f. However, more detailed comparison between both methods for elastoplastic seabed is needed. Indeed, a comparison can be found in the literature for a simplified analytical solution for fully dynamic and partially dynamic formulation for elastic seabed (Ülker et al., 2009). However, the results do not necessarily apply to elastoplastic seabed.

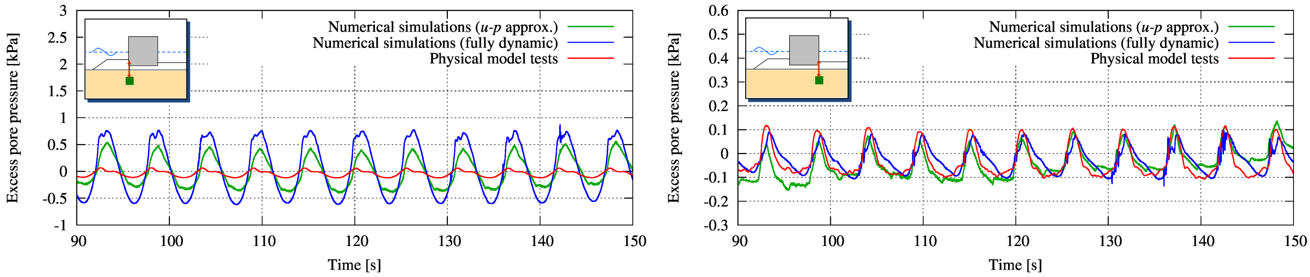

(a) Pore pressure underneath seaward edge of caisson; pressure transducer 32

(b) Pore pressure underneath shoreward edge of caisson; pressure transducer 36

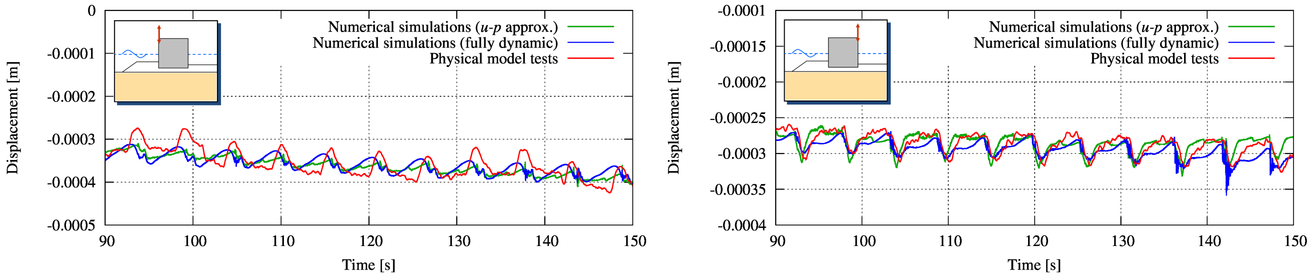

(c) Vertical displacement seaward edge of caisson; displacement meter 63

(d) Vertical displacement shoreward edge of caisson; displacement meter 64

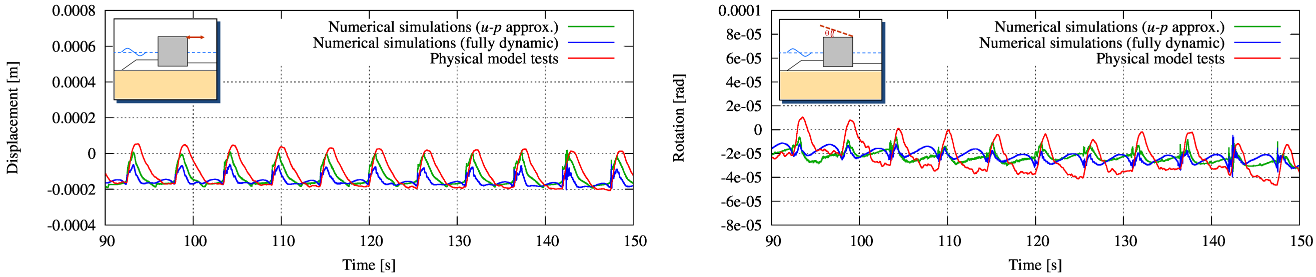

(e) Horizontal displacement; displacement meter 65

(f) Rotation of the caisson at top slab

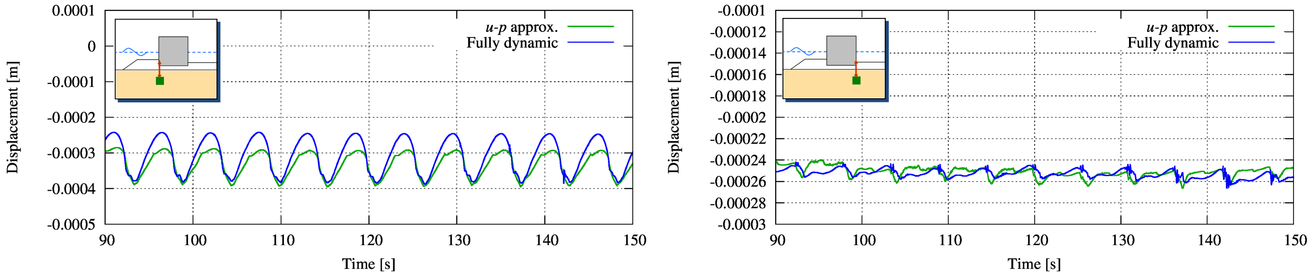

(g) Vertical displacement under seaward edge at position of pressure transducer 32

(h) Vertical displacement under shoreward edge at position of pressure transducer 36

Figure 5.10: Validation of the CFD-CSD model system using large-scale GWK tests for regular non-breaking waves (H = 0.4 m. and T = 5.5 s.)

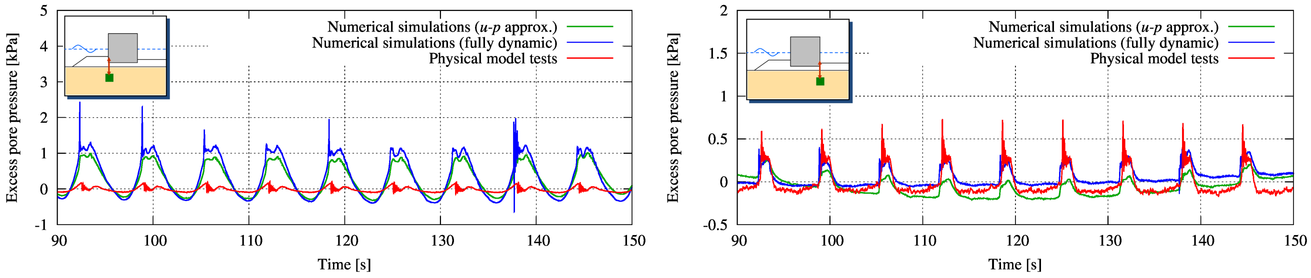

(a) Pore pressure underneath seaward edge of caisson; pressure transducer 32

(b) Pore pressure underneath shoreward edge of caisson; pressure transducer 36

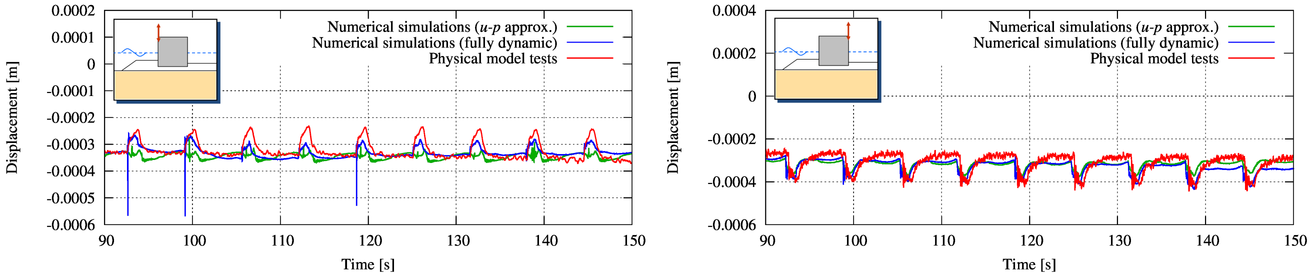

(c) Vertical displacement seaward edge of caisson; displacement meter 63

(d) Vertical displacement shoreward edge of caisson; displacement meter 64

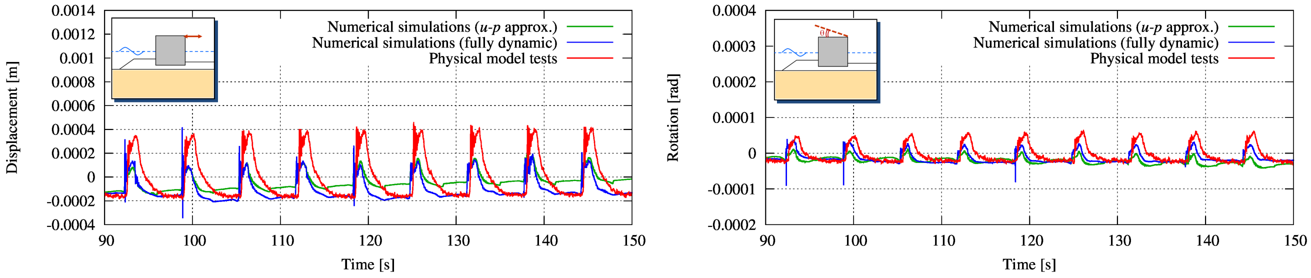

(e) Horizontal displacement; displacement meter 65

(f) Rotation of the caisson at top slab

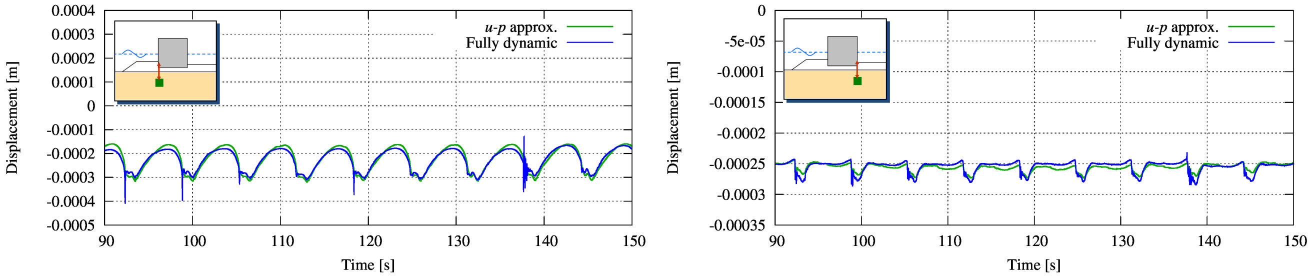

(g) Vertical displacement under seaward edge at position of pressure transducer 32

(h) Vertical displacement under shoreward edge at position of pressure transducer 36

Figure 5.11: Validation of the CFD-CSD model system using large-scale GWK tests for regular slightly breaking waves (H = 0.5 m. and T = 6.5 s.)

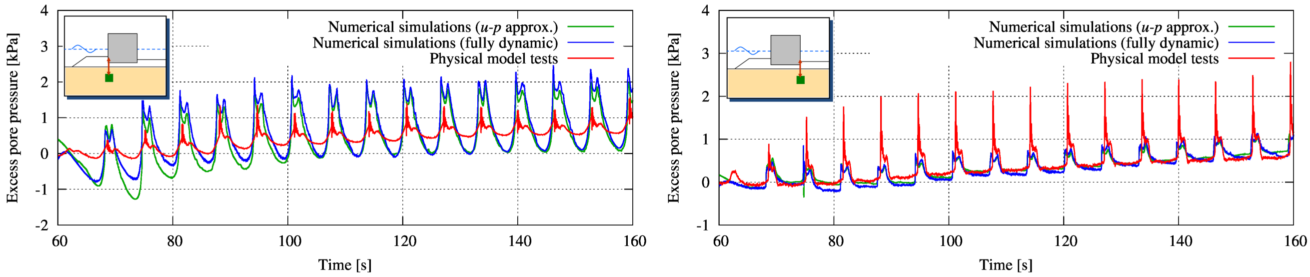

(a) Pore pressure underneath seaward edge of caisson; pressure transducer 32

(b) Pore pressure underneath shoreward edge of caisson; pressure transducer 36

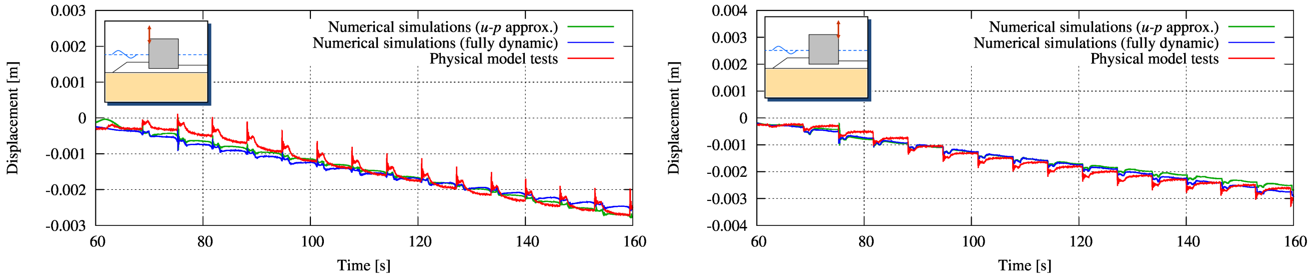

(c) Vertical displacement seaward edge of caisson; displacement meter 63

(d) Vertical displacement shoreward edge of caisson; displacement meter 64

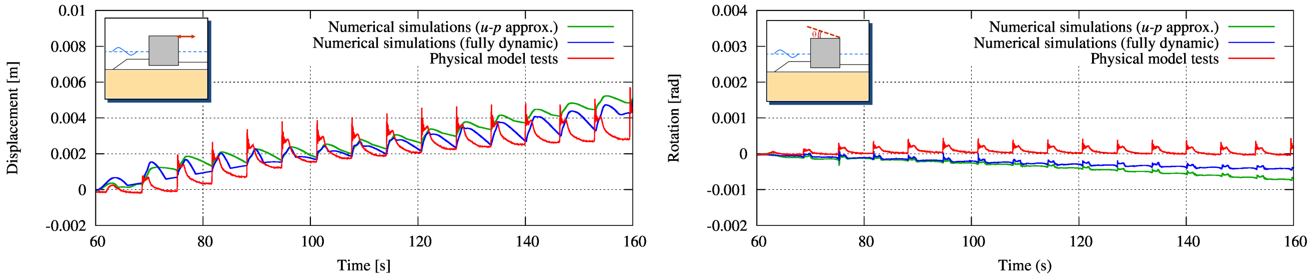

(e) Horizontal displacement; displacement meter 65

(f) Rotation of the caisson at top slab

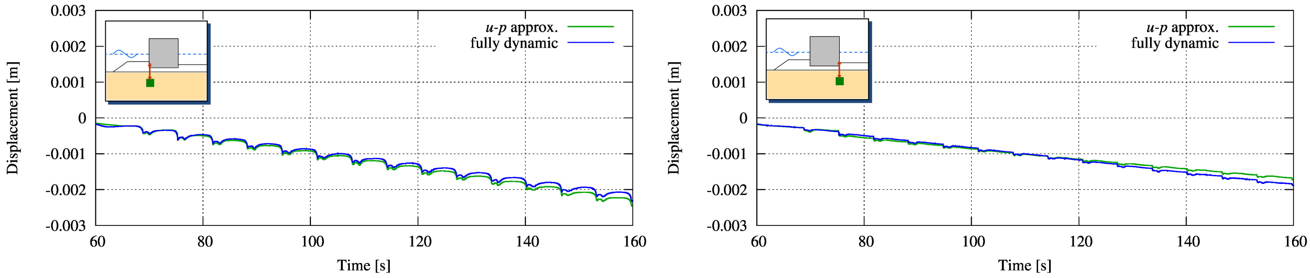

(g) Vertical displacement under seaward edge at position of pressure transducer 32

(h) Vertical displacement under shoreward edge at position of pressure transducer 36

Figure 5.12: Validation of the CFD-CSD model system using large-scale GWK tests for regular breaking waves (H = 0.7 m. and T = 6.5 s.)

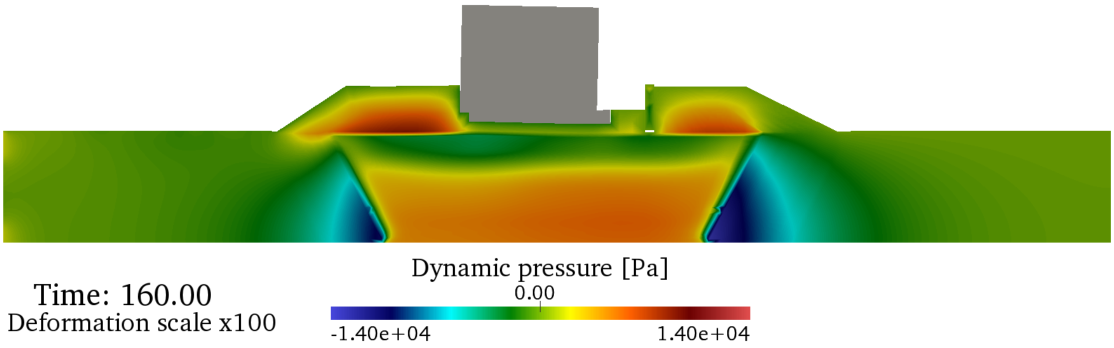

(a) The $u-p$ approximation: excess pore pressure

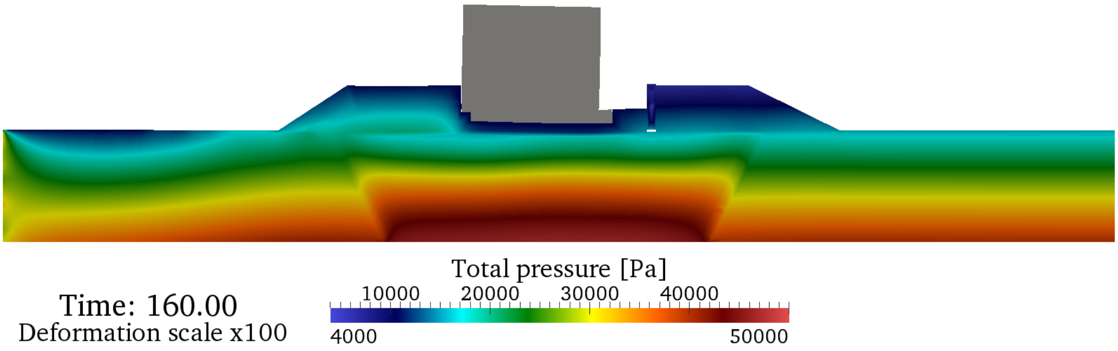

(b) The fully dynamic formulation: total pore pressure

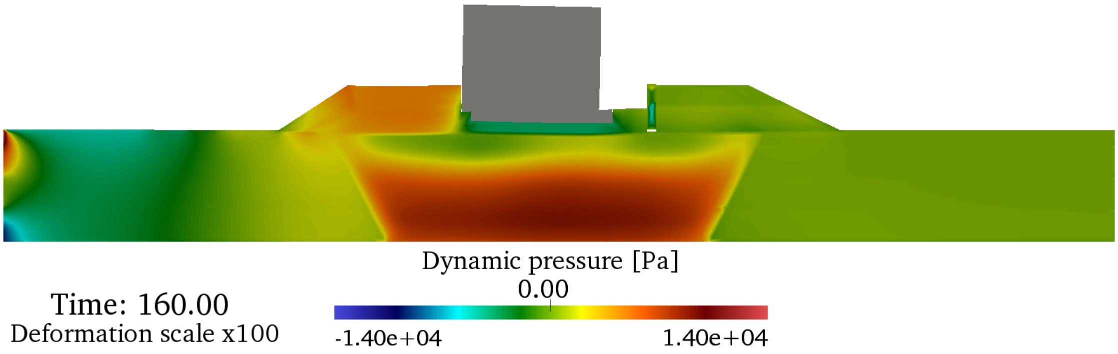

(c) The fully dynamic formulation: excess pore pressure

Figure 5.13: Cross section and Plan view of the caisson breakwater model (without measuring devices) (Oumeraci and Kudella, 2004)

5.3 Parameter Study for Monolithic Breakwater Analysis

Monolithic breakwaters can be considered rigid. Based on the rigidity of the structure, the caisson base which interfaces with the underlying foundation would retain its shape without any local deformation as long as no failure of the structural elements has occurred. It is then possible to group the parameters of the study problem into two groups: (i) Parameters associated with breakwater induced stresses on the foundation and (ii) parameters associated with the response of the seabed foundation. It is proposed that the former group of parameters be represented by a single parameter; namely the load eccentricity (the load eccentricity concept). Another representative parameter is also proposed for the latter group; namely the soil relative density. The soil properties can be linked directly to its relative density based on typical values from literature. A parameter study of these two representative parameters is herein presented.

5.3.1 Load eccentricity concept

For the analysis of the behaviour of monolithic breakwaters subject to wave attack, a representative parameter is proposed to account for the wave loading and the structural cross sectional properties. The parameter is the maximum shoreward eccentricity of the vertical load resultant during wave loading, which will be further referred to as *load eccentricity*. The load eccentricity is illustrated in Fig. 5.14, in which B is the width of the structure-foundation interface (caisson base), M is the total rotating moment calculated at the middle of width B by considering maximum horizontal wave force F_H, corresponding wave-induced uplift force F_U and caisson effective own weight W' (including bouncy effects).

The load eccentricity is calculated as $e = \frac{M}{F_V}$; where $F_V = W' - F_U$ is the vertical load resultant. The load eccentricity is further idealised for the structure-foundation interface width B to achieve the relative load eccentricity $\frac{e}{B}$. For this study, the relative load eccentricity $(\frac{e}{B})$ is calculated for the GWK tests from CFD simulations. Three examples for calculating the relative load eccentricity for GWK tests (used in model validation) are given in Fig. 5.15. The three examples represent low eccentricity (nonbreaking and slightly breaking waves) and high eccentricity (breaking wave impact). Further, eccentricity of breakwater's own weight will be referred to as own-weight eccentricity.

The *relative load eccentricity* (e/B) is used hereafter to develop a tentative classification system for step-wise failures of monolithic breakwaters (*the load eccentricity concept*).

5.3.2 Numerical parameter study

The CFD-CSD model system is used herein to extend the conditions tested in the GWK and to determine the coefficients needed for understanding the behaviour of sand foundations underneath monolithic breakwaters and for developing the simplified model presented in chapter 6. The tested wave conditions as well as the tested soil characteristics are presented below, followed by a discussion on the residual tilt and settlement of the caisson breakwater obtained from the numerical parameter study.

a. Tested wave conditions

Several regular waves were used for the parameter study. The wave characteristics were selected to provide a wide range of relative load eccentricity. The selected wave characteristics for the numerical parameter study are given in Table 5.3. The tested relative load eccentricities range from $e/B = 1.6\%$ to 200%. Table 5.3 shows also the used wave theories for generating the waves in the CFD model.

b. Tested soil properties

For the CSD model, the dimensions of the caisson were kept constant, while the relative load eccentricity change accordingly with applied wave conditions (as explained in Table 5.3). The tests were considered without an impermeable sheet. Four typical types of sands (according to relative density) are used for the parameter study. The different types of sand properties are given in Table 5.4 according to suggested typical values by Mazzoni et al. (2006) for sands of different relative densities.

c. Ciasson residual response

The simulated time for all numerical tests was kept constant to 100 seconds. The computed residual caisson tilt and settlement from different numerical tests are shown in Fig. 5.16. Interpretations of the results are presented in following sections of this chapter.

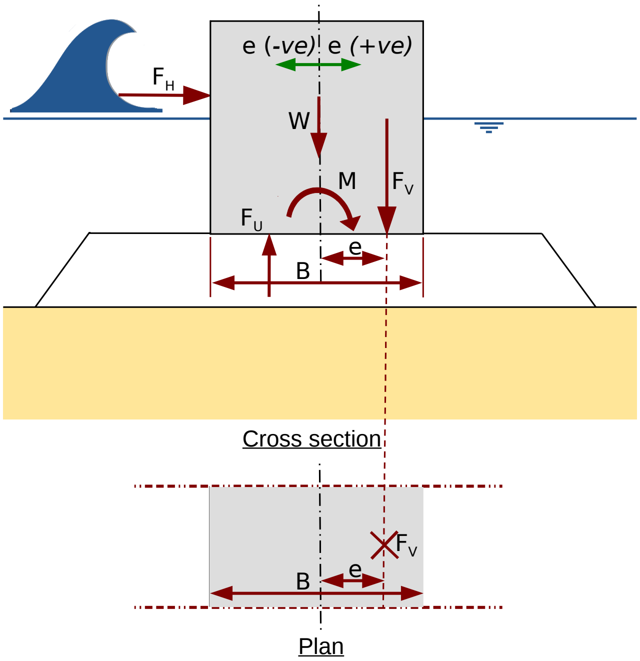

Figure 5.14: Sketch illustrating the *load eccentricity* parameter (positive eccentricity is shoreward of base centre)

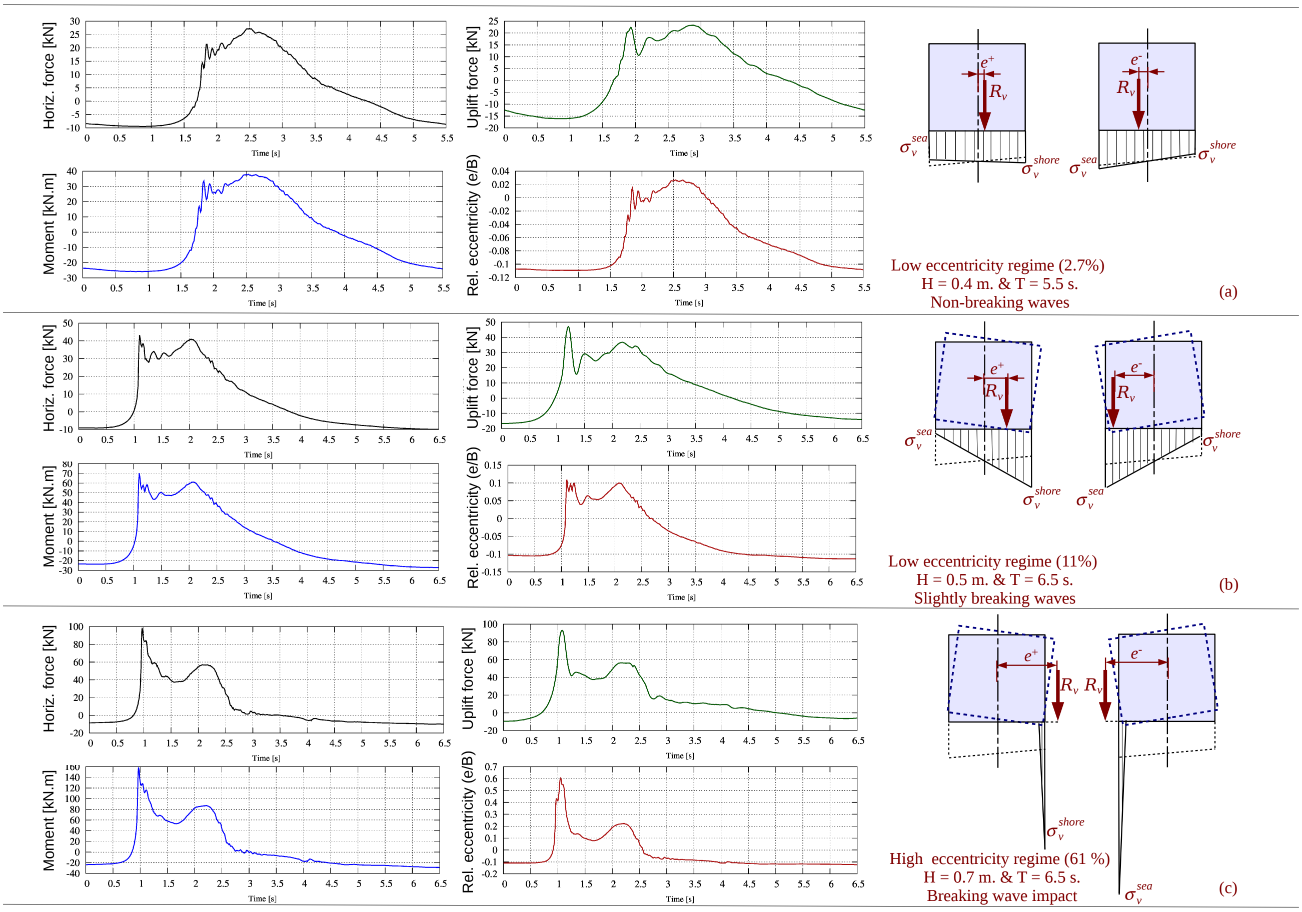

Figure 5.15: Relative load eccentricity ($\frac{e}{B}$) calculated from CFD simulations of selected GWK tests

Table 5.3: Maximum $+ve$ relative load eccentricity ($\frac{e}{B}$) of tested regular wave conditions (positive eccentricity is shoreward of base centre)

Wave height [m]	Wave period [s]	Wave theory	Relative eccentricity ($\frac{e}{B}\%$)
0.4	4.5	Stokes 2nd	1.6 %
0.5	6.5	Stokes 2nd	11 %
0.6	6.5	Stokes 2nd	27 %
0.7	5.5	Stokes 2nd	40 %
0.7	6.5	Stokes 2nd	61 %
0.9	5.5	Stream function	80 %
0.8	6.5	Stream function	100 %
0.9	6.5	Stream function	200 %

Table 5.4: Suggested typical values for sand foundation parameters based on soil relative density; these parametrs are not to be directly considered without proper soil testing (Mazzoni et al., 2006)

Sand type D_r %	Loose sand (15 % - 35 %)	Medium sand (35 % - 65 %)	Medium-dense sand (65 % - 85 %)	Dense sand (85 % - 100 %)
ρ [kg/m^3]	1700	1900	2000	2100
Ref. shear modul. [kPa] at p'_r = 80 kPa	5.5×10^4	7.5×10^4	10×10^4	13×10^4
Ref. bulk modul. [kPa] at p'_r = 80 kPa	1.5×10^5	2.0×10^5	3.0×10^5	3.9×10^5
Modulus of elasticity [kPa]	1.47×10^5	2.00×10^5	2.70×10^5	3.51×10^5
Poisson's ratio	0.336	0.333	0.35	0.35
Friction angle ϕ	29	33	37	40
Peak shear strain at p'_r = 80 kPa	0.1	0.1	0.1	0.1
Ref. press. (p'_r) [kPa]	80	80	80	80
Pressure dependence coefficient	0.5	0.5	0.5	0.5
Phase transformation angle	29	27	27	27
Contraction coeff.	0.21	0.07	0.05	0.03
Dilation coeff. 1	0	0.4	0.6	0.8
Dilation coeff. 2	0	2	3	5
Liquefaction factor 1 [kPa]	10	10	5	0
Liquefaction factor 2	0.02	0.01	0.003	0
Liquefaction factor 3	1	1	1	0
Voids ratio (e)	0.85	0.7	0.55	0.45
Porosity (n)	0.459	0.412	0.355	0.310
Hydraulic conductivity (k) [m/s]	1.50×10^{-5}	1.05×10^{-5}	0.70×10^{-5}	0.60×10^{-5}

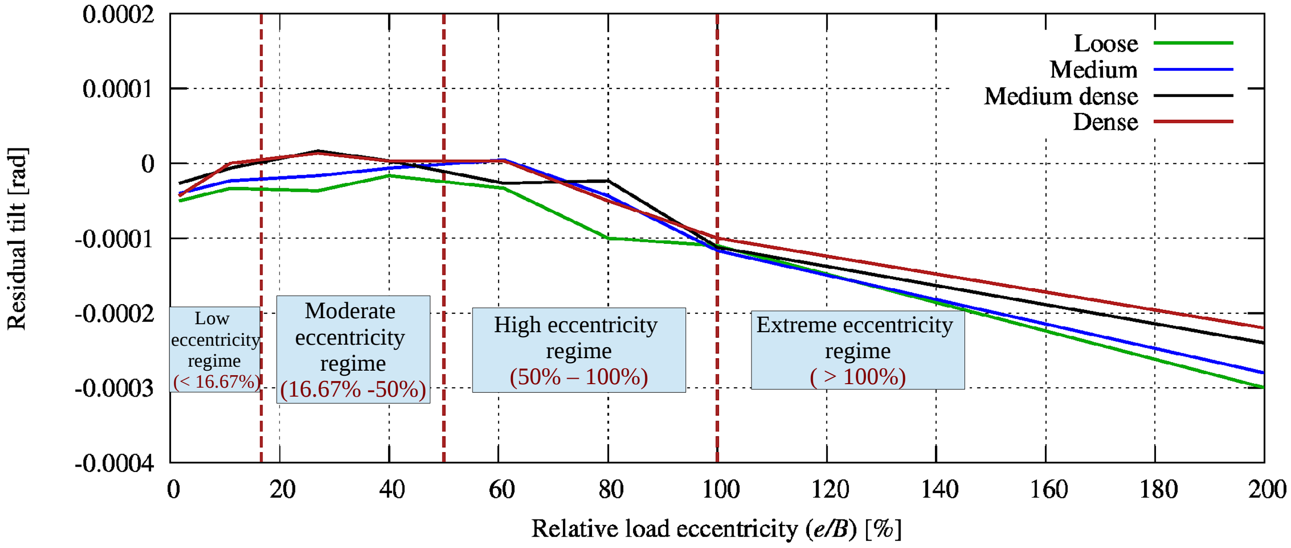

(a) Tilt

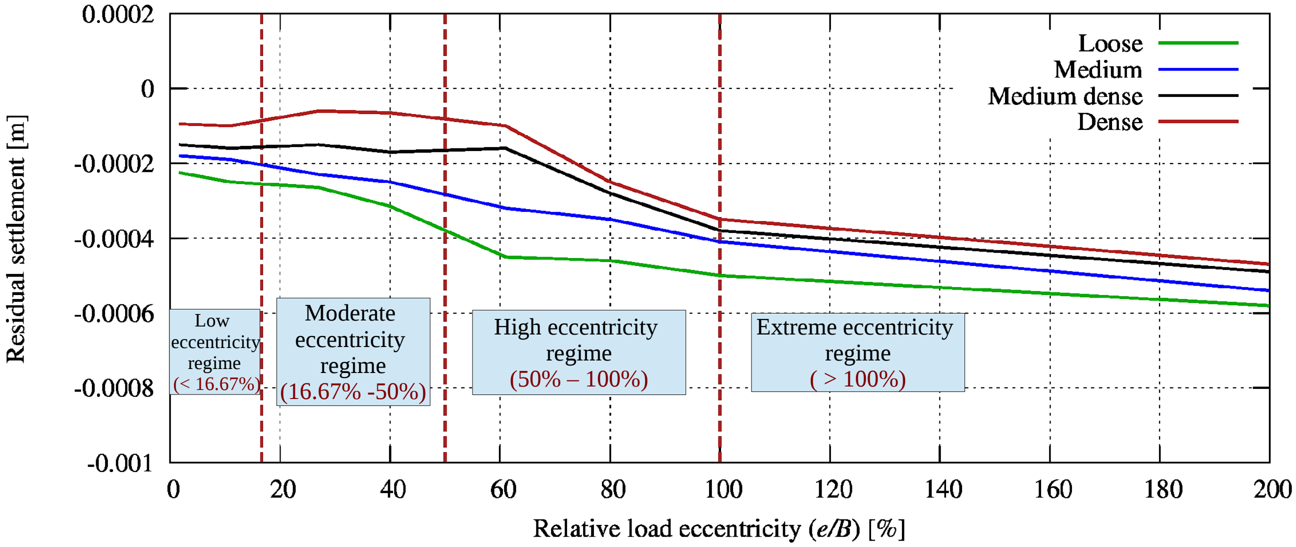

(b) Settlement

Figure 5.16: Residual response of monolithic breakwaters from numerical parameter study for a period of 100s. for each test

5.3.3 Stepwise failure

In this subsection, a tentative physical interpretation of the results of both numerical and GWK tests is proposed. This interpretation, which is mainly focused on the mechanism of the stepwise failure of caisson breakwaters subject to wave loads, might contribute to an improved understanding of a quite ambiguous phenomenon that may occur under non-extreme wave loads and may affect the functionality of monolithic breakwaters, which are generally designed for extreme wave conditions.

Stepwise failures, as used herein, are residual motions of the caisson breakwater due to the residual deformations of its soil foundation (e.g. differential settlements), which are induced by a series of dynamic wave load events. The term "stepwise failure" implies that this mechanism develops incrementally and is irreversible. For each wave load event, a small irreversible rotation of the caisson develops. Residual tilt was experienced by many monolithic breakwaters (e.g. Oumeraci (1994)). The rotation, due to this incremental mechanism, occurs even for caissons with uniform weight distribution and uniform soil conditions. Herein, it is proposed that the crucial parameter governing this type of rotational displacement is the relative load eccentricity e/B as defined in Fig. 5.14.

Typically, caisson breakwaters are built on rubble foundation rather than being based directly on the seabed. In the CSD model, both seabed and rubble foundations are considered as continua (macroscopic approach). Although this assumption is well justified for the sand foundation, it may be questionable for the rubble foundation, especially if the size of the rock units is large relative to the layer thickness, because further processes than those at the macroscopic scale might be more relevant. The effect of this limitation would be more apparent when relatively large sliding of the caisson is induced by a given wave event. Such processes associated with the rubble foundation cannot be reproduced with the new developed CSD model "*geotechFoam*".

Based on the modelling results and field observations (e.g. Oumeraci (1994)), the tilt of the caisson caused incrementally by wave-induced residual soil deformations can be directed either seaward or shoreward. According to the results from both physical and numerical modelling, the direction of the caisson tilt primarily depends on the wave loading conditions. The soil response to each wave load event depends mainly on the characteristics of this particular load event, but also on the soil characteristics just before that event. The effect of each single event in isolation most likely governs the seabed response. The cumulative and interactive effect of consecutive wave events is also important. Moreover, the the seabed response is also significantly affected by the properties of the structure (e.g. caisson mass and geometry).

Every wave load event on a vertical monolithic structure causes an eccentricity e of the vertical resultant force F_v at the structure-foundation interface. The $+ve$ eccentricity e of the wave loads in the shoreward direction (wave-crest at the structure) is always larger than the $-ve$ eccentricity in seaward direction (wave trough at the structure). This is valid for all wave loading cases. Based on the PROVERBS parameter map (Oumeraci et al., 2001) which has been adopted in design guidelines (e.g. CEM (2006)), wave loads on vertical monolithic structures can be classified in impact loads (strongly breaking waves) and non-impact loads (quasi-standing and slightly breaking), depending on relative wave height ($H_s^* = \frac{H_s}{h_s}$, where H_s is the wave height and h_s is the water depth) as well as on further relative parameters of the berm geometry.

The eccentricity for the wave load in shoreward direction (e^+) is significantly higher for impact loads than that of non-impact loads. Furthermore, the eccentricity ratio e^+/e^- is much higher for impact loads than for non-impact loads.

Considering Fig. 5.17, an idealisation of the caisson induced stresses/forces on the foundation under both edges of the breakwater is presented, assuming a stiff caisson. For breaking wave impact, the stresses on foundation are idealised as forces under both edges of the caisson for maximum stresses caused by impact and the structure restoration of original position. The load eccentricity conditions, which depends on the wave loading and the properties of the stiff caisson (base width B and own effective weight W'), may be classified in four main regimes:

- **Low load eccentricity regime ($e/B < 16.67\%$):** Generally for nonbreaking or slightly breaking wave loads causing no structure-foundation separation and no zero vertical stresses ($e > B/6$), here the own weight eccentricity has the highest effect on the exerted stresses under both sides of the caisson (Fig. 5.17a)

- **Moderate load eccentricity regime ($e/B = 16.67\% - 50\%$):** Slightly breaking wave loads or breaking wave impact of relatively small amplitude. For this regime the dynamic force from the restoration of the caisson to its original position after impact (seaward edge) is smaller than or equal to the force induced by wave impact/wave load for crest at the structure; shoreward edge (Fig. 5.17c)

- **High load eccentricity regime ($e/B = 50\% - 100\%$):** Breaking wave impact causing dynamic force from caisson restoration of original position (seaward edge) after impact that is larger than the force induced by wave impact (shoreward edge); however, no excessive sliding occurs (Fig. 5.17d)

- **Extreme load eccentricity regime ($e/B > 100\%$):** Severe breaking wave impacts most likely causing excessive sliding leading to erosion of rubble foundation under shoreward edge and may cause catastrophic failure of the structure (Fig. 5.17d and Fig. 5.23)

It should be noted that other factors may contribute to load eccentricity, e.g. possible tilt caused during breakwater placement or forces introduced by side rubble berms.

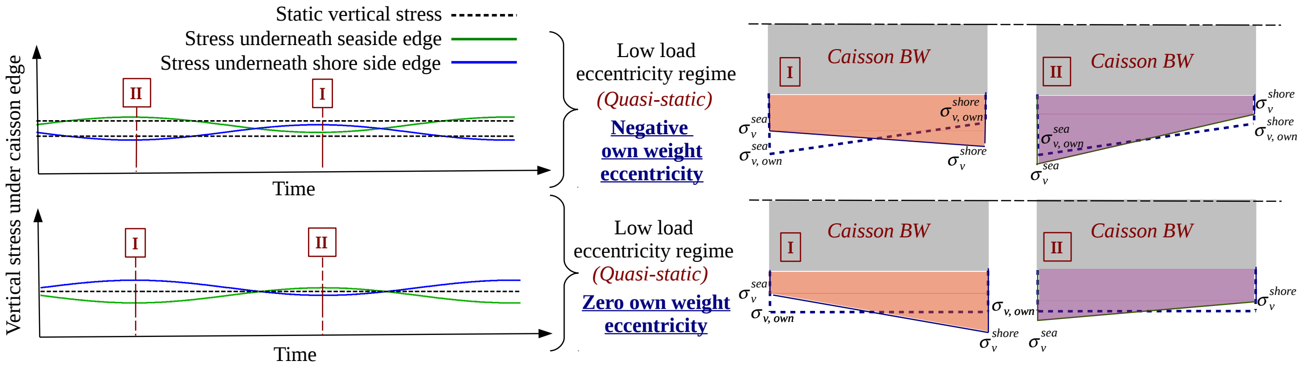

(a) Low eccentricity loading regime (e/B < 16.67%); with and without negative eccentricity from breakwater's own weight

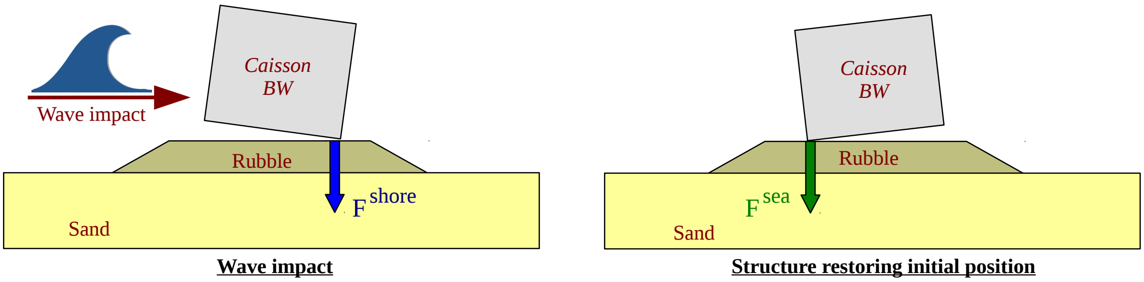

(b) Idealisation of breakwater induced stresses on the foundation for breaking wave impact as concentrated forces at shoreward and seaward edges

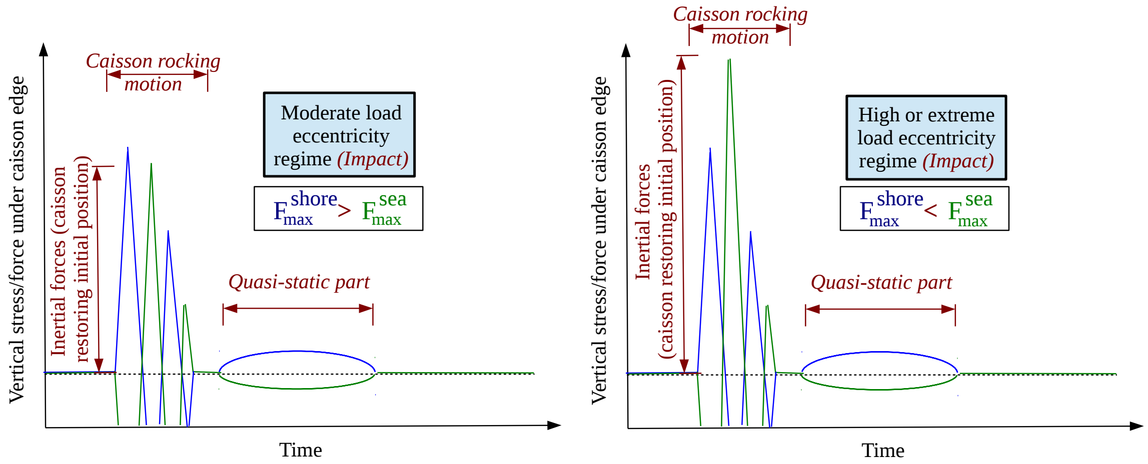

(c) Moderate load eccentricity regime

(d) High and extreme load eccentricity regimes

Figure 5.17: Idealisation of caisson-induced stresses/forces under both edges for different load eccentricity regimes

Fig. 5.18 is a sketch for comparison of eccentricities for different load eccentricity regimes. This figure is also applicable to wave forces. Low load eccentricity is associated with quasi-static wave loads, whereas for other regimes the load eccentricity (maximum shoreward eccentricity vertical resultant) is associated with wave impact. Moderate, high and extreme load eccentricity regimes vary in the severity of wave impact.

5.3.4 Role of Transient Pore Pressure Component

The transient component of pore pressure in seabed plays the main role in the seabed solid skeleton-pore fluid interaction with regard to the stepwise failure mechanism. Considering a single breaking wave

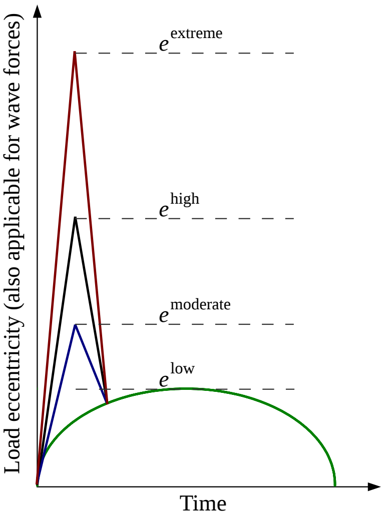

Figure 5.18: A sketch for comparison between different maximum eccentricities/forces of different load eccentricity regimes

impact on a caisson breakwater, Fig. 5.19, A high correlation/coupling can be found between the vertical displacement of both caisson edges and the transient pore pressure component in the seabed underneath both edges. As shown in Fig. 5.19a, an increase in incremental (per wave) differential settlement is caused directly by a single event of the wave load. It is observed that the wave impact is almost solely responsible for the increase in caisson tilt. The caisson rocking motion following the impact seems to be much less significant.

The pore pressure under the seaward edge progressively increases as the wave approach the structure (before the impact) due to directly wave-induced pore pressure. At wave impact, the pore pressure underneath shoreward edge significantly increases corresponding to the large vertical displacement of the caisson shoreward edge. Just after the impact, the situation is partially reversed while the caisson is restoring to its initial position causing an increase of the downward displacement of the seaward edge (with an increase in pore pressure beneath) and a decrease in shoreward downward displacement (with a decrease in pore pressure beneath). The caisson rocking oscillations then decay rapidly until the quasi-static phase of the wave loading is reached. Just after the quasi-static load phase is completed, the caisson tilt is shoreward. The final seaward tilt is reached only after the consolidation process of the seabed beneath the shoreward edge and the elastic restoration of the same edge.

Considering the consolidation (pore pressure dissipation) under both edges of the caisson, consolidation is found to be slower under the shoreward edge, which supports the observation in the numerical model validation that pore fluid compressibility maybe higher under the shoreward edge compared to that under the seaward edge. Higher pore fluid compressibility allows the soil to store more pore fluid when it is loaded with less increase in pore pressure and is accompanied by slower accumulation and dissipation of pore pressure.

5.3.5 Role of Residual Pore Pressure Component

The residual component of pore pressure is associated with the volumetric component of soil plastic strain. Increase (or positive) residual pore pressure is associated with plastic soil contraction, whereas decrease (or negative) residual pore pressure is associated with plastic soil dilation. Contractive or dilative soil response depends on the position of the stress state to the phase transformation line (see Fig. 2.10).

The *low load eccentricity regime*: Eccentricities cause very asymmetric loading on the seabed beneath the breakwater and hence the residual pore pressure is most likely negative (under both caisson edges). Never-

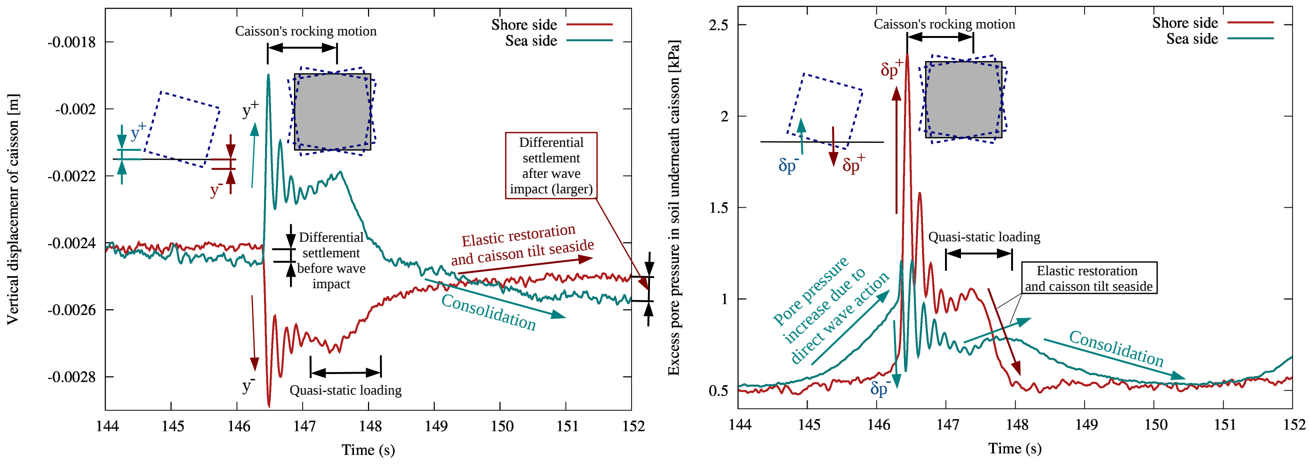

(a) (b)

Figure 5.19: Transient response for a single wave event from GWK test of regular breaking waves (H = 0.7 m. and T = 6.5 s.): (a) Vertical displacement and (b) Pore pressure in soil foundation (in transducers 32 and 36)

theless, plastic soil deformations develop causing residual displacements of the caisson (Fig. 5.20). In Fig. 5.20, a low-pass filter is applied to the measured signal from GWK to average the response by removing the transient component, which is necessary to present clearly the residual component of the response (trend). Because the developed plastic soil deformations and residual pore pressure are small, the negative pore pressure does not contribute much to increasing soil strength.

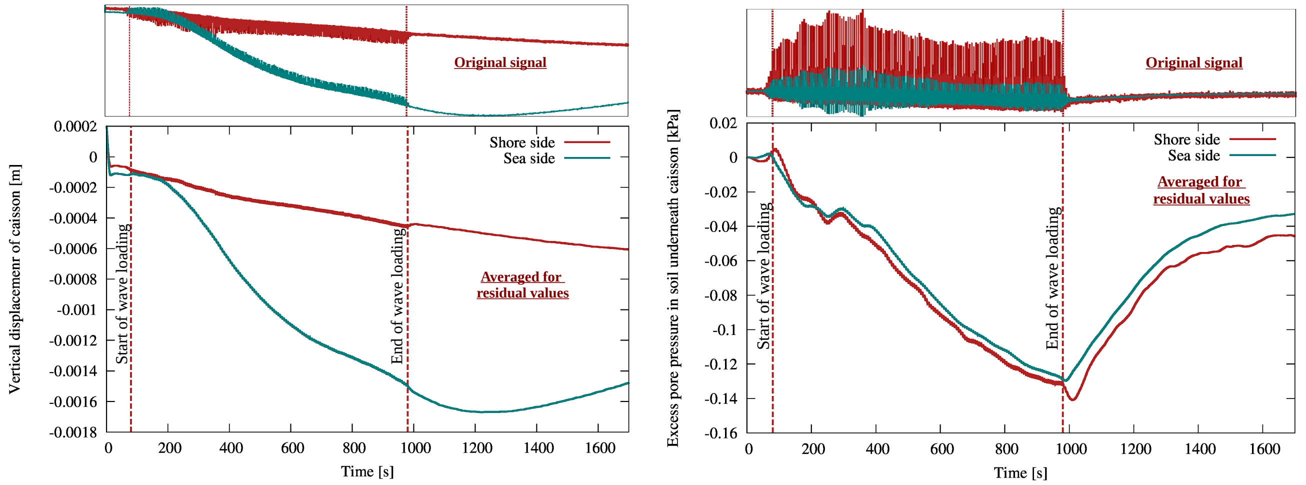

(a) (b)

Figure 5.20: Residual response of caisson and soil foundation from a GWK test with regular breaking waves (H = 0.5 m. and T = 6.5 s.; low load eccentricity regime): (a) Vertical displacement of seaward and shoreward caisson edges and (b) Pore pressure in soil foundation beneath both caisson edges

The *medium to high load eccentricity regimes*: Eccentricities, on the other hand, cause asymmetric loading on the seabed underneath the breakwater and hence the residual pore pressure is most likely positive. The increase in residual pore pressure depends on the amplitude and frequency of the waves as well as on the relative density and drainage conditions of the seabed. A residual pore pressure increase, and thus soil plastic contraction, tends to reduce with each load cycle (wave event) due to soil densification caused by cyclic loading. Residual pore pressure buildup increases the tendency of a monolithic breakwater to tilt seaward, as the seabed soil under the seaward edge is more vulnerable to the induced strength reduction than the seabed soil underneath the shoreward edge. The reduction in strength of the soil underneath the seaward edge is more significant because the soil loses momentarily the overburden pressure from the caisson during impact which causes a noticeable additional reduction in confinement pressure. This results in a weaker soil subject to the vertical dynamic force caused by the inertial effects of the caisson restoring its original position, Fig. 5.17.

The effect of residual pore pressure on the caisson residual tilt can be clearly observed in the first GWK test with a breaking wave impact, Fig. 5.21. At the start of this test, the residual vertical displacements at both seaward and shoreward sides is almost equal with a slight shoreward tilt (additional seaside resistance to loading caused by seaside side berm frictional resistance and overburden pressure effect on seabed). As the residual pore pressure on the seaside increases, a point is reached at which the rate of plastic vertical displacement and residual pore pressure increase (and consequently increase of rate of caisson residual tilt). This point is termed the Inflexion Point "I" by Kudella et al. (2006). From this test, it can be inferred that the increase in residual pore pressure not only increases the plastic response of the caisson, but a sufficient increase in residual pore pressure can also cause change in direction of the residual caisson tilt. Nevertheless, nontrivial buildup of residual pore pressure occurs only in case of regular breaking wave impacts, even under unfavourable drainage conditions (Kudella et al., 2006). Therefore, the effect of residual pore pressure buildup on the breakwater response would be much more apparent in controlled tests of regular breaking wave impacts as compared to natural sea state. Detailed analysis of the monolithic breakwater response to irregular waves can provide more information on the existence of the inflexion point under real field conditions and understanding thereof.

The second important point observed by (Kudella et al., 2006) is the so called Saturation Point "S", Fig. 5.21. This point clearly marks the maximum densification potential of the seabed soil under the given loading condition (e.g. load amplitude). The residual pore pressure would normally decrease after the saturation point, as the residual pore pressure generation is drastically reduced (due to soil densification) and is surpassed by pressure dissipation from normal drainage conditions. As expected, the residual pore pressure starts to decrease after the saturation point (Fig. 5.21b) until the residual pore pressure, at some point, rises again until the loading stops. The second increase in residual pore pressure is due to the effect of imposed unfavourable drainage conditions in the GWK tests (the impermeable PE-sheet), which allows pore pressure to dissipate until the pressure gradient between the measured point and the soil enclosed by the impermeable sheet vanishes. This causes pore pressure to buildup again with a rate smaller than that before the saturation point (dissipation is prevented).

Following the vertical displacements of both edges of the caisson, it is obvious that the vertical displacement gradient is correlated to the residual pore pressure gradient, with higher displacement gradients for positive pore pressure gradients and smaller displacement gradient for negative pore pressure gradient. The anticipated residual vertical displacements and pore pressure without an impermeable sheet are sketched in Fig. 5.21. Due to the large computational expense of the soil constitutive model combined with the frictional contact model, it was not possible to reproduce the complete test numerically. It is difficult to predict what would have occurred if the wave loading was considered for a longer period in this test. This test is significant, in being the first test with breaking wave impacts, which means no densification of the soil (due to wave loading) has occurred before that test.

The *extreme load eccentricity* regime, in which the caisson breakwater is subject to severe wave conditions is illustrated by one of the last GWK tests in Fig. 5.22. The inflexion and the saturation points can also be identified in Fig. 5.22b. However, because of the severe loading conditions (extreme load eccentricity regime), the caisson motion is considerable (e.g. sliding of almost 18 cm.) that caused the overlapped endings of the impermeable sheet to loose contact and mainly allowed for better drainage conditions. Here, one can see in Fig. 5.22b that no further residual pore pressure increase can be observed after the saturation point "S" was reached, i.e. no effect of the impermeable sheet.

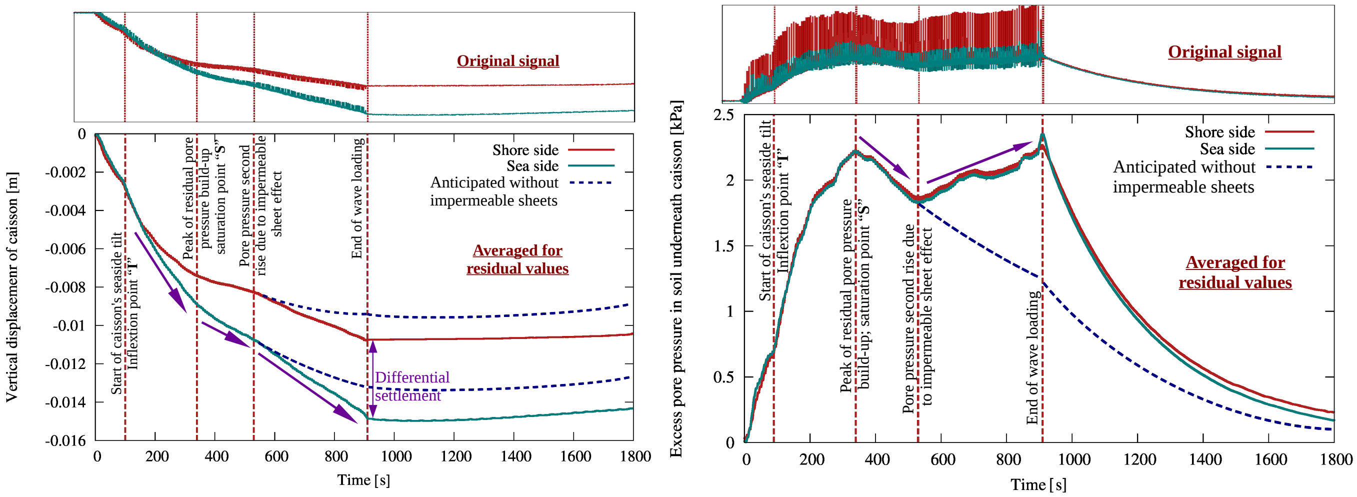

(a) (b)

Figure 5.21: Residual response from GWK test of regular breaking waves (H = 0.7 m. and T = 6.5 s.; high load eccentricity regime): (a) Vertical displacement and (b) Pore pressure in soil foundation

In Fig. 5.22a, one can notice that the caisson residual tilt is directed shoreward at the end of the test, unlike the computed seaward tilt by the numerical model system. Both the sliding and rocking response of the caisson in this test indicate that under extreme eccentricity regime, the coupling of caisson's rotation and sliding under impact load (Fig. 5.23) may cause new processes to emerge; namely erosion of the rubble foundation underneath the shore side of the caisson, resulting in a partial penetration of the sea side edge of the caisson in the rubble foundation, this can help explain the increasing sliding resistance and shoreward tilt. It may be inferred that this type of behaviour (extreme loading eccentricity regime) would most likely cause sliding failure of the caisson accompanied by shoreward tilt.

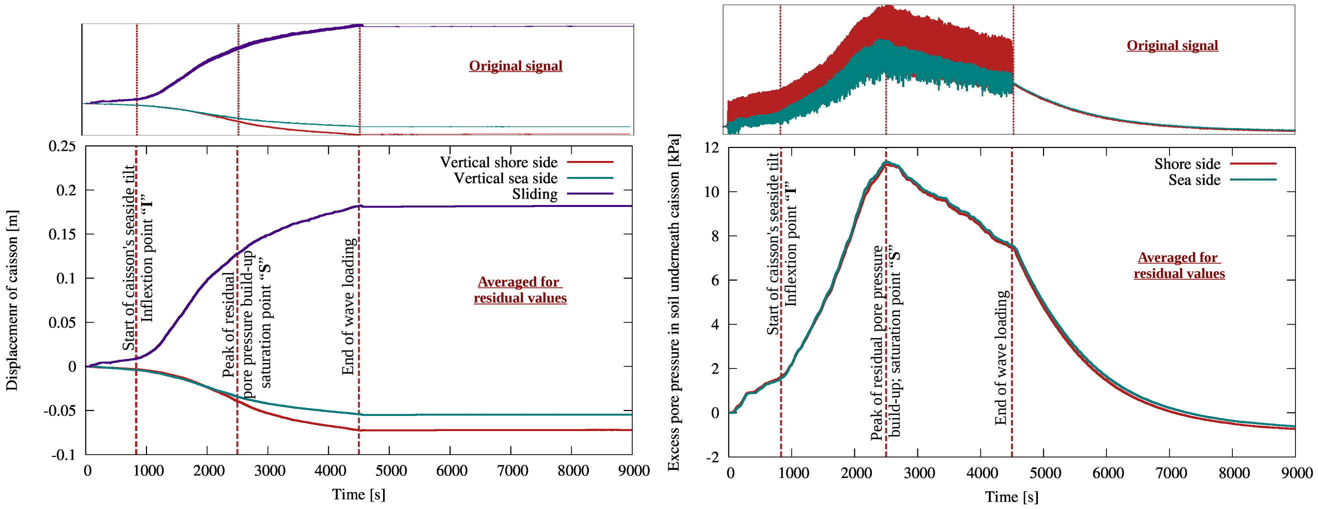

(a) (b)

Figure 5.22: Residual response from GWK test of regular breaking waves (H = 0.9 m. and T = 6.5 s.; extreme load eccentricity regime): (a) Vertical displacement and (b) Pore pressure in soil foundation

If the structure would suffer large sliding (e.g. not prevented from sliding by any additional measures other than friction) caused by the wave impact, the coupling between the breakwater's rotation and sliding response will most likely result in erosion of the rubble foundation under the shoreward edge of the structure and new processes (that are not considered in the numerical model) are present. Nevertheless, such excessive response would necessarily mean drastic failure of the structure as opposed to the long-term stepwise failure mechanism caused mainly by the soil foundation underneath the breakwater (as was the case for validation case in Fig. 5.21). A well-designed monolithic breakwater is expected to rarely experience an extreme load eccentricity regime during its lifetime.

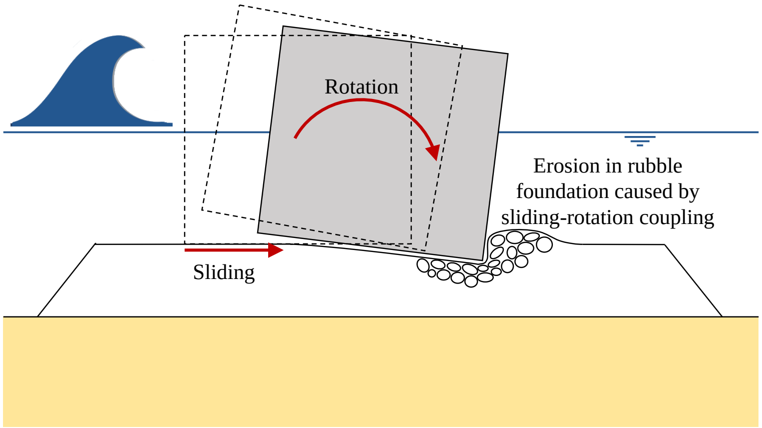

Figure 5.23: Breakwater failure under an extreme load eccentricity regime

5.3.6 Role of Structural and Hydraulic Configurations

a. Own weight eccentricity

Oumeraci et al. (2001) suggested a seaward own weight eccentricity up to 10% for optimal balance between seaward and shoreward failure for non-impact loads. Further, larger seaward eccentricities are recommended for significant impact loads. In the GWK tests (Kudella et al., 2006), an own weight eccentricity of 8% is considered.

In the present study, it was found that own weight seaward eccentricity has a beneficial effect on caisson residual tilt only for low to moderate load eccentricities. For low eccentricity regime, the tilt is in the seaward direction instead of the shoreward direction (see Fig. 5.17 and Fig. 5.16a). For moderate eccentricity regime, the caisson shoreward tilt is reduced or even eliminated (see Fig. 5.17 and Fig. 5.16a). Nevertheless, no gain was found from introducing own weight seaward eccentricity for large or extreme eccentricity regimes. It is even advisable to consider no seaward own weight eccentricity when it is fairly highly probable that the structure is subject to relevantly frequent large load eccentricities.

If extension of the base slab is considered to introduce the own weight eccentricity, the extension should be stiff enough to maintain the assumption of rigidity, especially for caissons with perforated walls.

b. Rubble berm

Rubble berms provide an overburden pressure on the underlying seabed soil relatively increasing its strength. The side friction between the berm and the caisson can reduce the loads exerted on the foundation underneath. Therefore, a rubble berm on one side of the caisson and not the other can reduce the probability and/or magnitude of tilt in its direction. Further, a side berm behind (adjacent to the shoreside of) the caisson would provide an added resistance to sliding and would be advisable for large eccentricity regimes.

c. Drainage conditions

For sands, the permeability is inversely correlated to relative density, which implies for loose sands (most vulnerable to partial liquefaction) the permeability is relatively high. As observed in the GWK tests, unfavourable drainage conditions can cause significant buildup of pore pressure for regular breaking wave impacts. Therefore, sites with poor drainage should be avoided or a solution to enhance drainage should be considered.

5.4 Concluding Remarks on the CFD-CSD Model System and Implications

In this chapter, the one-way coupling procedure of both hydrodynamic (CFD) and hydro-geotechnical (CSD) models is presented. The semi-coupled CFD-CSD model is then applied to reproduce large-scale physical model tests performed in the Large Wave Flume (GWK) on a caisson breakwater subject to wave attack. The experimental setup in GWK is described, including model configuration, measurement devices, construction procedure and properties of the soil foundation and further structure elements. Additionally, the idealizations for the numerical simulation of the experiments are outlined, including the material zones, their properties and boundary conditions.

The validation of the numerical model system against the GWK tests is performed for non-breaking, slightly breaking and breaking wave load conditions. The coupled model system successfully reproduces the GWK tests, for non-breaking, slightly breaking and breaking wave loads on caisson breakwaters.

A new concept, called the "load eccentricity concept", is proposed to describe the loading conditions and the structure configurations. It is based on the relative load eccentricity of the vertical load resultant ($\frac{e}{B}$). Using this concept, the response of the structure and its soil foundation can be classified in four regimes: low, moderate, large and extreme load eccentricity regimes. The seabed soil (sand) is described by its relative density (and consequent further properties), which are considered according to typical values from the literature. Combining the load eccentricity with the soil relative density, systematic numerical tests are performed to extend the range of conditions tested in the GWK. The numerical results and those from the GWK tests provide a departure basis for the development of a simplified model as presented in chapter 6.

Based on the results of the tests from the numerical model system and the physical model, an interpretation for the stepwise failure of monolithic breakwaters is proposed with special emphasis on the role of transient and residual pore pressure on the residual tilt of the breakwater.

In the following sections, the capabilities and limitations of the CFD-CSD model system are outlined and implications are drawn for the design of the cross-section of monolithic breakwaters.

5.4.1 Model System Capabilities and Limitations

Strong interactions of hydrodynamic processes and those related to a structure and its soil foundation can be numerically reproduced only through CFD-CSD model coupling. Coupling approaches exist which greatly differ in complexity and accuracy. In this study, different types of coupling procedures are applied. In the modelling of the soil as a porous media, a monolithic coupling approach is used in the CSD model to account for the strong pore fluid-solid skeleton interaction, whereas the simplest approach to coupling is considered for coupling the hydrodynamic (CFD) solver with the hydro-geotechnical (CSD) solver. The coupling between the solvers is implemented in one-way according to justifications presented in Section 5.1. Moreover, it was anticipated that for monolithic breakwaters such a semi-coupling procedure is sufficient to reproduce the physical experiments in which relatively small motions of a rigid caisson structure were observed.

Through the results of the more detailed analysis of the GWK tests and the results of the semi-coupled CFD-CSD model system, the capabilities and the limitations of the latter, including its constituents, could be identified and recommendations for further development could be drawn as outlined below.

a. Hydrodynamic model

The hydrodynamic model was generally successful in reproducing the horizontal wave forces on the structure including the effect of fluid compressibility. Nevertheless, the effect of entrapped/entrained air in breaking wave impact needs more attention for a more accurate reproduction. One of the likely explanations is the need for a more proper method to simulate air bubbles as a dispersed phase in water. Uplift forces are overestimated in the numerical computations. Nonetheless, this is addressed in the remarks on the coupling procedure.

b. Hydro-geotechnical model

The hydro-geotechnical model can successfully reproduce processes associated with strong solid skeleton-pore fluid interactions such as consolidation, fluid injection and direct wave load on the seabed. The model has proven successful in reproducing plasticity aspects of sands under cyclic loading (e.g. pore pressure buildup). Additionally, the model succeeded in reproducing soil densification after sufficient load cycles. Nevertheless, the continuum nature of the model makes it suitable only where the assumption of averaging the porous media (rubble foundation and soil underneath) is valid. However, the model is incapable of reproducing relatively micro-scale processes like the response of individual rubble stone units at the toe of structure under extreme wave loads (extreme load eccentricity), which is outside the scope of this study.

c. Soil constitutive modelling

The CSD model allows for the introduction of different soil constitutive models. A multi-surface plasticity model is implemented. The elastoplastic model can reproduce the soil processes relevant for this study; residual pore pressure and cyclic mobility. The constitutive model is computationally expensive. Parallel processing via domain decomposition enabled significant speed-up of simulations. For future work, it would be beneficial to implement the constitutive modelling solution by a Graphics Processing Unit (GPU) because updating the constitutive model for each cell requires no communication to other processes, and hence can efficiently take full advantage of GPU computing.

d. Contact modelling

Contact modelling plays a very important role in transferring the forces correctly from the structure to the underlying foundation. It is safe to say that without the inclusion of a proper methodology for modelling soil-structure interaction, no CSD model can be considered adequate for studying the response of monolithic breakwaters to wave loads. Nevertheless, the modelling of frictional contact between the structure and the foundation is not considered in models available in the litrature. The developed model system accounts properly for the frictional contact between the structure and the underlying foundation. Special care should be considered in the configuration of the contact to relax any artificial stresses from contact modelling without damping the actual stress exchange between both sides of the interface of the media considered.

e. Pore fluid compressibility

Pore fluid compressibility has a significant effect on the amplitude/fluctuation of transient component of the pore pressure and consequently also on the amplitude of the effective stress carried by the solid-skeleton. Hence, the effect on the stepwise mechanism is large. From the analysis and interpretation of the results, it is obvious that the pore pressure response is different under the seaward and shoreward sides of the breakwater. This means that the mechanism of air content may significantly differ on both sides inside the soil foundation (due to the wave loading conditions), so that the assumption of a single pore fluid mixture in this study should probably be revised. Modelling the pore fluid as multiphase instead of a single phase mixture with modelling air as a dispersed phase in the water phase will be required for the realization of a more accurate model in this regard. It will additionally help better understanding of the mechanics of a changing pore fluid compressibility during the wave loading.

f. Fully dynamic vs. partially dynamic Biot formulation

The fully dynamic approach has generally proven to be more accurate than the $u-p$ approximation, in terms of reproducing the response of the soil foundation of caisson breakwaters. This is especially the case with regards to the accumulation and dissipation of excess pore pressure as related to the total pressure which were not captured by the $u-p$ approximation. Furthermore, the fully dynamic approach can better reproduce the effect of the caisson rocking motions (vibration) after impact. Although the time difference for long time quasi-static simulations (i.e. consolidation of a soil column) is in favour of the $u-p$ approximation, the simulations with more transient nature, including contact and plasticity modelling, show much less difference in computational speed. The fully dynamic approach provides a more natural way to dampen artificial stresses (elastic waves). Although a comparison between both methods has been reported in the literature for a simplified analytical solution with an elastic seabed (Ülker et al., 2009), the results do not necessarily apply to elastoplastic seabed, so that a comparison between both methods is still missing.

g. Coupling procedure

The one-way semi-coupling procedure has facilitated the focus on the development of each solver separately (among other reasons stated in 5.1). Nonetheless, the one-way coupling procedure has proved to be questionable where strong interaction exists, especially for uplift pressures and the effect of fluid beneath the caisson on its motion. A two-way partitioned approach might be significantly more accurate in simulating wave-structure-foundation interaction and would provide a finer coupling resolution (more control over time and space interpolation of data transmitted between CFD and CSD solvers).

5.4.2 Recommendations for Design of Monolithic Breakwaters

In the light of the proposed *load eccentricity concept*, most of the measures reported in the literature to enhance the response of monolithic breakwaters (especially residual tilt) to wave loads have in common a reduction of the maximum load eccentricity. These include conventional measures as increasing the breakwater width in the cross-section and/or increasing its mass. More innovative measures are focused on reducing the horizontal wave impact by introducing open chambers with perforated walls facing the wave impact, to absorb some of the impact energy.

Based on the results of this study, a cross-section for monolithic breakwaters can be suggested, Fig. 5.24. In this cross section, a quarter circular arc is proposed to face the wave impact. This has the advantage of focusing the wave impact force in the center of the circle. Therefore, the vertical load eccentricity is reduced in two ways: (i) By directly transforming part of the wave force as a vertical stabilizing force that is directly proportional to the uplift force and (ii) controlling the location of the focusing point of the wave impact force. This proposed cross section allows for possible reduction in materials used for the whole structure. Additionally, horizontal wave impact loads are reduced (transformed to downward vertical loads) which reduces the sliding forces and increases the frictional resistance (increased stabilizing forces). Further, the sliding resistance can be increased by increasing the base roughness via serrations. The additional quarter-circular chamber can be utilized as an Oscillating Water Column (OWC) for wave energy extraction, to make the wave structure multi-purpose, thus enhancing its acceptance and cost aspects. Perforations can be introduced to the circular wall to reduce wave impact, with special care not to develop turbulence near OWC intake.

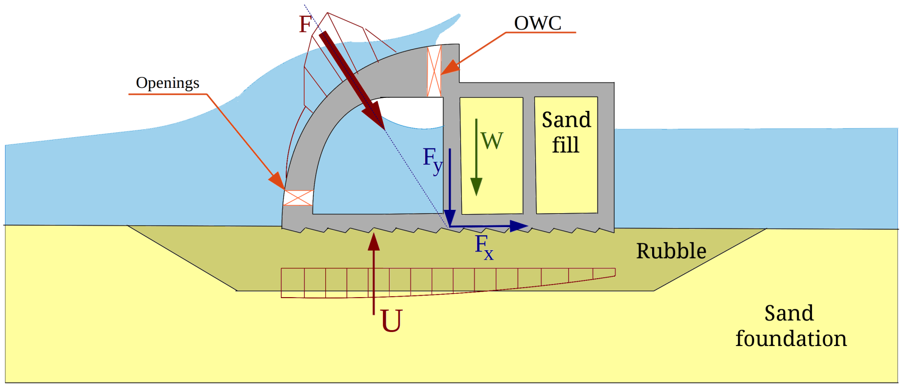

Figure 5.24: Proposed cross-section for monolithic breakwaters to enhance stability, reduce needed construction materials and enhance economical aspects of the structure

6 Simplified Model of Monolithic Breakwater Subject to Wave Loads

In this chapter, a simplified nonlinear dynamic model for the response of caisson breakwaters to wave loads, together with the necessary toolbox for practical implementation, is developed and validated. In addition to sliding and overturning, it can also predict stepwise failures (residual displacements), including the observed seaward residual tilt of caisson breakwaters. First, the development of the mass-spring-dashpot model is described, including the governing equations, the solver as well as the model input and attributes. Second, further features of the model are developed to account for soil structure interaction, soil elastoplastic response and model non-linearity. Third, the organization structure of the overall simplified model, called the "*caissonFoam*" solver, is outlined. Forth, values for the model parameters are recommended and the model is applied to reproduce the caisson breakwater tests in the large wave flume GWK. Finally, a summary of the capabilities and limitations of the new simplified model is provided.

6.1 3-DOF Mass-Spring-Dashpot Model

In this section, a simplified 3-DOF (Three Degrees Of Freedom) mass-spring-dashpot model for the analysis of monolithic breakwater response to water waves is presented. First, the governing equations and their implementation in a new solver are described. Further, the computation of wave loading as well as structural properties and dynamic attributes are given.

6.1.1 Model Description

For the model development, the monolithic breakwater (i.e. caisson breakwater) is assumed to undergo rigid body motion only, without any local deformations. This assumption is acceptable for such a massive concrete structure as long as no failure of any of its components has taken place. Hence, the structure can be modelled by a single mass model with three degrees of freedom: vertical, horizontal and rocking motions. The caisson is supported by an arbitrary number of vertical supports (springs and dashpots) at the breakwater-foundation interface to simulate soil-structure interaction for vertical and rotational motions. A horizontal dashpot is used to represent horizontal friction resistance against sliding. The model allows for an arbitrary number (with a minimum of two) of vertical supports. Ten vertical supports were considered for the calibration of this model. A sketch of the simplified 3DOF caisson model is given in Fig. 6.1. The 3-DOF model is governed by the (matrix) equation of motion, that reads:

$$\mathbf{M}\frac{\mathrm{d}^2\mathbf{u}}{\mathrm{d}t^2} + \mathbf{C}\frac{\mathrm{d}\mathbf{u}}{\mathrm{d}t} + \mathbf{K}\mathbf{u} = \mathbf{f}, \tag{6.1}$$

where $\mathbf{f}$ is the vector of forces acting on the structure (horizontal and vertical forces in addition to rotating moment calculated at pivot), $\mathbf{u}$ is the displacement vector (i.e. horizontal, vertical and rotational displacements of caisson at its rotation pivot), $\frac{\mathrm{d}\mathbf{u}}{\mathrm{d}t}$ and $\frac{\mathrm{d}^2\mathbf{u}}{\mathrm{d}t^2}$ are the velocity and acceleration vectors of the caisson at its pivot, $\mathbf{M}$, $\mathbf{C}$, and $\mathbf{K}$ are the mass, damping and stiffness matrices, respectively. The model Equation 6.1 can be expanded as:

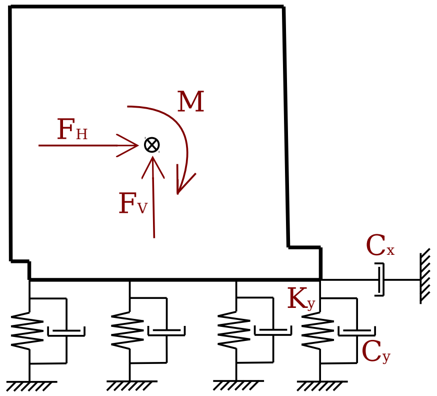

Figure 6.1: Concept of the simplified 3-DOF caisson model

$$
\begin{bmatrix} m_x & 0 & 0 \\ 0 & m_y & 0 \\ m_x y_P & m_y x_P & I_z \end{bmatrix}
\begin{Bmatrix} \frac{\mathrm{d}^2 u_x}{\mathrm{d}t^2} \\ \frac{\mathrm{d}^2 u_y}{\mathrm{d}t^2} \\ \frac{\mathrm{d}^2 \theta}{\mathrm{d}t^2} \end{Bmatrix}
+
\begin{bmatrix} c_x & 0 & 0 \\ 0 & \sum\limits_{i=1}^{n} c_{y_i} & -\sum\limits_{i=1}^{n} c_{y_i} x_{P_i} \\ 0 & -\sum\limits_{i=1}^{n} c_{y_i} x_{P_i} & \sum\limits_{i=1}^{n} c_{y_i} x_{P_i}^2 \end{bmatrix}
\begin{Bmatrix} \frac{\mathrm{d}u_x}{\mathrm{d}t} \\ \frac{\mathrm{d}u_y}{\mathrm{d}t} \\ \frac{\mathrm{d}\theta}{\mathrm{d}t} \end{Bmatrix}
$$
$$
+
\begin{bmatrix} 0 & 0 & 0 \\ 0 & \sum\limits_{i=1}^{n} K_{y_i} & -\sum\limits_{i=1}^{n} K_{y_i} x_{P_i} \\ 0 & -\sum\limits_{i=1}^{n} K_{y_i} x_{P_i} & \sum\limits_{i=1}^{n} K_{y_i} x_{P_i}^2 \end{bmatrix}
\begin{Bmatrix} u_x \\ u_y \\ \theta \end{Bmatrix}
=
\begin{Bmatrix} F_H \\ F_V \\ M \end{Bmatrix},
\tag{6.2}
$$

where F_H and F_V are resultants of horizontal and vertical forces acting on the caisson, respectively, M is the rotating moment acting at the current caisson pivot, u_x and u_y are the horizontal and vertical displacements of the caisson as a rigid body and θ is the caisson's rotation at its current pivot. The horizontal and vertical distances between the caisson centre of gravity and the current pivot location are x_P and y_P, respectively. Additionally, x_{P_i} is the horizontal distance between the i^{th} vertical support (spring and dashpot) and the current pivot. The caisson is supported by n number of vertical supports.

If the coefficients of the mass, damping and stiffness matrices are known, Eqs. 6.2 can be solved for caisson displacements considering a given load time-history. To transform the equations into first order differential equations, the following relations are considered:

$$
\begin{aligned}
y_0 &= u_x, \\
y_1 &= \frac{\mathrm{d}u_x}{\mathrm{d}t} = \frac{\mathrm{d}y_0}{\mathrm{d}t}, \\
y_2 &= u_y, \\
y_3 &= \frac{\mathrm{d}u_y}{\mathrm{d}t} = \frac{\mathrm{d}y_2}{\mathrm{d}t}, \\
y_4 &= \theta, \\
y_5 &= \frac{\mathrm{d}\theta}{\mathrm{d}t} = \frac{\mathrm{d}y_4}{\mathrm{d}t},
\end{aligned}
\tag{6.3}
$$

the system of equations (Eq. 6.2), is reduced to first order as:

$$\begin{aligned}
&\begin{bmatrix} m_x & 0 & 0 \\ 0 & m_y & 0 \\ m_x y_P & m_y x_P & I_z \end{bmatrix} \begin{Bmatrix} \frac{\mathrm{d}y_1}{\mathrm{d}t} \\ \frac{\mathrm{d}y_3}{\mathrm{d}t} \\ \frac{\mathrm{d}y_5}{\mathrm{d}t} \end{Bmatrix} + \begin{bmatrix} c_x & 0 & 0 \\ 0 & \sum\limits_{i=1}^{n} c_{y_i} & -\sum\limits_{i=1}^{n} c_{y_i} x_{P_i} \\ 0 & -\sum\limits_{i=1}^{n} c_{y_i} x_{P_i} & \sum\limits_{i=1}^{n} c_{y_i} x_{P_i}^2 \end{bmatrix} \begin{Bmatrix} y_1 \\ y_3 \\ y_5 \end{Bmatrix} \\
&+ \begin{bmatrix} 0 & 0 & 0 \\ 0 & \sum\limits_{i=1}^{n} K_{y_i} & -\sum\limits_{i=1}^{n} K_{y_i} x_{P_i} \\ 0 & -\sum\limits_{i=1}^{n} K_{y_i} x_{P_i} & \sum\limits_{i=1}^{n} K_{y_i} x_{P_i}^2 \end{bmatrix} \begin{Bmatrix} y_0 \\ y_2 \\ y_4 \end{Bmatrix} = \begin{Bmatrix} F_H \\ F_V \\ M \end{Bmatrix}
\end{aligned} \tag{6.4}$$

After the ordinary differential equations system is reduced to first order, the system can be solved simultaneously. The full system of equations reads:

$$\begin{aligned}
&\begin{bmatrix} 1 & 0 & 0 & 0 & 0 & 0 \\ 0 & m_x & 0 & 0 & 0 & 0 \\ 0 & 0 & 1 & 0 & 0 & 0 \\ 0 & 0 & 0 & m_y & 0 & 0 \\ 0 & 0 & 0 & 0 & 1 & 0 \\ 0 & m_x y_P & 0 & m_y x_P & 0 & I_z \end{bmatrix} \begin{Bmatrix} \frac{\mathrm{d}y_0}{\mathrm{d}t} \\ \frac{\mathrm{d}y_1}{\mathrm{d}t} \\ \frac{\mathrm{d}y_2}{\mathrm{d}t} \\ \frac{\mathrm{d}y_3}{\mathrm{d}t} \\ \frac{\mathrm{d}y_4}{\mathrm{d}t} \\ \frac{\mathrm{d}y_5}{\mathrm{d}t} \end{Bmatrix} + \\
&\begin{bmatrix} 0 & 0 & 0 & 0 & 0 & 0 \\ 0 & c_x & 0 & 0 & 0 & 0 \\ 0 & 0 & 0 & 0 & 0 & 0 \\ 0 & 0 & \sum\limits_{i=1}^{n} K_{y_i} & \sum\limits_{i=1}^{n} c_{y_i} & -\sum\limits_{i=1}^{n} K_{y_i} x_{P_i} & -\sum\limits_{i=1}^{n} c_{y_i} x_{P_i} \\ 0 & 0 & 0 & 0 & 0 & 0 \\ 0 & 0 & -\sum\limits_{i=1}^{n} K_{y_i} x_{P_i} & -\sum\limits_{i=1}^{n} c_{y_i} x_{P_i} & \sum\limits_{i=1}^{n} K_{y_i} x_{P_i}^2 & \sum\limits_{i=1}^{n} c_{y_i} x_{P_i}^2 \end{bmatrix} \begin{Bmatrix} y_0 \\ y_1 \\ y_2 \\ y_3 \\ y_4 \\ y_5 \end{Bmatrix} = \begin{Bmatrix} y_1 \\ F_H \\ y_3 \\ F_V \\ y_5 \\ M \end{Bmatrix}
\end{aligned} \tag{6.5}$$

According to Eq. 6.5, the derivatives are:

$$\begin{aligned}
F_0 &= \frac{\mathrm{d}y_0}{\mathrm{d}t} = y_1, \\
F_1 &= \frac{\mathrm{d}y_1}{\mathrm{d}t} = \frac{1}{m_x}\left(F_H - c_x y_1\right), \\
F_2 &= \frac{\mathrm{d}y_2}{\mathrm{d}t} = y_3, \\
F_3 &= \frac{\mathrm{d}y_3}{\mathrm{d}t} = \frac{1}{m_y}\left(F_V - \sum_{i=1}^{n} K_{y_i} y_2 - \sum_{i=1}^{n} c_{y_i} y_3 + \sum_{i=1}^{n} K_{y_i} x_{P_i} y_4 + \sum_{i=1}^{n} c_{y_i} x_{P_i} y_5\right), \\
F_4 &= \frac{\mathrm{d}y_4}{\mathrm{d}t} = y_5, \\
F_5 &= \frac{\mathrm{d}y_5}{\mathrm{d}t} = \frac{1}{I_z}\Bigg(M + \sum_{i=1}^{n} K_{y_i} x_{P_i} y_2 + \sum_{i=1}^{n} c_{y_i} x_{P_i} y_3 \\
&\quad - \sum_{i=1}^{n} K_{y_i} x_{P_i}^2 y_4 - \sum_{i=1}^{n} c_{y_i} x_{P_i}^2 y_5 - m_x y_P \frac{\mathrm{d}y_1}{\mathrm{d}t} - m_y x_P \frac{\mathrm{d}y_3}{\mathrm{d}t}\Bigg)
\end{aligned} \tag{6.6}$$

Considering a small time step for solution advancement, the load-time dependency (load time derivative) can be neglected. The elements of the Jacobian matrix can be calculated as given in Table 6.1.

This simplified system provides a time dependent framework for the analysis of caisson breakwaters. An ODE solver has been developed using the OpenFOAM framework (*caissonFoam*) to solve the ordinary

Table 6.1: Elements of the Jacobian matrix (partial derivatives)

	F_0	F_1	F_2	F_3	F_4	F_5
t	0	0	0	0	0	0
y_0	0	0	0	0	0	0
y_1	1	$\frac{-c_x}{m_x}$	0	0	0	$\frac{c_x y_P}{I_z}$
y_2	0	0	0	$-\frac{\sum_{i=1}^{n} K_{y_i}}{m_y}$	0	$\frac{\sum_{i=1}^{n} K_{y_i} x_{P_i} + x_P \sum_{i=1}^{n} K_{y_i}}{I_z}$
y_3	0	0	1	$-\frac{\sum_{i=1}^{n} c_{y_i}}{m_y}$	0	$\frac{\sum_{i=1}^{n} c_{y_i} x_{P_i} + x_P \sum_{i=1}^{n} c_{y_i}}{I_z}$
y_4	0	0	0	$\frac{\sum_{i=1}^{n} K_{y_i} x_{P_i}}{m_y}$	0	$-\frac{\sum_{i=1}^{n} K_{y_i} x_{P_i}^2 - x_P \sum_{i=1}^{n} K_{y_i} x_{P_i}}{I_z}$
y_5	0	0	0	$\frac{\sum_{i=1}^{n} c_{y_i} x_{P_i}}{m_y}$	1	$-\frac{\sum_{i=1}^{n} c_{y_i} x_{P_i}^2 - x_P \sum_{i=1}^{n} c_{y_i} x_{P_i}}{I_z}$

differential equations associated with the system. For initial value ODE problem, there are several methods in OpenFOAM, among which Runge-Kutta (RK), Kaps-Rentrop (KRR4) and Semi-Implicit Bulirsh-Stoer (SIBS). The Semi-Implicit Bulirsh-Stoer (SIBS) ODE solver is used for the solution of the (modified) system of equations for its better suitability for solving stiff equations (e.g. equation of motion).

6.1.2 Model Input and Attributes

a. Wave loads on structure

The developed 3-DOF model needs an input of time-history of loads on the monolithic breakwater. These loads should be prepared as resultant forces at the center of gravity of the breakwater's cross section. The resultant forces are: vertical and horizontal forces as well as the rotating moment calculated at the breakwater's CG (center of gravity). In the presented model, the loads on the breakwater's CG can be given as a direct input (e.g. from CFD simulations) or the forces can be calculated using simplified methods. The method for wave loads calculation is selected based on the parameter map shown in Fig. 6.2 (Kortenhaus and Oumeraci, 1998). The methods include the PROVERBS method for breaking wave impact alongside Sainflou's method for nonbreaking wave loads and Goda's method for slightly breaking waves. The model uses linear superposition to calculate the resultants (F_H, F_V and M) of wave loads on a caisson breakwater caused by many wave components to simulate irregular waves. Or by direct input of load-time history (e.g. from CFD simulations).

For the nonbreaking loads and loads from slightly breaking waves, the time variation of the forces was considered harmonic with an amplitude calculated from maximum or minimum value of force (e.g. from the Sainflou method). For the breaking wave impact, the time history of the breaking wave impact is considered according to the triangular shape suggested by the PROVERBS method, Fig. 6.3.

A comparison of wave loads calculated by empirical methods using the *caissonFoam* solver and wave loads calculated by means of CFD modelling for three different conditions of the large-scale physical caisson breakwater tests at the large wave flume (GWK) in Hannover is shown in Fig. 6.4, 6.5 and 6.6. As shown the maximum and minimum forces and moments calculated by *caissonFoam* using empirical methods underestimate values calculated by CFD simulations. Nevertheless, for breaking wave impact the PROVERBS method can estimate the horizontal wave impact (load peak) quite well. The breaking wave impact calculates by the PROVERBS method does not, however, reproduce either oscillations in forces after the impact (due to vibration of the entrapped air cushion) or the static load after the impact. The uplift force calculated by the PROVERBS method is smaller than that retrieved by CFD simulations. Nevertheless, as explained in

Chapter 3 the CFD model overestimates uplift pressures due to neglecting caisson motion and flexibility of the impermeable sheet underneath the rubble foundation and deformations of the sand foundation. The rotating moment at the caisson's CG calculated by the PROVERBS method has a negative value (anticlockwise, unlike the CFD results) because the horizontal force resultant position calculated by the PROVERBS method lies below the caisson's CG for the presented tests. Nevertheless, rotating moment at the caisson base will always be positive (clockwise).

b. Cross sectional properties of the structure

The parameters defining the geometry of the cross section of the caisson breakwater need to be determined. These are determined by the *caissonFoam* solver by considering the cross section as a polygon, Fig. 6.7, based on input coordinates for cross section vertices. The caisson cross sectional area is calculated as:

$$A_{caisson} = 0.5\left|\sum_{i=1}^{n} (x_i y_{i+1} - x_{i+1} y_i)\right| \tag{6.7}$$

The coordinates of the cross section centroid (also considered as the CG) are calculated by:

$$x_{CG} = \frac{1}{6A_{caisson}} \sum_{i=1}^{n} (x_i + x_{i+1}) (x_i y_{i+1} - x_{i+1} y_i) \tag{6.8}$$

$$y_{CG} = \frac{1}{6A_{caisson}} \sum_{i=1}^{n} (y_i + y_{i+1}) (x_i y_{i+1} - x_{i+1} y_i) \tag{6.9}$$

The moment of inertia of the cross section at the coordinates origin considering a two-dimensional polygon using Green's theorem:

$$I_O = \frac{m_{caisson}}{6} \frac{\sum_{i=1}^{n} \|\mathbf{P}_{i+1} \times \mathbf{P}_i\| ((\mathbf{P}_{i+1} \cdot \mathbf{P}_{i+1}) + (\mathbf{P}_{i+1} \cdot \mathbf{P}_i) + (\mathbf{P}_i \cdot \mathbf{P}_i))}{\sum_{i=1}^{n} \|\mathbf{P}_{i+1} \times \mathbf{P}_i\|} \tag{6.10}$$

$$I_O = \frac{m_{caisson}}{6} \frac{\sum_{i=1}^{n} (x_i^2 + y_i^2 + x_i x_{i+1} + y_i y_{i+1} + x_{i+1}^2 + y_{i+1}^2) \left|(x_i y_{i+1} - x_{i+1} y_i|\right)}{\sum_{i=1}^{n} \left|(x_i y_{i+1} - x_{i+1} y_i)\right|} \tag{6.11}$$

Where $\mathbf{P}_{i=1-n}$ are the polygon vertices of coordinates x and y. The moment of inertia of the cross section related to the CG can be calculated by the theory of parallel axis as:

$$I_{CG} = I_O + m_{caisson} ||CG||^2 \tag{6.12}$$

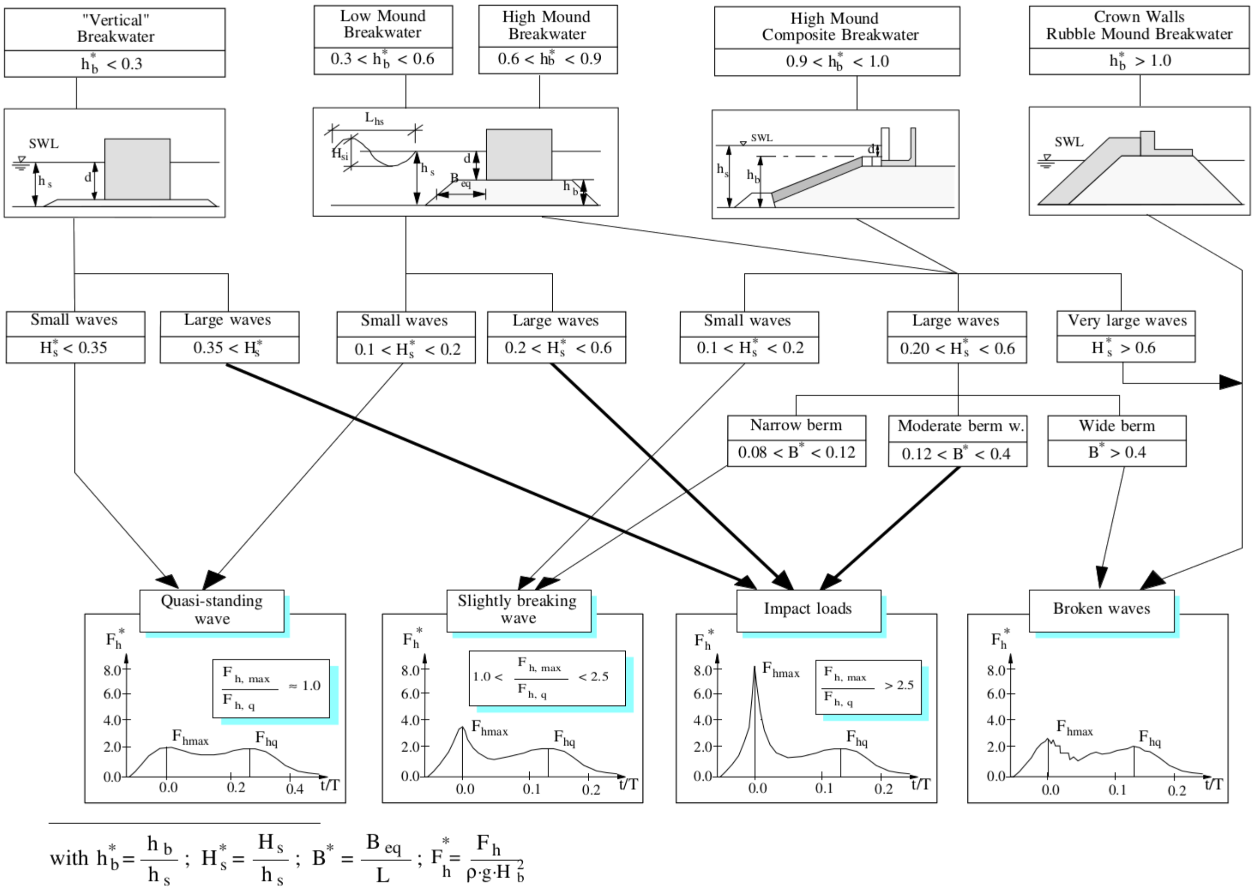

Figure 6.2: Parameter map for selecting method for calculating wave forces on caisson breakwater: H_{si} is the incident breaking wave height, H_b is the breaking wave height, L_{h_s} is wave length at water depth h_s, h_b is height of rubble mound, B_{eq} is length starting from $h_b/2$ to caisson foot and F_h is horizontal wave force (Kortenhaus and Oumeraci, 1998)

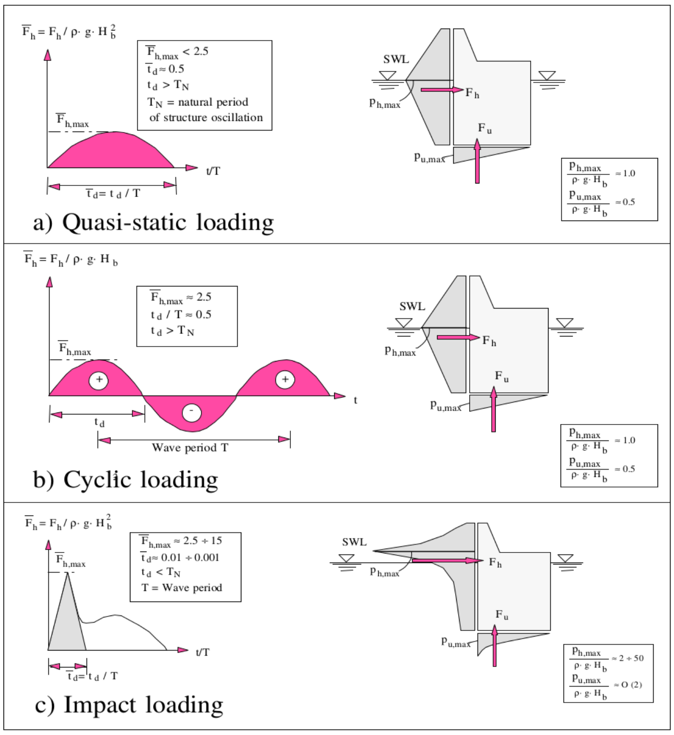

Figure 6.3: Specification of wave loading for monolithic structures. (Oumeraci et al., 1995)

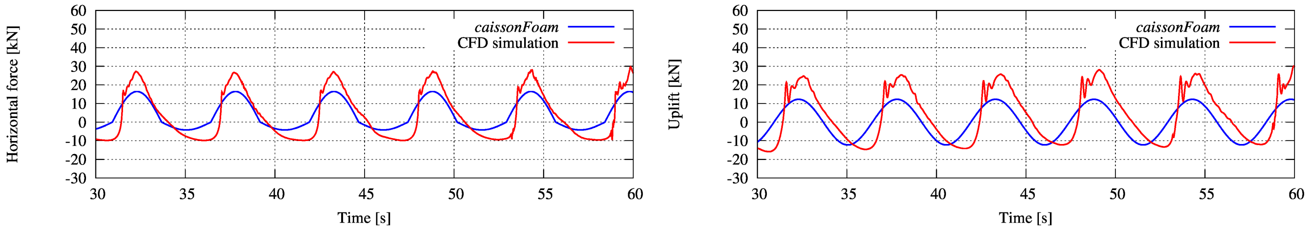

(a) Horizontal wave force (b) Uplift force

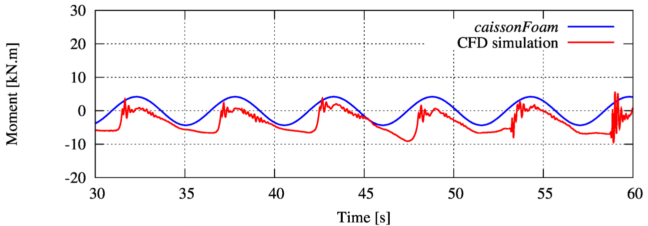

(c) Rotating moment at CG

Figure 6.4: Comparison between empirical forces from *caissonFoam* and forces from CFD simulations for GWK tests, non-breaking waves: H=0.4m and T=5.5s

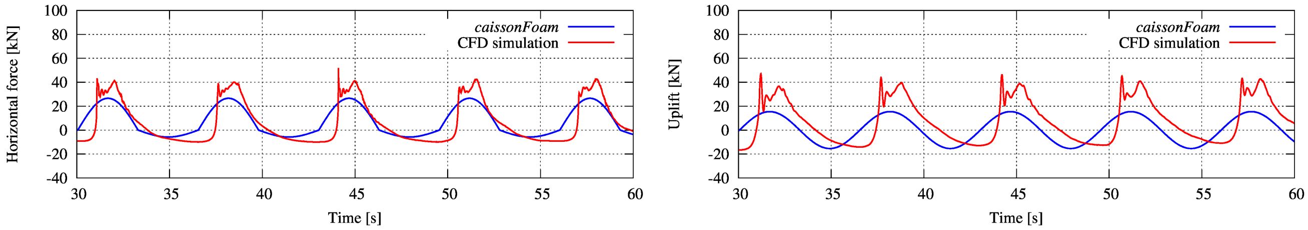

(a) Horizontal wave force (b) Uplift force

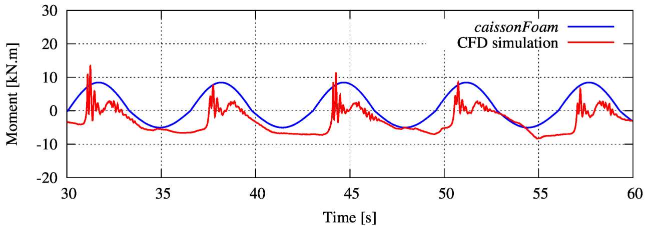

(c) Rotating moment at CG

Figure 6.5: Comparison between empirical forces from *caissonFoam* and forces from CFD simulations for GWK tests, slightly breaking waves: H=0.5m and T=6.5s

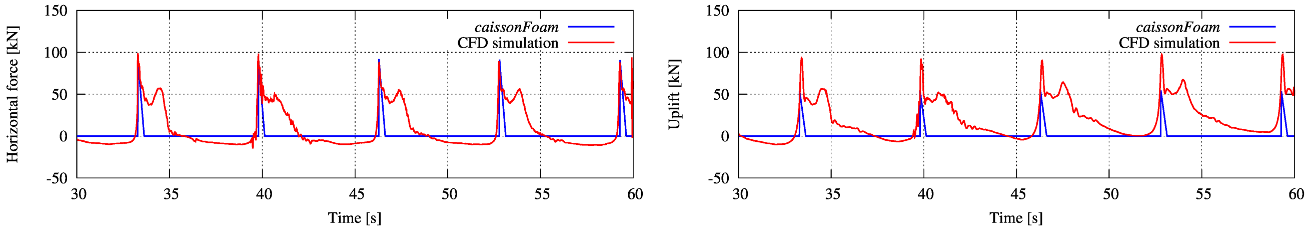

(a) Horizontal wave force (b) Uplift force

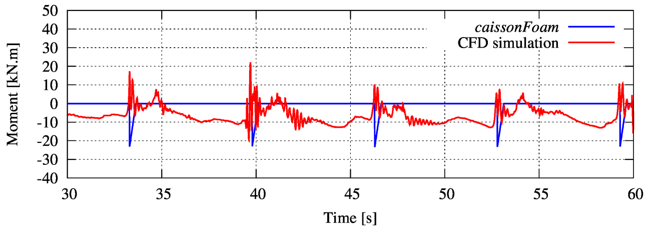

(c) Rotating moment at CG

Figure 6.6: Comparison between empirical forces from *caissonFoam* and forces from CFD simulations for GWK tests, breaking wave impact: H=0.7m and T=6.5s

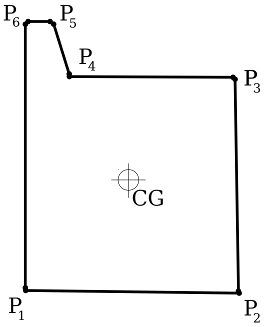

Figure 6.7: Defining the cross section of monolithic breakwater as a polygon

c. Dynamic attributes

The elements of the mass matrix are calculated as:

$$\begin{aligned} m_x &= m_{caisson} + m_{hyd,x} + m_{geo,x} \\ m_y &= m_{caisson} + m_{geo,y} \\ I_z &= I_{CG} + \Delta I + m_{hyd,\theta} + m_{geo,\theta} \end{aligned} \tag{6.13}$$

where $m_{hyd,x}$ and $m_{hyd,\theta}$ are the hydrodynamic added mass for the horizontal and rotational motions, respectively. The added hydrodynamic mass represent the relevant fluid mass that is forced to move with the structure when the structure is subject to impulsive oscillations, although, a larger portion of the surrounding fluid is (in a way) accelerated by structural motion. Oumeraci and Kortenhaus (1994) found that theoretical calculation of added hydrodynamic mass based on an incompressible and irrotational two dimensional potential flow theory approach (Hagen and Lundgren, 1977; Cooker, 1990) underestimate the added hydrodynamic mass retrieved from physical tests, they concluded that the theoretical expressions are of sufficient engineering accuracy and need not be refined. Therefore, the following theoretical expressions are used herein to describe the hydrodynamic masses (Oumeraci et al., 2001) as:

$$\begin{aligned} m_{hyd,x} &= 0.543\ \rho_w d^2 \\ m_{hyd,\theta} &= 0.218\ \rho_w d^2 \end{aligned} \tag{6.14}$$

where d is the water depth in front of the caisson.

On the other hand, the geodynamic added mass (m_{geo}) does not mean that an identifiable soil body is attached to the structure and has the same response, it is rather a fictious value needed to provide a better fit of results from linear models to actual structural response in case of loads in the low frequency range (Wolf, 1987). Therefore, no geodynamic added mass is considered in the nonlinear model of this study, in which the elastoplastic springs will be fit to results from physical model tests and from the validated coupled CFD-CSD model system.

$$m_{geo,x} = m_{geo,y} = m_{geo,\theta} = 0 \tag{6.15}$$

The final expressions for the system mass matrix elements reads:

$$\begin{aligned} m_x &= \rho_{caisson}\ \text{\it{V}}\!\!\!-_{cisson} + 0.543\ \rho_w d^2 \\ m_y &= \rho_{caisson}\ \text{\it{V}}\!\!\!-_{cisson} \\ I_z &= I_{CG} + \Delta I + 0.218\ \rho_w d^2 \end{aligned} \tag{6.16}$$

where $\rho_{caisson}$ is the average mass density of the caisson and $\text{\it{V}}\!\!\!-_{\text{cisson}}$ is the volume of the caisson (per one meter in the out of plane direction). The value of ΔI changes according to the position of the rotational pivot as explained in the next section.

The damping coefficient for the horizontal dashpot is calculated according to soil-structure interface as explained in the following section. For the damping coefficient of the vertical dashpots, a similar approach to Lysmer's analog is considered. In Lysmer's analog, a massless rigid disk resting on an elastic half-space is approximated as a single degree of freedom model and the vertical stiffness and damping coefficients are approximated to fit the half-space theory solution.

For this study, a similar one degree of freedom model of a massless rigid surface strip foundation resting on an elastic un-dampened half-plane is considered as explained in Wolf (1987). The results of the approximated model with the given expressions are in acceptably good agreement with the solution of the elastic half-space theory (Wolf, 1987). According to Wolf (1987), the damping coefficient for any vertical dashpot is given as:

$$c_{y_i} = \chi \frac{B_i}{2} \left(1 + 4\nu^2\right) (3.5 - 2\nu) \sqrt{\rho_s G} \tag{6.17}$$

where B_i is the width of the caisson base assigned to the i^{th} dashpot. G is the soil shear modulus, ρ_s is the density of the soil solid phase, ν is Poisson's ratio and χ is an additional factor of the damping coefficient to account for elastoplastic springs.

6.2 Features and Overall Structure of the Simplified Model

In this section, the features of the simplified model are presented. These include modelling soil-structure interaction; sliding, separation and reattachment of structure-foundation interface, change of pivot position according to the structure response and elastoplastic soil response. Hence, the model non-linearity is discussed. Further, the overall structure of the simplified model; i.e. the *caissonFoam* solver is outlined.

6.2.1 Soil-Structure Interaction

The soil-structure interaction features considered in the simplified model include the simulation of the soil structure contact regarding the following aspects: (i) the friction between structure and the foundation underneath, (ii) the soil-structure separation and reattachment and (iii) the change of the position of caisson pivot (center of rotation) according to the updated soil-structure interface.

The friction at the soil-structure interface is modelled via a horizontal dashpot which is only activated (nonzero damping coefficient) if the horizontal wave-induced force is larger than the static friction resistance at the contact surface. If the friction dashpot is activated, the damping coefficient is calculated from the caisson horizontal speed and the dynamic friction coefficient. The damping coefficient of the horizontal friction dashpot is calculated as:

$$c_x = \begin{cases} \frac{\left(W'_{caisson} - F_{uplift}\right)\mu_{dynamic}}{v_x}, & \text{if } F_H > F_{friction} \text{ and } |v_x| > 0 \\ 0, & \text{if } v_x = 0 \end{cases} \tag{6.18}$$

where $F_{friction}$ is the friction resistance of the soil-structure interface that is calculated from the vertical force ($W'_{caisson} - F_{uplift}$; where $W'_{caisson}$ is the effective weight of caisson) multiplied by a friction coefficient (μ), depending on the current state of the caisson breakwater; if no horizontal motion is initiated, the resistance is calculated from the static friction coefficient, whereas if the caisson has started the horizontal motion (with speed v_x), the friction resistance is calculated from the dynamic friction coefficient.

If for any time step, the maximum friction resistance is larger than the wave-induced horizontal force F_H and the caisson horizontal speed is zero, the equation of motion is not solved in the horizontal direction (zero increment of horizontal displacement). If F_H exceeds the friction resistance and the velocity of the horizontal dashpot is still zero (motion is initializing), the friction resistance is subtracted from F_H, because the damping coefficient of the horizontal dashpot is equal to zero. Only when the friction dashpot is fully operating ($c_x > 0$) is the full value of F_H realized.

As can be inferred from previous description, a perfectly plastic Coulomb friction model is used for soil-structure tangential interface; i.e. it is assumed that (i) friction is independent of contact area and (ii) dynamic friction is independent of slippage speed

In Fig. 6.8 and 6.9, the *caissonFoam* solver is used to test the sliding of the caisson configuration from the GWK tests for a regular breaking wave impact ($H = 0.7s$ and $T = 6.5s$). The model does not account for any additional horizontal supports for the caisson (other than that of the friction). The caisson's average density and friction coefficients are modified to test the sliding of the caisson. As shown, the model can reproduce the accumulation of sliding displacements from events of wave impact. The friction force (reaction from the horizontal dashpot) depends on the normal force (effective weight minus uplift force). The damping coefficient of the horizontal dashpot is negatively correlated to the horizontal velocity of the caisson.

The soil-structure separation and reattachment is simulated by deactivating and reactivating vertical springs and dashpots depending on the current caisson base position in relation to the current soil surface (including residual displacement) for each spring. The condition for deactivating any vertical soil spring (tested for all springs at each time step) is given by:

$$k_{y_i} = 0, \quad \text{if} \quad y_i > y_i^{residual} \tag{6.19}$$

where the vertical displacement y_i is positive upward. The vertical displacement is calculated at each spring and time step as (Fig. 6.10):

$$y_i^t = y_i^{t-\Delta t} + \Delta y_{caisson} - x_{P_i} \tan\left(\Delta\theta\right) \tag{6.20}$$

The spring displacement is calculated incrementally to account for changed pivot position during solution. The vertical velocity at the spring (for calculating dashpot reaction) is determined as:

$$v_i^t = \frac{\left(y_i^t - y_i^{t-\Delta t}\right)}{\Delta t} \tag{6.21}$$

The rocking motion of the structure and the related structural properties need to be defined at the rotational pivot of the structure. In this model, the location of the pivot is assumed to change according to the rotation of the structure and according to the characteristics of the foundation-structure interface. This change is accompanied by changes in the calculated rotating moment and the moment of inertia (both calculated at the current pivot). Although, the pivot location may change continuously, in this model discrete locations of the pivot are considered: (i) the caisson base seaward edge, (ii) the caisson base shoreward edge, (iii) the mid-point of active soil supports (springs under compression) and (iv) the CG of the caisson (if caisson-foundation contact is completely lost).

The selection of the pivot location is carried out as shown in Fig. 6.11. The moment of inertia is updated according to Eq. 6.16. The moment at the pivot is calculated as:

$$M_{pivot} = M_{CG} + \Delta M \tag{6.22}$$

The values of ΔI and ΔM are calculated as (Forces are positive upward and to the right):

$$\Delta I = m_{caisson} L_{Pivot-CG}^2 \tag{6.23}$$

$$\Delta M = F_H Y_{Pivot-CG} - (F_V - \sum F_i) X_{Pivot-CG} \tag{6.24}$$

Where $\sum F_i$ is the sum of reaction forces from springs and dashpots. $L_{Pivot-CG}$ is the distance between the caisson CG and the current pivot. $X_{Pivot-CG}$ and $Y_{Pivot-CG}$ are the difference between horizontal and vertical coordinates of the caisson CG and the current pivot.

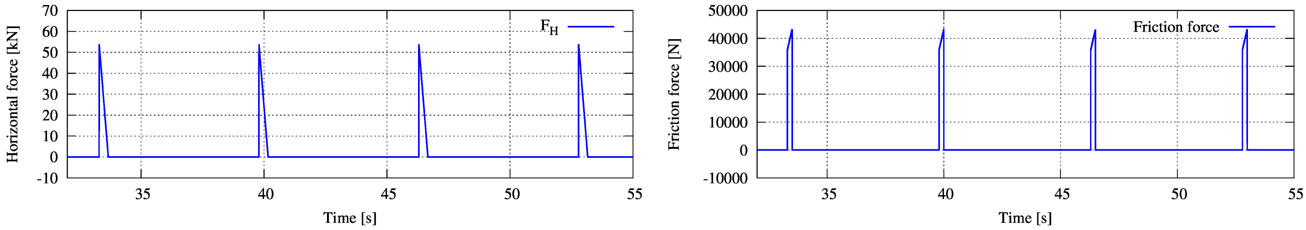

(a) Horizontal force

(b) Friction force: reaction from sliding dashpot

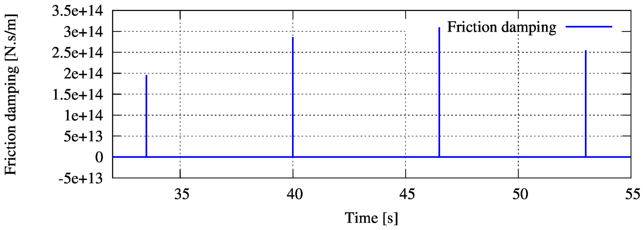

(c) Friction damping coefficient of the sliding(horizontal) dashpot

Figure 6.8: Horizontal wave forces, friction force and friction damping from *caissonFoam* for regular breaking waves with $H = 0.7m$ and $T = 6.5s$ for the GWK test configurations, caisson weight and friction coefficients modified to test sliding

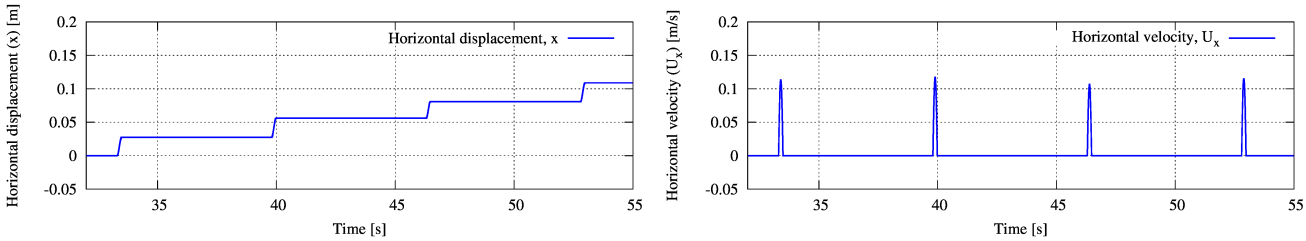

(a) Caisson's horizontal displacement

(b) Caisson's horizontal velocity

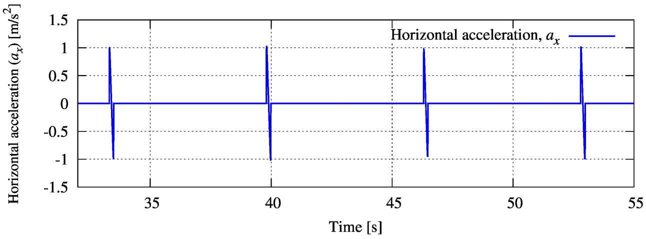

(c) Caisson's horizontal acceleration

Figure 6.9: Horizontal caisson response calculated from *caissonFoam* for regular breaking waves $H = 0.7m$ and $T = 6.5s$ for the GWK test configurations, caisson weight and friction coefficients modified to test sliding

A comparison of the results from the model for the calculated moment at the pivot and the rotation of the caisson for the changing pivot (according to soil-structure interaction) against the case of considering a constant pivot location at the mid-point of the caisson base is shown in Fig. 6.12 for linear elastic springs, with considering foundation-structure separation and reattachment. It is clear that the fluctuation of the moment due to changes in the location of the pivot (Fig. 6.12b) causes the caisson rotation to be an order of magnitude smaller than considering a fixed location of the pivot (Fig. 6.12c and 6.12d). This significant difference makes it clear that if the foundation-structure separation is considered by deactivating tension springs, one must also account for changes in the location of the pivot. From Fig. 6.12a, it is seen that the change in calculated moment due to change of the location of caisson center of gravity relevant to the fixed

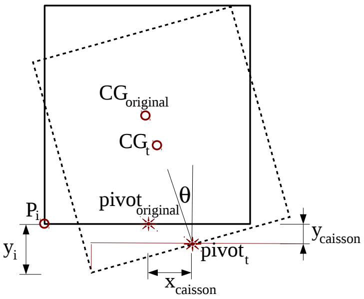

Figure 6.10: Vertical displacement at a position of a support (P_i) of the breakwater

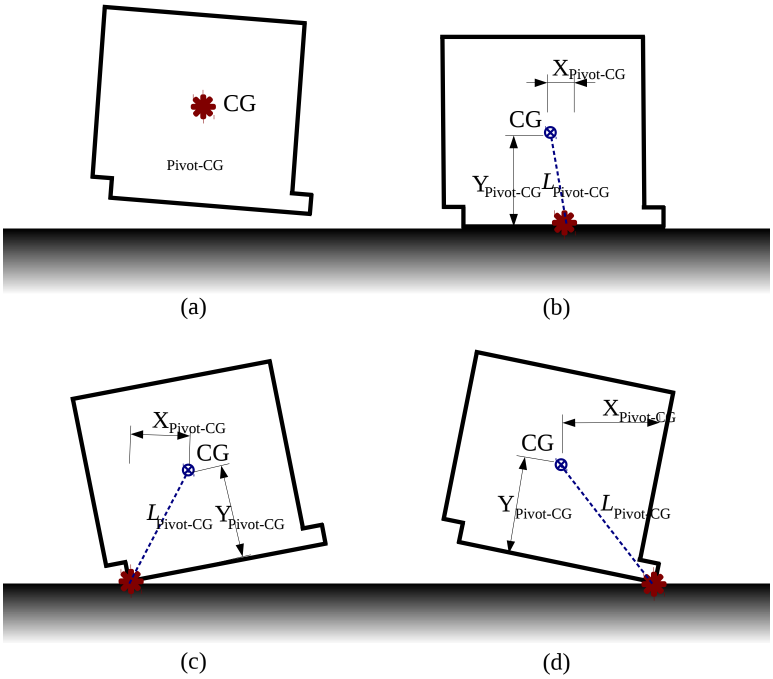

Figure 6.11: Criterion for selecting the location of the pivot: (a) caisson is totally separated from soil, the CG is the pivot, (b) Caisson resting on soil, pivot is the middle of activated supports, (c) rotation around seaward edge of caisson base and (d) rotation around shoreward edge of caisson base

pivot location is also captured by the model.

6.2.2 Soil Elastoplastic Response

In order to be able to model residual deformations of the monolithic breakwater using the simplified *caissonFoam* solver, the soil supports must be able to handle not only nonlinear force-displacement relationships but also a clear distinction between loading and unloading is required. Based on this distinction, different expressions are then applied to describe the loading and unloading force-displacement relationship; hence residual displacements can develop through the simulation.

Another important feature to consider is the effect of soil densification due to cyclic loading. This phenomenon is apparent in the results the GWK tests (Kudella et al., 2006) and is also well-reproduced by the CFD-CSD model system developed in Chapter 4. As seen in results from GWK tests and the results of the rocking plate on a sand box (Sumer et al., 2008), the pore pressure builds up in the cyclically loaded sand bed until a “saturation point” is reached after which the accumulated pore pressure tends to dissipate although the cyclic loading still persists. As the pore pressure buildup is associated with a soil contractive behaviour, soil densification (due to cyclic loading) means less contraction potential with further loading

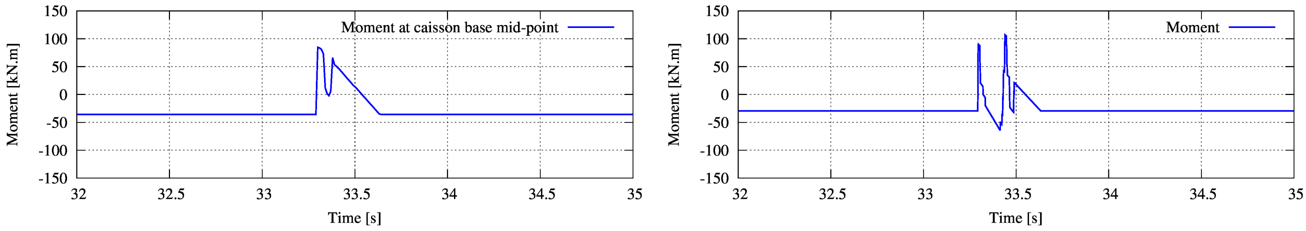

(a) Rotating moment at pivot with fixed location

(b) Rotating moment at the changing location of

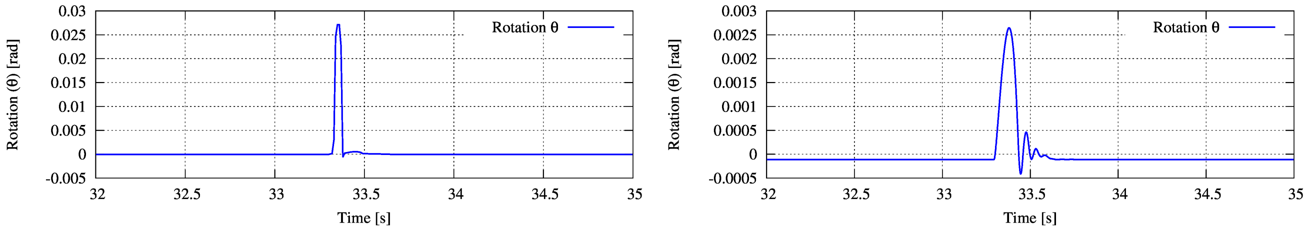

(c) Caisson rotation for pivot with fixed location (mid-point of caisson base)

(d) Caisson rotation for changing location of pivot according to criterion illustrated in Fig. 6.11

Figure 6.12: Comparison between moment and rotation calculated by *caissonFoam* for cases of fixed and changing location of the pivot (linear elastic springs considered with springs deactivated for tension to simulate soil-structure separation)

cycles. Further, this behaviour is associated with a reduced value of the increment of residual deformation with each wave impact (for every wave impact event the stepwise/incremental increase in residual deformation is slightly smaller than the former event). Soil densification is described in this model as an increment in load capacity and spring yield displacement as a function of the number of load cycles. In this way, the spring keeps getting stiffer with each load cycle. The concept of the elastoplastic spring (nonlinear loading and unloading force-displacement relationship with load cycle hardening) is shown in Fig. 6.13.

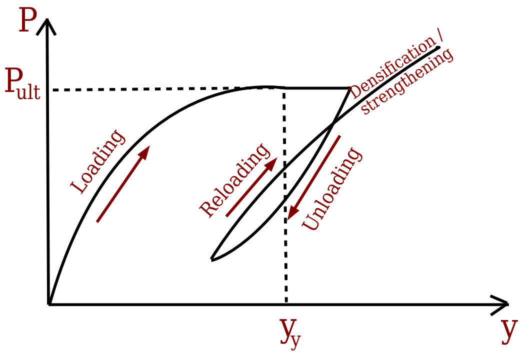

Figure 6.13: Concept of the elastoplastic spring

The force P_i^t for any of the i^{th} vertical spring at time t reads:

$$P_i^t = \begin{cases} 0 & \text{, if } y_i^t \geq y_i^r \text{ (tension cutoff)} \\ P_i^{t-\Delta t} & \text{, if } \Delta y_i = 0 \text{ (constant load)} \\ P_{ult} & \text{, if } y_i^t \leq y_y \text{ (perfect plasticity)} \\ P_{ult}\left(\alpha_l \left(\frac{y_i^t - y_i^*}{y_y}\right)^{\frac{1}{n_l}}\right) & \text{, if } y_y < y_i^t < y_i^r \text{ and } \zeta = 1 \text{ (loading)} \\ P_i^* - P_{ult}\left(\alpha_u \left(\frac{y_i^{**} - y_i^t}{y_y}\right)^{\frac{1}{n_u}}\right) & \text{, if } y_y < y_i^t < y_i^r \text{ and } \zeta = 0 \text{ (unloading)} \end{cases} \tag{6.25}$$

Where the displacement is positive upward. For the i^{th} spring, P_i^t and y_i^t are the force and vertical displacement at time t, $P_i^{t-\Delta t}$ is the force from the previous time step y_i^r is the accumulated residual displacement, y_y is the yield displacement, P_{ult} is the ultimate spring reaction (after which perfect plasticity is reached), P_i^* is the force at which unloading started, y_i^* is the displacement at which the loading/reloading phase started and y_i^{**} is the displacement at which the unloading phase started. The n and α parameters are fitted to results from parameter study and results of physical model tests for loading (n_l and α_l) and unloading (n_u and α_u) phases. The loading flag ζ can be defined as:

$$\zeta = \frac{\Delta y_i - |\Delta y_i|}{2\Delta y_i} \tag{6.26}$$

where spring displacement increment Δy_i can be calculated at any time t as:

$$\Delta y_i = y_i^t - y_i^{t-\Delta t} \tag{6.27}$$

This means that ζ is equal to unity if the spring is loaded and zero if the spring is unloaded. Soil densification is simulated by increasing the spring ultimate load and yield displacement as:

$$\begin{aligned} P_{ult} &= P_{ult}^0 \left(N_{cycle}\right)^{\beta} \\ y_y &= y_y^0 \left(\frac{1}{N_{cycle}}\right)^{\gamma} \end{aligned} \tag{6.28}$$

Where P_{ult}^0 and y_y^0 are the initial spring ultimate load and yield displacement, respectively. The densification depends on the number of loading cycles N_{cycle}. Parameters β and γ are fit to the results. Recommended values for the simplified model parameters are given in Subsection 6.3.1.

Figs. 6.14 and 6.15 show the response of the caisson from the GWK tests under regular breaking wave impact ($H = 0.7m$ and $T = 6.5s$) when supported by the proposed elastoplastic springs. The figures well-illustrate how the elastoplastic springs can "conceptually" reproduce residual vertical displacements and residual seaward tilting of the structure.

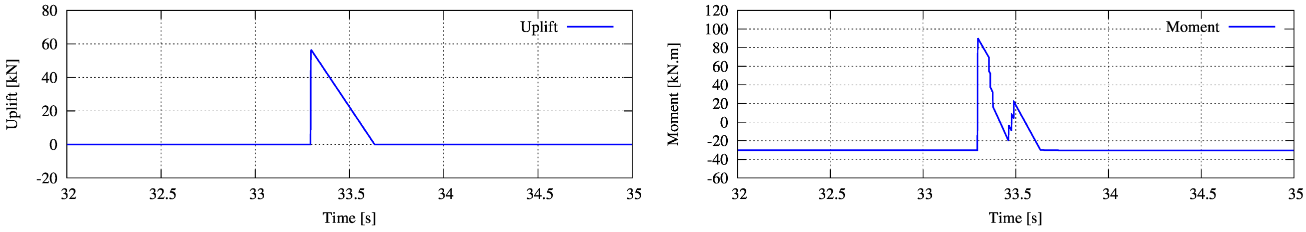

(a) Uplift force (b) Moment at pivot with changing locations

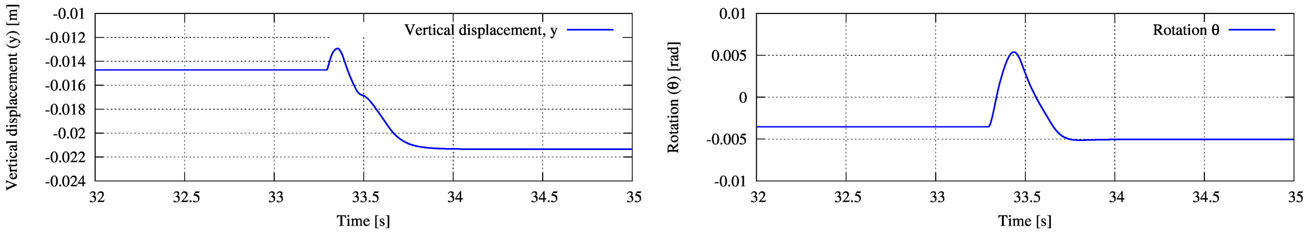

(c) Caisson vertical displacement (d) Caisson rotation

Figure 6.14: Uplift, moment, vertical displacement and rotation of caisson supported by elastoplastic vertical springs calculated by the *caissonFoam* solver for the case of regular breaking wave impact on the GWK caisson test with $H = 0.7m$ and $T = 6.5s$

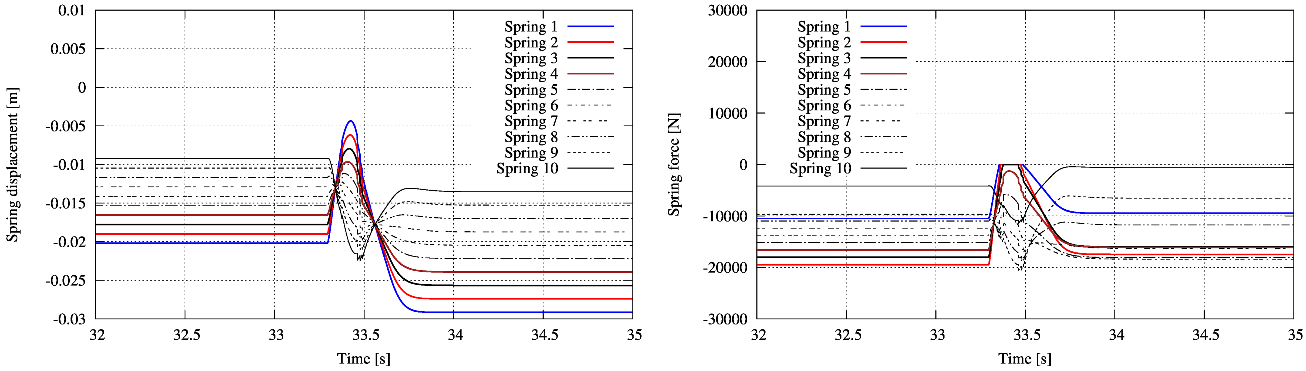

(a) Vertical displacement at the supporting springs (b) Vertical reaction (force) of the vertical springs

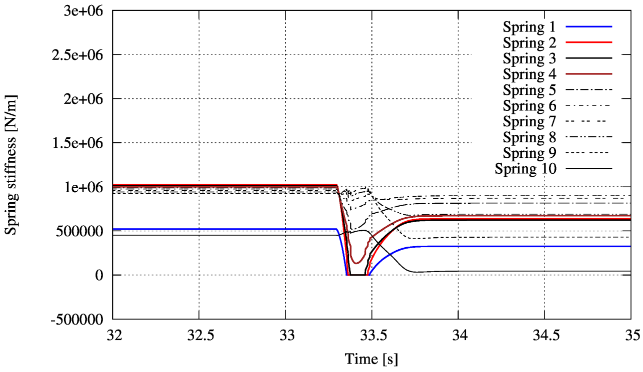

(c) Stiffness of vertical springs

Figure 6.15: Displacement, reaction and stiffness of elastoplastic vertical springs calculated by the *caissonFoam* solver for the case of regular breaking wave impact on the GWK caisson test $H = 0.7m$ and $T = 6.5s$, springs are numbered from left to right

6.2.3 Model Nonlinearrity

The model nonlinearity arises from the dependency of the model parameters (e.g. stiffness) upon the solution. Therefore, the solution is iterative. The nonlinearity for this model is induced by the following:

- Location of pivot changes according to caisson motion. Consequently, the rotational moment and the moment of inertia are updated accordingly
- Activation/deactivation of the horizontal dashpot according to the horizontal and vertical forces
- Dependency of the damping coefficient of the horizontal dashpot upon the horizontal velocity of the caisson (sliding) motion as well as upon the horizontal and vertical force resultants
- Activation/deactivation of the vertical springs/dashpots based on the vertical displacement at each support to simulate soil-structure separation/reattachment
- Nonlinear vertical springs with the stiffness coefficient updated each time step for a spring reaction which is nonlinearly dependent upon the vertical displacement and its incremental increase rate at the position of the spring
- Force-displacement relationship for the vertical springs with two expressions for loading and unloading conditions to describe residual displacements
- Dependency of the force-displacement relationship upon the number of loading cycles to model soil densification induced by cyclic loading

6.2.4 Organisation of the *caissonFoam* Solver

The simplified model is implemented in a new solver named *caissonFoam* within the OpenFOAM framework. The organization structure of the *caissonFoam* solver is outlined in Fig. 6.16. The solver is complemented by a newly developed software library named *libcaisson*. The main implementation of the solver contains the implementation of the governing equations, management of the time steps and management of output. The *libcaisson* library has three main *classes*: (i) The *caisson* class for computation of caisson properties, (ii) the *waveForces* class for computation of wave forces and (iii) the *springDashpot* class for implementation of foundation supports.

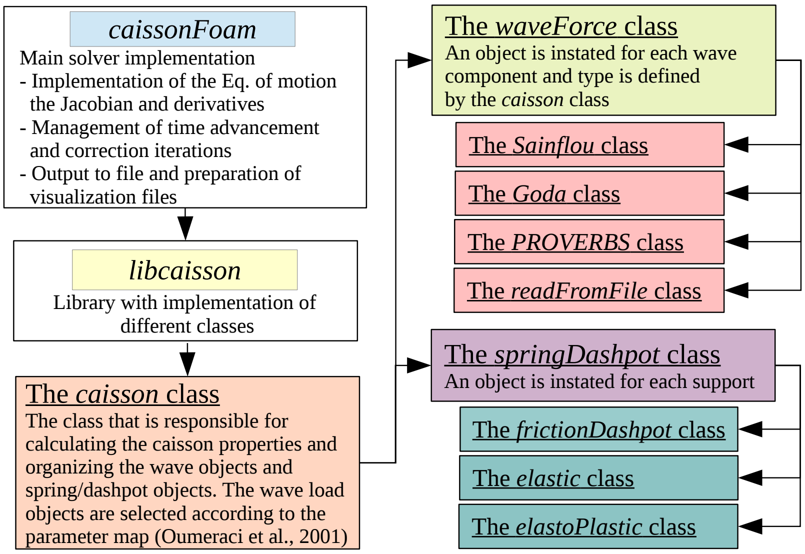

Figure 6.16: Organization of the *caissonFoam* solver

The workflow of the *caissonFoam* solver is illustrated in Fig. 6.17. The figure illustrates how the solver advances through time steps and how it copes with the nonlinearity by updating the model parameters every iteration depending on the results of the previous one.

6.3 Practical Implementation of the Simplified Model

6.3.1 Recommendations for Model Parameters

The parameters for the simplified model as described in sections 6.1.2 and 6.2.2 are calibrated, based on the results from the parameter study carried out by the CFD-CSD model in Chapter 5 and results from the GWK tests by Kudella et al. (2006). Some of the model parameters are kept constant due to their small effect on the model results. Parameters α_l and α_u (from Eq. 6.25) are kept equal to unity ($\alpha_l = \alpha_u = 1$) because no factoring of spring ultimate reaction in loading or unloading is needed. It is sufficient to consider the effects of soil densification (Eq. 6.28) only through the β coefficient and therefore the parameter γ is set to zero ($\gamma = 0$). The damping factor value ($\chi = 15$) was selected, which provides best comparison of response oscillation between results from *caissonFoam* and calibration data. The ultimate spring reaction (P_{ult}) is calculated from the soil bearing capacity (q_{ult}), which is calculated according to DIN 4017 for continuous shallow footings, Eq. 6.29.

$$q_{ult} = cN_c v_c + \gamma' dN_d v_d + \gamma' BN_B v_B \tag{6.29}$$

Where B is the width of the caisson breakwater's interface with the supporting foundation, c is soil cohesion (with $c = 0$ as non-cohesive sand is used in this study), d is the buried depth of caisson ($d = 0$ in this study

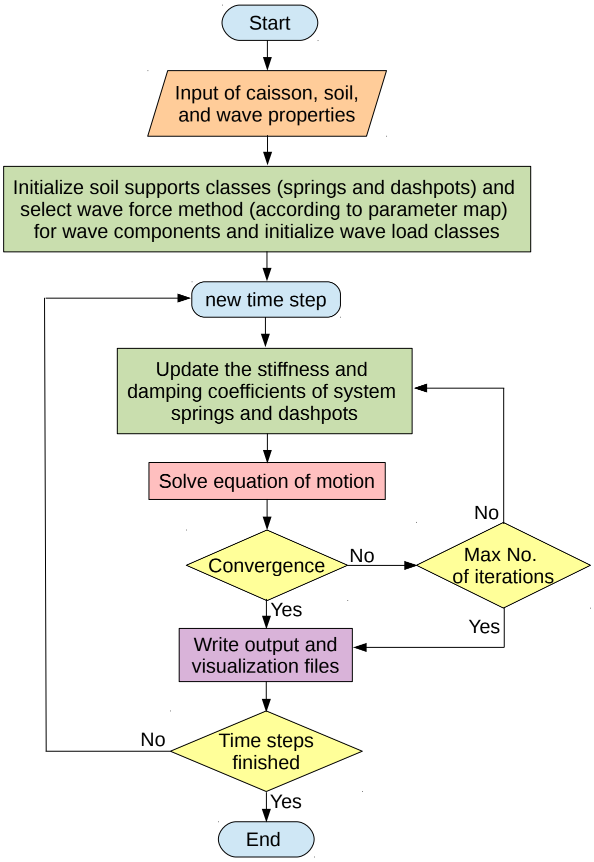

Figure 6.17: Algorithm of the *caissonFoam* solver

as well), $\gamma^{'} = \rho^{'}g$ is the soil effective bulk unit weight, v_c, v_d and v_B are shape coefficients (all equal to unity for strip footings), N_c, N_d and N_B are bearing capacity coefficients, calculated as:

$$N_d = e^{\pi \tan \phi'} \tan^2 \left(45^o + \phi^{'}/2\right) \tag{6.30}$$

$$N_c = (N_d - 1)\,/\tan \phi' \tag{6.31}$$

$$N_B = (N_d - 1) \tan \phi' \tag{6.32}$$

where $\phi^{'}$ is the effective angle of internal friction. The bearing capacity calculated for the four sand types considered in the parameter study (for $d = 0m$ and $B = 3.0m$), are given in Table 6.2.

Table 6.2: Calculated bearing capacity of different cohesionless soils considered in this study (using soil properties as proposed by Mazzoni et al. (2006))

	Loose	Medium	Medium dense	Dense
$\phi^{'}[^o]$	28	33	37	40
$\gamma^{'}[\mathrm{kN/m^3}]$	17	19	20	21
q_{ult} [kN/m^2]	372.04	928.81	1895.34	3340.71

For each spring, the ultimate resistance force P_{ult} is calculated using the ultimate bearing capacity q_{ult} and the service width of the spring (i.e. spring spacing for intermediate springs). The recommended model parameters are suggested based on two parameters: the load eccentricity (i.e. maximum positive eccentricity of vertical resultant load) and the relative soil density. The former describes the loading conditions as well as the structure properties, whereas the latter describes the soil properties. For the presentation of the model recommended parameters, four representative relative load eccentricity values and four representative relative soil density values are selected. The recommended values for the model parameters are given in Table 6.3.

Table 6.3: Recommended values for the simplified model parameters based on calibration using results from the systematic parameter study

Soil relative density [%]	Parameters	Relative eccentricity ($\frac{e}{B}$) [%]			
		11 %	61 %	100 %	200 %
loose (15 % - 35 %) $\phi = 29^o$	n_l	0.999	0.999	0.999	0.999
	n_u	1.001	1.0016	1.0021	1.0028
	β	-0.002	-0.005	-0.008	-0.01
	y_y	-0.20	-0.2	-0.20	-0.2
medium (35 % - 65 %) $\phi = 33^o$	n_l	0.999	0.999	0.999	0.999
	n_u	1.0008	1.001	1.0016	1.002
	β	-0.0008	-0.001	-0.0011	-0.0012
	y_y	-0.2	-0.2	-0.2	-0.2
med. dense (65 % - 85 %) $\phi = 37^o$	n_l	0.999	0.999	0.999	0.999
	n_u	1.0002	1.0002	1.001	1.0015
	β	-0.0003	-0.0004	-0.0005	-0.0006
	y_y	-0.2	-0.2	-0.2	-0.2
dense (85 % - 100 %) $\phi = 40^o$	n_l	0.999	0.999	0.999	0.999
	n_u	1.0001	1.0001	1.0007	1.001
	β	0.0	0.0	0.0	0.0
	y_y	-0.2	-0.2	-0.2	-0.2

6.3.2 Application of the Simplified Model to GWK Tests

In this subsection, the simplified model (as implemented in the *caissonFoam* solver) is applied to the GWK tests by Oumeraci and Kudella (2004) and Kudella et al. (2006). The primary objective of this application is to assess the capabilities and limitations of the simplified model (*caissonFoam*) in predicting the response of a caisson breakwater and its sand foundation to wave loads and particularly to breaking wave impacts. Herein, the results of tests No. 03 and No. 41 briefly described in Table 6.4 are selected from the whole GWK testing programme (refer to Oumeraci and Kudella (2004) for full description of the test programme) for the comparative analysis with the results of the simplified model:

- **Test No. 03** is the first test with breaking wave impact on the caisson breakwater model. Therefore, the sand foundation in this test can be assumed as not significantly densified so that the soil density can be assumed similar to that at the beginning of the tests. The loading conditions may be considered to represent the high eccentricity regime.
- **Test No. 41** is one of the last GWK tests with a high breaking wave impact and the greatest structural response (sliding failure of the caisson). The foundation in this test can be considered denser than initial conditions before the beginning of the test (i.e. measured soil properties), due to soil densification caused by previous tests. However, measured soil properties after the end of physical tests could

not be accurately considered for this test (considering significant soil densification caused by this test itself). The loading conditions may be considered to represent the extreme eccentricity regime.

Table 6.4: Characteristics of the GWK tests used for the comparison with the results from the simplified model

Test number	Date	e/B	Wave height [m]	Wave period [s]	Test duration [s]
03	10.09.2002	61% (high)	0.7	6.5	900
41	20.09.2002	200% (extreme)	0.9	6.5	6000

Considering test No. 03, (Table 6.4), the response of the caisson breakwater calculated by *caissonFoam* agrees relatively well with the GWK results, Fig. 6.18.

For the vertical residual displacement (settlement), Fig. 6.18a, the settlement rate is induced by wave impact is similar (compared to average value) before the inflexion point and after the saturation point. Between these two points, the physically recorded displacement rate is higher due to the increased pore pressure that reduce the shear strength of the sand foundation. This behaviour is not accounted for in the simplified model (i.e. *caissonFoam*). Basically, such a steady increase in residual pore pressure due to wave impact is more likely only feasible in highly controlled circumstances (e.g. physical tests with a long train of consecutive regular breaking wave impact).

For the rotational response of the structure (Fig. 6.18b), the computed results from *caissonFoam* agrees very well with the GWK results.

For the horizontal sliding of the structure (Fig. 6.18c), the results from *caissonFoam* agree very well with the physically recorded sliding (for friction coefficients of μ_{static} = 0.6 and $\mu_{dynamic}$ = 0.4) until approximately $t = 150s$, then no more sliding is recorded in the GWK. This is most likely due to the passive lateral pressure resistance of the rubble behind the caisson (restrained by the shutter beam, Fig. 6.19) that would be activated after sufficient sliding of the caisson. However, the passive resistance of the rubble berm cannot be reproduced (directly) by *caissonFoam*. Moreover, the transient component of the recorded signal is not reproduced by the simplified model. These oscillations are basically due to the caisson rocking motion recorded by the displacement meter at the top slab of the caisson, whereas in the simplified model, only a (purely plastic) dashpot at the caisson bottom is considered to represent frictional contact. The oscillations are not part of the caisson sliding, but rather part of the elastic (recoverable) rocking motion. The effect of rubble berms can be introduced by increasing the sliding resistance and the damping coefficient of the horizontal friction dashpot. However, this was not investigated in the current development of the simplified model.

The total wave loads (horizontal/uplift forces and rotational moment) on the caisson breakwater, as computed by *caissonFoam* are shown in Fig. 6.20. As shown in Fig. 6.20. These total loads acting on the structure (from the PROVERBS method as selected by the wave load parameter map) are equal for each event. However, the response is different for each event.

The response of the vertical supports is shown in Fig. 6.21 (spring stiffness, force and displacement); ten springs are considered; numbered from left to right. The first and last springs serve half the length served by intermediate springs (spacing of springs). Additionally, the response of the horizontal dashpot, which represents the frictional contact between the structure and the rubble foundation is given in Fig. 6.22. This includes the horizontal caisson's velocity and acceleration, the friction force and the damping coefficient of the horizontal friction damper. For each load event, when the horizontal load exceeds the maximum "static" friction resistance, the horizontal constraint on the caisson motion is temporarily removed and the frictional dashpot is activated with a variable damping coefficient calculated according to the horizontal velocity of the caisson motion in order to provide the maximum "dynamic" friction resistance at the dashpot (as a function of normal loads; caisson weight and uplift force).

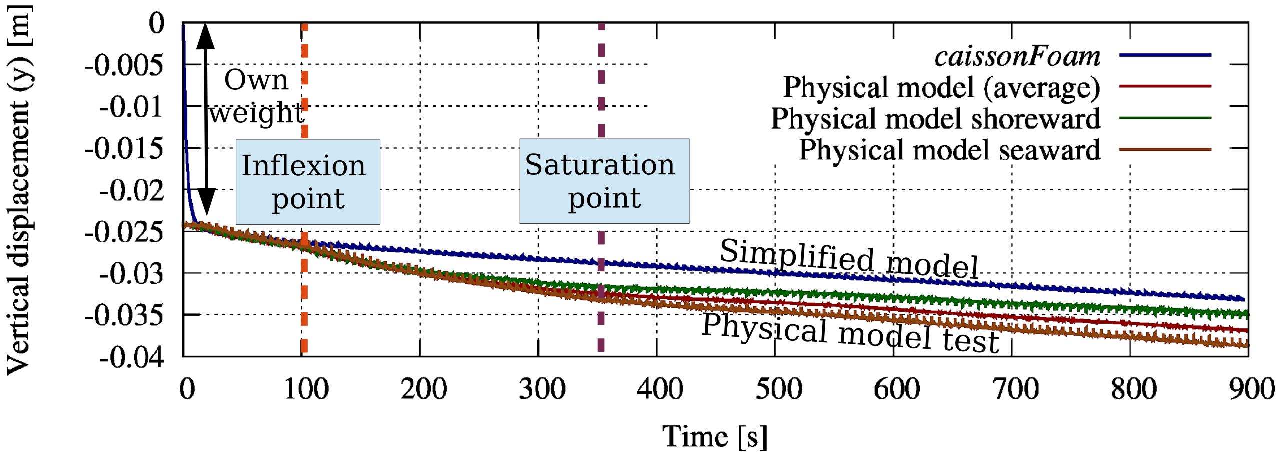

(a) Caisson settlement

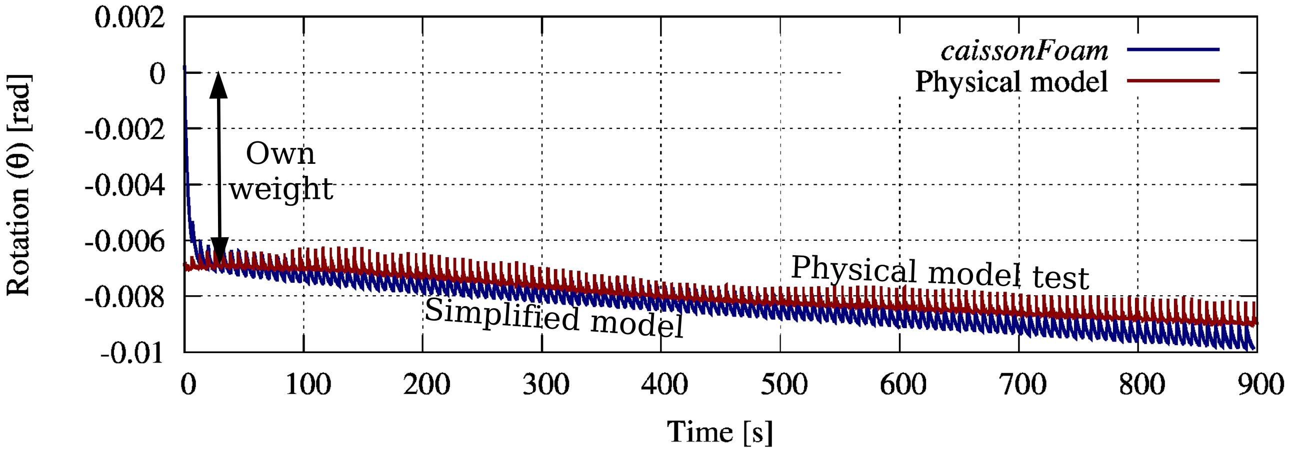

(b) Caisson tilt (negative is seeward direction)

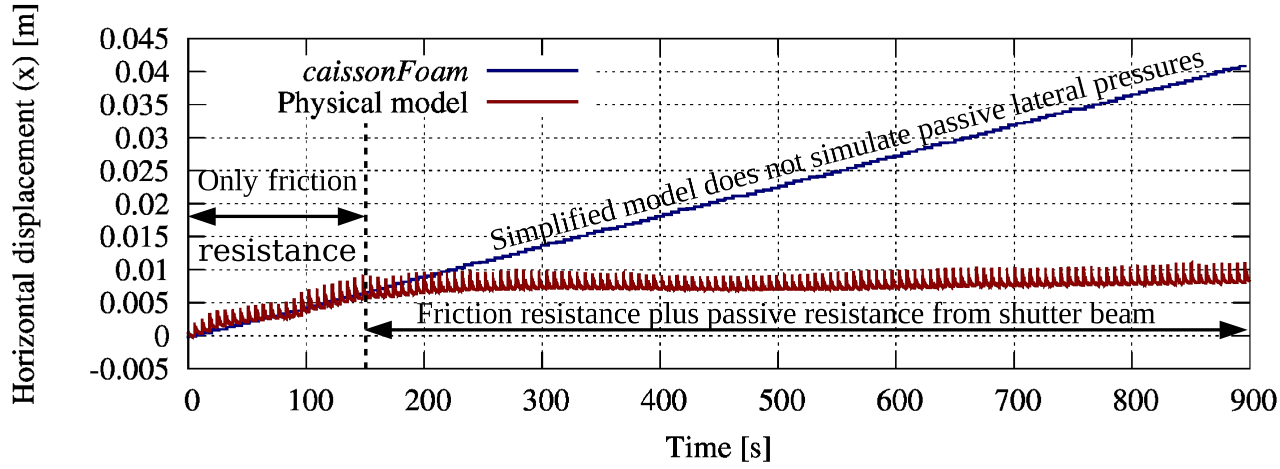

(c) Caisson sliding

Figure 6.18: Comparison between breakwater's response computed by *caissonFoam* against GWK measurements for test No. 03 with regular breaking waves: H=0.7m and T=6.5s (high load eccentricity regime)

Considering Test No. 41 (Table 6.4), the results of the simulation by *caissonFoam* as compared to those of the GWK test are shown in Fig. 6.23. Unlike in test No. 03, in test No. 41 the soil has undergone multiple densification processes induced by a significant number of high cyclic loading events. Nevertheless, the properties of the soil foundation at this state cannot be determined, though the soil properties were

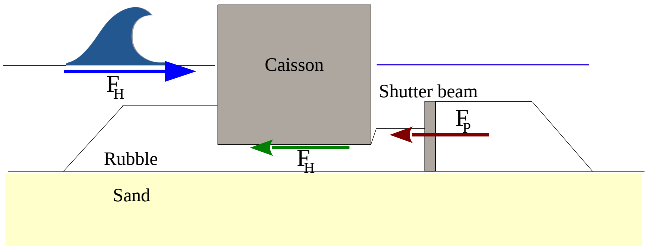

Figure 6.19: A sketch showing how horizontal wave load is resisted in the GWK tests by the sum of soil-structure friction and passive lateral load from the shutter beam; the passive lateral load is not simulated by *caissonFoam*

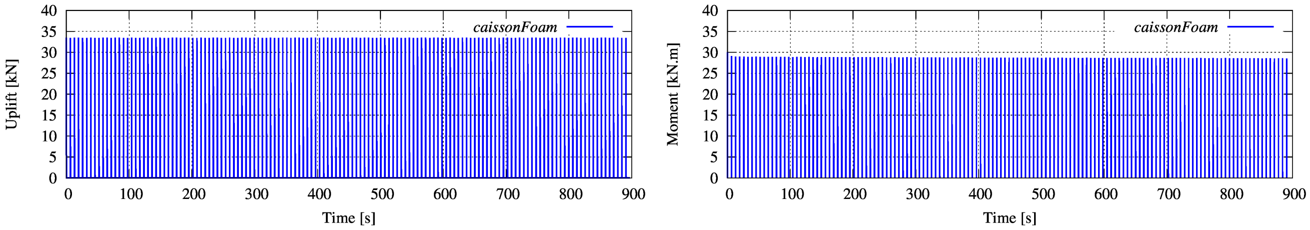

(a) Uplift force

(b) Rotational moment

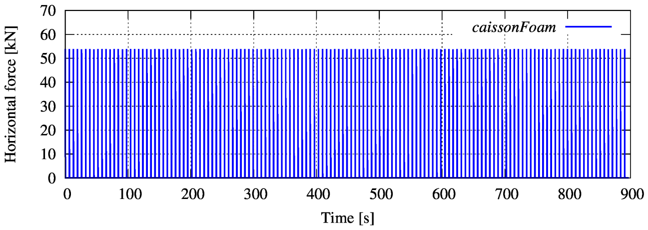

(c) Horizontal force

Figure 6.20: Total wave loads on breakwater as computed by *caissonFoam* for GWK test with regular breaking waves: H=0.7m and T=6.5s (high load eccentricity regime)

retrieved before and after the physical tests because test No. 41 is one of the tests that contributed significantly to soil densification. Therefore, similar soil properties as for test No. 03 are also used for the simulation of test No. 41 in order to provide a comparison between the response for both tests with the same soil conditions but basically different wave load conditions.

For the vertical residual displacement (settlement) (Fig. 6.23a), the calculated values from the simplified model overestimates the measured values in GWK test No. 41, as expected, due to enhanced soil properties caused by densification from previous tests that was not accounted for in the simplified model input.

For the rotational response of the structure (Fig. 6.23b), the caisson tilt is shoreward unlike the computed seaward tilt. This is most likely due the the coupling of caisson rotation and sliding that occurs in the extreme load eccentricity regime, as explained in Subsection 5.3.3 (see Fig. 5.23). As explained earlier, this coupling may cause new processes to emerge; namely erosion of the rubble foundation underneath the shoreward edge of the caisson resulting in small partial embedment of the shoreward edge of the caisson, this can also explain the nonlinear increase in sliding resistance (as seen in Fig. 5.22a). From the comparison using test No. 41, it can be concluded that the simplified model (similar to the CFD-CSD model system) is not valid for the extreme load eccentricity regime, in which the caisson response is accompanied with excessive sliding of the breakwater.

For the horizontal sliding of the structure, the measured sliding of the structure in GWK is equal to 18 cm in the presence of the shutter beam and the shoreward berm (Fig. 5.22a). The retrieved sliding from *caissonFoam* is much higher (only friction resistance; possible effect of passive foundation pressure

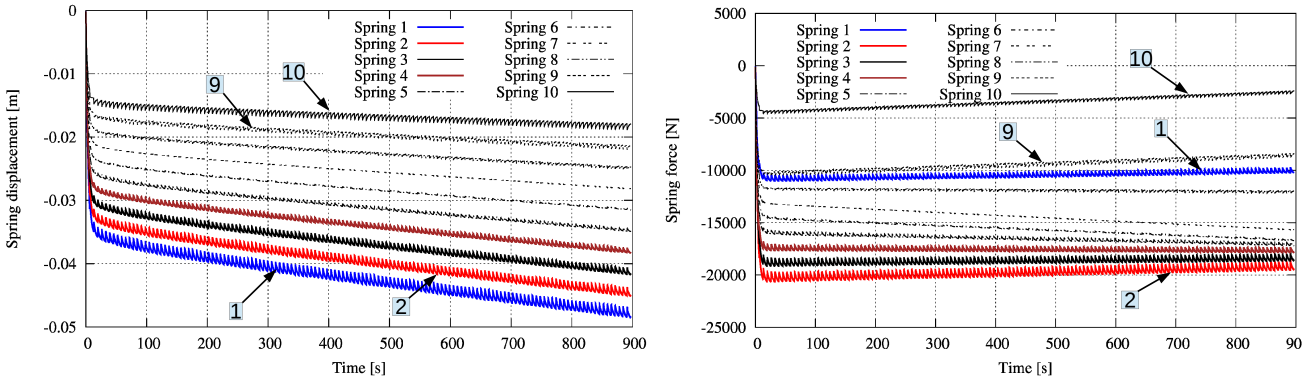

(a) Vertical displacement (b) Restoring forces

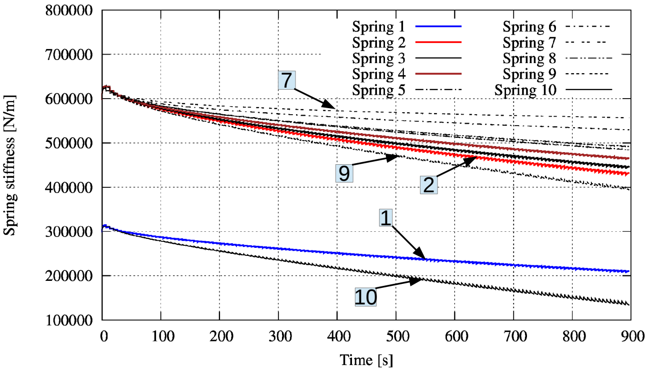

(c) Stiffness

Figure 6.21: Response and parameters of the simplified model supports as computed by *caissonFoam* for GWK test of regular breaking waves with H=0.7m and T=6.5s (springs are numbered from left to right with the first and last springs servicing half the length assigned to intermediate springs; spacing of springs; high load eccentricity regime)

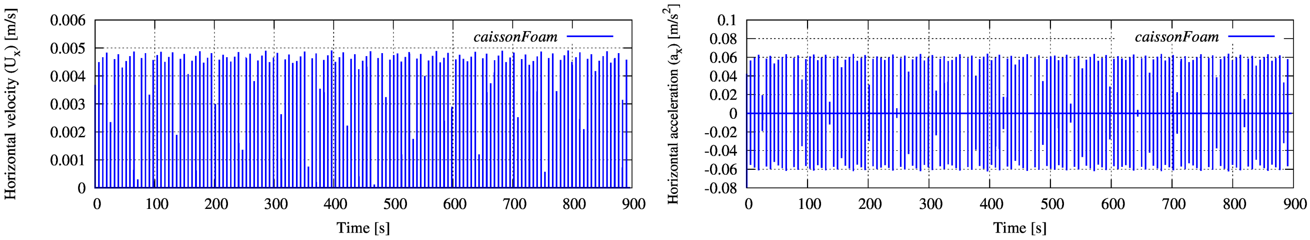

(a) Horizontal velocity of caisson sliding (b) Horizontal acceleration

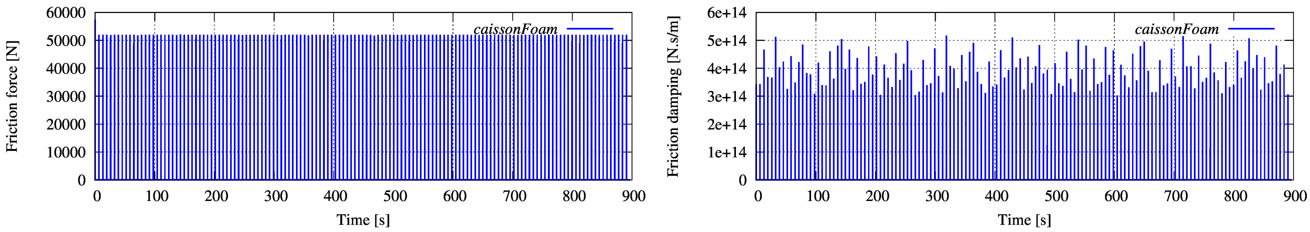

(c) Friction forces (d) Damping coefficient for horizontal friction dashpot

Figure 6.22: Response and parameters of the simplified model horizontal support (sliding response) as computed by *caissonFoam* for GWK test for regular breaking waves with H=0.7m and T=6.5s (high load eccentricity regime)

reaction is not accounted for in the simplified model). By inspecting the recorded sliding in the GWK test, it is nonlinear implying several stages of response, which supports the interpretation of the coupled caisson rotation and sliding response causing incremental partial embedment of the shoreward edge in the rubble foundation.

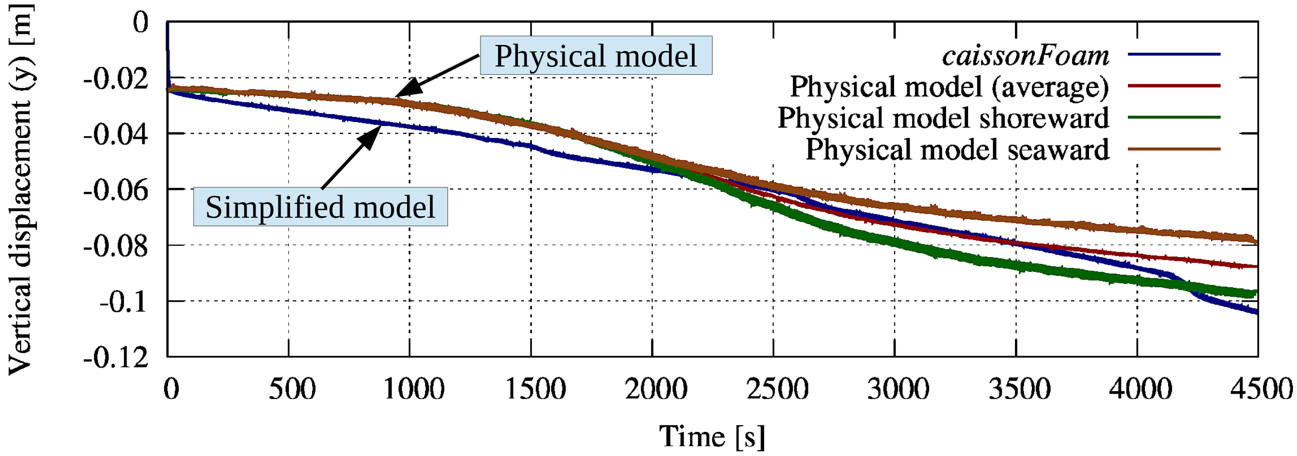

(a) Caisson settlement

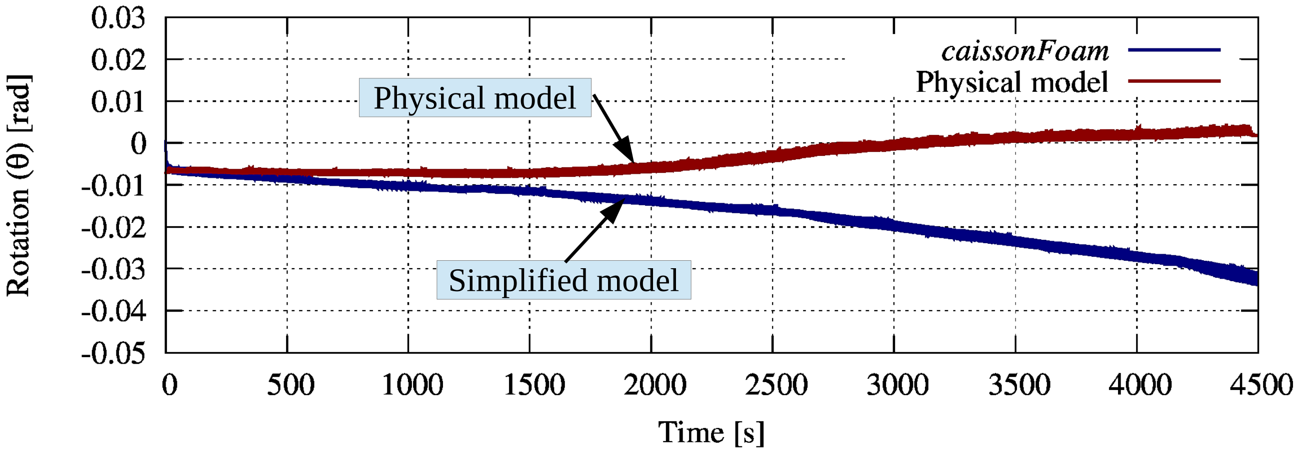

(b) Caisson tilt (negative is seaward direction)

Figure 6.23: Comparison between breakwater response computed by *caissonFoam* against GWK measurements for test No. 41 with regular breaking waves with H=0.9m and T=6.5s (extreme load eccentricity regime)

6.4 A Discussion on Capabilities and Limitations of the Simplified Model

In this chapter, a simplified model for monolithic breakwaters subject to wave loading was developed, calibrated and validated. The model is a nonlinear 3-DOF mass-spring-dashpot model with focus on the stepwise failure mechanism. The main features of the simplified model are:

- Calculation of the wave loads according to the PROVERBS parameter map or by direct input (e.g. from CFD)
- Properties of a monolithic breakwater are calculated for a (generic) polygon cross-section. Further, the properties of the monolithic breakwater cross section can be input directly to account for any irregularities (input as: area, mass, moment of inertia and center of gravity)
- Vertical springs/dashpots are activated/deactivated at each support to simulate soil-structure separation/reattachment

- The location of the rotation pivot changes according to caisson motion. Consequently, the rotational moment and the moment of inertia are updated accordingly
- A horizontal dashpot to simulate friction resistance, which is only activated if the horizontal force exceeds static friction resistance
- Elastoplastic nonlinear springs (for residual displacement)
- The spring properties are updated based on the number of loading cycles to simulate densification of the soil due to cyclic loading

Further, the simplified model is based on the assumption that the monolithic breakwater is not surrounded by any rubble protection (berm) or any other obstacle hindering partially or completely sliding, i.e. the effects of such configurations are not simulated by this simplified model. Hence, sliding is resisted only by structure-foundation friction.

The simplified model is capable of reproducing caisson sliding (for each load event), overturning (if it occurs) and residual displacement of caisson breakwater (including residual breakwater tilt and settlement).

Recommendations for the parameters to be used in the model are given, based on the model calibration using the numerical results obtained from the CFD-CSD model system described in Chapter 5. The model is applied to reproduce two selected tests performed in GWK under basically different wave load conditions corresponding to high and extreme load eccentricity regimes. For the former eccentricity condition, the model can predict relatively well the residual stepwise settlement and tilt of the monolithic breakwater. The significance of the stepwise response in the high load eccentricity regime is that it has the potential to render well designed structures out-of-service after sufficient loading events that may be considered moderate.

On the other hand, it was shown that for the extreme load eccentricity regime, i.e. for extreme wave loads that cause excessive displacements of the breakwater, neither the simplified model nor the numerical CFD-CSD model system are applicable, as new processes (not considered in both models) such as the erosion of the rubble foundation beneath the shoreward edge of the monolithic structure emerge. The new processes, obviously resulting from a strong coupling of rotational and sliding motion under extreme wave loads, drastically change the anticipated response of the structure. Such loading conditions are associated with excessive sliding of the breakwater, which would be apparent in results of the simplified model.

The simplified model represents a good tool for preliminary analysis of monolithic breakwaters. The use of this model should be followed by more elaborate numerical and physical tests for the final design of monolithic breakwaters.

7 Summary, Concluding Remarks and Implications

This study primarily aims at providing a substantially improved understanding of the stepwise failure of monolithic breakwaters subject to wave attack as observed in the laboratory and under field conditions. Therefore, a semi-coupled CFD-CSD model system was developed to simulate wave-structure-foundation interaction for vertical monolithic breakwaters subject to non-breaking and breaking wave loads. The validated numerical model system was used for a parameter study to extend the spectrum of available results from large-scale model tests. Based on the analysis of the numerical parameter study and the available laboratory data and the subsequent improved understanding of the processes involved in the response of the structure-soil foundation interaction under wave attack, a simplified nonlinear dynamic 3-DOF model was developed that can simulate the residual displacements (stepwise failure) of the structure under different wave loads.

In this concluding chapter, the most original contributions are briefly outlined and the key results are summarized. Finally, the implications of these results for the engineering practice and for further research are drawn.

7.1 Most Original Contributions of the Thesis

Overall, the development and systematic validation of the new hydro-geotechnical solver "*geotechFoam*" might be considered as the major contribution of the entire thesis. It accounts for the interaction between the fluid and the solid phases of porous media (via monolithic coupling) with the introduction of a new method to solve Biot's fully coupled fully dynamic equations as an extension to the Navier-Stokes equations. The solver has multi-material interface correction, elasto-plasticity (that can account for partial liquefaction and cyclic mobility) and frictional contact modelling for an accurate simulation of the soil behaviour and soil-structure interaction.

Moreover, the OpenFOAM multiphase incompressible Eulerian CFD solver with volume-averaged porous media is extended by introducing a simplified compressibility term which enhances the modelling of breaking wave impact (as validated by the GWK tests) at less computational expense and by adding several options for the application of seepage laws that account for viscous, inertial, transitional and transient flow.

A link between the aforementioned models to build a coherent semi-coupled model system for the analysis of the wave loading and response of monolithic breakwaters and their soil foundations has been developed in a framework which has the potential for further development and extension to other engineering and academic applications. The semi-coupled CFD-CSD model system was applied successfully to large-scale caisson breakwater GWK tests for non-breaking, slightly breaking and breaking wave loads.

Based on the modelling results, a substantially improved insight into the relative importance of transient and residual pore pressure as well as other parameters (e.g. own weight eccentricity) on the residual displacements of the structure subject to wave impact loads has been achieved. Furthermore, a concept of load eccentricity is proposed and successfully applied for the interpretation and classification of stepwise failures of monolithic breakwaters.

Finally, a new simplified 3-DOF model, including the necessary toolbox for its implementation, is developed and calibrated, which is capable to simulate residual sliding, settlement and tilt of monolithic breakwaters induced by wave loads. The simplified model was applied successfully to the GWK tests.

7.2 Summary of Key Results

Hydrodynamic (CFD) model

(i) Extreme horizontal breaking wave impact forces on the caisson could be well reproduced by the CFD model while the associated uplift forces were overestimated. This might certainly be due to the effect of the rocking motion on the uplift pressure as well as to the deformable impermeable sheet underneath the rubble foundation, which was simulated in the CFD model as non-deformable, (ii) using the Reynolds-Averaged turbulence model ($k - \omega - SST$) from OpenFOAM may dampen the water waves over long propagation distances (e.g. the GWK). However, using a Large-Eddy-Simulation (LES) turbulence model, provided better results also for wave impact load and (iii) by considering a linear elastic fluid compressibility model (bulk modulus calculated according to the VOF function) that describes only volume change instead of the commonly used density change, the oscillations of the pressure/force after initial breaking wave impact could be well-reproduced. These oscillations are important because they may cause the structure (in certain situations) to resonate.

Hydro-Geotechnical (CSD) model

(i) The segregated algorithm was successfully used for the fully coupled, fully dynamic poro-mechanical analysis and enabled easy addition and manipulation of different parts of the model (e.g. soil constitutive model), (ii) the proposed fully dynamic PISO based approach was successful in solving the fluid momentum balance directly instead of considering it implicitly in the mass conservation equation (e.g. the $u - p$ approach). Hence, the total pore pressure instead of the excess pore pressure in other approximations is obtained. Moreover, the results from the fully dynamic model show that the generation/dissipation of excess pore pressure is affected by the ratio of the excess pore pressure to the total (hydrostatic included) pore pressure, (iii) neglecting pore fluid convection for the presented fully coupled, fully dynamic model is not advisable as it is a term of the implicit part of the discretised mixture momentum balance equation and neglecting it does actually reduce the speed of the solution, (iv) the $u - p$ approximation reduces the computational time significantly for quasi-static poroelastic problems (without contact modelling) and should be considered for the specific cases where the effect of the pore fluid acceleration is not relevant to the soil skeleton, (v) the transient response of both soil phases (e.g. pore pressure and skeleton deformation) is significantly affected by the pore fluid compressibility as defined by soil degree of saturation S. For most cases, $S = 98.83\%$ provided the best fit against analytical and validation data; however, it was found that fluid compressibility is different under both edges of the caisson in the GWK tests (by analysing GWK results and their comparison to results of the numerical model system) and (vi) the buildup of pore pressure and subsequent densification of sand foundation underneath a caisson breakwater were successfully reproduced by the CSD model using the multi-surface plasticity sand constitutive model.

Semi-coupled CFD-CSD model system

(i) It is evident that two-way coupling of both models is a necessary step to achieve better results, (ii) introducing the aforementioned recommended enhancements to the CFD and the CSD models will inherently enhance the performance of the coupled model system and (iii) the semi-coupled model system is applicable to low, moderate and high load eccentricity regimes. However, for extreme load eccentricity regime, the model system cannot simulate the effect of caisson sliding-rotation coupling that causes partial embedment of shoreward edge of caisson in the rubble foundation.

Improved knowledge on stepwise failure of monolithic breakwaters

(i) The *load eccentricity concept* was introduced to represent wave loading and structural properties of the caisson and further used to classify response of monolithic breakwaters to wave loading, (ii) four types of sand were used for the study defined by their relative densities (loose, medium, medium-dense and dense) and typical values for parameters of each sand type were considered for the study, (iii) A numerical parameter study for different load eccentricities and soil relative densities are conducted and used to enhance understanding of the stepwise failure mechanism and to develop a simplified model, (iv) stepwise failure of monolithic breakwaters is studied, idealised and classified into four *load eccentricity* regimes: low, moderate, high and extreme. Differences between the regimes are discussed and tentative *load eccentricity* values for their boundaries are proposed and (v) the role of transient and residual components of pore pressure on the residual displacements of the structure are discussed. Further, the effects of own weight eccentricity, rubble berms and drainage conditions on stepwise failure of monolithic breakwaters are also discussed.

Simplified 3-DOF monolithic breakwater model
(i) Parameters of the simplified model are calibrated using the results of the numerical parameter study, (ii) the simplified model is applicable to low, moderate and high load eccentricity regimes. However, and similarly to the CFD-CSD model system it cannot be applied to extreme load eccentricity regime, as the model cannot simulate the effect of caisson sliding-rotation coupling that causes partial embedment of shoreward edge of caisson in the rubble foundation, (iii) stepwise sliding of monolithic breakwater can be simulated only for the frictional resistance of sliding; effect of passive resistance from rubble side berms cannot be simulated and (iv) considering change in pivot location reduces the breakwater rocking motion significantly and should be considered with springs that model soil-structure separation and reattachment.

7.3 Implications for Practice and Further Research

Implications for the engineering practice
The simplified nonlinear 3-DOF model (*caissonFoam*) can be used for preliminary analysis of monolithic breakwaters, with the use of only two representative parameters: The load eccentricity and the soil relative density. The simplified model uses empirical methods for calculating wave loads on vertical structures and it can also be used with a CFD model for retrieving forces on monolithic breakwaters with nonconventional cross sections. Further, structural response can be tentatively anticipated based on the proposed load eccentricity concept by estimating the load eccentricity regime of the breakwater.

Based on the gained understanding of the wave-structure-foundation interaction and on the proposed concept of load eccentricity, the optimal shape and features of a monolithic breakwater can be determined as exemplarily demonstrated in Subsection 5.4.2. This might be particularly the case for multi-purpose caisson structures (e.g. wave energy harvesting, amenity) which generally require innovative and more complex shapes.

The new CFD-CSD model system can be used for more elaborate analysis of monolithic breakwaters and other innovative types of structures subject to wave loads. Further, the CFD-CSD model system can be used to optimize design of coastal and offshore structures.

Implications for further research and development
For the hydrodynamic (CFD) model, the major need for further development is to enhance the simulation of the compressibility effect of entrapped/entrained air on breaking wave impacts by describing air as a dispersed phase in water. For the CSD model "*geotechFoam*", the new proposed solution of Biot's equations using the PISO algorithm may be adapted to introduce stress analysis of porous media to Volume-Averaged CFD models (e.g. VARANS). This might result in an invaluable framework for the simulation of deforming porous media instead of the widely used "fixed matrix". Consequently, changes in the local porosity (and also permeability) of porous media can be updated based on changes in volumetric strain. "*geotechFoam*" can be improved by introducing more material constitutive models as well as more models for the solid contact problem (convinient through modularity of the solver). Moreover, the introduction of multiphase pore fluid with air as a dispersed phase in water will help further study the observed difference in pore

fluid compressibility under both edges of caisson in the GWK tests.

For the CFD-CSD model system, a two-way coupling, though computationally much more expensive, might substantially improve the results, particularly for extreme wave loads with subsequent large rocking motions of the gravity structure where the motions and the uplift loading of the structure are strongly interdependent.

Furthermore, the interaction of the structure and rubble foundation needs to be formulated through a more appropriate approach that can also describe large displacement/separation of parts of the rubble foundation as well as the transport of smaller particles through large pores. The latter development might also be particularly important for the assessment of the stability of filters commonly used in almost all marine structures. Finally, the research challenge in the aforementioned need is for further development for linking soil liquefaction and seabed scour (sediment transport) to simulate post-liquefaction and re-solidification of the seabed.

Finally, for the simplified 3-DOF model, a more elaborate friction model might be introduced and the elastoplastic spring can be fitted to a wider spectrum of results including different own weight eccentricities. The effect of rubble side berms can be introduced to the model as a horizontal elastoplastic spring.

Bibliography

Adalier, K., Elgamal, A.-W., and Martin, G. R. (1998). "Foundation liquefaction countermeasures for earth embankments." *Journal of geotechnical and geoenvironmental engineering*, 124(6), 500–517.

Allsop, N., McKenna, J., Vicinanza, D., and Wittaker, T. (1996). "New design methods for wave impact loading on vertical breakwaters and seawalls." *Coastal Engineering Proceedings*, 1(25).

Allsop, N. and Vicinanza, D. (1996). "Wave impact loadings on vertical breakwaters: development of new prediction formulae." *Proceedings International Harbour Congress*, 275–284.

Arulmoli, K., Muraleetharan, K. K., Hossain, M. M., and Fruth, L. S. (1992). *VELACS Verification of Liquefaction Analyses by Centrifuge Studies Laboratory Testing Program: Soil Data Report.* Earth Technology Corporation.

Atluri, S. and Zhu, T. (1998). "A new meshless local Petrov-Galerkin (MLPG) approach in computational mechanics." *Computational mechanics*, 22(2), 117–127.

Aubry, D., Hujeux, J., Lassoudiere, F., and Meimon, Y. (1982). "A double memory model with multiple mechanisms for cyclic soil behaviour." *Proceedings of the Int. Symp. Num. Mod. Geomech*, 3–13.

Bagnold, R. (1939). "Interim report on wave-pressure research." *London, En.*

Balakrishnan, A., Kutter, B., and Idriss, I. (1997). "Liquefaction remediation at bridge sites-centrifuge data report for BAM02." *Center for Geotechnical Modeling Data Report UCD/CGMDR*, 97, 07.

Bardenhagen, S., Brackbill, J., and Sulsky, D. (2000). "The material-point method for granular materials." *Computer methods in applied mechanics and engineering*, 187(3), 529–541.

Beaty, M. and Byrne, P. (1998). *Geotechnical Earthquake Engineering and Soil Dynamics III.* ASCE, Chapter "An effective stress model for predicting liquefaction behaviour of sand", Edited by: Dakoulas, P., Yegian, M. and R. D. Holtz.

Belytschko, T., Lu, Y. Y., and Gu, L. (1994). "Element-free galerkin methods." *International journal for numerical methods in engineering*, 37(2), 229–256.

Berberovic, E. (2010). "Investigation of free-surface flow associated with drop impact: Numerical simulations and theoretical modeling." Ph.D. thesis, TU Darmstadt/FG Strömungslehre und Aerodynamik, Germany.

Bierawski, L. G. and Maeno, S. (2004). "VOF-FEM numerical model of submerged breakwater on permeable bottom." *J. Appl. Mech*, 7, 945–952.

Bierawski, L. G., Maeno, S., Gotoh, H., and Harada, E. (2002). "DEM-FEM model of the outflow of backfilling sand from behind a seawall under wave motion." *Proc., 5th Int. Conf. on Hydro-Science and Engineering.*

Biot, M. A. (1941). "General theory of three-dimensional consolidation." *Journal of applied physics*, 12(2), 155–164.

Biot, M. A. (1962). "Mechanics of deformation and acoustic propagation in porous media." *Journal of applied physics*, 33(4), 1482–1498.

Biot, M. A. (1965). *Mechanics of incremental deformations: theory of elasticity and viscoelasticity of initially stressed solids and fluids, including thermodynamic foundations and applications to finite strain.* Wiley New York.

Boer, R. (2005). *Trends in continuum mechanics of porous media*, Vol. 18. Springer.

Boulanger, R. W. and Seed, R. B. (1995). "Liquefaction of sand under bidirectional monotonic and cyclic loading." *Journal of geotechnical engineering*, 121(12), 870–878.

Bullock, G., Obhrai, C., Peregrine, D., and Bredmose, H. (2007). "Violent breaking wave impacts. part 1: Results from large-scale regular wave tests on vertical and sloping walls." *Coastal Engineering*, 54(8), 602–617.

Byrne, P. M., Park, S.-S., Beaty, M., Sharp, M., Gonzalez, L., and Abdoun, T. (2004). "Numerical modeling of liquefaction and comparison with centrifuge tests." *Canadian Geotechnical Journal*, 41(2), 193–211.

Byrne, P. M., Roy, D., Campanella, R. G., and Hughes, J. (1995). "Predicting liquefaction response of granular soils from pressuremeter tests." *Static and Dynamic Properties of Gravelly Soils*, 122–135.

Cardiff, P., Karač, A., and Ivanković, A. (2012). "Development of a finite volume contact solver based on the penalty method." *Computational Materials Science*, 64, 283–284.

Castro, G. (1975). "Liquefaction and cyclic mobility of saturated sands." *Journal of the Geotechnical Engineering Division*, 101(6), 551–569.

CEM (2006). *Coastal engineering manual.* Engineering Manual 1110-2-1100, in 6 Volumes. Coastal Engineering Research Center, US Army Corps of Engineers, Washington, DC.

Chan, A. H.-C. (1988). "A unified finite element solution to static and dynamic problems of geomechanics." Ph.D. thesis, University College of Swansea, UK.

Chandler, H. (1985). "A plasticity theory without drucker's postulate, suitable for granular materials." *Journal of the Mechanics and Physics of Solids*, 33(3), 215–226.

Chandler, H. (1990). "Homogeneous and localised deformation in granular materials: a mechanistic model." *International Journal of Engineering Science*, 28(8), 719–734.

Chandler, H. and Sands, C. (2007). "An optimization structure for frictional plasticity." *Proceedings of the Royal Society A: Mathematical, Physical and Engineering Science*, 463(2084), 2005–2020.

Chandler, H. and Sands, C. (2010). "Including friction in the mathematics of classical plasticity." *International journal for numerical and analytical methods in geomechanics*, 34(1), 53–72.

Chang, W.-J., Rathje, E. M., Stokoe II, K. H., and Cox, B. R. (2004). "Direct evaluation of effectiveness of prefabricated vertical drains in liquefiable sand." *Soil Dynamics and Earthquake Engineering*, 24(9), 723–731.

Chen, W.-F. and Baladi, G. Y. (1985). *Soil plasticity: Theory and implementation.* Elsevier.

Cheng, Y.-Z., Jiang, C.-B., and Wang, Y.-Y. (2009). "A coupled numerical model of wave interaction with porous medium." *Ocean Engineering*, 36(12), 952–959.

Collins, I. and Houlsby, G. (1997). "Application of thermomechanical principles to the modelling of geotechnical materials." *Proceedings of the Royal Society of London. Series A: Mathematical, Physical and Engineering Sciences*, 453(1964), 1975–2001.

Collins, I. and Kelly, P. (2002). "A thermomechanical analysis of a family of soil models." *Geotechnique*, 52(7), 507–518.

Cooker, M. (1990). "The interaction between steep water waves and coastal structures." Ph.D. thesis, University of Bristol, UK.

Coussy, O. (2004). *Poromechanics.* John Wiley & Sons.

Coussy, O. (2007). "Revisiting the constitutive equations of unsaturated porous solids using a lagrangian saturation concept." *International Journal for Numerical and Analytical Methods in Geomechanics*, 31(15), 1675–1694.

Coussy, O., Pereira, J.-M., and Vaunat, J. (2010). "Revisiting the thermodynamics of hardening plasticity for unsaturated soils." *Computers and Geotechnics*, 37(1), 207–215.

Cuomo, G., Lupoi, G., Shimosako, K.-i., and Takahashi, S. (2011). "Dynamic response and sliding distance of composite breakwaters under breaking and non-breaking wave attack." *Coastal Engineering*, 58(10), 953–969.

Dafalias, Y. F. (1986). "Bounding surface plasticity. i: Mathematical foundation and hypoplasticity." *Journal of Engineering Mechanics*, 112(9), 966–987.

Dangar, R. and Nuh, S. (1980). "Endochronic-critical state models for sand." *Journal of the Engineering Mechanics Division*, 106(5), 951–968.

Darve, F. and Labanieh, S. (1982). “Incremental constitutive law for sands and clays: simulations of monotonic and cyclic tests.” *International Journal for Numerical and Analytical Methods in Geomechanics*, 6(2), 243–275.

De Groot, M., Andersen, K., Burcharth, H., Ibsen, L., Kortenhaus, A., Lundgren, H., Magda, W., Oumeraci, H., and Richwien, W. (1996). “Foundation design of caisson breakwaters, publication 198.” *Norwegian Geotechnical Institute, Oslo, Norway.*

De Groot, M., Bolton, M., Foray, P., Meijers, P., Palmer, A., Sandven, R., Sawicki, A., and Teh, T. (2006a). “Physics of liquefaction phenomena around marine structures.” *Journal of waterway, port, coastal, and ocean engineering*, 132(4), 227–243.

De Groot, M., Kudella, M., Meijers, P., and Oumeraci, H. (2006b). “Liquefaction phenomena underneath marine gravity structures subjected to wave loads.” *Journal of waterway, port, coastal, and ocean engineering*, 132(4), 325–335.

Desrues, J. and Chambon, R. (1993). “A new rate type constitutive model for geomaterials: CLoE.” *Modern Approaches to Plasticity*, 309–324.

Detournay, E. and Cheng, A.-D. (1993). *Comprehensive rock engineering: principles, practice, and projects.* Pergamon Press, Chapter 5: Fundamentals of Poroelasticity.

DIN 4017 (2006). “Berechnung des grundbruchwiderstands von flachgründungen, calculation of design bearing capacity of soil beneath shallow foundations (in german).” *German Institute for Standardization.*

Dobry, R. and Abdoun, T. (1998). “Post-triggering response of liquefied sand in the free field and near foundations.” *Geotechnical Earthquake Engineering and Soil Dynamics III*, ASCE, 270–300.

Dobry, R., Taboada, V., and Liu, L. (1995). “Centrifuge modeling of liquefaction effects during earthquakes.” *Proc. 1st Intl. Conf. On Earthquake Geotechnical Engineering, IS-Tokyo*, 14–16.

Einav, I. and Collins, I. F. (2008). “A thermomechanical framework of plasticity based on probabilistic micromechanics.” *Journal of Mechanics of Materials and Structures*, 3(5), 867–892.

Eisenberg, M. and Phillips, A. (1971). “A theory of plasticity with non-coincident yield and loading surfaces.” *Acta Mechanica*, 11(3-4), 247–260.

El Safti, H. and Oumeraci, H. (2011). “Wave-structure-foundation interaction for gravity marine structures - state of the art and study plan outline.” *Technical report of the Leichtweiß-Institute for Hydraulic Engineering and Water Resources, Internal Report No. 1012*, TU Braunschweig, Germany.

Elgamal, A., Parra, E., Yang, Z., and Adalier, K. (2002). “Numerical analysis of embankment foundation liquefaction countermeasures.” *Journal of Earthquake Engineering*, 6(4), 447–471.

Elgamal, A., Yang, Z., Parra, E., and Ragheb, A. (2003). “Modeling of cyclic mobility in saturated cohesionless soils.” *International Journal of Plasticity*, 19(6), 883 – 905.

Fenton, G. A. and Griffiths, D. (2003). “Bearing-capacity prediction of spatially random $c - \varphi$ soils.” *Canadian geotechnical journal*, 40(1), 54–65.

Forchheimer, P. (1901). “Wasserbewegung durch boden.” *Z. Ver. Deutsch. Ing*, 45(1782), 1788.

Gens, A. and Potts, D. (1988). “Critical state models in computational geomechanics.” *Engineering Computations*, 5(3), 178–197.

Ghaboussi, J., Garrett Jr, J., and Wu, X. (1990). “Material modeling with neural networks.” *Proceedings of the international conference on numerical methods in engineering: theory and applications, Swansea, UK*, 701–717.

Ghaboussi, J., Garrett Jr, J., and Wu, X. (1991). “Knowledge-based modeling of material behavior with neural networks.” *Journal of Engineering Mechanics*, 117(1), 132–153.

Ghaboussi, J. and Momen, H. (1982). “Modeling and analysis of cyclic behavior of sands.” *Soil mechanics-transient and cyclic loads*, 313–342.

Ghaboussi, J. and Wilson, E. L. (1972). “Variational formulation of dynamics of fluid-saturated porous elastic solids.” *Journal of the Engineering Mechanics Division*, 98(4), 947–963.

Goda, Y. (1974). “New wave pressure formulae for composite breakwaters.” *Coastal Engineering Proceedings*, 1(14).

Goda, Y. (1994). “Dynamic response of upright breakwaters to impulsive breaking wave forces.” *Coastal engineering*, 22(1), 135–158.

Goda, Y. (2010). *Random seas and design of maritime structures*. World Scientific Publishing Company.

Gudehus, G. (2006). “Seismo-hypoplasticity with a granular temperature.” *Granular Matter*, 8(2), 93–102.

Hagen, A. and Lundgren, L. (1977). “The dynamics of vertical face breakwaters under the influence of shock pressures.” M.S. thesis, University of Denmark, ISVA, Lyngby.

Herle, I. and Gudehus, G. (1999). “Determination of parameters of a hypoplastic constitutive model from properties of grain assemblies.” *Mechanics of Cohesive-frictional Materials*, 4(5), 461–486.

Herle, I. and Kolymbas, D. (2004). “Hypoplasticity for soils with low friction angles.” *Computers and Geotechnics*, 31(5), 365–373.

Hirai, H. (1987). “An elastoplastic constitutive model for cyclic behaviour of sands.” *International journal for numerical and analytical methods in geomechanics*, 11(5), 503–520.

Houlsby, G. (1982). “A derivation of the small-strain incremental theory of plasticity from thermodynamics.” *In: Proc. lUTAM Conf. Deformation and Failure of Granular Materials*, 109–118.

Houlsby, G. and Puzrin, A. (2000). “A thermomechanical framework for constitutive models for rate-independent dissipative materials.” *International Journal of Plasticity*, 16(9), 1017–1047.

Houlsby, G. T. (1981). “A study of plasticity theories and their applicability to soils.” Ph.D. thesis, University of Cambridge Cambridge, UK.

Hsu, J. and Jeng, D. (1994). “Wave-induced soil response in an unsaturated anisotropic seabed of finite thickness.” *International Journal for Numerical and Analytical Methods in Geomechanics*, 18(11), 785–807.

Hsu, J., Jeng, D., and Lee, C. (1995). “Oscillatory soil response and liquefaction in an unsaturated layered seabed.” *International journal for numerical and analytical methods in geomechanics*, 19(12), 825–849.

Hsu, J., Jeng, D., and Tsai, C. (1993). “Short-crested wave-induced soil response in a porous seabed of infinite thickness.” *International Journal for Numerical and Analytical Methods in Geomechanics*, 17(8), 553–576.

Hsu, T.-J., Sakakiyama, T., and Liu, P. L.-F. (2002). “A numerical model for wave motions and turbulence flows in front of a composite breakwater.” *Coastal Engineering*, 46(1), 25 – 50.

Hull, P. and Müller, G. (2002). “An investigation of breaker heights, shapes and pressures.” *Ocean engineering*, 29(1), 59–79.

Hur, D.-S., Kim, C.-H., Kim, D.-S., and Yoon, J.-S. (2008). “Simulation of the nonlinear dynamic interactions between waves, a submerged breakwater and the seabed.” *Ocean Engineering*, 35(5), 511–522.

Hur, D.-S., Kim, C.-H., and Yoon, J.-S. (2010). “Numerical study on the interaction among a nonlinear wave, composite breakwater and sandy seabed.” *Coastal Engineering*, 57(10), 917–930.

Hur, D.-S. and Mizutani, N. (2003). “Numerical estimation of the wave forces acting on a three-dimensional body on submerged breakwater.” *Coastal Engineering*, 47(3), 329–345.

Hur, D.-S., Nakamura, T., and Mizutani, N. (2007). “Sand suction mechanism in artificial beach composed of rubble mound breakwater and reclaimed sand area.” *Ocean Engineering*, 34(8), 1104–1119.

Hutter, K., Laloui, L., and Vulliet, L. (1999). “Thermodynamically based mixture models of saturated and unsaturated soils.” *Mechanics of Cohesive-frictional Materials*, 4(4), 295–338.

Hwang, C., Morgenstern, N., and Murray, D. (1971). “On solutions of plane strain consolidation problems by finite element methods.” *Canadian Geotechnical Journal*, 8(1), 109–118.

Imai, G. and Xie, C. (1990). “A constitutive model based on damage mechanics principles.” *Soils Found., P185-194. Publ Toronto, University of Toronto*, 30, P142–154.

Ioka, S., Masuda, K., and Kubo, S. (2007). “Singular stress field near the edge of interface of bonded dissimilar materials with an interlayer.” *International journal of solids and structures*, 44(18), 6232–6238.

Ishihara, K. (1985). "Stability of natural deposits during earthquakes." *Proceedings of the 11th international conference on soil mechanics and foundation engineering*, Vol. 1, 321–376.

Iwan, W. D. (1967). "On a class of models for the yielding behavior of continuous and composite systems." *Journal of Applied Mechanics*, 34, 612.

Jacobsen, N. G., Fuhrman, D. R., and Fredsoe, J. (2012). " A Wave Generation Toolbox for the Open-Source CFD Library: OpenFoam® ." *Int. J. Numerl. Meth. Fluids*, 70(9), 1073–1088.

Jasak, H. (1996). *Error Analysis and Estimation for the Finite Volume Method with Applications to Fluid Flows*. University of London.

Jasak, H. and Weller, H. (2000a). "Application of the finite volume method and unstructured meshes to linear elasticity." *Int. J. Num. Meth. Engineering*, 48(2), 267–287.

Jasak, H. and Weller, H. (2000b). "Finite volume methodology for contact problems of linear elastic solids." *Proceedings of 3rd International Conference of Croatian Society of Mechanics, Cavtat/Dubrovnik*, 253–260 (September).

Jeng, D. (1996). "Wave-induced liquefaction potential at the tip of a breakwater: an analytical solution." *Applied ocean research*, 18(5), 229–241.

Jeng, D. (1997). "Wave-induced seabed instability in front of a breakwater." *Ocean Engineering*, 24(10), 887–917.

Jeng, D. (2003a). "A general finite element model for wave-seabed-structure interaction." *Numerical analysis and modelling in geomechanics*, 59–100.

Jeng, D. and Hsu, J. (1996). "Wave-induced soil response in a nearly saturated sea-bed of finite thickness." *Geotechnique*, 46(3), 427–440.

Jeng, D. and Li, J. (2006). "Numerical model for wave-induced residual pore pressure in a porous seabed around the head of a breakwater." *Coastal Engineering*, 4533.

Jeng, D. S. (2003b). "Wave-induced sea floor dynamics." *Applied Mechanics Reviews*, 56(4), 407–429.

Jeng, D.-S. (2010). "Porous model for wave-seabed-structure interaction: PORO-WSSI (Ver. 1)." *Research report No. R2010-1*, University of Dundee, UK.

Jeng, D.-S. and Cha, D. (2003). "Effects of dynamic soil behavior and wave non-linearity on the wave-induced pore pressure and effective stresses in porous seabed." *Ocean Engineering*, 30(16), 2065–2089.

Jeng, D. S., Cha, D., Lin, Y., and Hu, P. (2001). "Wave-induced pore pressure around a composite breakwater." *Ocean Engineering*, 28(10), 1413–1435.

Jeng, D.-S. and Ou, J. (2010). "3D models for wave-induced pore pressures near breakwater heads." *Acta mechanica*, 215(1-4), 85–104.

Jeng, D.-S., Ye, J.-H., Zhang, J.-S., and Liu, P.-F. (2013). "An integrated model for the wave-induced seabed response around marine structures: Model verifications and applications." *Coastal Engineering*, 72, 1–19.

Jianhong, Y. (2012). "Numerical modelling of consolidation of 2-D porous unsaturated seabed under a composite breakwater." *Mechanics*, 18(4), 373–379.

Jianhong, Y., Dongsheng, J., Liu, P.-F., Chan, A., Ren, W., and Changqi, Z. (2014). "Breaking wave-induced response of composite breakwater and liquefaction in seabed foundation." *Coastal Engineering*, 85, 72–86.

Klammer, P., Oumeraci, H., and Partenscky, H. (1994). "Oscillatory motions and permanent displacements of caisson breakwaters subject to impulsive breaking wave loads." *Coastal Engineering Proceedings*, 1(24).

Klisinski, M. (1988). "Plasticity theory based on fuzzy sets." *Journal of Engineering Mechanics*, 114(4), 563–582.

Klisinski, M., Abifadel, N., Runesson, K., and Sture, S. (1991). "Modelling of the behavior of dry sand by an elasto-plastic "fuzzy set" model." *Computers and Geotechnics*, 11(3), 229–261.

Kobayashi, N. and Wurjanto, A. (1990). "Numerical model for waves on rough permeable slopes." *Journal of Coastal Research*, 149–166.

Kochina, P. I. (1962). "Theory of ground water movement." *Princeton, NJ, Princeton University Press.*

Kolymbas, D. (1991). "An outline of hypoplasticity." *Archive of applied mechanics*, 61(3), 143–151.

Kolymbas, D. and Wu, W. (1993). "Introduction to hypoplasticity." *Modern approaches to plasticity*, 213–223.

Kortenhaus, A. and Oumeraci, H. (1998). "Classification of wave loading on monolithic coastal structures." *Coastal Engineering Proceedings*, 1(26).

Kortenhaus, A., Oumeraci, H., Kohlhase, S., and Klammer, P. (1994). "Wave-induced uplift loading of caisson breakwater." *Coastal Engineering Proceedings*, 1(24).

Kudella, M. and Oumeraci, H. (2004a). "Pore pressure development in the sand bed underneath a caisson breakwater." *Coastal Engineering conference*, Vol. 29-4, ASCE American society of Civil Engineers, 3800.

Kudella, M. and Oumeraci, H. (2004b). "Wave-induced transient and residual pore pressure in the sand bed underneath a caisson breakwater—processes leading to liquefaction." *Cyclic behaviour of soils and liquefaction phenomena*, 411–424.

Kudella, M. and Oumeraci, H. (2006). "Development of residual pore pressure in the sand bed beneath a caisson breakwater." *Coastal Engineering conference*, Vol. 30-5, ASCE American society of Civil Engineers, 4554.

Kudella, M. and Oumeraci, H. (2008a). "Experimental and numerical study of the response of a sandbed beneath a caisson breakwater subject to cyclic wave load." *Proceedings of the 31st International Conference on Coastal Engineering*, Hamburg, Germany, 3619–3631.

Kudella, M. and Oumeraci, H. (2008b). "Untersuchungen von Küstenschutzbauwerken mit dem numerischen RANS-Modell COBRAS." *FZK-Kolloquium: Potenziale für die Maritime Wirtschaft*.

Kudella, M., Oumeraci, H., De Groot, M., and Meijers, P. (2006). "Large-scale experiments on pore pressure generation underneath a caisson breakwater." *Journal of Waterway, Port, Coastal, and Ocean Engineering*, 132(4), 310–324.

Kumagai, T. and Foda, M. A. (2002). "Analytical model for response of seabed beneath composite breakwater to wave." *Journal of Waterway, Port, Coastal, and Ocean Engineering*, 128(2), 62–71.

Lade, P. V. (1977). "Elasto-plastic stress-strain theory for cohesionless soil with curved yield surfaces." *International Journal of Solids and Structures*, 13(11), 1019–1035.

Lade, P. V. and Inel, S. (1997). "Rotational kinematic hardening model for sand. part I concept of rotating yield and plastic potential surfaces." *Computers and Geotechnics*, 21(3), 183–216.

Le Méhauté, B. et al. (1976). *An introduction to hydrodynamics and water waves*. Springer-Verlag New York.

Lee, F. H., Leung, C. F., and Zhang, X. Y. (2005). *Frontiers in Offshore Geotechnics: ISFOG 2005*. Balkema-proceedings and monographs in engineering, water, and earth sciences, Taylor & Francis, Chapter 61: Performance of caisson breakwater subjected to breaking wave loads.

Lewis, R. W. and Schrefler, B. A. (1998). *The finite element method in the deformation and consolidation of porous media*. John Wiley and Sons Inc., New York, NY.

Lin, P. (2008). *Numerical Modeling of Water Waves*. Taylor & Francis.

Lin, P. and Karunarathna, S. (2007). "Numerical study of solitary wave interaction with porous breakwaters." *Journal of Waterway, Port, Coastal, and Ocean Engineering*, 133(5), 352–363.

Lin, P. and Liu, P. L.-F. (1998). "A numerical study of breaking waves in the surf zone." *Journal of fluid mechanics*, 359(1), 239–264.

Ling, H. I., Cheng, A. H.-D., Mohri, Y., and Kawabata, T. (1999). "Permanent displacement of composite breakwaters subject to wave impact." *Journal of waterway, port, coastal, and ocean engineering*, 125(1), 1–8.

Liu, P. (1985). "Wave-induced pressure under gravity structure." *Journal of Waterway, Port, Coastal, and Ocean Engineering*, 111(1), 111–120.

Liu, P., Lin, P., Chang, K., and Sakakiyama, T. (1999). "Numerical modeling of wave interaction with porous structures." *Journal of Waterway, Port, Coastal, and Ocean Engineering*, 125(6), 322–330.

Liu, X. and García, M. H. (2006). "Numerical simulation of sea bed response under waves with coupled solver of biot consolidation equations and free surface water flow." *proceeding of ISOPE PACOMS*.

Lu, J.-F. and Jeng, D.-S. (2007). "A half-space saturated poro-elastic medium subjected to a moving point load." *International Journal of Solids and Structures*, 44(2), 573–586.

Lubliner, J. (1974). "A simple theory of plasticity." *International Journal of Solids and Structures*, 10(3), 313–319.

Lubliner, J., Taylor, R., and Auricchio, F. (1993). "A new model of generalized plasticity and its numerical implementation." *International journal of solids and structures*, 30(22), 3171–3184.

Lugni, C., Brocchini, M., and Faltinsen, O. (2010a). "Evolution of the air cavity during a depressurized wave impact. I. the kinematic flow field." *Physics of fluids*, 22, 056101.

Lugni, C., Brocchini, M., and Faltinsen, O. (2010b). "Evolution of the air cavity during a depressurized wave impact. II. the dynamic field." *Physics of fluids*, 22, 056102.

Madsen, O. (1978). "Wave-induced pore pressures and effective stresses in a porous bed." *Geotechnique*, 28(4), 377–393.

Manzari, M. T. and Dafalias, Y. F. (1997). "A critical state two-surface plasticity model for sands." *Geotechnique*, 47(2), 255–272.

Mase, H., Sakai, T., and Sakamoto, M. (1994). "Wave-induced pore water pressures and effective stresses around breakwater." *Ocean Engineering*, 21(4), 361–379.

Masuoka, T. and Takatsu, Y. (1996). "Turbulence model for flow through porous media." *International Journal of Heat and Mass Transfer*, 39(13), 2803–2809.

Mazzoni, S., McKenna, F., Scott, M. H., Fenves, G. L., et al. (2006). "OpenSees command language manual." *Pacific Earthquake Engineering Research (PEER) Center.*

Mccorquodale, J. A., Hannoura, A.-A. A., and Sam Nasser, M. (1978). "Hydraulic conductivity of rockfill." *Journal of Hydraulic Research*, 16(2), 123–137.

McKenna, F. et al. (2014). "Open System for Earthquake Engineering Simulations (OpenSees), <http://opensees.berkeley.edu/>.

Mira, P., Tonni, L., Pastor, M., and Fernandez Merodo, J. (2009). "A generalized midpoint algorithm for the integration of a generalized plasticity model for sands." *International journal for numerical methods in engineering*, 77(9), 1201–1223.

Mizutani, N., Mostafa, A. M., and Iwata, K. (1998). "Nonlinear regular wave, submerged breakwater and seabed dynamic interaction." *Coastal Engineering*, 33(2), 177–202.

Moshagen, H. and Torum, A. (1975). "Wave induced pressures in permeable seabeds." *Journal of the Waterways Harbors and Coastal Engineering Division*, 101(1), 49–57.

Mostafa, A. M., Mizutani, N., and Iwata, K. (1999). "Nonlinear wave, composite breakwater, and seabed dynamic interaction." *Journal of Waterway, Port, Coastal, and Ocean Engineering*, 125(2), 88–97.

Mroz, Z. (1967). "On the description of anisotropic work hardening." *Journal of the Mechanics and Physics of Solids*, 15(3), 163–175.

Mroz, Z., Norris, V., and Zienkiewicz, O. (1978). "An anisotropic hardening model for soils and its application to cyclic loading." *International Journal for Numerical and Analytical Methods in Geomechanics*, 2(3), 203–221.

Mroz, Z., Norris, V., and Zienkiewicz, O. (1979). "Application of an anisotropic hardening model in the analysis of elasto–plastic deformation of soils." *Geotechnique*, 29(1), 1–34.

Mroz, Z., Norris, V., and Zienkiewicz, O. (1981). "An anisotropic, critical state model for soils subject to cyclic loading." *Geotechnique*, 31(4), 451–469.

Mynett, A. and Mei, C. (1982). "Wave-induced stresses in a saturated poro-elastic sea bed beneath a rectangular caisson." *Geotechnique*, 32(3), 235–247.

Nakayama, A. and Kuwahara, F. (1999). "A macroscopic turbulence model for flow in a porous medium." *Transactions-American society of mechanical engineers journal of fluids engineering*, 121, 427–433.

Nazem, M., Carter, J., and Airey, D. (2009). "Arbitrary Lagrangian-Eulerian method for dynamic analysis of geotechnical problems." *Computers and Geotechnics*, 36(4), 549–557.

Nazem, M., Sheng, D., Carter, J. P., and Sloan, S. W. (2008). "Arbitrary lagrangian–eulerian method for large-strain consolidation problems." *International journal for numerical and analytical methods in geomechanics*, 32(9), 1023–1050.

Nemat-Nasser, S. and Zhang, J. (2002). "Constitutive relations for cohesionless frictional granular materials." *International Journal of Plasticity*, 18(4), 531–547.

Niemunis, A. *Extended hypoplastic models for soils.*

Niemunis, A. and Herle, I. (1997). "Hypoplastic model for cohesionless soils with elastic strain range." *Mechanics of Cohesive-frictional Materials*, 2(4), 279–299.

Noorzad, R., Safari, S., and Omidvar, M. (2009). "The effect of structures on the wave-induced liquefaction potential of seabed sand deposits." *Applied Ocean Research*, 31(1), 25–30.

Nova, R. and Wood, D. (1979). "A constitutive model for sand in triaxial compression." *International Journal for Numerical and Analytical Methods in Geomechanics*, 3(3), 255–278.

Okusa, S. (1985). "Wave-induced stresses in unsaturated submarine sediments." *Geotechnique*, 35(4), 517–532.

OpenCFD Ltd. (2012). "OpenFOAM, the open source CFD toolbox, user guide".

Ou, J. (2009). "Three-dimensional numerical modelling of interaction between soil and pore fluid." Ph.D. thesis, PhD Thesis, University of Birmingham, UK.

Oumeraci, H. (1994). "Review and analysis of vertical breakwater failures—lessons learned." *Coastal Engineering*, 22(1), 3–29.

Oumeraci, H. (2004). *Planning and design of ports and marine terminals.* Thomas Telford, London, Chapter "Caisson breakwaters", Edited by: Agershou, H.

Oumeraci, H., Burcharth, H., De Rouck, J., Juhl, J., and Losada, M. (1995). " Coastal structures - overview of MAST-2 projects." *XXVIth IAHR Congress-Hydra 2000, Seminar 1: The EC Marine Science and Technology Programme (MAST)* , 70(9), 37 pp.

Oumeraci, H., Klammer, P., and Partenscky, H. (1993). "Classification of breaking wave loads on vertical structures." *Journal of waterway, port, coastal, and ocean engineering*, 119(4), 381–397.

Oumeraci, H. and Kortenhaus, A. (1994). "Analysis of the dynamic response of caisson breakwaters." *Coastal Engineering*, 22(1), 159–183.

Oumeraci, H. and Kortenhaus, A. (1997). "Wave impact loading-tentative formulae and suggestions for the development of final formulae." *Proceedings 2nd Task 1 Workshop, MAST III, PROVERBS-Project: Probabilistic Design Tools for Vertical Breakwaters.*

Oumeraci, H., Kortenhaus, A., Allsop, N., De Groot, M., Crouch, R., Vrijling, J., and Voortman, H. (2001). *PROVERBS-Probabilistic Design Tools for Vertical Breakwaters.* Taylor and Francis, Amsterdam, The Netherlands.

Oumeraci, H. and Kudella, M. (2004). "Liquefaction around marine structures (LIMAS) work package 3." *Technical report of the Leichtweiß-Institute for Hydraulic Engineering and Water Resources*, TU Braunschweig, Germany, 119 pp.

Oumeraci, H., Partenscky, H., Kohlhase, S., and Klammer, P. (1992). "Impact loading and dynamic response of caisson breakwaters." *Coastal Engineering Proceedings*, 1-23.

Parra-Colmenares, E. J. (1996). "Numerical modeling of liquefaction and lateral ground deformation including cyclic mobility and dilation response in soil systems." Ph.D. thesis, Rensselaer Polytechnic Institute, Troy, NY., USA.

Pastor, M., Zienkiewicz, O., and Chan, A. (1990). "Generalized plasticity and the modelling of soil behaviour." *International Journal for Numerical and Analytical Methods in Geomechanics*, 14(3), 151–190.

Pastor, M., Zienkiewicz, O., and Leung, K. (1985). "Simple model for transient soil loading in earthquake analysis. II. non-associative models for sands." *International Journal for Numerical and Analytical Methods in Geomechanics*, 9(5), 477–498.

Prévost, J. (1985). "A simple plasticity theory for frictional cohesionless soils." *International Journal of Soil Dynamics and Earthquake Engineering*, 4, 9–17.

Prévost, J.-H. (1977). "Mathematical modelling of monotonic and cyclic undrained clay behaviour." *International Journal for Numerical and Analytical Methods in Geomechanics*, 1(2), 195–216.

Prévost, J.-H. (1978). "Plasticity theory for soil stress-strain behavior." *Journal of the Engineering Mechanics Division*, 104(5), 1177–1194.

Puech, A. and Foray, P. (2002). "Refined model for interpreting shallow penetration CPTs in sands." *Offshore Technology Conference*, Offshore Technology Conference, Houston, Texas, 6–9.

Rahman, M. and Jaber, W. (1986). "A simplified drained analysis for wave-induced liquefaction in ocean floor sands." *Soils and foundations*, 26(3), 57–68.

Richart, F. E., Hall, J. R., and Woods, R. D. (1970). *Vibrations of soils and foundations.* Prentice-Hall International Series in Theoretical and Applied Mechanics. Prentice-Hall.

Richwien, W. and Perau, E. (2000). "Pore pressure and soil pressure in sandy subsoil beneath a caisson breakwater." *Some Aspects on Subsoil Failure of Vertical Breakwaters, Forschungsberichte aus dem Fachbereich Bauwesen der Universität Essen*, 83, 71–162.

Rollins, K. M. and Seed, H. B. (1990). "Influence of buildings on potential liquefaction damage." *Journal of geotechnical engineering*, 116(2), 165–185.

Rowe, P. (1981). "Use of large centrifuge models for offshore and nearshore works." *Symposium on Geotechnical Aspects of Coastal and Offshore Structures*, Bangkok, 21–33.

Rowe, P., Craig, W., and Procter, D. (1976). "Model studies of offshore gravity structures founded on clay." *Proc. 1st Int. Conf. Behaviour of Offshore Structures (BOSS'76), Trondheim*, 439–448.

Sainflou, M. et al. (1928). "Essai sur les digues maritimes verticales." *Annales des Ponts et Chaussées (in French), Paris 98 (11)*, 4.

Sakakiyama, T. and Liu, P. L.-F. (2001). "Laboratory experiments for wave motions and turbulence flows in front of a breakwater." *Coastal engineering*, 44(2), 117–139.

Sandven, R., Husby, E., Husby, J., Jonland, J., Roksvåg, K., Sthli, F., and Tellugen, R. (2007). "Development of a sampler for measurement of gas content in soils." *Journal of waterway, port, coastal, and ocean engineering*, 133(1), 3–13.

Sawicki, A. (1987). "An engineering model for compaction of sand under cyclic loading." *Engineering Transactions*, 35(4), 677–693.

Sawicki, A. and Świdziński, W. (1989). "Pore pressure generation, dissipation and resolidification in a saturated subsoil." *Soils and foundations*, 29(4), 62–74.

Sawicki, A. and Świdziński, W. (2007). "Simple mathematical model for assessment of seismic-induced liquefaction of soils." *Journal of waterway, port, coastal, and ocean engineering*, 133(1), 50–54.

Sheng, D., Wriggers, P., and Sloan, S. (2007). "Application of frictional contact in geotechnical engineering." *International Journal of Geomechanics*, 7(3), 176–185.

Shimosako, K., Takahashi, S., and Tanimoto, K. (1994). "Estimating the sliding distance of composite breakwaters due to wave forces inclusive of impulsive forces." *Coastal Engineering Proceedings*, 1(24).

Shiomi, T. and Tsukuni, S. (1998). *Poromechanics.* Taylor & Francis, Chapter "Applicntion of Root's dynamic equation to seismic liquification problem", Edited by: Thimus, Jean-François.

Sidarta, D. E. (2000). "Neural network-based constitutive modeling of granular material." Ph.D. thesis, University of Illinois at Urbana-Champaign, USA.

Stickle, M. M. (2010). "Sobre la respuesta dinámica del terreno bajo la acción del oleaje en cajones fondeados en suelos arcillosos." Ph.D. thesis, Caminos, Spain.

Sture, S. (1999). "Constitutive issues in soil liquefaction." *Proceedings in Physics and Mechanics of Soil Liquefaction. Balkema, Rotterdam*, 133–143.

Sulsky, D. (2002). "A numerical study of compaction of dry granular material." *MRS Proceedings*, Vol. 759, Cambridge Univ Press, MM3–1.

Sulsky, D., Chen, Z., and Schreyer, H. L. (1994). "A particle method for history-dependent materials." *Computer Methods in Applied Mechanics and Engineering*, 118(1), 179–196.

Sumer, B. M. and Fredse, J. (2002). *The mechanics of scour in the marine environment.* World Scientific Publishing Company.

Sumer, S. K., Sumer, B. M., Dixen, F. H., and Fredsoe, J. (2008). "Pore pressure buildup in the subsoil under a caisson breakwater." *Proceedings of the ISOPE, 6th -11th July, Vancouver, Canada, pp. 664-671.*

Tamagnini, C., Viggiani, G., and Chambon, R. (2000). "A review of two different approaches to hypoplasticity." *Constitutive modelling of granular materials*, Springer, 107–145.

Tejchman, J., Bauer, E., and Tantono, S. (2007). "Influence of initial density of cohesionless soil on evolution of passive earth pressure." *Acta Geotechnica*, 2(1), 53–63.

The OpenFOAM-Extend Project (2014), <http://www.extend-project.de/>.

Thornton, C. (2000). "Numerical simulations of deviatoric shear deformation of granular media." *Géotechnique*, 50(1), 43–53.

Torum, A. (2007). "Wave-induced pore pressures—air/gas content." *Journal of waterway, port, coastal, and ocean engineering*, 133(1), 83–86.

Tsai, C. (1995). "Wave-induced liquefaction potential in a porous seabed in front of a breakwater." *Ocean Engineering*, 22(1), 1–18.

Tsai, C., Lee, T., and Hsu, J. (2000). "Effect of wave non-linearity on the standing-wave-induced seabed response." *International journal for numerical and analytical methods in geomechanics*, 24(11), 869–892.

Tsai, C.-P. and Lee, T.-L. (1995). "Standing wave induced pore pressures in a porous seabed." *Ocean engineering*, 22(6), 505–517.

Tsai, Y., McDougal, W., and Sollitt, C. (1990). "Response of finite depth seabed to waves and caisson motion." *Journal of waterway, port, coastal, and ocean engineering*, 116(1), 1–20.

Tuković, Ž., Ivanković, A., and Karač, A. (2013). "Finite-volume stress analysis in multi-material linear elastic body." *International Journal for Numerical Methods in Engineering*, 93(4), 400–419.

Ülker, M. and Rahman, M. (2009). "Response of saturated and nearly saturated porous media: Different formulations and their applicability." *International journal for numerical and analytical methods in geomechanics*, 33(5), 633–664.

Ülker, M., Rahman, M., and Guddati, M. (2010). "Wave-induced dynamic response and instability of seabed around caisson breakwater." *Ocean Engineering*, 37(17), 1522–1545.

Ülker, M., Rahman, M., and Guddati, M. (2012). "Breaking wave-induced response and instability of seabed around caisson breakwater." *International Journal for Numerical and Analytical Methods in Geomechanics*, 36(3), 362–390.

Ülker, M., Rahman, M., and Jeng, D.-S. (2009). "Wave-induced response of seabed: Various formulations and their applicability." *Applied Ocean Research*, 31(1), 12–24.

Vaid, Y. P. and Chern, J.-C. (1983). "Effect of static shear on resistance to liquefaction." *Soils sand Foundations*, 23(1), 47–60.

Valanis, K. (1970). "A theory of viscoplasticity without a yield surface. part 1. general theory." *Report no.*, DTIC Document.

Valanis, K. (1975). "On the foundations of the endochronic theory of viscoplasticity." *Archiwum Mechaniki Stosowanej*, 27(5), 857–868.

Valanis, K. and Read, H. (1982). "A new endochronic plasticity model for soils." *Soil mechanics-Transient and cyclic loads*, 30, 375–417.

Van der Poel, J. and De Groot, M. (1998). "Cyclic load tests on a caisson breakwater placed on sand." *Proceedings of the International Conference Centrifuge*, Vol. 98-1, 403–408.

Van Gent, M. (1995). "Porous flow through rubble-mound material." *Journal of waterway, port, coastal, and ocean engineering*, 121(3), 176–181.

Van Gent, M., Tonjes, P., Petit, H., and Van den Bosch, P. (1995). "Wave action on and in permeable structures." *Coastal Engineering Proceedings*, 1(24).

Van Gent, R. (1993). *Stationary and Oscillatory Flow Through Coarse Porous Media.* Communications on hydraulic and geotechnical engineering. Delft University of Technology, Faculty of Civil Engineering.

Vermeer, P. (1978). "A double hardening model for sand." *Geotechnique*, 28(4), 413–433.

Vermeer, P., Beuth, L., and Benz, T. (2008). "A quasi-static method for large deformation problems in geomechanics." *Proceedings of the 12th international conference of international association for computer methods and advances in geomechanics (IACMAG), Goa, India*, 55–63.

Verruijt, A. (1969). "Elastic storage of aquifers." *Flow through porous media*, 331–376.

Verruijt, A. (1982). "Approximations of cyclic pore pressures caused by sea waves in a poro-elastic half-plane." *Soil mechanics—Transient and cyclic loads*, 3, 37–51.

Verruijt, A. and Van Baars, S. (2007). *Soil mechanics.* VSSD.

Walkden, M., Wood, D., Bruce, T., and Peregrine, D. (2001). "Impulsive seaward loads induced by wave overtopping on caisson breakwaters." *Coastal engineering*, 42(3), 257–276.

Wang, H. F. (2000). *Theory of linear poroelasticity: with applications to geomechanics and hydrogeology.* Princeton University Press.

Wang, Y., Zhou, Z., and Yang, H. (2005). "Vibrating-uplift rocking motion of caisson breakwaters under various breaking wave impact forces." *Applied Mathematics and Mechanics*, 26(5), 579–586.

Wang, Y.-Z. (2001). "Motion and stability of caisson breakwaters under breaking wave impact." *Canadian Journal of Civil Engineering*, 28(6), 960–968.

Wang, Z.-L., Dafalias, Y. F., and Shen, C.-K. (1990). "Bounding surface hypoplasticity model for sand." *Journal of engineering mechanics*, 116(5), 983–1001.

Weller, H. (2008). "A new approach to VOF-based interface capturing methods for incompressible and compressible flow." *OpenCFD Ltd., Technical Report TR/HGW/04.*

Wolf, J. P. (1987). "Soil-structure-interaction analysis in time domain." *Structural mechanics in reactor technology*, Prentice-Hall, Englewood Cliffs, NJ.

Wu, W. and Kolymbas, D. (1990). "Numerical testing of the stability criterion for hypoplastic constitutive equations." *Mechanics of materials*, 9(3), 245–253.

Wu, W. and Kolymbas, D. (2000). "Hypoplasticity then and now." *Constitutive modelling of granular materials*, Springer, 57–105.

Yamamoto, T., Koning, H., Sellmeijer, H., and Van Hijum, E. (1978). "On the response of a poro-elastic bed to water waves." *Journal of Fluid Mechanics*, 87(1), 193–206.

Yang, Z. and Elgamal, A. (2001). "Sand boil mechanisms and effects on liquefaction-induced ground deformations." *15th Intl. Conference on Soil Mechanics and Geotechnical Engineering, Istanbul, Turkey*, 345–350.

Yang, Z. and Elgamal, A. (2004). "A multi-surface plasticity sand model including the lode angle effect." *Proceedings of the 17th ASCE Engineering Mechanics Conference*, 13–16.

Yang, Z. and Elgamal, A. (2008). "Multi-surface cyclic plasticity sand model with lode angle effect." *Geotechnical and Geological Engineering*, 26(3), 335–348.

Yang, Z., Elgamal, A., and Parra, E. (2003a). "Computational model for cyclic mobility and associated shear deformation." *Journal of Geotechnical and Geoenvironmental Engineering*, 129(12), 1119–1127.

Yang, Z., He, L., Bielak, J., Zhang, Y., Elgamal, A., and Conte, J. (2003b). "Nonlinear seismic response of a bridge site subject to spatially varying ground motion." *16th ASCE Engineering Mechanics conference, Seattle, Washington*, 1–7.

Ye, J., Jeng, D., Wang, R., and Zhu, C. (2013). "Validation of a 2-D semi-coupled numerical model for fluid–structure–seabed interaction." *Journal of Fluids and Structures*, 42, 333–357.

Ye, J., Jeng, D., Wang, R., and Zhu, C. (2015). "Numerical simulation of the wave-induced dynamic response of poro-elastoplastic seabed foundations and a composite breakwater." *Applied Mathematical Modelling*, 39(1), 322–347.

Ye, J., Zhang, Y., Wang, R., and Zhu, C. (2014). "Nonlinear interaction between wave, breakwater and its loose seabed foundation: A small-scale case." *Ocean Engineering*, 91, 300–315.

Yu, H.-S. (2006). *Plasticity and geotechnics*, Vol. 13. Springer.

Zen, K., Jeng, D., Hsu, J., and Ohyama, T. (1998). "Wave-induced seabed instability: Difference between liquefaction and shear failure." *Soils and foundations*, 38(2), 37–47.

Zen, K., Umehara, Y., and Finn, W. (1986). "A case study of the wave-induced liquefaction of sand layers under damaged breakwater." *Proceedings of the 3rd Canadian Conference on Marine Geotechnical Engineering*, St. John's, Newfound-land, 505–520.

Zen, K. and Yamazaki, H. (1990). "Mechanism of wave-induced liquefaction and densification in seabed." *Soil and Foundations*, 30(4), 90–104.

Zhang, J.-S., Jeng, D.-S., and Liu, P.-F. (2011). "Numerical study for waves propagating over a porous seabed around a submerged permeable breakwater: PORO-WSSI II model." *Ocean Engineering*, 38(7), 954–966.

Zhang, X. (2006). "Behaviour of caisson breakwater subject to breaking waves." Ph.D. thesis, National University of Singapore, Singapore.

Zhang, X., Lee, F., and Leung, C. (2009a). "Tilt displacement of caisson breakwater due to wave loading." *Géotechnique*, 59(1), 17–27.

Zhang, X., Leung, C., and Lee, F. (2009b). "Centrifuge modelling of caisson breakwater subject to wave-breaking impacts." *Ocean Engineering*, 36(12), 914–929.

Zhang, Y., Yang, Z., Bielak, J., Conte, J., and Elgamal, A. (2003). "Treatment of seismic input and boundary conditions in nonlinear seismic analysis of a bridge ground system." *16th ASCE Engineering Mechanics Conference*, University of Washington, Seattle, USA, 16–18.

Zienkiewicz, O., Chan, A. H. C., Pastor, M., Schrefler, B. A., and Shiomi, T. (1999). *Computational geomechanics with special reference to earthquake engineering*. John Wiley & Sons.

Zienkiewicz, O., Chang, C., and Bettess, P. (1980). "Drained, undrained, consolidating and dynamic behaviour assumptions in soils." *Geotechnique*, 30(4).

Zienkiewicz, O., Chang, C., and Hinton, E. (1978). "Non-linear seismic response and liquefaction." *International Journal for Numerical and Analytical Methods in Geomechanics*, 2(4), 381–404.

Zienkiewicz, O., Leung, K., and Pastor, M. (1985). "Simple model for transient soil loading in earthquake analysis. i. basic model and its application." *International journal for numerical and analytical methods in geomechanics*, 9(5), 453–476.